Max-Planck-Institut für Kolloid- und Grenzflächenforschung

Toward Ultimate Control of Polymerization and Catalytic Property: A Combination of Metal-Organic Frameworks and ATRP

Dissertation

zur Erlangung des akademischen Grades
Doktor der Naturwissenschaften (Dr. rer. nat.)
in der Wissenschaftsdisziplin „Kolloid- und Polymerchemie"

eingereicht an der
Mathematisch-Naturwissenschaftlichen Fakultät
der Universität Potsdam

von

Hui-Chun Lee

Geboren am 14.06.1989
aus Kaohsiung, Taiwan

Potsdam-Golm, im November, 2017

Acknowledgement

Acknowledgement

It reminisces me the day I left home, a sunny day in Taiwan. My feeling was extremely complicated, afraid, nervous and exciting, because I had prepared for this moment for a long time and was going to explore this world, but this time without my beloved family. Always, time flies faster than our imagination. It has been more than two years since I am here in German to pursue my doctor degree, a country where I am getting used to. The concerns in language, culture and social life have been resolved one by one with the help of people in the MPI big family and their positive encouragement as well as accompany.

At the beginning, I would like to devote me appreciation toward Deutscher Akademischer Austauschdienst (DAAD). As a governmental sector, it provides foreign students opportunity to go on their research education in German with both powerful financial and life support, and it also serves as an approvement of us scholarship holders'capacity. It's my pleasure to be imparted with this grant and conduct my doctor research in Germany, since the working condition here in Europe is quite different from Asia where time is usually strappted and therefore limited deep thinking.

Although the work is sometimes harsh, I really enjoy this two-year experiment life. I would like to thank Prof. Markus Antonietti for giving the chance to work here with other interdisciplinary researchers in Kolloidchemie , and because of his reliance and support the topics can be conducted and achieved in a very efficient fashion. Besides, I would like to thank my group leader, Dr. Bernhard Schmidit, the research will not be such vivid without his trust and open mind, even though we always fight for distinct opinions. My secondary supervisor, Prof. Helmut Schlaad, always encourages me to experience the life in varied ways to balance the hard Lab working a daily living. Due to my limited polymer and material background, I would like to thank Prof. Uwe Schilde for the strong assistance in crystal analysis, Prof. Krzysztof Matyjaszewski for the helpful discussion and suggestion, and Prof. Ming-Chia Li for the instruction and illustration of organic synthesis.

This thesis can't be completed without tremendous assistance from people. I would like to thank Marlie for always taking care of our Lab and measuring incredible amount of SEC samples during my two-year study, and Irina and Regina for teaching how to use the glovebox and BET individually. They three technicians are just like my Mama in Germany, sharing their positive wishes and warm embraces to me while I was depressed. It's is also a nice experience to work with my colleagues Jochen, Chris, Noah, Baris, Kook, Jianrui and Youjia.

Except the working life, I am pretty sure, the annualy Christmas Party holded by Mica and Axel always gathers us, me, Max, Vale, Martina, Afro, Robeta, Jack, Selin and Elliot, together. Just like a lovely big family, we enjoy the Greek Robin cake, Italian Tiramisu, home-made pizza, Turkish Hummus, German Glühwein and Chinese hot pot, chatting and sharing with others our individual life. I am pretty sure the friendship and attitude towards life is the most treasure part I have learned during this voyage. Besides, as the only one Taiwanese in this huge campus, I also appreciate the thoughtful consideration from all Chinese friends who speak similar language like me and cook dishes with my reminiscent flavors. Without my Chinese group, I might suffer from a longer hard time for home sick.

Last but also the most important, I would like to thank my family. With their understanding, I am able to conduct my study in a foreign country far away from my hometown, Taiwan, with devoted concentration. Thanks my parents to taking care of our family and grandparents while they are handing on their business. Also, thanks my uncles, aunties, cousins and my dear sister and brother for

Acknowledgement

their encouragement and inspiration during this period, enabling me to defeat the each-time depression. It's always amazing to my dear partner Ying. Sometimes, I feel proud of ourselves, because we are dared to take adventure to explore this eminent world, enjoy in the process and finally become further mature together. How lucky am I to have such nice family in my life.

In the end, I would like to reemphasize my appreciation to people who I meet during this period, and my life is significantly enriched with the treasure memory formed by all of you.

HC

MPI, Golm, 18/12/2017

致謝

致謝

一樣的時光飛逝。

記得當初拎著兩只行李箱，身上背著筆電、書，手裡抱著新買德規的大同電鍋，踏出家門，開始一個人的旅程！

初來乍到，所有一切歐洲的事物對我而言都是考驗！熟悉的 ICE、TGV、巧克力、超市讓我無時無刻不想家；陌生的環境、語言、文化不斷的挑戰與顛覆我舊有的認知及適應力。腹背受敵，潰不成軍是家常便飯！好在，過往在清華的訓練還算扎實，在德國的生活就從起床開始戰鬥，轉變到漸漸適應，以及現在的部分認同。即將邁入下個階段。

能夠到德國來唸博士班，首先必須感謝德國政府 DAAD 的獎學金，不僅限於生活上的補助，它也是對過去研究成果的認可，並提供許多機會讓留德學生能夠進一步認識所處環境的文化。沒有 DAAD，我想，或許我沒有機會體驗到這麼獨特且難忘的，記憶。

一路上，從 Mannheim 的德語課到 MPI 的實驗室人生，感謝好多朋友的幫助，讓離家好遠好遠的我，知道世界很大，真的很大！若想要好好的探索這個世界，不留下太多遺憾，我沒有多餘的時間蜷縮在角落、自怨自艾，學會調適自己的情緒，面對正面與負面的自己，與自己對話、相處才能讓我不虛此行，更加強壯！感謝 Sarori、Anne、Mario、Natsuki 以及 Koh 一起的兩個月德語人生與南德小村莊初體驗。

念博士班的目的，就像每一次的旅行，對我而言依舊是難以定義。做實驗的辛苦和掙扎，大概只有曾經身歷其中的人才有辦法揣摩那其中的甘甜和苦澀！很開心我有機會嘗試，也很高興自己跨出了那一步，那機會和過程如此難能可貴！脫離我的舒適圈，才有機會認清自己想要和需要的是什麼，也才會更加珍惜並滿足自己所擁有的一切並學會尊重那屬於別人的光輝！同碩士班畢業時我對自己的形容，我還是桀敖不馴，但不同的是，我開始學著放慢腳步，在焦急的時候讓自己喘口氣、在森林裡雪中慢跑、觀察周遭景觀的變化。慢慢來，好像真的有比較快！

就這樣，兩年過去了，好像念博士班是附帶價值般，柏林馬拉松完賽，雖然還不是很多，但我們的足跡開始在歐洲這片大陸上散開！

實驗室人生中，感謝 Prof. Markus Antonietti 的支持與信賴，讓我有機會在 Kolloidchemie Institute 盡情地嘗試努力地玩科學。這絕對是在台灣，難能可貴的經驗！感謝我的 group leader Dr. Bernhard Schmidt，因為他的絕對信任和對科學的開放想法，讓做實驗和博士班充滿許多可能。兩年的博士生涯，無論是在實驗或是日常生活中，因為有了好多人的鼓勵、砥礪和陪伴，讓這段日子雖然辛苦但不孤單！感謝 Mica、Axel、Max、Vale、Martina、Afro、Robeta、Jack、Selin、Elliot，每年的 Christmas Party 都讓我覺得好溫馨，圍繞著希臘的 Robin Cake、義大利的提拉米蘇、德國 Glühwein、創意 pizza、土耳其 Hummus、火鍋餃子，我們就像個大家庭，彼此加油打氣，安撫我們離鄉背井想家的心靈。當然還有害羞的 Sasha，和他教我的烏克蘭 Sasha Mama Soups。

實驗上的未知與複雜程度，使得博士班的難度更甚碩士班，但感謝好多人的幫助和建議，我們一起逐一地克服了。謝謝 Marlies、Irina、Regina 她們就像我在德國的媽媽，耐心的陪我練習德

致謝

文，在我遇到阻礙時鼓勵我，給我她們溫暖的擁抱和祝福。謝謝遠在台灣的明家學長，從碩士班罩到博士班，讓沒有化學底子的我，也有模有樣的學起別人做合成和分析，一圓我見到兩位偶像老師 Prof. Krzysztof Matyjaszewski 和 Prof. Axel H.E. Müller 的宿願！

作為全 MPIKG 唯一的台灣人，感謝所有跟我說一樣語言夥伴的照顧，高博、鞏江、帶我進入 MOF 領域的孫博，常常餵食我的惠娟，王博和婷婷學姊、聰霄、春祥、Eddie、曉茜、葉舟、衛懿，每天早上被我嚇到的健瑞以及他的爸爸們，謝謝你們大家的陪伴和照顧。即便我們離開了 MPI，回到各自的城市，奔波忙碌，我們會再見面的，延續二樓 Coffee Corner 的微醺暢談。

最後

謝謝我的家人

謝謝爸媽，在處理公司繁雜業務的同時，還要時不時擔心時常"失聯"的女兒，照顧自己同時還要兼職寵物褓姆，幫我們照顧阿公阿嬤。

謝謝威、怡婷和舅舅舅媽們，幫我們照顧媽媽。讓孩子都不在身邊的她，不至於太孤單。

謝謝李小群和李小輝，常常很累、失去鬥志的時候，只要跟你們聊聊天或看到你們的留言，就會恢復一點。雖然我們離的好遠好遠，以後也不見得能陪在彼此身邊，但我想我們知道，李家小屁孩的韌性，即便努力的讓自己往嚮往的方向奔去，家是我們的心之所向，不曾改變。

謝謝老大。從沒想過，兩個人可以一起玩遍歐洲，"順便"念書，一起經歷的好多事，讓距離對於我們越來越不是問題，豐富了生活，也使彼此更加有默契，有時想想這樣的經歷真是獨特。謝謝，我在德國唯一的親人。

我的寶貝，你過的好嗎？謝謝你代替我，陪著媽媽。2017/04/27 你是我博士班最大的遺憾。我相信，你知道我有多想念你。希望你過得好好的。

HC

2017/12/18 MPI, Potsdam

Abstract

Abstract

Reversible-deactivation radical polymerization (RDRP) is without any doubt one of the most prevalent and powerful strategies for polymer synthesis, by which well-defined living polymers with targeted molecular weight (MW), low molar dispersity ($Đ$) and diverse morphologies can be prepared in a controlled fashion. Atom transfer radical polymerization (ATRP) as one of the most extensive studied types of RDRP has been particularly emphasized due to the high accessibility to hybrid materials, multifunctional copolymers and diverse end group functionalities via commercially available precursors. However, due to catalyst-induced side reactions and chain-chain coupling termination in bulk environment, synthesis of high MW polymers with uniform chain length (low $Đ$) and highly-preserved chain-end fidelity is usually challenging. Besides, owing to the inherited radical nature, the control of microstructure, namely tacticity control, is another laborious task. Considering the applied catalysts, the utilization of large amounts of non-reusable transition metal ions which lead to cumbersome purification process, product contamination and complicated reaction procedures all delimit the scope ATRP techniques.

Metal-organic frameworks (MOFs) are an emerging type of porous materials combing the properties of both organic polymers and inorganic crystals, characterized with well-defined crystalline framework, high specific surface area, tunable porous structure and versatile nanochannel functionalities. These promising properties of MOFs have thoroughly revolutionized academic research and applications in tremendous aspects, including gas processing, sensing, photoluminescence, catalysis and compartmentalized polymerization. Through functionalization, the microenvironment of MOF nanochannel can be precisely devised and tailored with specified functional groups for individual host-guest interactions. Furthermore, properties of high transition metal density, accessible catalytic sites and crystalline particles all indicate MOFs as prominent heterogeneous catalysts which open a new avenue towards unprecedented catalytic performance. Although beneficial properties in catalysis, high agglomeration and poor dispersibility restrain the potential catalytic capacity to certain degree.

Due to thriving development of MOF sciences, fundamental polymer science is undergoing a significant transformation, and the advanced polymerization strategy can eventually refine the intrinsic drawbacks of MOF solids reversely. Therefore, in the present thesis, a combination of low-dimensional polymers with crystalline MOFs is demonstrated as a robust and comprehensive approach to gain the bilateral advantages from polymers (flexibility, dispersibility) and MOFs (stability, crystallinity). The utilization of MOFs for in-situ polymerizations and catalytic purposes can be realized to synthesize intriguing polymers in a facile and universal process to expand the applicability of conventional ATRP methodology. On the other hand, through the formation of MOF/polymer

Abstract

composites by surface functionalization, the MOF particles with environment-adjustable dispersibility and high catalytic property can be as-prepared.

In the present thesis, an approach via combination of confined porous textures from MOFs and controlled radical polymerization is proposed to advance synthetic polymer chemistry. $Zn_2(bdc)_2(dabco)$ (Znbdc) and the initiator-functionalized Zn MOFs, ZnBrbdc, are utilized as a reaction environment for in-situ polymerization of various size-dependent methacrylate monomers (i.e. methyl, ethyl, benzyl and isobornyl methacrylate) through (surface-initiated) activators regenerated by electron transfer (ARGET/SI-ARGET) ATRP, resulting in polymers with control over dispersity, end functionalities and tacticity with respect to distinct molecular size. While the functionalized MOFs are applied, due to the strengthened compartmentalization effect, the accommodated polymers with molecular weight up to 392,000 can be achieved. Moreover, a significant improvement in end-group fidelity and stereocontrol can be observed. The results highlight a combination of MOFs and ATRP is a promising and universal methodology to synthesize versatile well-defined polymers with high molecular weight, increment in isotactic trial and the preserved chain-end functionality.

More than being a host only, MOFs can act as heterogeneous catalysts for metal-catalyzed polymerizations. A Cu(II)-based MOF, $Cu_2(bdc)_2(dabco)$, is demonstrated as a heterogeneous, universal catalyst for both thermal or visible light-triggered ARGET ATRP with expanded monomer range. The accessible catalytic metal sites enable the Cu(II) MOF to polymerize various monomers, including benzyl methacrylate (BzMA), styrene, methyl methacrylate (MMA), 2-(dimethylamino)ethyl methacrylate (DMAEMA) in the fashion of ARGET ATRP. Furthermore, due to the robust frameworks, surpassing the conventional homogeneous catalyst, the Cu(II) MOF can tolerate strongly coordinating monomers and polymerize challenging monomers (i.e. 4-vinyl pyridine, 2-vinyl pyridine and isoprene), in a well-controlled fashion. Therefore, a synthetic procedure can be significantly simplified, and catalyst-resulted chelation can be avoided as well. Like other heterogeneous catalysts, the Cu(II) MOF catalytic complexes can be easily collected by centrifugation and recycled for an arbitrary amount of times.

The Cu(II) MOF, composed of photostimulable metal sites, is further used to catalyze controlled photopolymerization under visible light and requires no external photoinitiator, dye sensitizer or ligand. A simple light trigger allows the photoreduction of Cu(II) to the active Cu(I) state, enabling controlled polymerization in the form of ARGET ATRP. More than polymerization application, the synergic effect between MOF frameworks and incorporated nucleophilic monomers/molecules is also observed, where the formation of associating complexes is able to adjust the photochemical and electrochemical properties of the Cu(II) MOF, altering the band gap and light harvesting behavior. Owing to the tunable photoabsorption property resulting from the coordinating guests, photoinduced

Abstract

Reversible-deactivation radical polymerization (PRDRP) can be achieved to further simplify and fasten the polymerization.

More than the adjustable photoabsorption ability, the synergistic strategy via a combination of controlled/living polymerization technique and crystalline MOFs can be again evidenced as demonstrated in the MOF-based heterogeneous catalysts with enhanced dispersibility in solution. Through introducing hollow pollen pivots with surface immobilized environment-responsive polymer, PDMAEMA, highly dispersed MOF nanocrystals can be prepared after associating on polymer brushes via the intrinsic amine functionality in each DMAEMA monomer. Intriguingly, the pollen-PDMAEMA composite can serve as a "smart" anchor to trap nanoMOF particles with improved dispersibility, and thus to significantly enhance liquid-phase photocatalytic performance. Furthermore, the catalytic activity can be switched on and off via stimulable coil-to-globule transition of the PDMAEMA chains exposing or burying MOF catalytic sites, respectively.

Content

Content

Content

Content

1. Introduction

The modern world without polymers is hard to imagine. A wide variety of polymer materials are utilized in the contemporary society in the form of bulk, blends or block copolymers either in liquid, crystals, gels, micellar, colloidal or multiple layer phases. No matter what kind of combination is taken, it will be implied by the collective behavior of multiple polymer chains, resulting in particular material property,[1] such as daily food, containers, gasoline and synthetic fibers.

Traditional radical polymerization (RP) is employed to synthesize polymers within the range of 100 million tonnes worldwide each year. However, due to the very limited uniformity and mixed structure in these polymers, polymers prepared by RP are mostly applied for commodity product with low precision requirement, such as plastics, rubbers and fibers. For high-value applications, precise control over architectures, compositions and functionalities of polymers is highly demanded, because it is a prerequisite to obtain functional materials with desired properties. Therefore, the establishment of controlled / living radical polymerization[2] or the so-called reversible-deactivation radical polymerization (RDRP) has been developed to refine and advance synthetic polymer science.[3]

Atom transfer radical polymerization (ATRP) is one of the most extensive studied branches of RDRP, by which well-defined living polymers with targeted molecular weight (MW), low dispersity ($Đ$) and diverse topology can be prepared.[4-8] Compared to other RDRP strategies, such as nitroxide mediated polymerization (NMP) and reversible addition-fragmentation chain transfer (RAFT), the universality and comparability of ATRP are wider, contributing higher accessibility to hybrid materials, multifunctional copolymers and diverse end group functionalities. However, attributed to catalyst-induced side reactions and chain-chain termination in bulk environment, high MW polymers with controlled molecular weight distribution (MWD) and high chain-end fidelity are usually hardly achieved.[9-10] When it comes to control of microstructure, inherited radical nature makes tacticity control difficult for ATRP as well. Furthermore, the utilization of large amounts of non-reusable transition metal catalysts which lead to laborious purification or product contamination and tedious reaction procedures all delimit the scope ATRP techniques.

The precision of microstructure in natural products has always been a role-model for synthetic polymers.[11-12] Natural polymerizations demonstrate that an universal principle towards well defined biopolymers is the design of proper confined space as microenvironment for specific molecular interaction.[13-14] Chaperones, for example, as one of the most important bio-machinery equipped with the characteristic hollow-shaped chamber conduct the assembly and folding of polypeptides so as to give native bio-macromolecules with defined tertiary structure and proper function.[15] Furthermore, the precision of steric structure can be re-strengthened with the incorporation of specific trigger factors

inside the hollow chamber.[16] Another example is the primer-directed approach for transcription of large DNA sequences. [17] Theoretical studies also point out that well-defined high MW polymers with improved end group fidelity can be synthesized by taking advantage of the compartmentalization effect which considerably restrains the termination and deactivation processes.[18-19] As a result, inspired by nature, researchers have utilized porous materials such as liquid crystals,[20] stereoregular polymers,[21-22] porous silica,[23-24] zeolites,[25-26] and metal-organic frameworks (MOFs)[27-28] as confined environment for polymerizations to improve controllability of polymer structures.

Triggered by the thriving development of material sciences, fundamental polymer science is collaterally undergoing a significant transformation.

MOFs are a new category of porous materials which unify both organic and inorganic properties, featuring well-ordered crystal structure, high specific surface area, tunable pore sizes / shapes and high degree of tailorable surface functionalities. These advantageous properties have contributed to a profound connection to significantly enhance progression of applications, such as gas processing,[29-30] sensing,[31-32] catalysis,[33-36] and confined space for polymerization.[37-39] Taking advantage of the highly adjustable channel microenvironment, the sites of functional groups and the structure of the channels in MOFs becomes highly specified for individual guest monomers, and then after in-situ polymerization high-dimensional polymers with controlled structures can be synthesized, giving unprecedented polymers with advanced structure and distinct properties.

Along with polymer synthesis, catalytic materials are of importance in scientific and industrial fields. Due to the high transition metal density, accessible catalytic sites[40] and the featuring highly-diversified categories as well as the convenient separation, MOFs have been predicted as potential heterogeneous catalysts which may contribute unprecedented performance highly comparable to current catalytic materials. Therefore with the ever-developing MOF science, the introduction of MOF complexes into multiple dimensions can provide other promising probability to explore the catalytic potential of MOFs and at the same time to develop state-of-the-art catalysts.

In the present thesis, the utilization of MOFs for catalytic purpose and intriguing polymer synthesis will be mainly emphasized in the following pages.

2. Research Background and Literature Overview

2.1 Atom Transfer Radical Polymerization

2.1.1 Reversible deactivation radical polymerizations (RDRP)

Within the past decades, reversible-deactivation radical polymerization (RDRP) is regarded as one of the most robust and prevalent strategies for polymer synthesis due to ever-advanced procedures which enable (co)polymerization of comprehensive monomers to fabricate well-defined polymers.[4, 41] Especially, through a reversible deactivation procedure, a dynamic equilibrium between dormant species and propagating radicals can be achieved; therefore the chain transfer and termination can be reduced efficiently ($\approx$ 1-10 mol %) which realizes the characteristic living/controlled property and gives access to polymers with desired molecular weight (MW), low molecular weight dispersity ($Đ$), diverse composition, topology and functionality (Figure 2.1a).[3, 41-43]
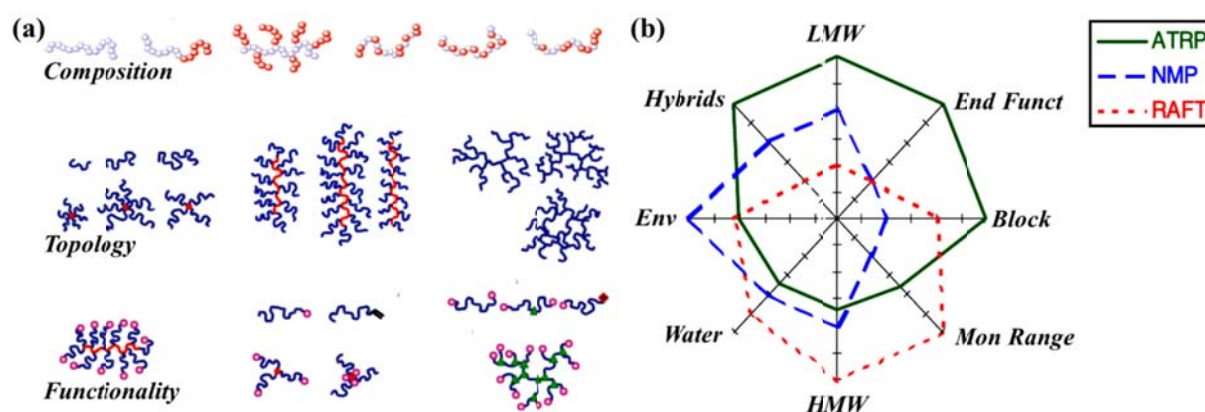
Figure 2.1 (a) Complex architecture devised by combination of multiple structural factors. (b) Comparison of NMP, ATRP and RAFT in the areas related to the synthesis of high molecular weight polymers (HMW), low molecular weight polymers (LMW), end functional polymers (End Funct), block copolymers (Blocks), range of polymerizable monomers (Mon Range), synthesis of various hybrid materials (Hybrids), environmental issues (Env) and polymerization in aqueous media (Water). Figure (a) reprinted with permission from Nature Chemistry (2009)[42] and Figure (b) reprinted with permission from Elsevier (2007).[41]

Several techniques have been established to reach such an equilibrium, for examples, atom transfer radical polymerization (ATRP),[5, 44] nitroxide mediated polymerization (NMP)[7, 45] and the reversible addition-fragmentation chain transfer (RAFT) process.[46-47] Generally, the required dynamic equilibrium can be approached via two directions. On one hand, the propagating radicals are reversibly deactivated to form dormant species which can be repeatedly reactivated either by the transition metal (i.e. ATRP), or the persistent radical effect (i.e. NMP). On the other hand, the degenerate transfer between propagating radicals and a dormant species is applied with the utilization of external radical

sources, which is namely degenerative transfer radical polymerization (DTRP), such as RAFT.[41] All RDRP techniques have in common that degree of polymerization (*DP*) increases linearly corresponding to monomer conversion and low *Đ* are achieved, or block copolymers can be obtained by sequential monomer addition. However, each system features advantages and drawbacks according to different purpose and reaction condition (Figure 2.1b),[48] and the developed strategies are required to be improved to expand the usability.[41, 48] Comparatively, ATRP provides wider universality and comparability owing to the higher accessibility to hybrid materials, multifunctional block copolymers and facile end-functionalization. Other properties including commercially available initiators and widely-accepted temperatures all make ATRP a powerful tool for polymer synthesis.

2.1.2 Mechanism and Kinetics

ATRP is a catalytic process which is mediated via redox-active transition metal complexes including Cu, Ag, Ru, Fe, Mo, Os.[49] Take the most prevalent Cu^I/L and $Br-Cu^{II}/L$ (L = halide ligands) as an example, the polymerization is predominately controlled by an equilibrium between propagating radicals ($P_n\cdot$) and dormant species (P_n-Br). Depending on active rate constant k_{act}, the dormant species periodically react with reduced Cu complexes, Cu^I/L, acting as activators to intermittently form propagating radicals ($P_n\cdot$) accompanied with oxidized Cu complexes, $Br-Cu^{II}/L$, serving as deactivators (Scheme 2.1).[5] Reversely, the deactivators react with the propagating radicals to re-form the dormant species and the activator under the rate constant of deactivation (k_{deact}).

The rate of ATRP (R_p) depends on the propagation constant (k_p) and the concentrations of monomer ([M]) as well as growing radicals ($[P_n\cdot]$). The radical concentration fluctuates according to the ATRP equilibrium constant ($K_{ATRP} = k_{act}/k_{deact}$) and the concentration of dormant species ($[P_n-Br]$), activators (Cu^I/L), and deactivators ($Br-Cu^{II}/L$), as shown in Equation 1:

$$R_p = k_p[M][P_n \bullet] = k_p K_{ATRP} \frac{[P_n \bullet][Cu^I/L][M]}{[Br-Cu^{II}/L]} \tag{1}$$

The polymerization rate increases in line with catalysts activity (K_{ATRP}), but it could decrease due to radical termination which results in a higher concentration of deactivators and then lower $[Cu^I/L]/[Br-Cu^{II}/L]$ ratio. The quality of synthesized polymers can be evaluated based on the polydispersity index or molecular weight dispersity (PDI = $M_w/M_n = Đ$). Equation 2 shows ideally how *Đ* is influenced by the degree of polymerization (DP_n), the concentration of dormant species (P_n-Br) and deactivator ($Br-Cu^{II}/L$), constants of propagation (k_p) and deactivation (k_{deact}), and monomer conversion (p), under the assumption of fast initiation without chain termination or chain transfer.[50-51]

$$\frac{M_w}{M_n} = 1 + \frac{1}{DP_n} + \frac{k_p[P_n-Br]}{k_{deact}[Br-Cu^{II}/L]}\left(\frac{2}{p} - 1\right) \tag{2}$$
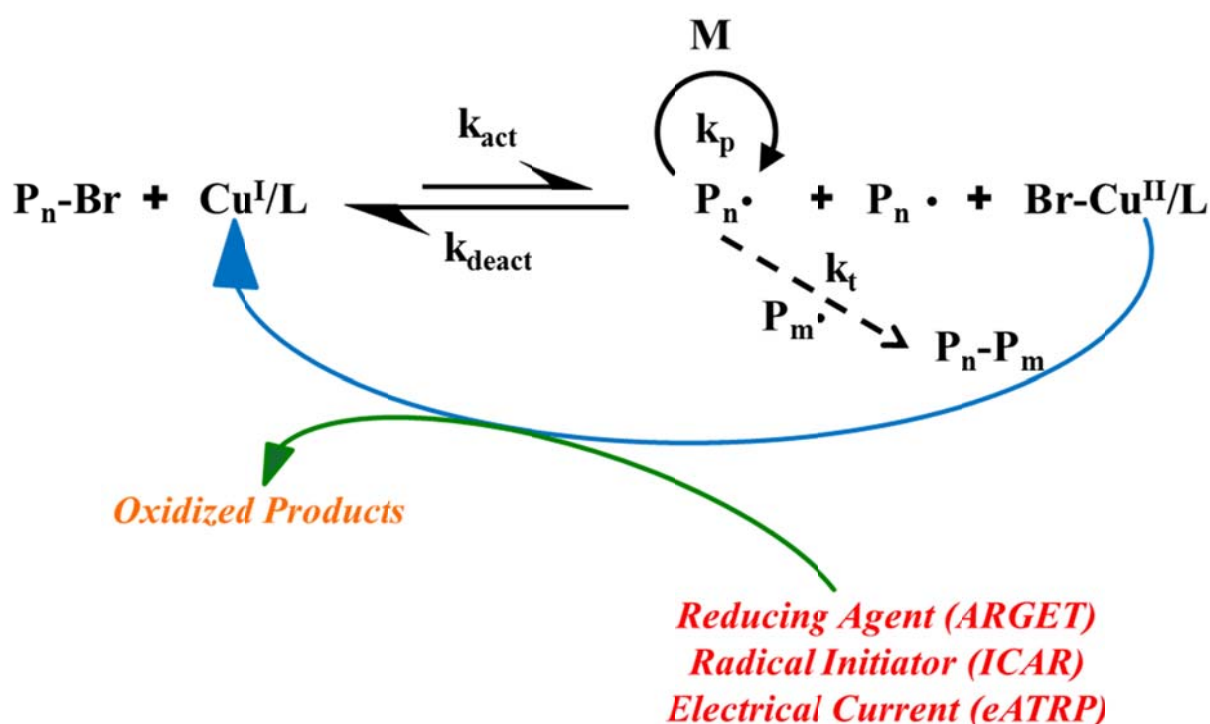
Scheme 2.1 Mechanism of currently evolved ATRP systems with the fundamental ATRP pathway depicted in dark. The modified processes depicted in color are activators regenerated by electron transfer (ARGET), initiators for continuous activator regeneration (ICAR) and electrochemical controlled ATRP, separately. In the modified systems the Cu^I/L activator is continuously regenerated from the X−Cu^{II}/L deactivator in all systems using a free radical initiator (ICAR), reducing agents (ARGET), or an electrical current (eATRP).

2.1.3 Applicability and Reaction Conditions

Referring to Equation 2, well-defined polymers with lower Đ can be achieved by choosing a catalyst which deactivates the propagating chains faster (smaller k_p/k_{deact}), increasing the concentration of deactivator, reducing the concentration of dormant species (higher MW attempt), or targeting on higher conversion. However, for a given monomer, the combined structure of catalyst/ligand complex, monomer/dormant concentration and applied reaction conditions can result in distinct polymerization processes by varying the values of k_{act},[52] k_{deact},[53-54] and K_{ATRP}[54-55] as well.

A small K_{ATRP} ($\sim10^{-9}$ to$\sim10^{-4}$) is a prerequisite for a low radical concentration and minimized termination, and consequently, guides for catalytic complex selection have been launched to match a catalyst with a proper initiator/ligand[56] to optimize the polymerization of specific monomer. As illustrated in Figure 2.2,[53] by using the same initiator, ethyl α-bromoisobutyrate (EBIB), the K_{ATRP} can be significantly altered while associating with ligands in different structures. Generally, the reactivity of catalysts is in line with the comprised amount of nitrogen in the applied ligand, by which Cu^{II} ions

can be stabilized in a better way; namely, the activity increase following the stream: aryl amine < aryl imine << alkyl imine < pyridine ≈ alkyl amine.[53, 57-59]
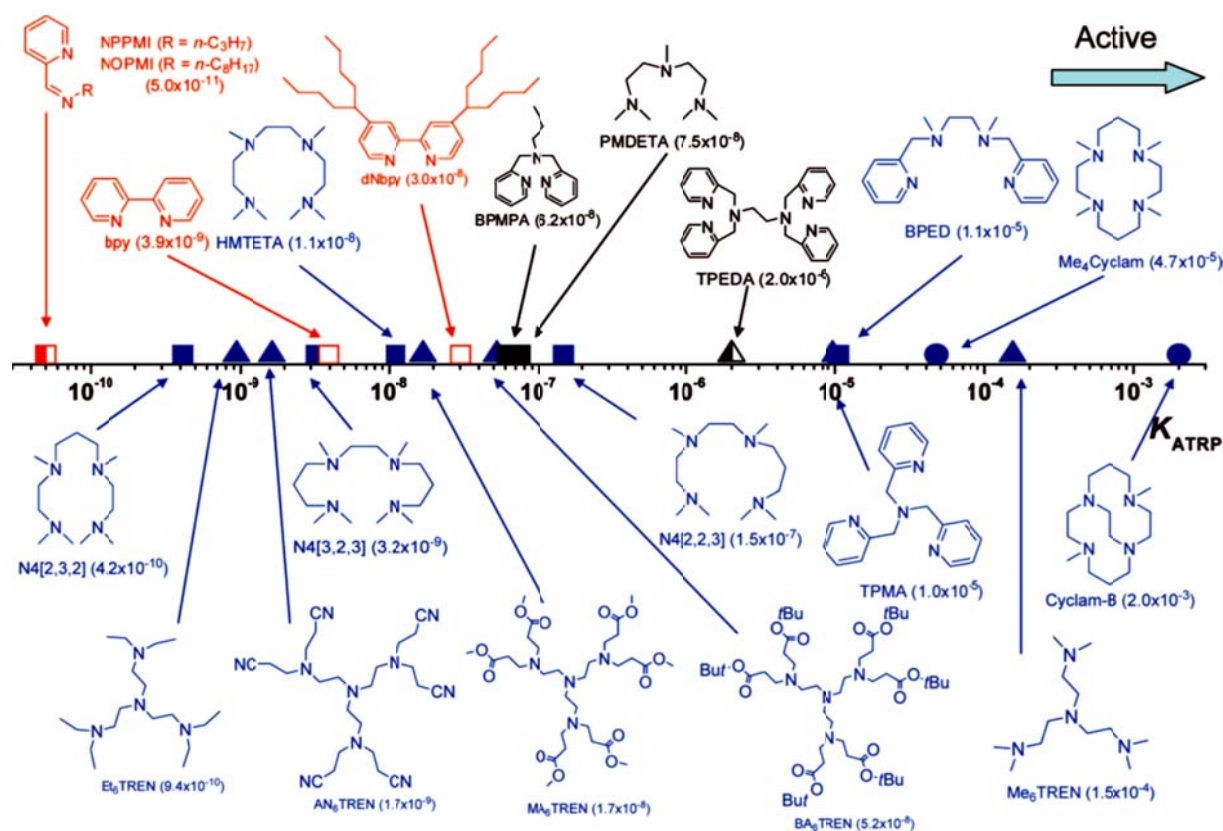
Figure 2.2 ATRP equilibrium constants (K_{ATRP}) for various N-based ligands using EBIB as the initiator and Cu^{I}Br as catalyst. The ligands contain different amount of N are indicated by colors: red for N2; black for N3 and N6; blue for N4. The molecular structures of ligands are distinguished by symbols: solid for amine/imine; open for pyridine; left-half-solid for mixed; □ for linear; Δ for branched; ○ for cyclic. Figure reprinted with permission from American Chemical Society (2008).[53]

Similarly, applying the same catalytic complex, Cu^{I}X / tris[(2-pyridyl)methyl]amine (TPMA), the K_{ATRP} can be adjusted via choosing initiators with different structures as well (Figure 2.3).[53] Typically, the equilibrium constant increases following the substitution degree, radical-stabilizing group and the leaving group of the applied initiator. That is, a tertiary ester contributes a higher K_{ATRP} than a secondary and then a primary one; a nitrile substituent next to the C-X bond is more active than phenyl groups and then to ester groups; the Br atom as the leaving group is more reactive than Cl and then iodide (I).

As a result, accessible to a wide range of initiators and catalyst/ligand complexes, ATRP can provide tailor-made reaction equilibrium constants to optimize the polymerization process of specific monomer with targeting polymerization purpose.
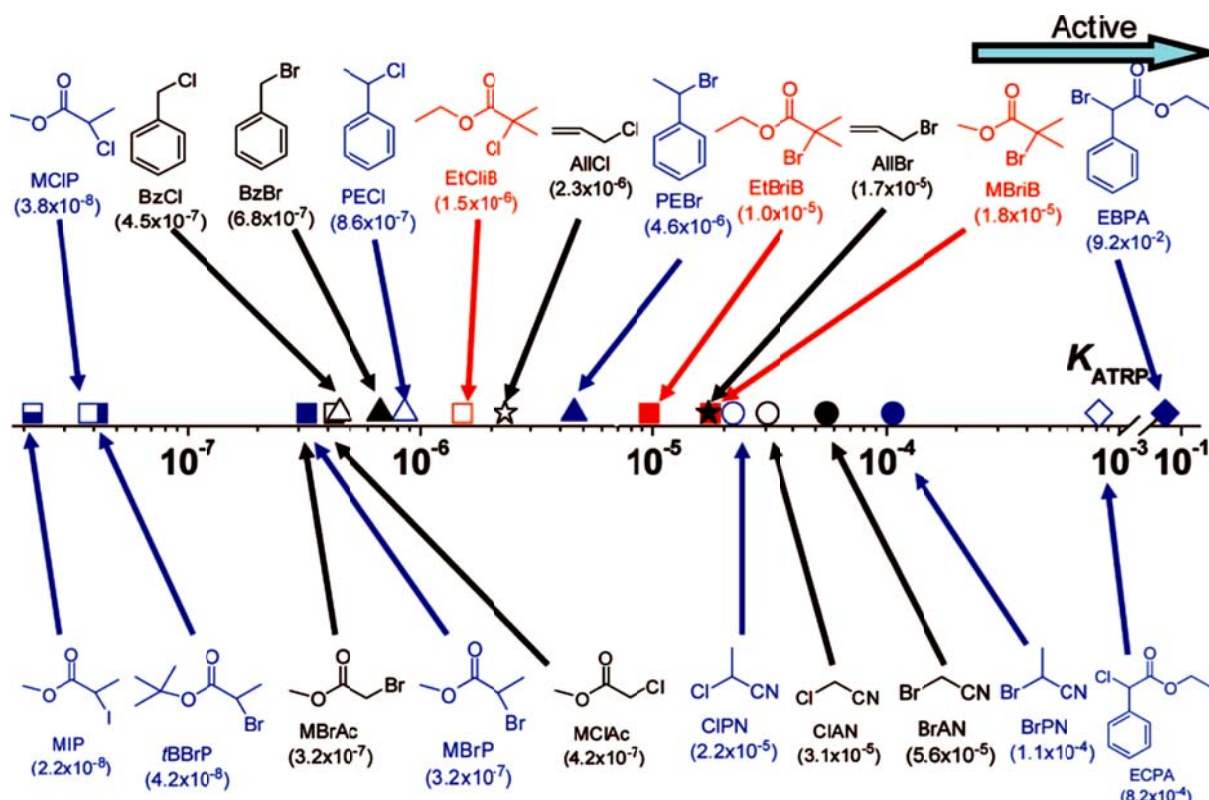
Figure 2.3 ATRP equilibrium constants for various initiators using $Cu^I X/TPMA$ (X = Br or Cl). The initiators comprised in different substitution degree are separated by colors: red for 3°; blue for 2°; black for 1°. The incorporated halogens are grouped by different symbol: solid for R-Br; open for R-Cl; bottom-half-solid for R-I; Δ for phenyl; $\square$ for ester; $\circ$ for nitrile; $\lozenge$ for phenyl ester; $\stackrel{\star}{\star}$ for allyl. Figure reprinted with permission from American Chemical Society (2008).[53]

2.1.4 Activators Regenerated by Electron Transfer (ARGET) ATRP

Activators regenerated by electron transfer (ARGET) was developed as a modification of conventional ATRP employing a modified initiation process.[60-61] In the presence of excess reducing agent including ascorbic acid, tin(II) 2-ethylhexanoate, glucose, and N-containing molecules,[62-63] the initiation step starts from the continuous reduction of $X\text{-}Cu^{II}/L$ species to active $Cu^I X/L$ and conventional ATRP is subsequently conducted (referred to Scheme 2.1).[64] Through the in-situ reduction process, ATRP can be conducted with ppm amounts of Cu catalyst, by which a "green" polymerization with suppressed biradical termination, improved end group fidelity and high MW polymers becomes more accessible. However, to compensate the low amount of catalysts, a higher amount of ligand is usually required, leading to more complicated reaction processes.[64-65]

Due to additional reducing agent, ARGET ATRP has higher tolerance to oxygen and has been successfully extended to aqueous solutions, which indeed expands the potential for industrial synthesis and preparation of bio-conjugated hybrid materials.[66-67] Furthermore, combining surface-initiated strategy (SI-ARGET ATRP)[68] and the photosensitivity of Cu ions, the visible light-triggered SI-

ARGET ATRP can be performed successfully to prepare composites with well-defined chain length, designed morphology and diverse compositions.[69] As a result, owing to the strengthened properties, refined control over polymerization and extended feasibility, the (SI)ARGET ATRP is applied in the present thesis.

2.1.5 Photoinitiated ATRP

Recently, the control over activation−deactivation equilibrium was achieved by various stimuli,[70] such as photochemical,[71-73] pressure,[74-75] and electrochemical.[76] The applied stimuli is predicted to reduce energy barriers to trigger the critical initiation or activation-deactivation process reversibly, and to accumulate activators efficiently so as to increase polymerization rate under mild condition. Consequently, photopolymerization with advantages of faster reaction rates, lower catalyst loading and spatial control ability can surpass the traditional thermal strategy. Currently, the photoinduced Reversible-deactivation radical polymerization (PRDRP) can be achieved by visible light with[77-79] or without[79-82] the utilization of specialized photoinitiators, sensitizers and dyes, synthesizing well-defined polymers with featuring living property.

PhotoATRP has received considerable attention owing to the facile process, less additives required, and the feasibility of using visible/sunlight.[63, 83-84] Although the detailed mechanism of radical formation and activator (re)generation in the photochemical system is still not clear, previous studies have pointed out that alkyl halide activation via excited Cu^I complexes photochemically is not kinetically significant.[84-85] Namely, the photo ATRP with conventional Cu catalysts and ligands must proceed by radical formation and activator (re)generation, instead of enhanced activity of the Cu^I complex. Five parallel pathways are listed in Scheme 2.2 (1)-(5),[80, 84, 86-87] and generally speaking these processes could be regarded as a combination of initiators for continuous activator (re)generation (ICAR) ATRP and ARGET ATRP, because Cu^{II} ion are reduced under light in a term of electron transfer as in ARGET while resulting in halogen radicals for initiation, as in ICAR ATRP.

Simulation and experimental results reveal that the fundamental mechanism of Cu-mediated photoATRP is a combination of photoARGET ATRP and photoICAR ATRP.[83] The dominant radical (re)generation process is the ARGET like photochemical reducing Cu^{II} ions by excess amines (pathway 5). As eminent electron donors amines are oxidized to promptly produce the Cu^I complex and amine-centered radical cations which initiate a new chain after proton transfer.[88] Besides, radicals are generated synergistically between alkyl halide and the ligand, referring to a photochemical ICAR ATRP with occurrence 10 times slower than the ARGET counterpart (pathway 4). Other processes mentioned contribute to merely a minor portion. The overview of mechanism is illustrated in Scheme 2.2,[83] indicating the operation of classic ATRP to supplement radical balance and control the polymerization predominantly via photo ARGET ATRP with the combination of photo ICAR ATRP.
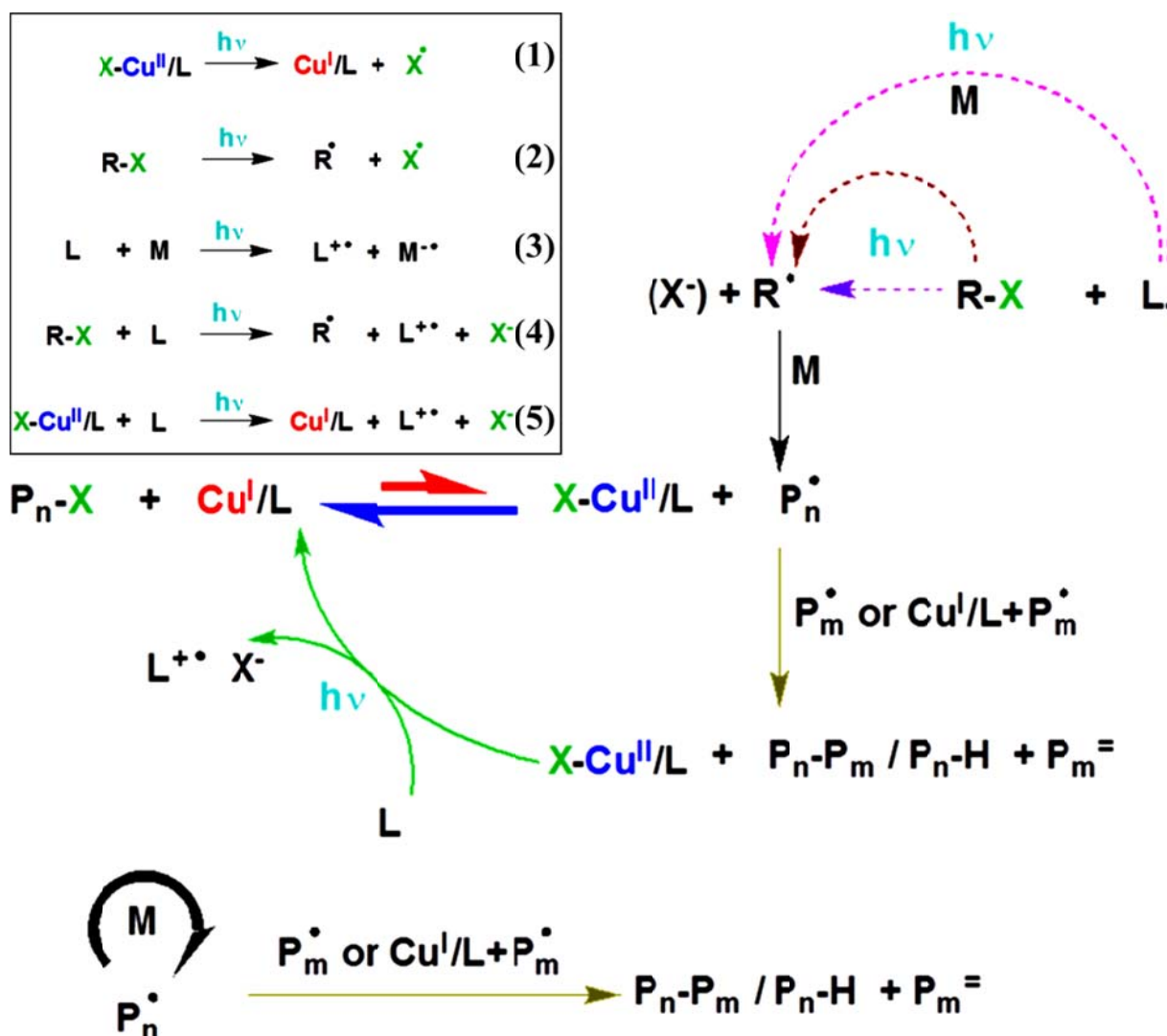
Scheme 2.2 Proposed mechanism of photochemical ATRP with five suggested activator (re)generation pathways. The dominated reaction are depicted in bold, reactions that dictate the polymerization rate are in thin solid lines, and reactions with a small contribution are presented as dashed lines. The five pathways: (1) Direct reduction of X−Cu^{II}/L; (2)-(4) Generation of radicals by reactions of an alkyl halide and/or a ligand; (5) Photochemical reduction of Cu^{II} by an electron donor (i.e. amines or nitrogen-containing molecules). Figure reprinted with permission from American Chemical Society (2014).[83]

2.2 Compartmentalized ATRP

ATRP was originally developed in homogeneous bulk environment,[41] but distinct properties are observed in dispersed systems ascribed to the mass transfer,[89-90] distribution/partition of reactants[91-92] and particularly the compartmentalization effect.[19, 93-96] Compartmentalization can be divided into the segregation and the confined space effect.[89, 96-97] Segregation means reactants are located separately being unable to react; in contrast, the confined space effect means reactants react faster in a smaller space due to an increased local concentration. Take emulsion polymerizations as example, considering only propagating radicals, the compartmentalization contributes to isolated radicals, usually resulting in higher polymerization rates (R_p) and higher MW than bulk counterparts.[18, 98]

Different from typical emulsion polymerization, both propagating radicals and deactivator species have to be considered in compartmentalized ATRP, once concentration of deactivator is sufficiently low. Theoretically, in small particles (diameter, d < 500 nm), when the deactivator (Cu^{II} complex) is not compartmentalized, segregation reduces the termination rate, and then results in higher R_p with broaden molecular weight distribution (MWD). The broad MWD is attributed to a lower termination rate avoiding accumulation of deactivator, which reduces deactivation rate and enhances polymerization of more monomers per activation-deactivation cycle.[91, 99] However, in the case deactivators are compartmentalized, besides the improved livingness imparted from segregated radicals, according to particle sizes the confined space effect may hasten polymerization by increasing propagating radical concentration or slow down the reaction via enhancing deactivation process, leading to a narrower MWD.[6, 96, 100]

Up to now the compartmentalized ATRP was experimentally demonstrated to give poly(butyl methacrylate) with high MW of 989,900 and low $Đ$ = 1.25, in term of miniemulsion with weight-average diameter <110 nm.[101-102] Achievement of such high MWs remaining good control/livingness is currently challenging via bulk polymerizations.

2.2.1 Theoretical Model Development

The compartmentalized ATRP is modeling by polymerization of *n*-butyl acrylate (*n*BA) using CuBr/ 4,4'-dinonyl-2,2'-bipyridine (dNbpy) at 110 ºC in a dispersed condition under an assumption of constant N_p (total particle number) throughout the polymerization.[96] Referring to the homogeneous bulk system,[3, 45] the modified Smith-Ewart Equation is applied to model the compartmentalized ATRP, as shown in Equation (3)-(7).[19, 96]

$$\frac{\mathrm{d}N_i^j}{\mathrm{d}[\mathrm{t}]} = N_A v_p k_{act}[\mathrm{PBr}][\mathrm{CuBr}]\left(N_{i-1}^{j-1} - N_i^j\right)$$

$$+\frac{k_t}{N_A v_p}\left[(i+2)(i+1)N_{i+2}^j - (i)(i-1)N_i^j\right] + \frac{k_{deact}}{N_A v_p}\left[(i+1)(j+1)N_{i+1}^{j+1} - (i)(j)N_i^j\right] \tag{3}$$

where PBr is alkyl halide, N_i^j is the particle number of propagating radical P· (i) and CuBr$_2$ (j), v_p is the particle volume and N_A is Avogadro's number. k_{deact} and k_{act} represent rate coefficients for deactivation and activation processes, separately. The average numbers of P· ($\bar{n}_p$.) and CuBr$_2$ ($\bar{n}_{CuBr_2}$) per particle can be represented as:

$$\bar{n}_p. = \frac{1}{N_p} \sum_i \sum_j i\, N_i^j \tag{4}$$

$$\bar{n}_{CuBr_2} = \frac{1}{N_p} \sum_i \sum_j j\, N_i^j \tag{5}$$

where $N_p = \sum_i \sum_j N_i^j$ is the total particle number. The overall concentrations of P· and CuBr$_2$ in the organic phase can be represented as:

$$[P\cdot] = \frac{1}{N_A v_p} \frac{1}{N_p} \sum_i \sum_j i\, N_i^j \tag{6}$$

$$CuBr_2 = \frac{1}{N_A v_p} \frac{1}{N_p} \sum_i \sum_j j\, N_i^j \tag{7}$$

Owing to the high concentration in polymerization system, monomer molecules are not in the compartmentalized situation, and therefore the dynamic concentration is determinable. This assumption is also feasible to the activation reaction between PX and CuX, two reactants with high concentration.
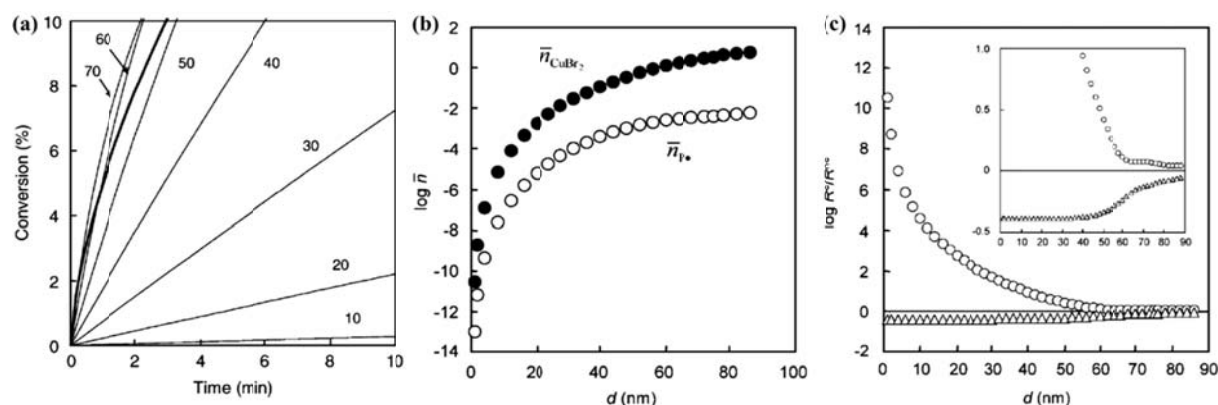
Figure 2.4 (a) Simulated conversion versus time for ATRP of nBA in dispersed systems with varied particle diameters compared to bulk. (b) Simulated $\bar{n}_p$. and $\bar{n}_{CuBr_2}$ within a particle at 10% conversion. (c) Ratios of simulated (non)compartmentalized termination (Δ) and deactivation (○) rates as functions of d at 10% conversion. Polymerization condition: $[n\text{BA}]_0$:$[\text{PBr}]_0$:$[\text{CuBr/2dNbpy}]_0$= 200:1:1. Figure reprinted with permission from John Wiley and Sons (2006).[96]

2.2.2 Compartmentalization Effects on Polymerization Rate

The simulated conversion evolution versus time for the conducted ATRP of nBA in dispersed conditions with varied particle sizes using bulk state as reference is shown in Figure 2.4a.[96] The result

indicates that the polymerization rate (R_p) decreases significant in line with particle size, especially while d $\leq$ 40 nm. Correspondingly, when the particle size is shrinking, both $\bar{n}_p$ and $\bar{n}_{CuBr_2}$ are reduced as well (Figure 2.4b).[96] However, because P· and CuBr$_2$ are generated in pairs and the deactivation rate is also increased by the confined space effect, the R_p at this condition is determined by the number of monomers included in an activation-deactivation cycle, relating to the interval time before deactivation [$=N_A v_p / k_{deact}$]. Namely, in extremely small particles ($d < 40$ nm), the activation frequency is proportional to merely the volume in organic phase. The result suggests that under homogeneous condition, the activation frequency can be increased by conducting polymerization under a more confined condition, resulting in a higher polymerization rate.

2.2.3 Compartmentalization Effect on Termination and Deactivation

Equations (8)-(11) are applied to calculate and compare the compartmentalized rates (R^c) and the corresponding non-compartmentalized rates (R^{nc}).

$$R_{deact}^c = \frac{k_{deact}}{(N_A v_p)^2} \frac{1}{N_p} \sum_i \sum_j ij\, N_i^j \tag{8}$$

$$R_t^c = \frac{2k_t}{(N_A v_p)^2} \frac{1}{N_p} \sum_i \sum_j i(i-1)\, N_i^j \tag{9}$$

$$R_{deact}^{nc} = k_{deact}[\text{P·}][\text{CuBr}_2] \tag{10}$$

$$R_t^{nc} = 2k_t[\text{P·}]^2 \tag{11}$$

The distinct transformation of $R_{deact}^c / R_{deact}^{nc}$ and R_t^c / R_t^{nc} at 10% conversion versus d can be observed in Figure 2.4c.[96] Due to the confined space effect the deactivation rate is dramatically increased, giving the larger $R_{deact}^c / R_{deact}^{nc}$ value while d is decreasing. Conversely, the R_t^c / R_t^{nc} decreases in line with d between the range 30-90 nm and then remains steady, resulting in retarded termination process. Therefore in ideal ATRP without termination, transfer and side reactions, the Đ is determined by the repeated times of activation–deactivation cycles towards the targeted MW;[3] that is, Đ can be reduced by increasing the conducted cycle number. The confined space effect-resulted enhanced deactivation rate in small particles leads to higher cycle number, contributing to well-controlled polymerization with lower Đ; moreover, the retarded termination results in higher livingness. In summary, compartmentalization has the benefits of improving both control and livingness under the cost of slower polymerization rate, and via interpretation of the confined space effect and the segregation effect the compartmentalized effect can be exploited to improve control/livingness in ATRP, especially in high MW attempt.

Chapter II

2.3 Metal-Organic Frameworks (MOFs)

Metal–organic frameworks (MOFs) are infinitely extended networks formed by metal ions and bridging organic ligands[103-104] which have attracted tremendous attention over the last decades.[105-106] Due to the promising advantages of porous structure with high surface areas, tunable pore sizes and devisable topologies, applications have driven the ever-growing interest in this newly-developed material,[107] igniting researches[30-31, 108-110] in adsorption, separation, sensing, drug delivery, luminescence, catalysis, and especially as hosts for (in)organic molecules.[111-113]

2.3.1 Design and Synthesis of MOFs

The characteristic metal – ligand network of MOFs ranging from one dimensional (1D) to 3D can be designed and constructed by enormous secondary binding units (SBU) with different applied metal ions and bridging ligands (Figure 2.5).[29, 114] Once the metal cations which act like nodes in the framework are determined (Figure 2.5a), the organic bridging anions, such as carboxylates, are utilized to balance the system charge and connect the metallic nodes (Figure 2.5b).[29, 115-116] Benzene-comprised multi-carboxylate ligands with unique angles (i.e. 120º, 180º or others), spacers (longer or shorter) and metal binding sites (i.e. 2, 3 or more) are prevalent and usually chosen for the synthesis of multidimensional MOFs. While the neutral bridging ligands are applied,[116-118] charge is balanced by the counter ions of original metal salt, such as Cl^-, NO_3^-, SO_4^{2-} or BF_4^-. These non-charged ligands are predominantly contributed by nitrogen containing heterocyclic molecules which can not only act as a linear spacer bridging metal connectors but can further serve as a hydrogen-bond acceptor to diversify the microenvironment inside the MOF framework.[119] Generally, rigid bridging linkers are preferred among all available linkers in order to gain thermally stable and robust porous frameworks which can retain the MOF integrity even after the elimination of supporting guest molecules.

Nowadays many alternative methods are established to prepare MOFs including mechanochemistry using a mechanical ball mill to replace solvents,[120-121] sonochemistry,[122] electrochemistry[123] and microwave irradiation.[124-126] However, the solvo- or hydrothermal synthesis[127-128] is still one of the most prevalent methods for MOF syntheses, by which organic ligands and metal salts are mixed in high boiling, polar solvents such as water, dialkyl formamides, dimethyl sulfoxide (DMSO) or acetonitrile to react at relatively low temperatures ($\leq$ 300 ºC). Through tuning parameters applied in solvothermal strategy (i.e. reacting temperature, concentrations of metal salt and ligand, pH of solution, etc.), distinct MOF structures can be fabricated. Several kinds of MOFs are currently synthesized in large industrial scale and commercially available.
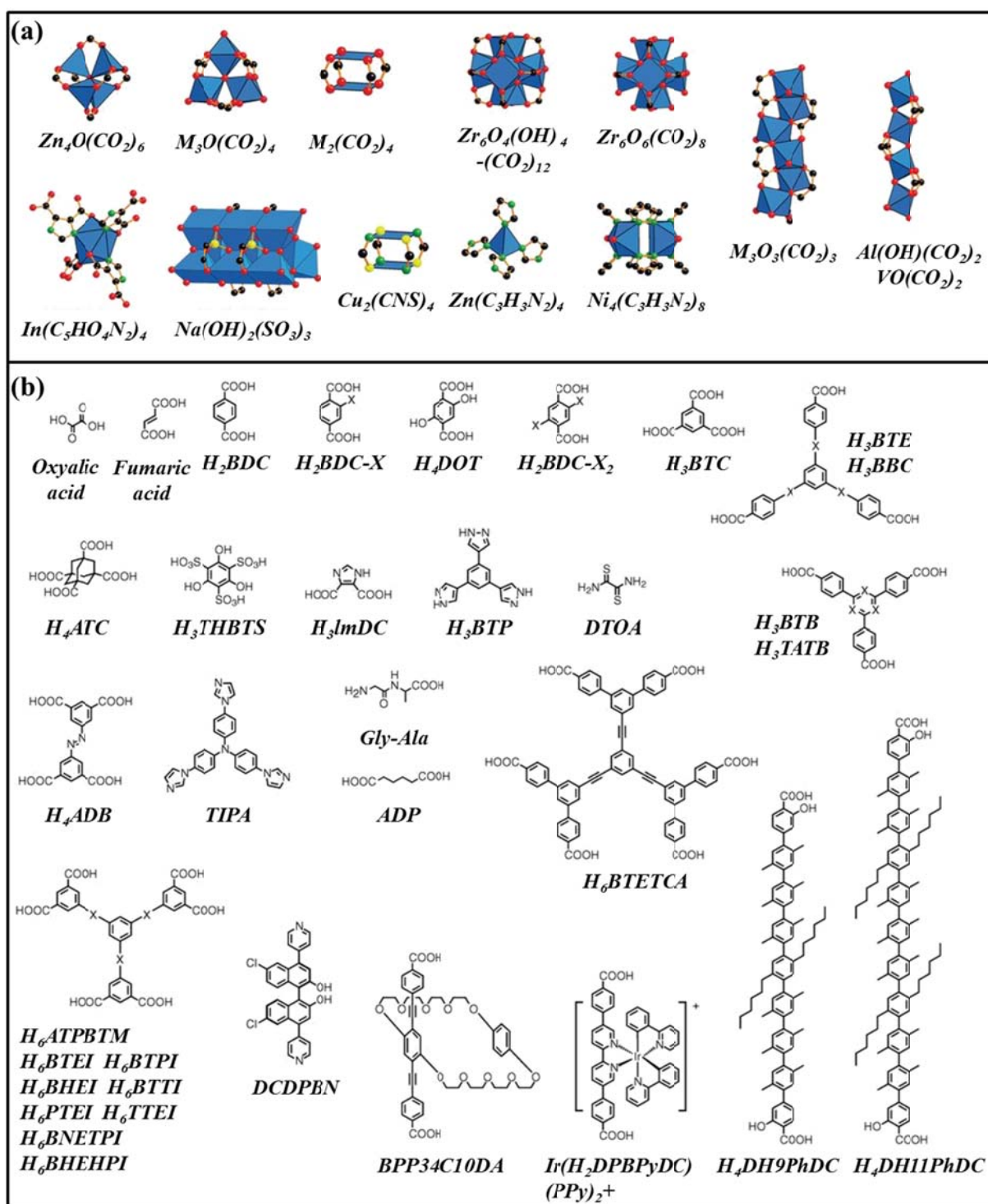
Figure 2.5 Illustration of constructed molecular building unites: (a) inorganic secondary binding units and (b) organic binding ligands. Figure reprinted with permission from The American Association for the Advancement of Science (2013).[29]

2.3.2 Topology and Pore Features of MOFs

In MOF structure design, the specific secondary building unit (SBU) usually dictates the final topology of framework, and especially the metal-cluster-based SBUs reveal the intrinsic bonding affinity between metal ion and ligands.[128] Typically, 4 different kinds of SBUs can be identified.[129]

Namely, from simple to complicated, the structure can be arranged in a trigonal or a square plane of the metal atoms, a tetrahedron alignment of metal atoms surrounded by an oxyanion in the middle, and a tetragonal arrangement with a di-metal paddlewheel in the center. Regardless of the structure, each metal pair is linked coordinatively by the ligands orienting the linker molecules in a highly controlled fashion.

Owing to high crystallinity, MOFs possess a defined microporous structure ($d < 2$ nm). However, materials with large pores, such as mesopores (20 nm $< d < 50$ nm) or even macropores ($d > 50$ nm), are more appealing and suitable for common host–guest reactions. Recently, via increasing the length of the organic linker, series of isoreticular MOFs (i.e. MOF-74) with tunable pore sizes from 1.4 to 9.8 nm can be fabricated under constant topology.[130] The large-pore MOFs will enable the incorporation of larger reactants, and the tunable the pore size can furthermore expands as well as improve the dimension/diffusivity of includable guest molecules.

2.3.3 Functionalization of MOFs

It is highly accepted that the framework topology of MOFs is predominantly dependent on the incorporated metal ions and organic ligands, resulting in distinct pore size and shape and even chemical functionality of the whole framework as well as the material performance.[124, 131-132] As a result, increasing effort was devoted to alter the intrinsic properties of MOFs by functionalization in order to improve or modify the host – guest interactions, and allow fine-tuning of the pore environment with designed properties. Two general strategies are established to prepare functionalized MOFs: the pre- or post-synthetic functionalization (Figure 2.6).[133-134]

At the beginning, via mixing the pre-modified ligand during the solvothermal step, the targeting functionality can be incorporated into a MOF during crystallization process. This co-crystalization or prefunctionalization approach allows the preparation of multivariate (MTV) MOFs with pendant but simple substituents, such as – Br, – NH_2, – CH_3, lining along the pore channels (Figure 2.6a).[133] The facileness and widely applicability offered by this strategy gives rise to a variety of functionalized MOFs ranging from the IRMOFs (Isoreticular Meta – Organic Framework),[135] ZIFs (Zeolitic Imidazolate Frameworks),[136] to MIL-53 (Material Institut Lavoisier)[137] series of materials without undesirable change or breaking the original structure. By applying this strategy, more than one type of linkers can be included in a MOF crystal, leading to plenty of framework structure built-up by two (or more) linkers with diversified material properties. Nevertheless, the stability of functional ligands throughout the harsh solvothermal conditions (i.e. high temperature and/or pressures) restrains the feasibility of this approach, delimiting the scope of functional groups within the MOFs.
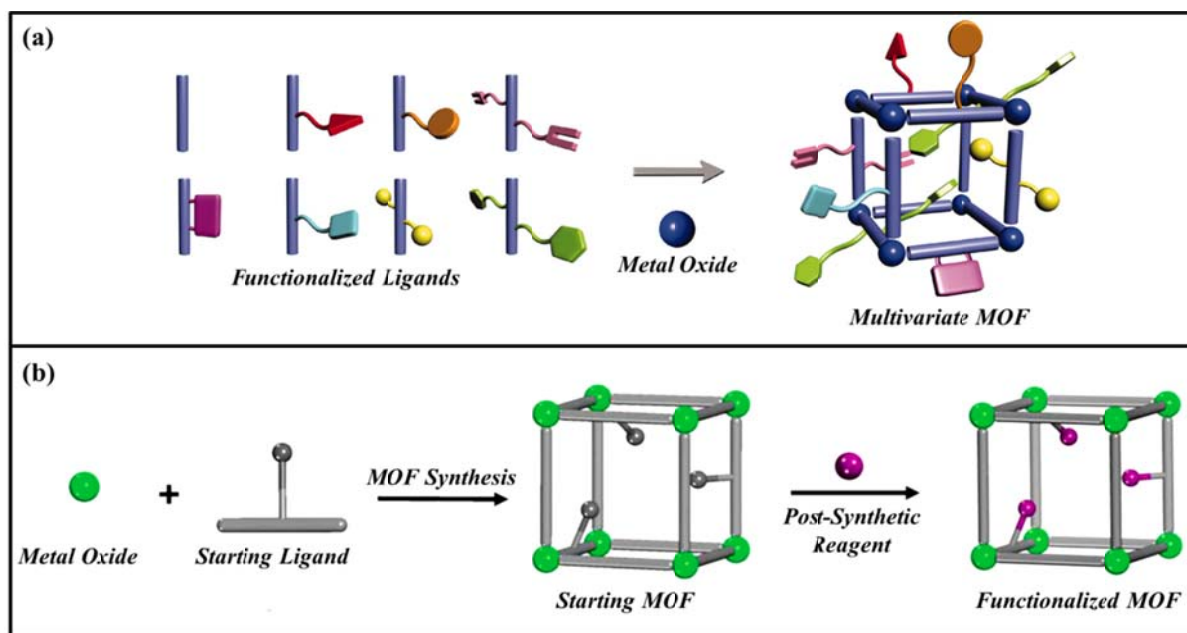
Figure 2.6 Illustration of functionalized MOFs obtained by (a) prefunctionalized strategy and (b) post-synthetic modification (PSM). Figure (a) reprinted with permission from The American Association for the Advancement of Science (2010)[133] and Figure (b) reprinted with permission from Royal Society of Chemistry (2010).[134]

On the other hand, post-synthetic modification (PSM) opens another route towards functionalized MOFs (Figure 2.6b),[134, 138-140] which is featured by conducting a chemical modification on a pre-formed framework in a heterogeneous synthesis. PSM has proven to be a competitive alternative to the pre-functionalization approach owing to the improved control over types and amount of comprised functional groups on the framework,[141-142] making it a promising tool for preparing topologically identical, but functionally diverse MOFs.[143] Similarly, the two most critical consideration while using PSM are the size of used reagent which has to be smaller than the MOF cavity and functionalization has to be conducted under the condition which the targeted MOF will not be destroyed.[144-145] Moreover, considering to the mass transduction within MOF frameworks, the modification efficiency might be lower or less uniform.

Considering the predominant role of MOF microstructure towards polymer properties, functionalization uniformity and high modification efficiency, the prefunctionalization technique is applied in the present thesis to synthesize the initiator-functionalized MOFs. Since the controlled MW is one of the features of ATRP, the evenly distributed initiator struts during crystallization process can ensure the investigation of polymer properties given by control/living polymerization.

2.4 MOF-Polymer Composites

Among material properties of MOFs, tunable nanochannels is one of the most outstanding advantage which makes MOF an excellent accommodation for various of guest molecules, serving as a promising platform to elucidate the chemistry resulting from host – guest effect.[111-113] In an attempt to investigate the synergic effect between host and guest molecules, the development in MOF-polymer nanohybrid has been particularly emphasized. The hybridization strategy serves as an alternative to convert the randomly-entangled polymer chains into highly controlled polymer population with well-defined chain conformation, unique composition and unanticipated properties.[27] More than an accommodation, heterogeneous catalysis is another promising application of MOFs. However, the drawbacks like less malleability and processibility attributing to the highly crystalline innate has been a long-term restriction, restraining the catalytic property and applicability of MOFs in films or membranes.[146] In this regard, the soft and low dimension polymers can be an universal solution to balance the trade-off property via grafting polymer brushes on the MOF surface. In general, integration of organic polymers and crystalline MOFs opens an avenue to develop advanced complexes with unprecedented performances which could surpass the individual components.[147-149]

2.4.1 Confined Polymerization within MOFs

Templating strategy is one of the most facile ways to obtain hybrid materials and to synthesize well-controlled polymers with hierarchical structure inherited from porous frameworks. Up to now in situ polymerization has been widely conducted in porous zeolites or organic materials. However, owing to the microporous geometry with limited pore size, the polymerization of monomers with size larger than 6 Å is forbidden.[150-154] The designable pore features in size, shape and surface functionalities make MOFs advantageous to act as unique nanosized niches for polymerization in terms of radical, ionic, oxidative and electrochemistry.

Free radical polymerization of styrene in one-dimensional nanochannels of $Zn_2(bdc)_2(dabco)$ (bdc = 1,4-benzenedicarboxylate, dabco = triethylenediamine) has been conducted to fabricate highly controlled polystyrene (PS) with narrower $Đ$,[37] improved tacticity[155-156] and defined structure (Figure 2.7).[157-160] It has been pointed out that ascribing to the host-guest and compartmentalization effect, porous structure of host MOF (i.e. regularity, dimension, shape, microenvironment, etc.) will significantly affect the microstructure of accommodated polymers. For example, a polymer with refined tacticity can be obtained from MOFs with uniform porous structure (i.e. unimodal pore size distribution),[155] bulky substitution groups,[37] or unsaturated metal sites (UMS).[156] That is, when a polymerization is conducted within a MOF with regular and narrower pore size, the isotactic ratio of polymers can be increased, because the host-guest effect and space-saving isotactic conformation compared to syndiotactic counterpart.[161] Besides, when a MOF host is comprised of large substituents or UMS, the stereoregularity can be improved as well due to the strengthened nanoconfined effect and

association between guest monomers and Lewis acid metal sites. The associated researches strongly suggest that through confined polymerization, MOFs are promising candidates to synthesize polymer products with adjustable tacticity.
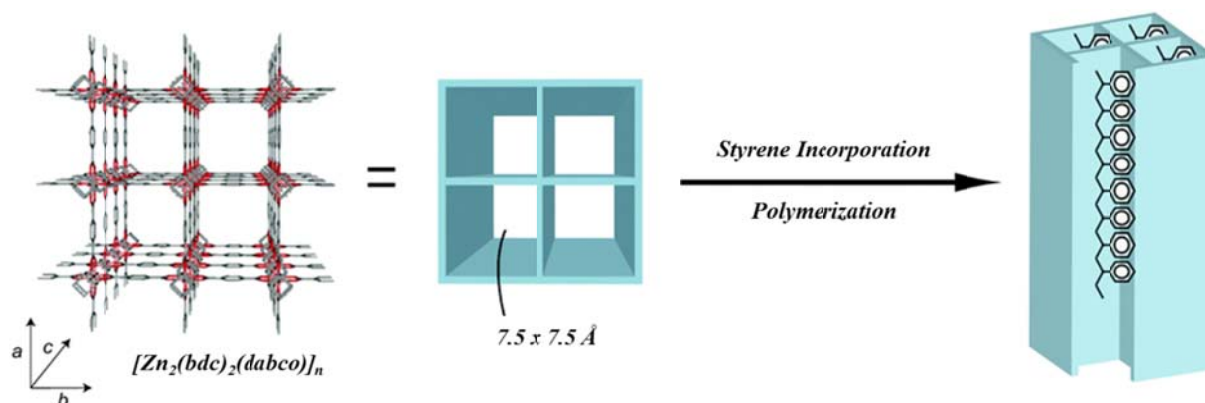
Figure 2.7 Concept of the polymerization of styrene in the nanochannels of $Zn_2(bdc)_2(dabco)$. Figure reprinted with permission from Royal Society of Chemistry (2005).[157]

Both kinds of ionic polymerization, cationic and anionic, have been demonstrated inside the confined nanochannels of MOFs. Cationic ring-opening polymerization of 1,6-anhydrob-D-glucose in 1D La(btb) (btb = 1,3,5-benzentrisbenzoate) gave a linear-like polysaccharide which is distinct from the ill-defined structure obtained from conventional bulk solution.[162] On the other hand, controlled and selective anionic polymerizations of substituted acetylenes in 1D nanochannels of $Cu_2(pzdc)_2(pyrazine)$ (pzdc = 2,3-pyrazinedicarboxylate) contribute to the trans-form dominant conjugation ascribing to the confined space and the utilization of basic carboxylate oxygen atoms as both binding and catalytic sites.[163] Both cases again evidence that by selecting proper metal ions and functional ligands, dynamic microenvironment in MOF nanochannels can be precisely designed with varied acidity, functionality and oxidation-reduction activity. Therefore, decorated with specific active spots in the nanochannels, MOFs can be utilized as hosts and catalysts to capture and polymerize specific monomers in an extraordinary way.

Oxidative polymerization is a general strategy to prepare various widely-applied π-conjugated polymers,[164] and the in situ polymerization inside MOF channels can direct the alignment of π-conjugated polymers to strengthen and diversify material properties. Oxidative polymerization is classified into two categories: chemical- and electrooxidative polymerization. Redox-active metal ions can act as oxidizing agents to synthesize π-conjugated polymers.[165] A chemical-oxidative polymerization of pyrrole was conducted within $Cu_3(btc)_2$ (HKUST-1; btc = 1,3,5-benzenetricarboxylate), where accessible Cu^{II} ions were reduced to Cu^{I} ions to trigger the oxidative polymerization of pyrrole. Via the same host, HKUST-1, electropolymerization of aniline inside the nanoconfined spaces was recently launched,[166] by which the polymerization can be carried out under

milder condition and controlled in a more precise manner (i.e. through varying applied current density or electrical potential).

2.4.2 Polymerization of Comprised Ligands

Because of the designable geometry of MOFs, polymerizable ligands can be located in proper space to polymerize with each other or by reacting with a cross-linker to form conjugated polymers directly inside the framework.[28, 167] Take the cyclodextrinMOF (CD-MOF) for instance, the original CD-MOF was highly soluble in water. After the ligands were crosslinked by the hydroxyl groups, the cross-linked CD-MOF became insoluble and gel particles with expanded volume were fabricated.[168]

In another case, the polymerizable ligand, 2,5-divinyl-terephthalic acid (dvtpa), was blended with bdc under a given ratio to form a cross-linkable MOF, $Cu_2(dvtp)_x(bdc)_{1-x}(dabco)$.[160] The host MOF was then cross linked with the accommodated polymer chains to gain a vinyl polymer with alignment control (Figure 2.8).[160] Besides, due to the template structure from host MOF, the obtained polymers retain morphology of the host MOF, but higher glass transition temperatures (T_g) and enhanced chemical as well as thermal resistance are presented compared to reference polystyrene (PS).
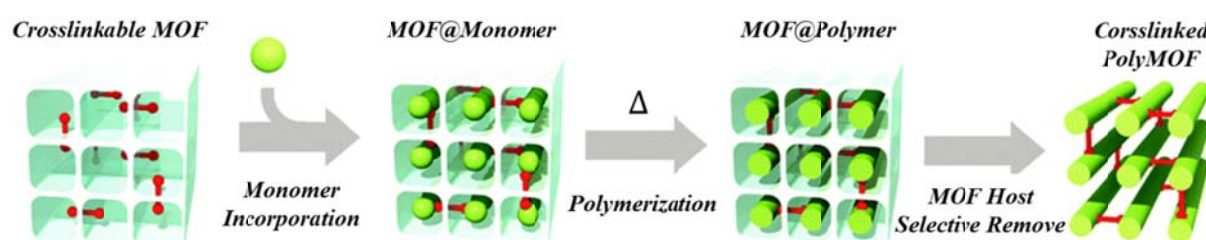
Figure 2.8 Concept of cross-polymerization between the host MOF framework and guest monomers. Figure reprinted with permission from Nature Chemistry (2013).[160]

Typically, the MOF-comprised ligands can be involved in polymerization reactions in two strategies: (I) polymerization with each other located in the framework; or (II) reaction with extra added monomers. One critical prerequisite to the applied reactions is the stability of MOF structure throughout the process. In the first concept, the cross-linkable ligands have to be embedded in the frameworks with suitable spacing and orientation for proper polymerization between adjacent neighbors. Differently, the incorporation of polymerizable ligands into MOF structures, and design of versatile pore features suitable for accommodated guest are the two major concerns when the second strategy is chosen.

2.4.3 Incorporation of Polymer-Binding Ligands

To solve the limitation from fragile MOF crystals, functionalization on these solids with soft polymers is a promising and universal manner to synthesize materials with refined stability, dispersibility and flexibility. These hybrid complexes inherit highly porous and robust crystalline

geometry from MOFs with additional flexibility, processibility and other unique properties (i.e. stimuli-responsive property) imparted by the polymer counterpart. Similarly, two major strategies, pre-synthetic or post-synthetic, have been developed to unite the polymer chains together with the MOF particles.

Via the pre-synthetic method, a specialized block copolymer with one ligand-comprising block was utilized to interact with metal ions to from the MOF/polymer derivatives. Illustration in Figure 2.9,[169] after annealing with metallic ions (Zn^{2+}), low dimensional (1D) polymer chains containing with bdc ligands in the backbone were incorporated and converted into high dimensional (3D) crystalline MOF/polymer complexes, or the so-called polyMOFs equipped with the combined characteristics from polymers and MOFs components.[169]
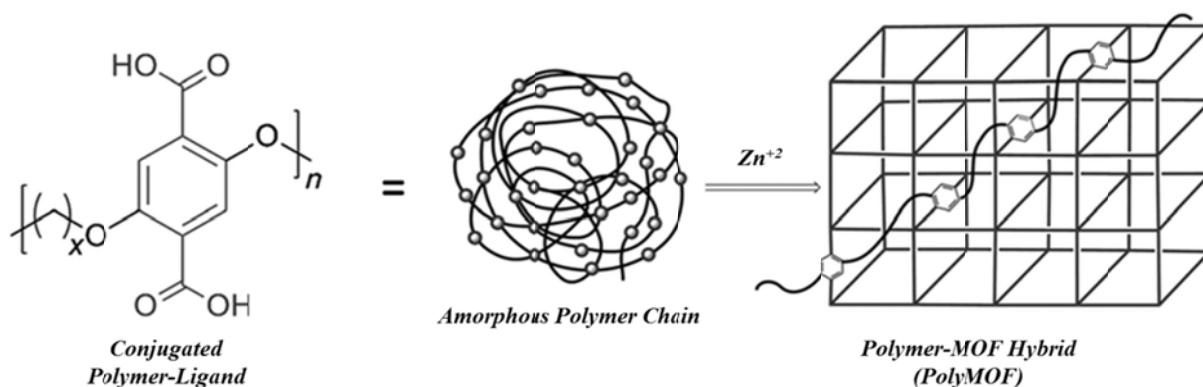
Figure 2.9 The strategy to convert a one dimensional (1D), linear polymer chain to a 3D, porous, polyMOF crystalline material. Figure reprinted with permission from John Wiley and Sons (2015).[169]

Differently, in the post-synthetic method, polymers are attached to pre-synthesized MOF particles by the "grafting to" or "grafting from" method. The "grafting to" is conducted by conjugating the pre-synthesized polymer chains directly to the MOFs to gain extra properties. For example, the MOFs covalently attached with poly(*N*-isopropylacrylamide) (PNIPAM), a stimuli-responsive polymer, can act as a environment-responsive carrier for controlled release.[170] Although the "grafting to" strategy is very facile to fabricate hybrid complexes and alter material properties, the modification degree, such as grafting density, conformation and thickness, is challenging to be controlled owing to the steric hindrance of the preformed polymer chains. In this regard, the "grafting from" method which grafts the polymer chains from the material surface by using highly mobile monomers can serve as an alternative with improved controlled ability.[171-172] To conduct the surface-initiated functionalization, a polymerization-initiation motif has to be immobilized on the MOF in advance.

Functionalization with polymers can provide other advantages to arbitrarily adjust the surface property of MOF particles, and thus provide an efficient solution to unshackle the MOF crystals from

aggregation and poor dispersibility which have severely restricted their applications in solution state catalysis.[173] However, the polymer functionalization is also a trade-off technology, because the incorporated polymers can alter the material properties under the sacrifice of blocking the active sites or decreasing porosity, which will adversely retard the catalytic performance of the formed composites.[174] In summary, combining low-dimensional polymers with crystalline MOFs is a promising and comprehensive strategy which enables the integrated complexes to gain the bilateral advantages from polymers (flexibility, dispersity) and MOFs (stability, crystallinity). Nevertheless, an universal method to further optimize performance of composites or even break the trade-off resulting from these functionalized techniques is still absent and has to be developed.

2.5 MOFs as Heterogeneous Catalysts

Catalysis is of importance in both scientific and industrial fields. Owing to their intrinsic hybrid nature, MOFs are highly compatible to either organic or inorganic materials. Together with their tunable pore features, adjustable adsorption behavior, diversified components, easy separation and robust structures, all indicate application in heterogeneous catalysis.[132, 175-179] Within the ever-developing MOF science, an in depth realization of their advantages and limitations can help current researchers to explore the catalytic potential of MOFs and to develop state-of-the-art catalysts.

2.5.1 Potential Advantages and Disadvantages

Several strategies to diversify the catalytic capability of a given MOF scaffold are summarized in Scheme 2.3.[178] In addition to the highest porosity, designable pore size, shape and microenvironment make MOFs highly advantageous compared to other crystalline porous materials, such as zeolites, silica and aluminum oxide (AAO), that have very limited diversity of structures. Without any doubt, the high versatility of MOFs is one of the eminent advantages for catalytic attempts, because beyond feasible catalytic sites, a tailor-made microenvironment for high-degree precise host-guest interaction could be realized.[180]
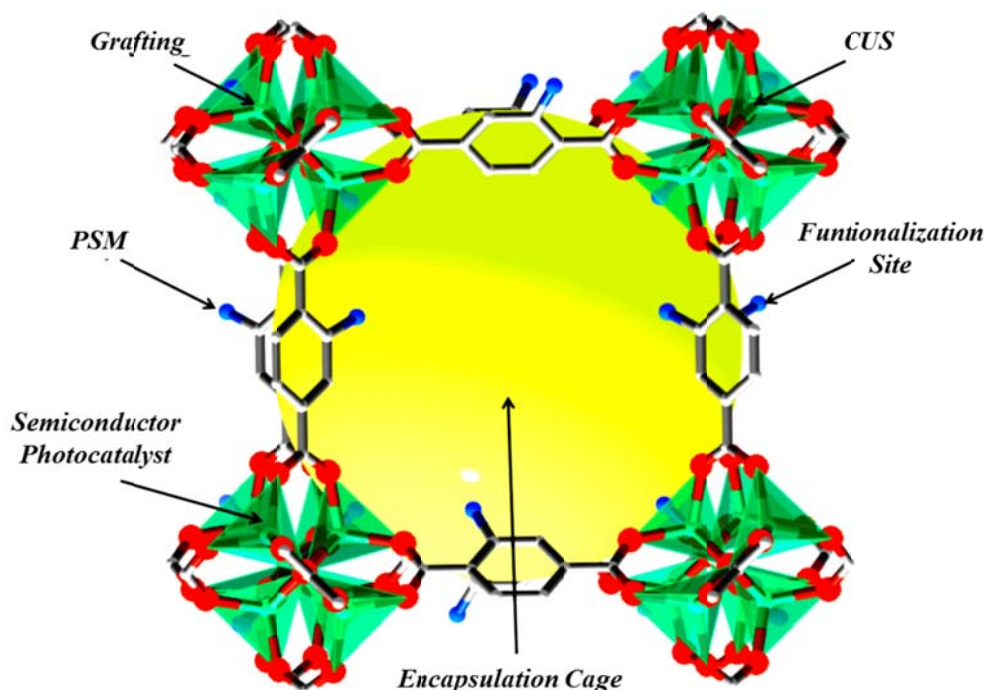
Scheme 2.3 Strategies to Diversify Catalytic Moieties within a MOF Scaffold. Figure reprinted with permission from American Chemical Society (2013).[178]

MOFs can serve as catalysts through the following strategies. First, the catalytic function is basically implemented by both the organic linkers[181] and the inorganic metal nodes,[182] which can be constructed via direct synthesis of the desired morphology or by the post functionalization to further

modified the material properties.[36, 133-134, 138, 183-184] Second, the ligands with functionalized organic groups can trigger reactions like organocatalysts. Third, the porous body of MOFs can act as a physical space where the catalytic reaction takes place or as a confined space where catalytic species are encapsulated, stabilized and oriented.[185-186] Generally, the MOF may merely act as a spectator or passive medium to disperse the catalytic complexes, or it can participate in the catalytic reaction in terms of stabilizing transitional metals, orienting guest molecules, or introducing additional active sites.

Understanding the current limitations of MOFs can provide another important viewpoint to develop feasible catalytic applications. Although few kinds of MOFs with extraordinary robust structures have been discoverd,[187-189] most of other MOFs are usually criticized for their sensitivity to moisture and open air, spontaneous hydrolysis, phase transitions or amorphization during time.[190-191] Moreover, the degradation of frameworks in special solvents or in acidic/basic solutions are all serious drawbacks that delimit the application scope of MOF as a heterogeneous catalyst. Consequently, improvement of the thermal and chemical resistance in MOF population to a certain degree at which the catalytic processes can still be carried out properly is an urgent task waiting to be solved.

2.5.2 Designed Catalytic Property of MOFs

MOFs are comprised of three distinct groups where the catalytic function can be well allocated: the metallic nodes, the organic linkers, and the porous structure.[114] Some as-synthesized active MOFs containing metal ions that are coordinatively unsaturated sites (CUS) can directly coordinate to substrates to catalyze a chemical reaction. The use of CUS-containing MOFs is one of the most facile and widely exploited applications. In this category, one of the coordination positions is occupied by a weakly associated guest molecule (i.e. solvent molecule or water), which can be easily eliminated without destroying the crystalline structure. Examples of this as-synthesized active MOFs are the HKUST-1-Cu,[192] and the MIL-101-Cr.[187] After removing the guest molecules to form a coordination vacancy, the resulting metal center can act as a Lewis acid with high affinity toward electrons. If the metal oxide nodes whose electronic configuration resembles to that of a semiconductor, the semiconducting ability could be observed on these materials,[193-194] resulting in photocatalytic properties.[193-196]

When it comes to organic linker-oriented catalytic reactions, the MOF framework might act as a robust organocatalyst.[197-199] 2-Aminoterephthalate (NH_2bdc) is one of the most fundamental ligands which impart MOFs with several functionalities, since the incorporated amino groups can pass on basic properties to the material, resulting in association with different strength (figure 2.10a).[199]1,3,5-Benzene tricarboxylic acid tris[*N*-(4-pyridyl)-amide] (4-btapa) is another well-known example of a ligand containing two types of functional groups that have been used to prepare MOFs.[181] The ligand coordinates to the metal ions via the N atom of pyridine, and the non-coordinated amide groups can be used as active sites for base catalysis. To avoid the undesired association between metal ions and

active functionalities, various strategies, such as utilization of protecting groups,[200-201] postsynthetic ligand exchange[202-204] and mixed-linkers (MIXMOFs),[205-207] are used during the preparation of MOFs with reactive functional groups.
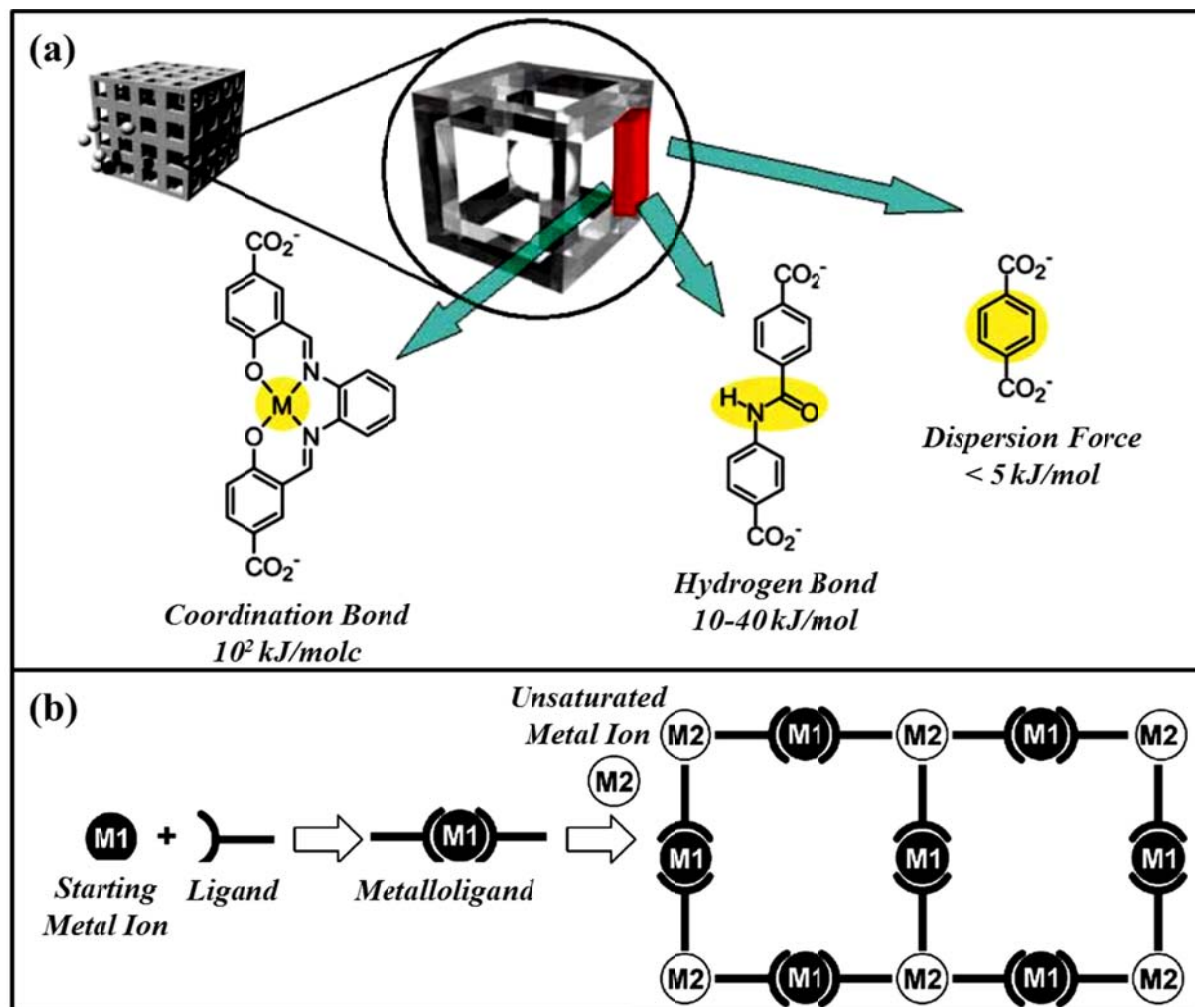
Figure 2.10 Illustration of surface engineering on MOF nanochannels by introduction of (a) multifunctional ligands and (b) an unsaturated metal center by metalloligands. Figure reprinted with permission from Royal Society of Chemistry (2006).[199]

An alternative to introduce active metal sites into a MOF framework is via applying a suitable organic linker to bind the first metal ion to form a metal coordination complex (metalloligand). Thus, this metalloligand is used as a secondary linker to coordinate with secondary ions to form the MOF structure (Figure 2.10b).[199] Through this strategy the microenvironment ranging from oxidation state, electronic properties, and coordination/chiral environment can be designed with high-degree of precision.[199, 208]

Last, the highly porous MOF structure can be utilized as reaction environment or as a cage to encapsulate reactive species. Once active species are trapped in the porous cage,[209-211] the mobility of these molecules is restricted. However, enhanced catalytic properties could be observed due to the

confinement effect. To achieve encapsulation in a porous matrix, the entrapped complexes must be so small that they can fit into the cavity of the cage and meanwhile larger than the openings to avoid leakage. Considering to the critical pore dimension, the conventional impregnation is less available, and by contrast two other approaches have been demonstrated. The first one is through assembling the active species directly within the cavity of porous cage, the so-called "ship in bottle" strategy. The second approach is by assembling the support around the active species, also known as a "bottle around ship" or "templated synthesis" strategy.

2.5.3 Unique Niches for Application

The huge diversity of structures and composition of MOFs, together with facile functionalization to incorporate versatile catalytic active sites/functional groups at the metal nodes, at the linking ligands or inside the pores, offers unique and unprecedented potential to MOF engineering for catalytic applications. Nevertheless, it is obvious that the currently prevalent conventional catalysts can hardly be replaced by MOFs for the synthesis of materials in large-amount bulk, especially in fields with low specificity requirement. These traditionally applied catalysts have the advantages of low cost and higher stability than MOFs, and are constantly applied by industry. Therefore, to expand potential of MOFs in the future catalysis area, attempts shall be targeted on applying these well-defined crystalline solids in reactions where their highly dynamic property can be exploited to surpass other catalysts. As a result, the transformations that are too complicated to conventional catalysts will become suitable targets for MOFs, for instance, chemo-/enantio/regioslective reactions, one-pot multicomponent coupling reactions and step-dependent sequential reactions.[212-213] It is believed that, in not too distant future, MOFs as highly-tailorable heterogeneous catalysts will find unique application niches in asymmetric catalysis, one-pot multicomponent coupling/tandem reactions, or combined reactions.[214-216] These, additionally with light harvesting applications (i.e. photocatalysis), are probably the scenarios in which MOFs can outperform traditional catalysts.[217-218]

2.6 Photoconductivity of MOFs

Recently, the potential usage of MOFs in the field of photocatalysis has stimulated thriving interest due to large surface area, well-ordered porous structure and tunable, versatile organic linkers/metal nodes complexes, which impart MOFs promising photo-physical and chemical properties.[211, 219-221] These photocatalytic materials can be prepared by combining the luminescent metal clusters with adjustable organic linkers, as well as incorporation of specialized guest molecules to optimize the light absorption behavior and to diversify the surface functionality of MOFs.[106, 222-223] Thus modulation of MOFs to realize superior visible light-driven photocatalysis in different areas is of utmost importance.

2.6.1 Electrical- and Photoconductivity of MOFs

Three categories of electrical conductivity are prevalently utilized to distinguish the electrical property of a material at room temperature (RT): insulator ($\leq 10^{-10}$ S/cm), semiconductor (10^{-10}-10^{1} S/cm) and metal (10^{1}-10^{5} S/cm).[224] To evaluate the electrical behavior in a reliable way, the thermal variation of MOF's electrical conductivity is traced within the linear Ohmic function. Take the MIL-125(Ti) as an example, an electrical conductivity of $\sim 10^{-5}$ cm^{2}/Vs was determined under UV irradiation (340 nm), and the value decreased in line with the temperature, indicating the thermal-dependent charge transport in MOFs.[225-227]

Distinct from conventional semiconductors with a band structure, a localized model was identified in MOFs, where the charges ''jump'' by a photon-assisted quantum tunneling mechanism.[228] The conductivity illustrated by this hopping model can be represented by a modified Arrhenius Equation:

$$\sigma = \sigma_0 \exp\left[-\left(\frac{T_0}{T}\right)^{a}\right] \tag{19}$$

where σ_0 (localization length) and T_0 (phonon frequency) are related to the electronic density of the states at the Fermi level, the exponent a is related to the electronic dimensionality, $a = 1/(1 + D)$, D is the dimensionality. Based on the above analysis, it is suggested that MOFs with 1D structure are more conductive than 2D- and 3D-MOFs.[224]

In the case of inorganic semiconductor photocatalysts, while excited by light the negative electrons (e^-) will be translocated to the conduction band (CB) and a positive hole will remain on the valance band (VB), which reacts with the adsorbed reactant separately.[229-230] A similar mechanism happens in organic semiconductor as well. However, the energy level is differently described as the highest occupied molecular orbital (HOMO) and the lowest unoccupied molecular orbital (LUMO).[231-233] Although the detailed mechanism is still unclear in MOF systems, considering to the optical transition and the visible photocatalytic performance, MOFs have long been regarded as semiconductors[193, 234-235] with theoretical band gaps between 1.0 and 5.5 eV.[236-238] In order to understand the electronic and

optical properties of MOF, MOF-5 has recently been investigated systematically.[193-194, 239-240] The photo-induced charge separation (e- and h+) like that in semiconductor has been reported in MOF-5 nanoparticles, and the formed charge carriers can act photocatalytically with oxidative/reductive ability (Figure 2.11a).[194] The actual conduction band (CB) energy was estimated to be +0.2 V versus NHE with a band gap of 3.4 eV.[193] However, the detailed mechanism of how the charge carriers are generated and migrate in the MOF and where the oxidative/reductive reaction process is conducted has not been fully understood yet.
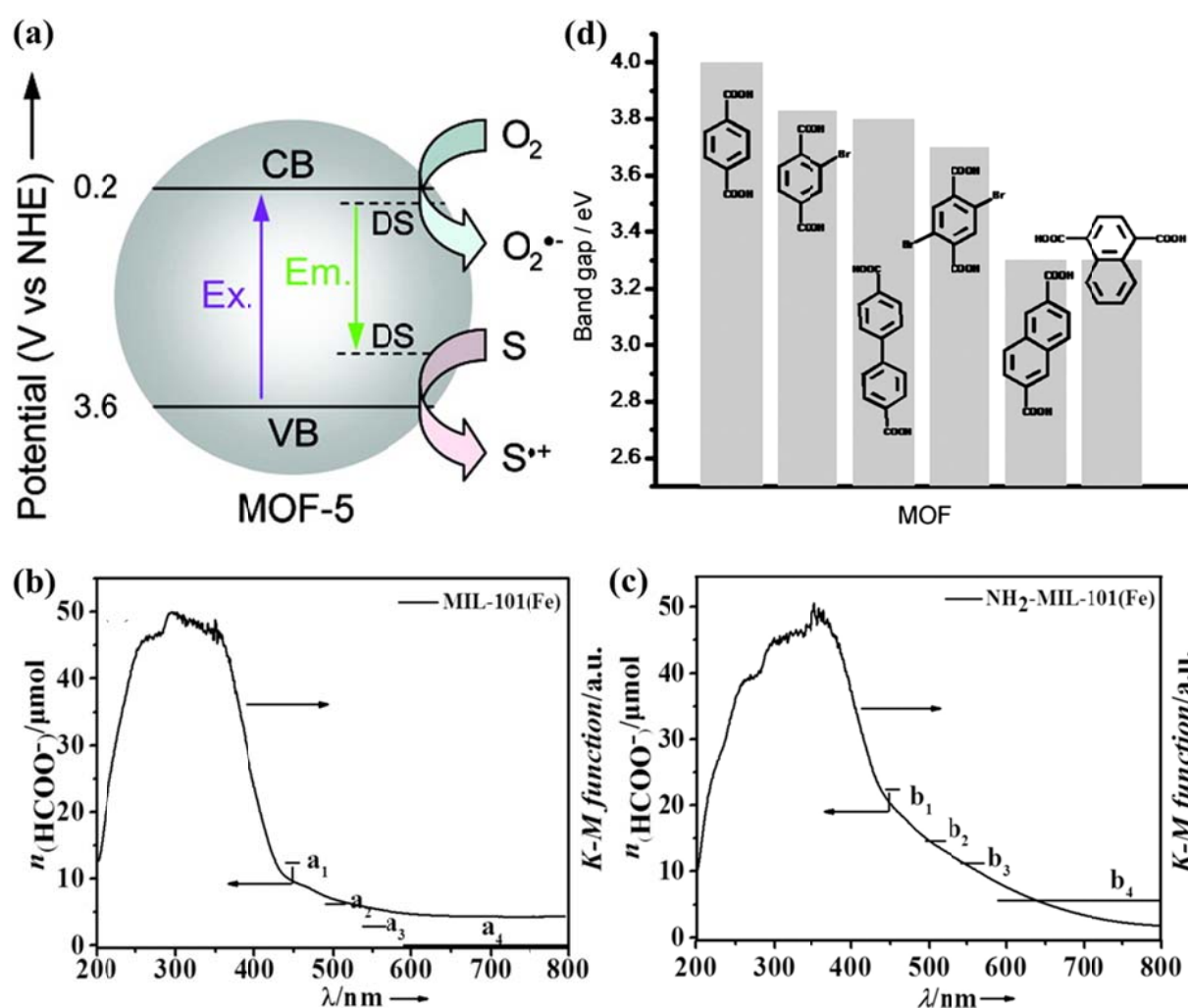
Figure 2.11 (a) The proposed photocatalytic mechanism of MOF-5, illustrating by the conduction band (CB), valence band (VB), defect state (DS), excited band gap (Ex.) and defect emission (Em.). The wavelength-dependent HCOO- evolution by using (b) MIL-101(Fe) and (c) NH$_2$-MIL-101(Fe). (d) Tunable band gaps of MOF-5 by varying the comprised ligand. Figure (a)[194] and (b)/(c)[241] reprinted with permission from American Chemical Society (2008 and 2014), and Figure (d) reprinted with permission from John Wiley and Sons (2008).[242]

2.6.2 Proposed mechanism for charge transfer

Up to now, the photocatalytic properties have been reported for several MOFs, such as MOF-5,[191, 193-194, 243] UiO-66-Zr,[188, 196] MIL-101-Fe[241, 244-246] and MIL-125-Ti.[247-250] For the above mentioned systems, once excited by light, the comprised linkers can act as build-in antennas to harvest light and then deliver the photo-excited charge carriers to central metal clusters, revealing the so-called linker-to-metal-cluster charge transfer (LCCT) mechanism.

In other MOFs, the metal clusters containing photosensitive metal ions can be directly excited and induce the electron transfer subsequently. For instance, the Fe–O cluster in the Fe-containing MOFs (i.e. MIL-101(Fe), MIL-53(Fe) and MIL-88B(Fe) can be directly excited and transfer the electron from O^{2-} to Fe^{3+} to form active Fe^{2+} and finally to commence photocatalysis.[241, 244-245]

The other functionalized MOFs, such as NH_2-MIL-101(Fe), a dual excitation pathway was conducted instantaneously in a MOF. Namely, the amine groups from the functionalized ligands are excited and transfer the electrons to Fe centers via the LCCT, and meanwhile the Fe-O clusters can be excited as well. This synergic effect between functionalized ligands and metal ions which expands the light absorption range toward visible light and thus enhanced the catalytic performance by 3 times can be observed in the MIL-101(Fe) system while compared to the inert MOF (Figure 2.11b and c).[241]

2.6.3 Modified Photocatalytic Performance

Although significant progress has been made in using MOFs as photocatalysts, the photocatalytic efficiency still cannot reach the practical requirement. Fortunately, due to the inherent nature including porous structure with large surface area and high versatility of linkers/metal clusters, several strategies have been developed to improve the photocatalytic performance, for example, alternation of organic linkers/metal clusters or incorporation of extra addition complexes to expand visible light absorption, to improve charge separation, and to activate reactant more efficiently.

2.6.3.1 Modulation of Organic Linkers

Because one critical step in a photocatalyst is light harvesting to generate charge carriers, the photocatalytic system can be directly benefited from expanded absorption wavelength. By adjusting the functional organic linkers of MOFs, the ligand-to-metal charge-transfer (LMCT) transition will be coincidently changed, and thus the light absorption behavior can be effectively enhanced.[196, 251-252] A series of isoreticular MOFs with different organic linkers were fabricated, namely terephthalic acid (IRMOF-1, MOF-5), 2-bromoterephthalic (IRMOF-2) acid, 2,5-dibromoterephthalic acid, biphenyl-4,4'-dicarboxylic acid (IRMOF-9), 1,4-naphthalenedicarboxylic (IRMOF-7) acid and 2,6-naphthalenedicarboxylic (IRMOF-8) acid. The band gap energies of these MOFs are determined by UV/Vis spectroscopy and summarized in Figure 2.11d.[242] At the beginning, a band gap of 4 eV was determined in the MOF-5 with intrinsic bdc ligand. Once the comprised ligand was replaced, the band

gap changes dramatically as anticipated by theoretical results.[237] All the 6 selected functional ligands were electron-donating molecules, but with different type of functional groups (Br or aromatic ring); besides, both naphthalene linkers share the same value of band gap ($\approx$ 3.3 eV). The result provides a guide line for ligand-dependent MOF bandgap, and illustrates that the semiconductor behavior of is highly designable via selection ligands with miscellaneous substituents.

2.6.3.2 Modulation of the Structure of Metal Clusters

Consistent with the MOF-5 system, another theoretical investigation based on the density functional theory (DFT) indicates that the band gap of MOF-5 can be altered via substitution of the metal oxide, Zn_4O, with X_4Y (X = Zn, Cd, Be, Mg, Ca, Sr, Ba; Y = O, S, Se, Te) in the node, resulting band gaps ranging from 1.7 to 3.6 eV owing to the electronic states of Y atoms in the X_4Y nodes and C atoms in the organic bdc linkers. The decreasing band gap and the red-shifted absorption edge are following the trend of O $\rightarrow$ S $\rightarrow$ Se $\rightarrow$ Te.[253] The result is also duplicable in other MOF systems[241] and therefore can serve as an instruction to design MOFs with capacity to harvest and utilize visible-light.

3. Outline

Precise control over architectures, compositions and functionalities of polymers has been a long-standing goal in synthetic polymer chemistry, as it is a prerequisite to obtain functional macromolecules with desired properties.[42, 254-255] Over the past decades, RDRP techniques including NMP, RAFT and ATRP have provided access to polymers with predetermined molecular weight, low dispersity ($Đ$), tailor-made topology, and living end functionality.[4-8] Among these strategies, ATRP is more advantageous because of the higher compatibility to hybrid materials, facile preparation of multifunctional copolymers and miscellaneous end-functionalities. Other properties including commercially available initiators and widely-adapted reaction conditions all point to ATRP as an eminent methodology for polymer synthesis. However, there are also long-term struggles which delimit the application of ATRP to some degree. For example, due to catalyst-induced biradical termination in bulk state, synthesis of high MW polymers is challenging, resulting in high $Đ$ and loss of chain-end functionality. Moreover, due to the innate radical polymerization, tacticity control has been another arduous challenge for ATRP. While considering utilized catalysts, the non-reusable transition metal catalysts in high concentration and tedious reaction procedures which lead to laborious purification and product contamination are other drawbacks of using ATRP techniques.

MOFs are new-emerging porous materials comprised by metallic nodes and organic linkers, featuring well-ordered robust structure, high specific surface area, tunable pore sizes/shapes and specific tailorable surface functionalities. These promising properties have significantly boosted diverse applications, such as gas processing,[29-30] sensing,[31-32] catalysis,[33-36] and confined space for polymerization.[37-39] In the present thesis, the utilization of MOFs in catalysis and intriguing polymer synthesis will be further emphasized (Scheme 3.1).

In Chapter 4, an inert MOF structure will be employed as host for various monomers with different sizes to conduct ARGET ATRP controlled polymerization inside the confined nanochannels. Previous study has theoretically advocated that the compartmentalization effect can serve as an universal niche to synthesize higher MW polymers with controlled $Đ$. Experimental results also point out by free radical polymerization of vinyl monomers inside MOFs, the improved tacticity in accommodated polymers can be observed.[155, 157] Nevertheless, the uncontrolled MW, relatively high $Đ$ and dead chain-end functionality resulting from free radical polymerization prevent subsequent macromolecular engineering. Therefore, replacing the conventional free radical polymerization by ARGET ATRP, the combination of MOF's compartmental space with sustainable controlled polymerization mechanism can diversify polymer composites with expanded properties. To get deeper insight of host-guest interaction for polymer manipulation, functionalized MOFs with polymerization initiating moieties are designed and used for polymerization in a refined confined environment as well.
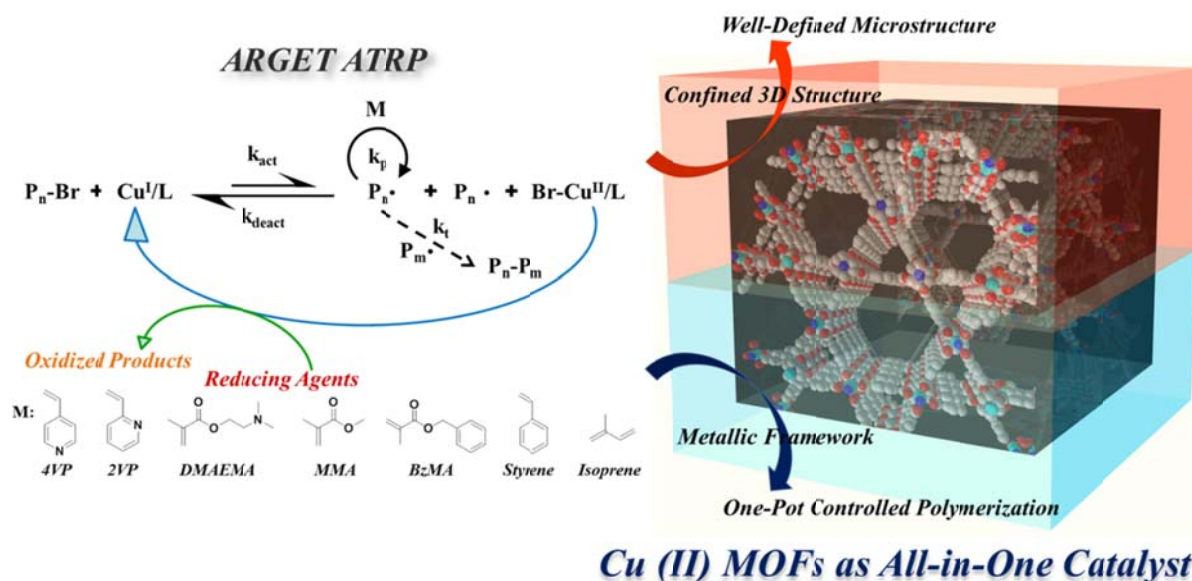
Scheme 3.1 Concept of combining MOF crystals with ARGET ATRP to synthesize ever-advanced complexes with unanticipated performances.

Interestingly, during the abovementioned study using Zn MOFs as hosts for in-situ polymerization, the catalytic property of the isoreticular Cu(II) MOF, $Cu_2(bdc)_2(dabco)$, was observed by triggering the polymerization in the bulk phase spontaneously without the addition of $CuBr_2$ as a homogeneous catalyst. Consequently, owing to this surprising phenomenon, the catalytic capability of Cu(II) MOFs is further investigated.

In Chapter 5 and 6, the Cu(II)-based MOF, $Cu_2(bdc)_2(dabco)$, has been demonstrated as a heterogeneous, universal catalyst to polymerize varous kinds of monomers via controlled ARGET ATRP based on thermal (Chapter 5) or visible light-irradiation treatment (Chapter 6). In a traditional ATRP process, the necessity for catalysts and associated ligands complicates reaction processes, and inevitable interactions resulting from monomers, catalysts (i.e. 4-vinylpyridine (4VP) and CuBr)[9,10] and ligands (i.e. isoprene and PMDETA) together with non-reusable catalyst all limit the feasibility of this methodology. Due to the infinitely expanded crystal structure comprised by accessible catalytic metal sites co-jointed by organic linkers, the utilization of Cu(II) MOF, namely $Cu_2(bdc)_2(dabco)$, as a heterogeneous catalyst-ligand complex is probed to catalyse ARGET ATRP of various monomers, such as benzyl methacrylate (BzMA), styrene, MMA, DMAEMA, and used for challenging monomers (e.g. 4VP, 2VP and isoprene), in a well-controlled and living fashion. As a result, a time-consuming synthetic procedure is significantly simplified, and chelating side reactions within the polymerization mixtures are avoided. Moreover, considering the particle size of a few hundred nanometers, the MOF catalyst can be easily collected by centrifugation and reused for other polymerizations.

Extended from Chapter 5, the adjustable optical properties of MOF catalysts according to the guest monomers with varied association strength toward Cu ions are further illuminated in Chapter 6. Comprehensive studies have evidenced that the band gaps and light harvesting property of MOFs are highly designable via varying the organic linkers or introducing guest molecules in the structures. Other reports also evidence that nitrogen-containing molecules, such as TEA, DMAEMA and vinyl pyridines, are able to act as reducing agents to activate the metal catalytic centers under light irradiation.[62-63, 256-258] Therefore, through forming complexes with various nucleophilic monomers/molecules, series of photochemical and electrochemical properties of the Cu(II) MOF are investigated in Chapter 5. Based on the tunable photoabsorption property, photoinduced Reversible-deactivation radical polymerization (PRDRP) can be realized under visible-light irradiation and requires no photo-specialized initiators, sensitizers or complexed ligands. Owing to the advantage of photopolymerization, the polymerization processes can be further fastened and temporal control during the reaction becomes achievable.

The eminent catalytic property of MOFs, especially $Cu_2(bdc)_2(dabco)$, has been demonstrated in the previous works, and consequently the concept to push the catalytic performance towards a higher level is presented in Chapter 7. It is common that the performance of heterogeneous catalysts can be improved efficiently through decreasing particle size or increasing dispersibility. However, the intrinsically coordinated inorganic property makes MOF crystals usually brittle and easily aggregated/clogged which inevitably retards mass transfer, reduces interfacial area, and then restrics the catalytic capability. To conquer this long-term problem,[173, 259-260] "smart" polymer grafted pollen grains (*P*-pollen) are devised. Via surface initiated ARGET ATRP (SI-ARGET ATRP) pollen grains are grafted with responsive poly(2-(dimethylamino)ethyl methacrylate) (PDMAEMA) brushes, acting as environment-responsive tentacles to capture and disperse MOF nanoparticles (nanoMOF) in solutions. Owing to the restricted mobility, intrinsic amine functionality and responsive property of densely grafted polymers, PDMAEMA, the *P*-pollen can serve as a potential stabilizer for various MOFs to prepare well-dispersed MOF@*P*-pollen composites without debilitating their catalytic potential. Furthermore, via applying the environment-responsive behaviour of tentacles, the associated nanoMOFs can be exposed (catalytic active) or buried (catalytic inactive) reversibly to give the state-of-the-art catalytic performance with switchable on-off capability in visible light-triggered copper(I) catalyzed azide–alkyne cycloaddition (CuAAC)   and   dye   degradation   model   reactions.

4. Functionalized MOFs as Unique Niches for Highly-Defined Polymerization Reactions

4.1 Introduction

A facile and universal method to improve control in high molecular weight systems and stereoregularity is presented in this chapter. It is well known that precise control over architectures, compositions and functionalities of polymers has been a long-standing goal in synthetic polymer chemistry.[42, 254-255] Attributed to catalyst-induced side reactions and chain-chain termination in bulk environment, high molecular weight polymers with controlled $Đ$ and high chain-end fidelity are usually hardly achieved.[9-10] Although a few ultra-high-molecular-weight (UHMW, $M_n > 10^6$) polymers have been successfully synthesized by modified-ATRP and RAFT, specialized conditions such as high pressure,[75, 261] high concentration,[262] or heterogeneous reaction media[102] are required. Moreover, tacticity control has been another arduous challenge for RDRP.[263-265]

Inspired by nature, researchers have utilized porous materials such as liquid crystals,[20] stereoregular polymers,[21-22] porous silica,[23-24] zeolites,[25-26] and metal-organic frameworks (MOFs)[27-28] as confined polymerization environment to improve control over polymer structures. Up to now polymerization of vinyl monomers inside of MOFs is still limited to the free radical process, which results in uncontrolled MW, relatively high $Đ$ and dead chain-end functionality preventing subsequent macromolecular engineering. Functionalized MOFs can be easily prepared via prefunctionalization which introduces deliberated heterogeneous struts, forming multivariate composites with consistently ordered structures.[133, 266 134, 155] In such a way, polymerization initiating/mediating moieties can be incorporated directly in the frameworks, which enable tailored nanochannels for host-guest interactions and confined size-dependent polymerizations.[160, 267]

In the present Chapter, a strategy combining porous MOFs and activators regenerated by electron transfer (ARGET) ATRP, is proposed to unshackle current limitations and improve the precision of synthetic polymer chemistry comprehensively. Specifically, ARGET ATRP is conducted to gain the advantages of mild conditions, higher oxygen tolerance and lower catalyst demand.[5] As shown in Scheme 4.1, MOFs are designed and fabricated to investigate the nanoconfinement effect on controlled polymerization. The inert [Zn$_2$(bdc)$_2$(dabco)]$_n$ (abbreviated as Znbdc, **1a**) (bdc = benzene-1,4-dicarboxylic acid and dabco = 1,4-diazabicyclo[2.2.2]octane) was employed at first,[268-269] and then series of initiator-functionalized [Zn$_2$(bdc)$_{2-x}$(Brbdc)$_x$(dabco)]$_n$ (abbreviated as ZnBrbdc) (Brbdc = initiator functionalized bdc) were prepared by a mixed-ligand strategy incorporating bdc and Brbdc

with varied Brbdc fractions of 10% (**2a**), 20% (**2b**) and 50% (**2c**) to realize surface-initiated ARGET ATRP (SI-ARGET ATRP).
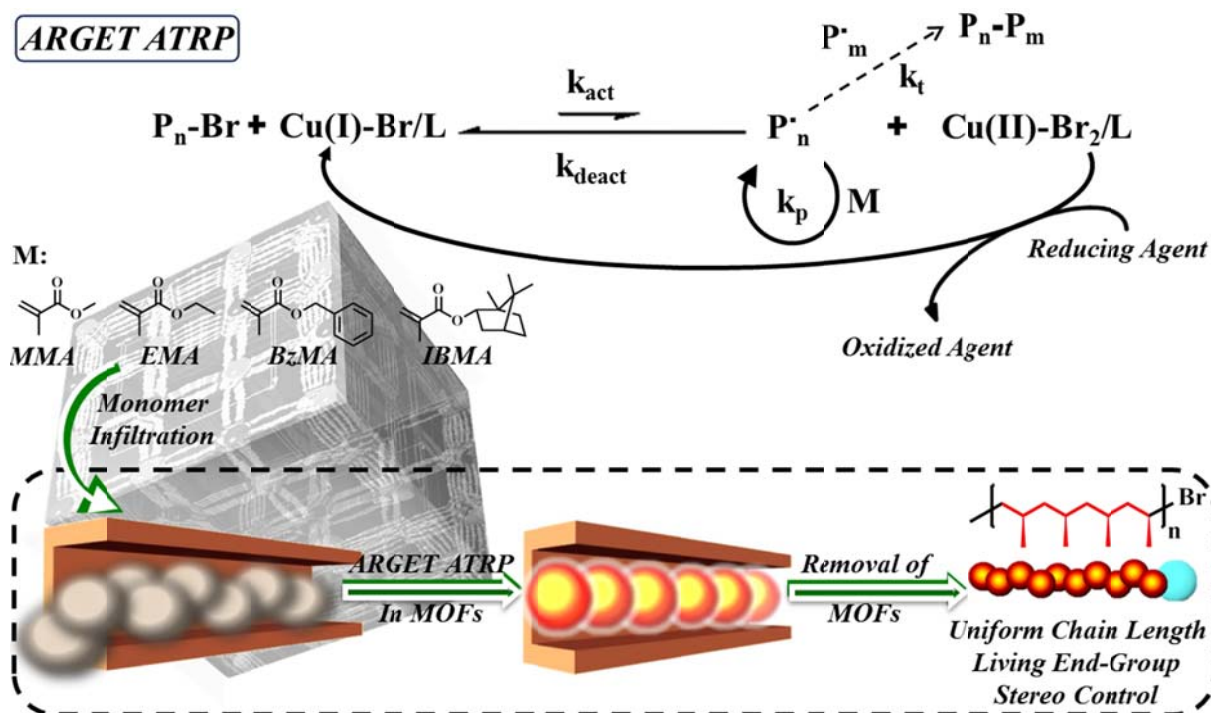
Scheme 4.1 Overview of ARGET ATRP in MOF confined environment to synthesize well-defined polymers in an universal and facile fashion.

First, monomers with various molecular sizes, such as methyl methacrylate (MMA), ethyl methacrylate (EMA), benzyl methacrylate (BzMA) and isobornyl methacrylate (IBMA), were individually infiltrated into the MOF nanochannel. ARGET ATRP was carried out to polymerize the monomer in a controlled fashion and polymers were obtained after the removal of MOF hosts. For comparison, **1a** was utilized as confined space for conventional ARGET ATRP using freely suspended initiator in the feeding mixture; in contrast, SI-ARGET ATRP was initiated directly inside the nanochannel by initiator-ligand (Brbdc) without addition of free initiator. Adapting the confinement strategy demonstrated in nature, a combination of functionalized MOFs and ATRP techniques enables the facile preparation of high molecular weight polymers with low *Đ*, living chain-end functionality and improved control in tacticity.

4.2 Results and Discussion

4.2.1 Fabrication of Host Zn MOFs

In order to constructed the ATRP-oriented MOFs, the initiator-functionalized ligand, Brbdc, was first synthesized according to the literature and characterized by NMR (Figure 4.1).[270] Due to guest-dependent dynamic framework flexibility (i.e. resemblance to proteins with reaction centers which reagents can fit into),[271] and continuous porous structure that can accommodate various vinyl

monomers, $[Zn_2(bdc)_2(dabco)]_n$ (1a) was chosen as host framework.Moreover, the host framework was extended to the initiator functionalized $[Zn_2(bdc)_{2-x}(Brbdc)_x(dabco)]_n$ (**2a**, **2b** and **2c**) by partial replacement of bdc with Brbdc, for example, 10, 20 and 50%, to realize SI-ARGET ATRP and to study the effect on polymer molecular weight, controlled polymerization and guest size effect (Figure 4.2).
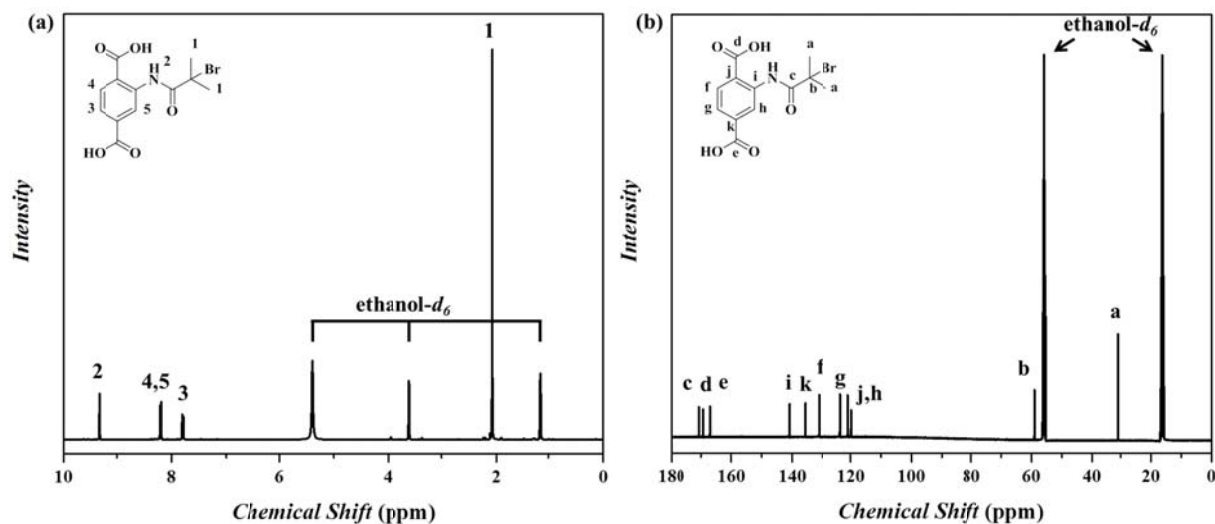
Figure 4.1 NMR spectrum of the synthesized Brbdc in ethanol-*d6*: (a) ^{1}H NMR and (b) ^{13}C NMR.

Analysis of MOF structures was performed via single crystal X-ray diffraction as well as optical microscopy. A tetragonal framework was clearly observed for **1a** (Figure 4.2a) with a surface area of 2200 m^2/g and pore volume of 0.71 cc/g (Figure 4.3a and Table S1), corresponding PXRD profile (Figure 4.5a).[40] However, while **2a** showed high resemblance to 2b in X-ray pattern, **2b** was defined as a tetragonal system with spacing group I 4/mcm, channel size 5.8 x 5.8 Å and calculated cell volume 4381.0(3) $Å^3$. On the other hand, a hexagonal system with spacing group P6/mmm was annotated to **2c** with two channel populations which are 5.2 and 17.3 Å in diameter and 3902.6(2) $Å^3$ as cell volume (Table 4.1, Figure 4.2 b-c, Figure 4.3). Field-emission scanning electron microscopy (FE-SEM) was conducted to study the synthesized crystals in depth (Figure S3).
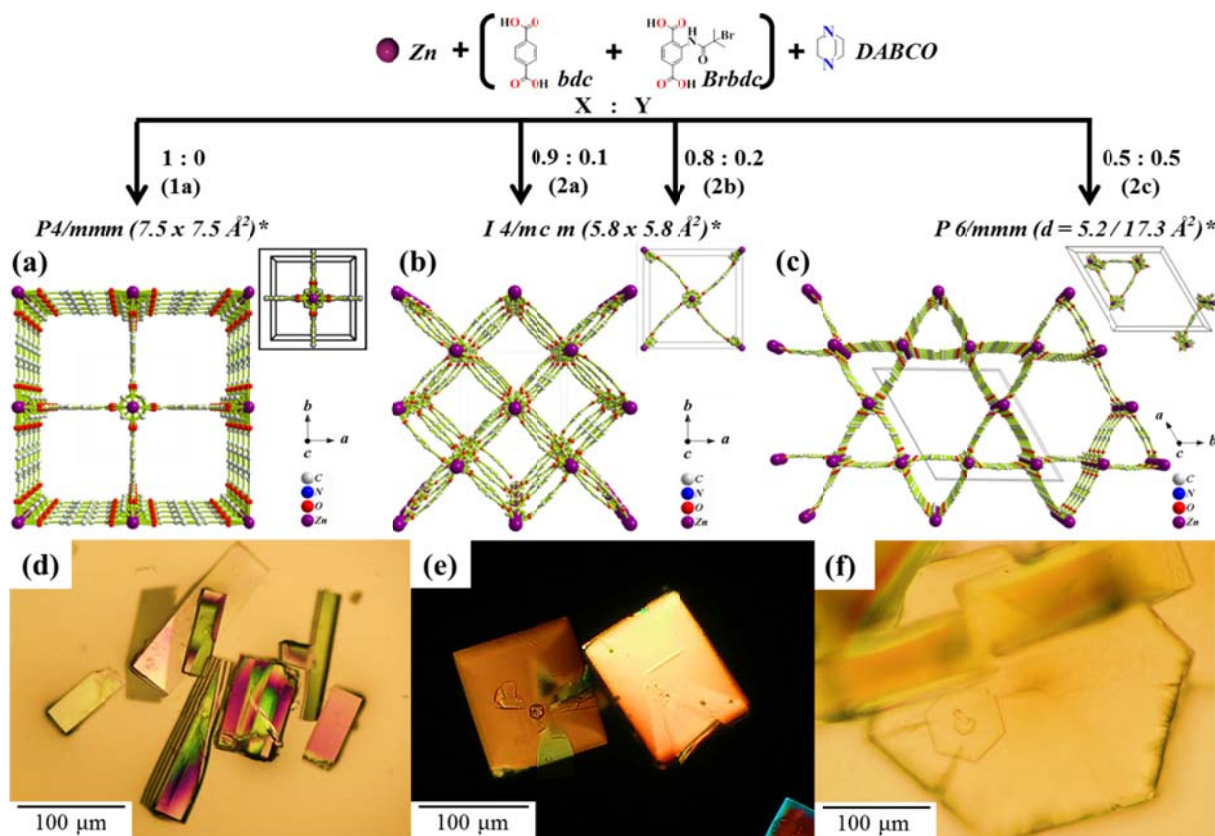
Figure 4.2 Single crystal X-ray diffraction derived structure of (a) **1a**, (b) **2a** and **2b** and (c) **2c**, and insets indicate the structure of basic unit cell. All the structures are depicted along *c* axis, and hydrogen atoms are omitted for clarity. Corresponding optical micrographs (d), (e) and (f) observed with polarized light. * The single crystal X-ray structure of 1a was present with the solvent-free structure re-depicted from CCDC 238860; the 2a/b and 2c in this study were presented with guest solvent molecules.

Table 4.1 Crystal data, details of data collections and structure refinement of **2b** and **2c** with the general composition [$Zn_2(bdc)_2(dabco) \cdot x$ DMF]; x = 3.44-4.40.

Compound	2b	2c
Empirical formula	$Zn_2(bdc)_2(dabco)$ · 3.44 DMF	$Zn_2(bdc)_2(dabco)$ · 4.40 DMF
Formula weight (g/mol)[a]	863.52	863.52
Crystal system	tetragonal	hexagonal
Space group	I 4/mcm (No 140)	P6/mmm (No 191)
a (Å)	15.0812(5)	21.5725(5)
b (Å)	15.0812(5)	21.5725(5)
c (Å)	19.2621(8)	9.6834(3)
α (°)	90	90
β (°)	90	90
γ (°)	90	120
Cell volume (Å^3)	4381.0(3)	3902.6(2)
Z	4	3
ρ_{calc} (g/cm^3)	1.31	1.10
μ (mm^{-1})	1.15	0.97
F(000)	1800	1350
Theta range (°)	3.20 - 24.98	2.37 – 25.00
Total reflections	43453	64103
Unique reflections	1048	1383
Parameters	49	54
R_1/wR_2 [I > 2σ(I)]	0.0389/0.0907	0.0273/0.0744
R_1/wR_2 (all data)	0.0643/0.1014	0.0331/0.0777
Goodness-of-fit	1.083	1.070
Largest difference peak and hole (e· Å$^{-3)}$	0.392/-0.292	0.255/-0.255

[a] Calculated without solvent.
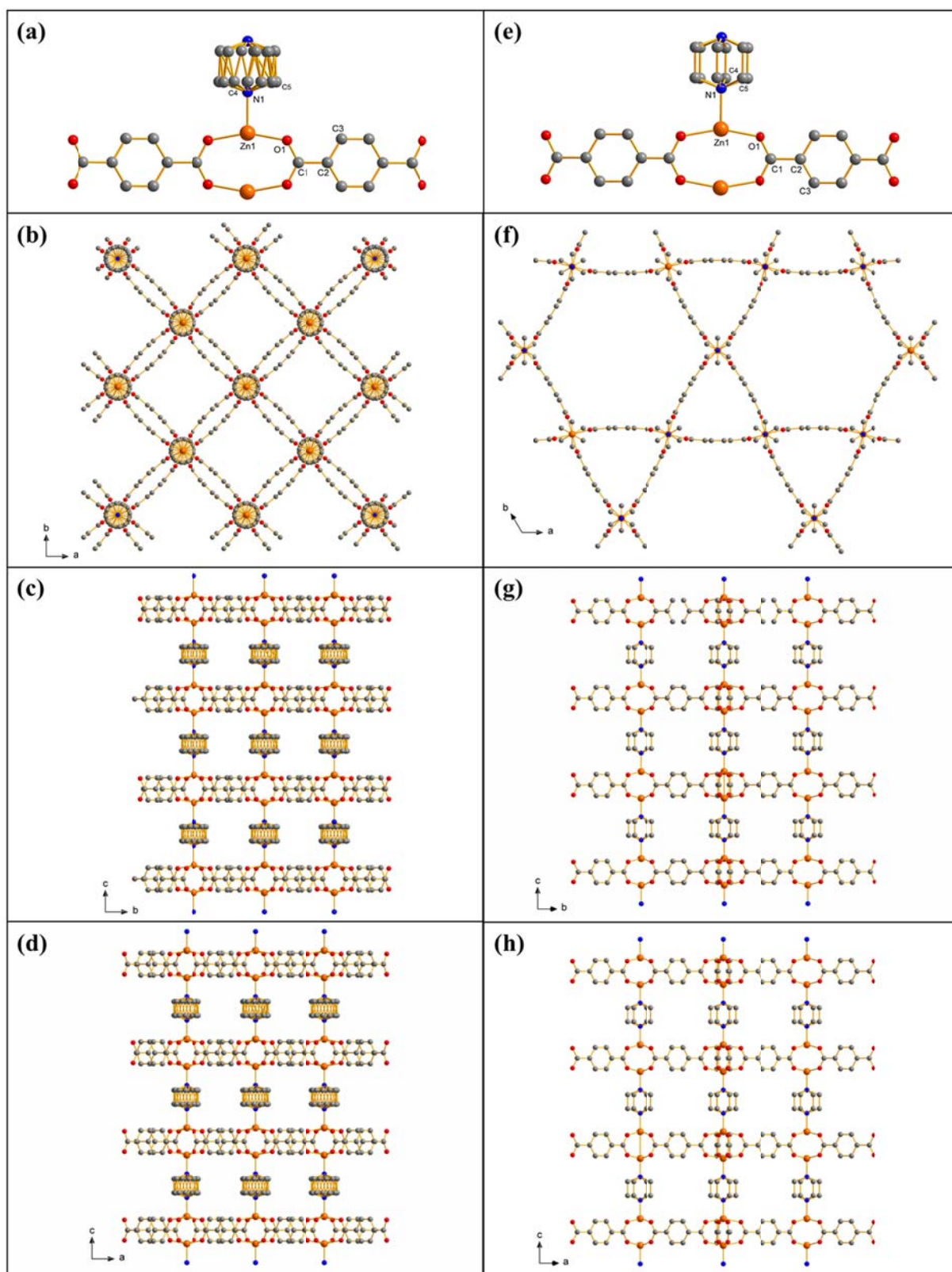
Figure 4.3 X-ray structure of **2b** (a) and **2c** (e). Hydrogen atoms were omitted for clarity, and atoms of the asymmetric unit are labelled. The 3D framework of **2b**/**2c** looking down the **c** axis (b)/(f); looking down the a axis (c)/(g); looking down the b axis (d)/(h).

The PXRD of as-fabricated functionalized MOFs exhibits high resemblance with the individual simulation resulting from single-crystal structures (Figure 4.4), indicating the formation of pure crystalline phases.
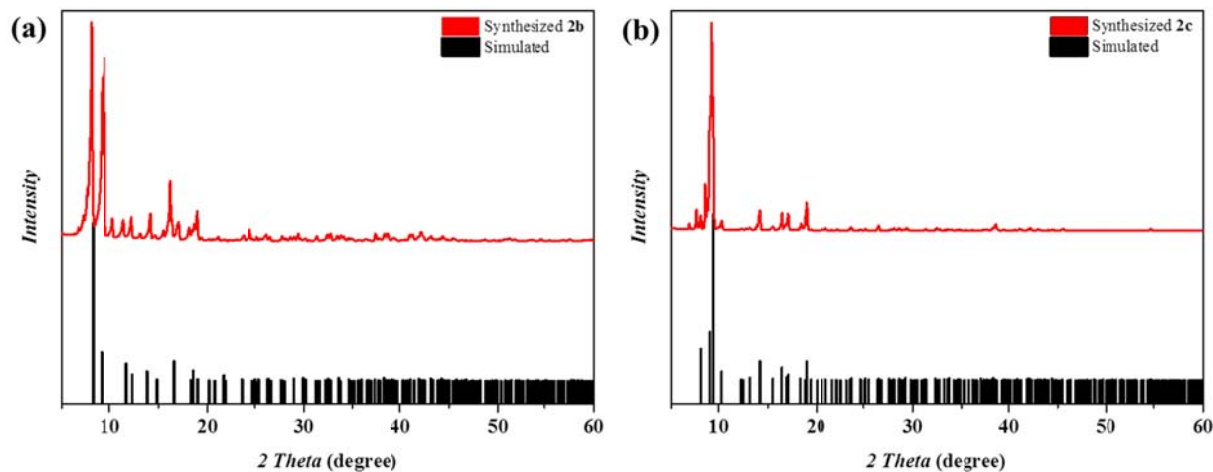
Figure 4.4 PXRD profiles of as-synthesized (a) **2b** and (b) **2c** compared to simulated diffraction profiles calculated from the single crystal X-ray derived structure and the empirical formula according to Table 1.

Closely related to **1a**, **2a** and **2b** were defined as a tetragonal system as well but with space group of *I4/mcm*. For **2b** with solvent guest molecules a channel size of 5.8 x 5.8 Å^2 along *c* axis and an aperture of 1.4 x 3.3 Å^2 along *a* and *b* can be observed, giving a void volume of 2483 Å^3 which is corresponding to 56.7 % of the total cell with approximately 3.44 DMF molecules. On the other hand, a hexagonal crystal system with space group *P6/mmm* was annotated to **2c** with two channel populations which are 5.2 and 17.3 Å in diameter, interlinked with channels along *a* and *b* axes with smaller diameter (3.4 Å) giving a solvent-accessible void volume of 2530 Å^3 (64.8 % of the total cell volume) filled with about 4.4 molecules of DMF. The determined structures of **2a/b** and **2c** were shown with bent bdc linkers, comparing to the solvent-free **1a** where the bdc ligands linking to the Zn_2 paddle wheel units are linear.[268] Although the MOF hosts for polymerization is in the powder state, the PXRD of as-fabricated MOFs exhibits high resemblance with the individual simulation resulting from single-crystal structures (Figure 4.4), indicating the formation of same microstructures and pure crystalline phases.

To verify the amount of incorporated initiator moieties, ICP-OES was utilized to quantify the incorporation of Br atoms originating from Brbdc (Figure 4.5a). Compared to the target amount, less amount of Brbdc was incorporated into the frameworks. The blending amount of Brbdc vs. the ICP-determined amount was 10% vs. 0.25% for **2a**, 20% vs. 0.66% for **2b**, and 50% vs. 2.6% for **2c**, respectively; no Br atoms are observed in 1a. Besides, a gradual increase of brown color can be observed with increasing Br incorporation (Figure 4.5b). Due to its increased molecular size Brbdc has

less molecular mobility than bdc, resulting in lower probability to be integrated into the frameworks during crystallization process. Nevertheless, a linear relation between targeted and incorporated Brbdc can be clearly identified, which means predeterminable molecular weight via varying the initiator ratio can be expected.
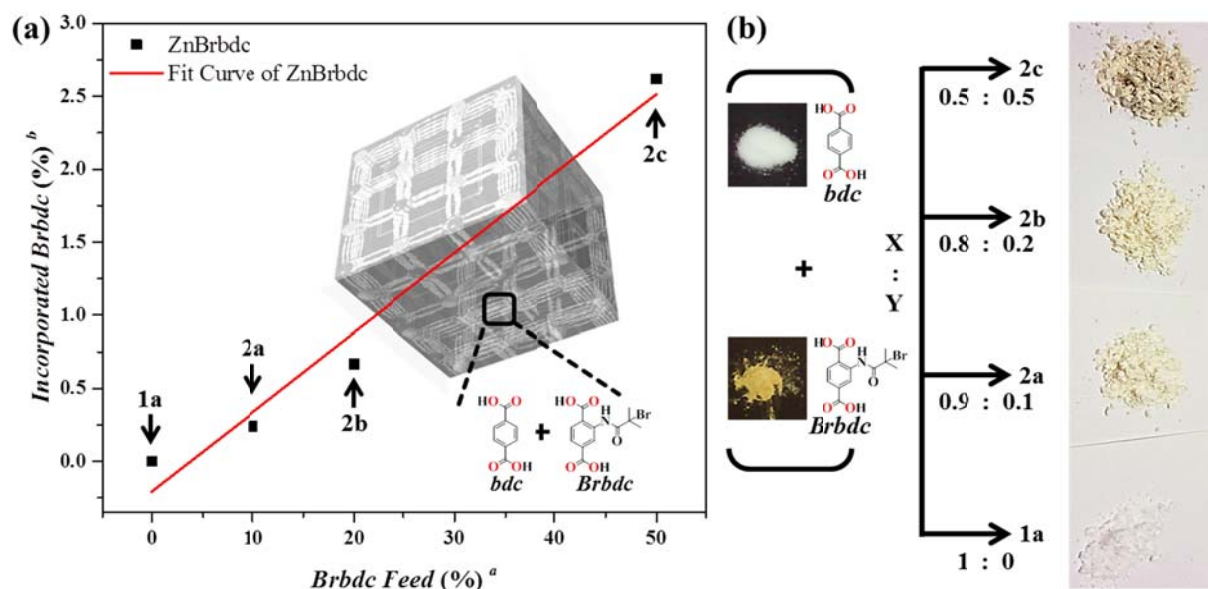
Figure 4.5 (a) Incorporated concentration (%) of initiator-functionalized ligand, Brbdc, in the as-fabricated (a) **1a**, (b) **2a**, (c) **2b** and (d) **2c**. (b) Color variation from original bdc to initiator functionalized Brbdc, and the as-fabricated **1a**, **2b** and **2c**. [a] The theoretical ratio of initiator-functionalized ligand, Brbdc, to bdc ligands within the initial crystallization solution. [b] Determined via ICP-OES.

The porosity and accessible surface area of initiator functionalized MOFs was estimated by N_2 adsorption measurements (Figure 4.6), revealing the micropore-dominant type I isotherm with BET surface area and pore volume of 1970 m^2/g and 0.76 cc/g for **2a**, and 2100 m^2/g and 0.78 cc/g for **2b**. However, a type IV isotherm with H4 hysteresis loop can be identified in **2c**, giving surface area of 1972 m^2/g and pore volume of 0.74 cc/g. The adsorption type of **2c** reveals its two fold pore distribution property having both micro- and mesopores. Interestingly, with the increment of Brbdc in MOFs, a transition in crystal morphology is obvious. The transformed from original **1a** with *P4/mmm* primitive symmetry cell and channel size 7.5 x 7.5 $Å^2$, to the isostructural **2a/b**, and then to the **2c** with hexagonal lattice and two-dimension channel distribution, advocating the higher incorporation amount of the Brbdc with varied channel architecture and a higher void-space volume. Owing to the sterically-demanding initiator functional group, square grid geometry with dihedral angle close to 90º is less favorable. Consequently, significant twisting is the case forming a stretched trigonal phase of **2c** with the highest Brbdc fraction, which is in line with N_2 adsorption results. The comprehensive characterization confirms the successful preparation of the original **1a** and functionalized **2a-c**.
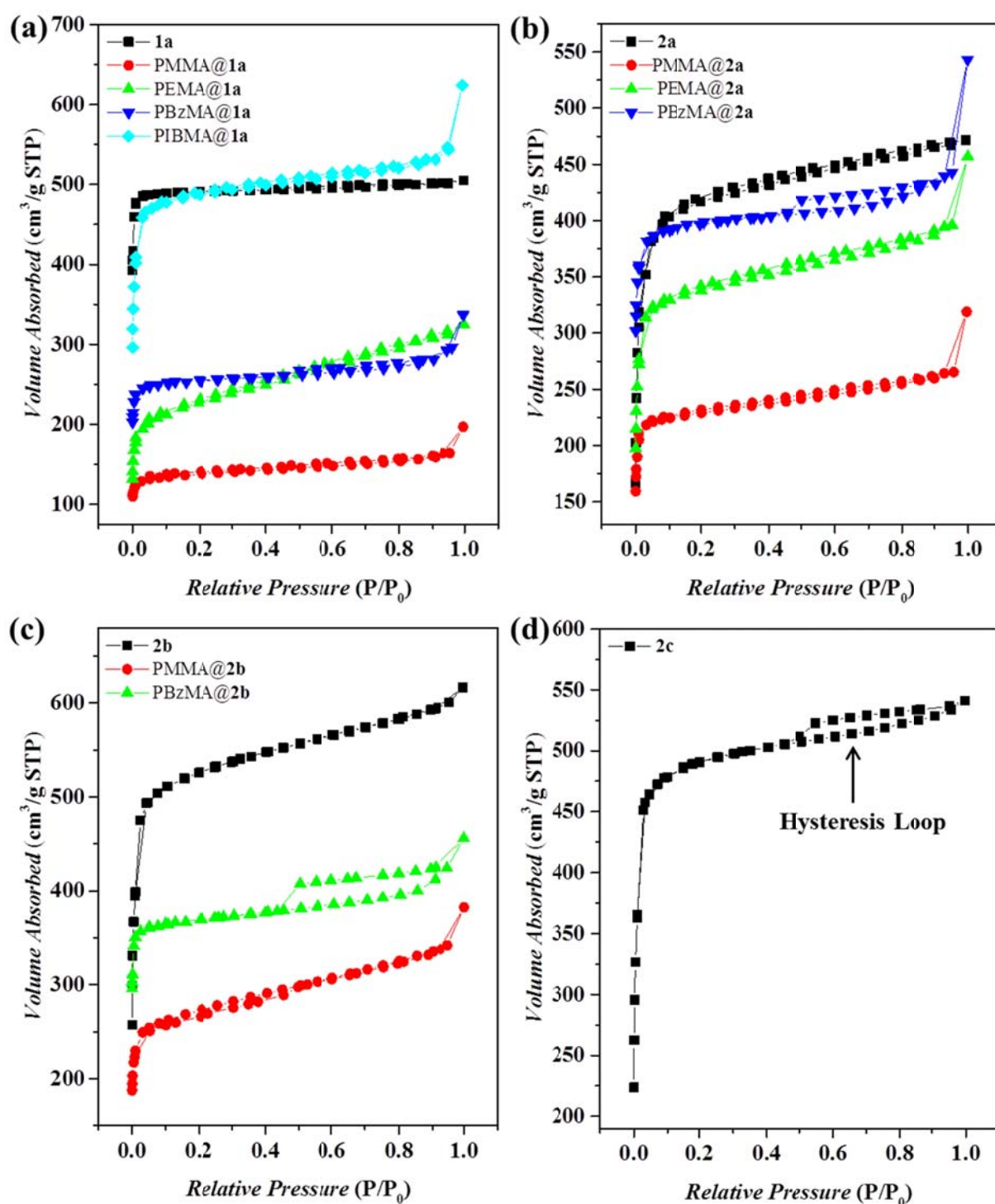
Figure 4.6 N_2 adsorption-desorption isotherm of (a) **1a**, (b) **2a** and (c) **2b** before and after polymerization of monomers. (d) as-synthesized 2c.

To preserve comparability **2a** and **2b** with similar tetragonal symmetry were utilized in comparison to **1a** in the following polymerization processes. Although the slightly different pore textures, **1a**, **2a** and **2b** are all featured with one-dimensional aromatic nanochannels formed along the *c*-axes, and another much narrower apertures with length around 4 Å which are too strapped to vinyl

monomers polymerization.[37] Therefore, it is suggested that the polymerization processes happened mainly in the the a/b window along the c axis.

4.2.2 ARGET ATRP in Confined Environment of MOFs

Controlled polymerization of methacrylates with various molecular sizes, MMA (5.7 × 4.1 Å), EMA (6.2 × 4.1 Å), BzMA (7.8 × 5.3 Å) and IBMA (9.9 × 8.2 Å), inside the confined nanochannel of **1a**, **2a** and **2b** was carried out to investigate the host-guest confinement effect (Scheme 4.2). **1a** was utilized as a reference host to conduct conventional ARGET ATRP of monomers with EBIB as initiator. SI-ARGET ATRP was carried out in **2a** and **2b** using incorporated Brbdc as intrinsic initiator. Although the amine dabco in MOF structure could serve as a potential reducing agent, it was found that extra addition of dabco is necessary to trigger the polymerization process.
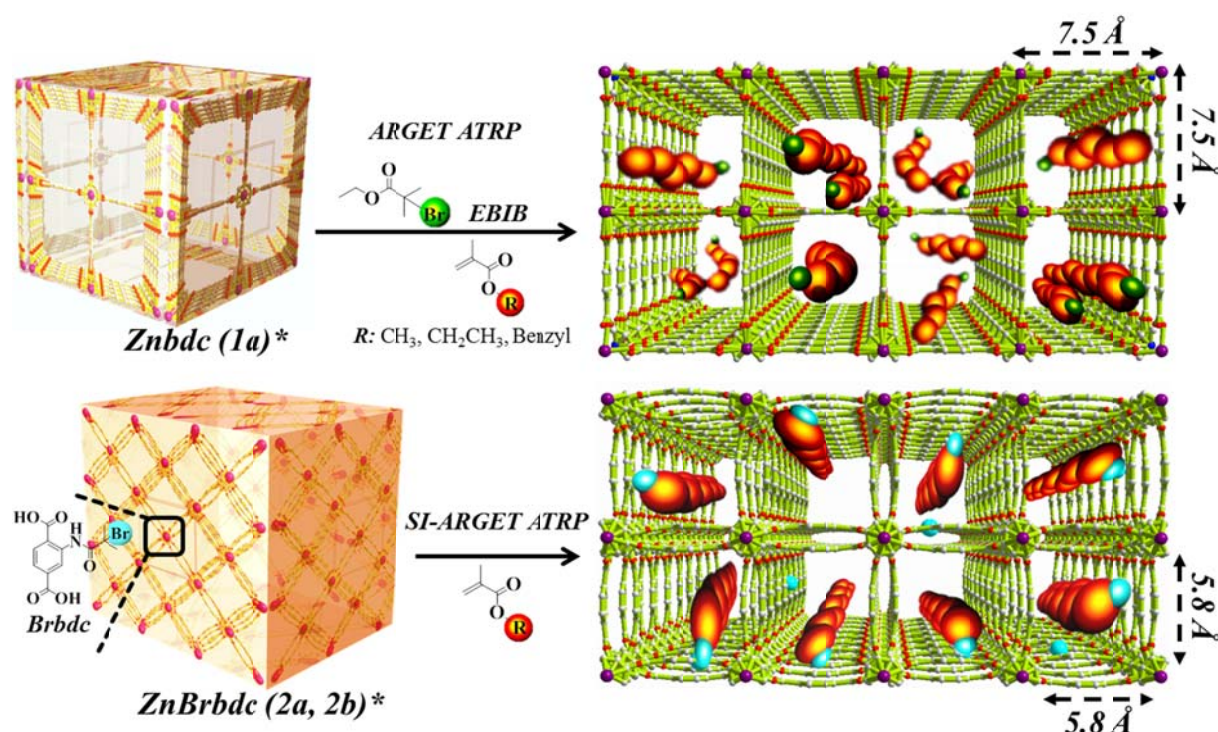
Scheme 4.2 Illustration for conventional ARGET ATRP in 1a and SI-ARGET ATRP in initiator-functionalized 2a and 2b. * The single crystal X-ray structure of 1a was present with the solvent-free structure re-depicted from CCDC 238860; the 2a/b and 2c in this study were presented with guest solvent molecules.

The incorporation of methacrylate polymers in MOFs was identified by ATR-FTIR, compared the corresponding vibration bands from the as-synthesized MOFs with polymer-incorporated composites (polymer@MOF) (Figure 4.7). Different to the original **1a** host (Figure 4.7a), the signals around 1720 cm^{-1} and 1140 cm^{-1} can be assigned to the C=O and C-O-C groups in methacrylate polymer chains. However, when the bulkiest monomer, IBMA, was used, the polymer absorption signal is insignificant in PIBMA@**1a**. A reason might be the molecular size of IBMA (9.9 × 8.2 Å) which is much larger than the pore size of MOF hosts (7.5 × 7.5 Å). Thus, no polymerization of IBMA is proceeding in the

MOF. Generally, the functionalized MOF, **2a**, exhibits more complicated IR absorption than the native **1a** due to the incorporation of Brbdc, but the signals from incorporated polymers (i.e. PMMA, PEMA and PBzMA) can be identified (Figure 4.7b).
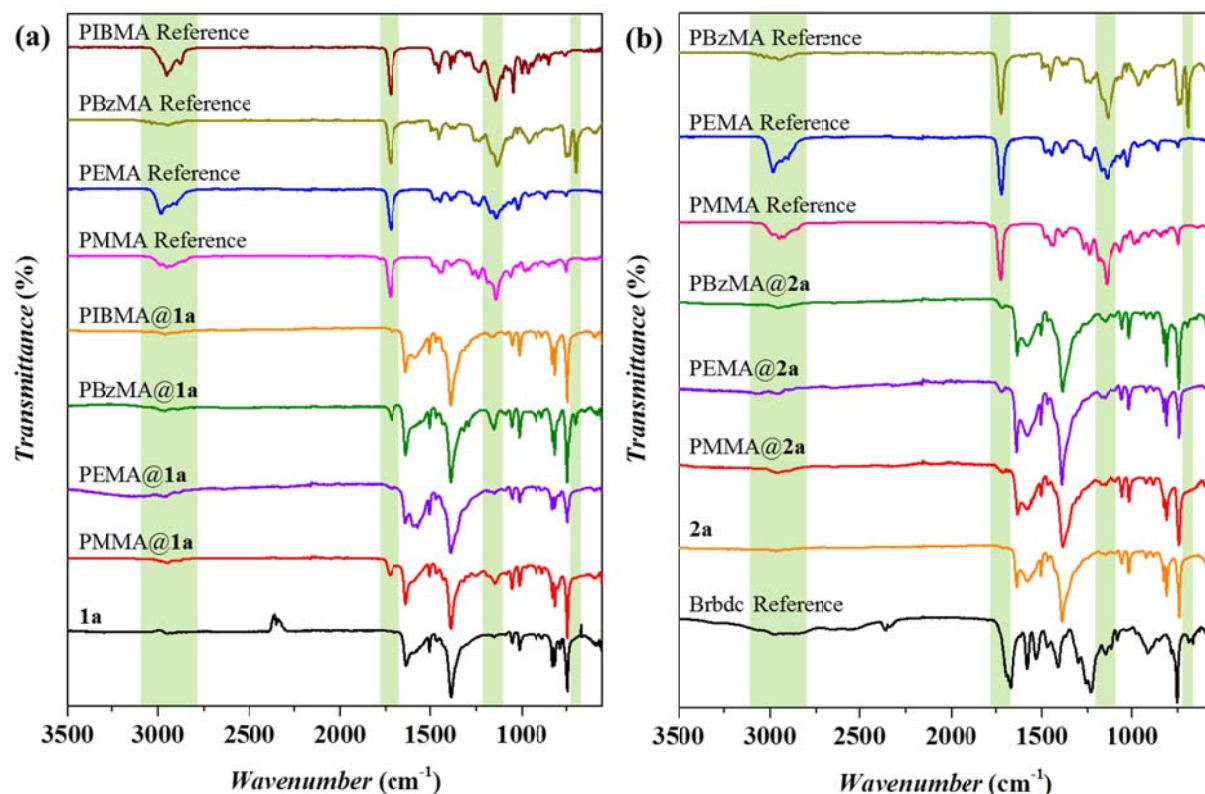
Figure 4.7 ATR-FTIR spectra: (a) **1a** and (b) **1b** before and after polymerization of different monomers.

The preservation of MOF structures throughout the polymerization procedures was confirmed via PXRD (Figure 4.8). Consistent profiles were obtained with only slight variation of relative peak intensity and minor shift after polymerization, which can be attributed to the host-guest effect in nanochannels, as another evidence for polymer incorporation. The most significant deviation was identified in the case of PMMA@**1a** that can be ascribed to the smaller molecular size of MMA; while the MOF nanochannel is increasingly filled, electron density contrast and relative diffraction intensity will be altered more obviously compared to bulkier monomers.

The incorporation of polymer in porous structures can be further confirmed through N_2 gas physisorption analysis (Figure 4.6 a-c). Due to the polymer chain incorporation, the BET surface area *vs.* pore volume in **1a** decreased from 2200 m^2/g *vs.* 0.73 cc/g to 550 m^2/g *vs.* 0.23 cc/g in PMMA@**1a**, 550 m^2/g *vs.* 0.23 cc/g in PEMA@**1a**, 1040 m^2/g *vs.* 0.45 cc/g in BzMA@**1a** and 1970 m^2/g *vs.* 0.71 cc/g in PIBMA@**1a**. The most significant pore filling phenomenon is found in case of the smallest monomer, MMA, and conversely, the infiltration of bulky IBMA is insignificant, which points to the size-selective feature of MOFs. All results from ATR-FTIR and BET as well as PXRD refer to the same expectation. Similar trends were observed in initiator functionalized MOFs as well (Figure 4.6 b

and c). For example, the BET surface area *vs.* pore volume of as-synthesized **2a** declined from 2000 m^2/g *vs.* 0.76 cc/g, to 930 m^2/g *vs.* 0.37 cc/g after polymerization of MMA (PMMA@**2a**). The pore-filling effect is also observed by using other monomers (Figure 4.6 b and c, Table S1). Worth to mention is the successful polymerization of BzMA with the molecule size (7.8 × 5.3 Å) slightly larger than the MOF nanopores (**1a**:7.5 × 7.5 Å and **2 a-b**: 5.8 × 5.8 Å), which can be ascribed to the flexible framework of Zn MOFs and the tilted alignment of BzMA monomers in the MOF channel. However, these two effects are not sufficient to allow polymerization of bulky IBMA (9.9 × 8.2 Å).
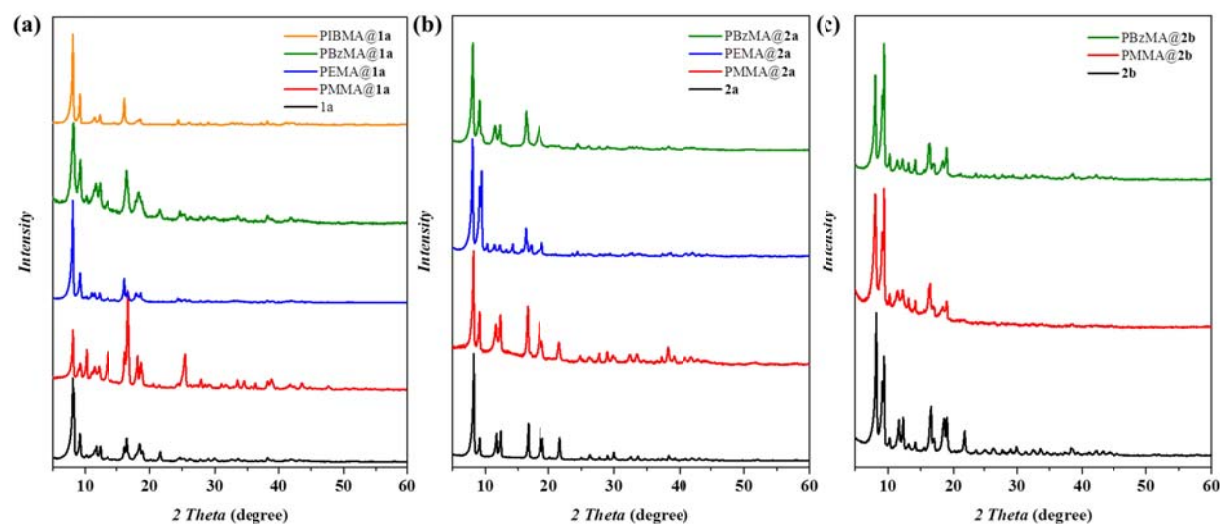
Figure 4.8 Corresponding PXRD profiles of (a) 1a, (b) 2a and (c) 2b before and after polymerization with different monomers.

4.2.3 Characterization of MOF-derived Polymers

After the removal of host MOFs via EDTA-Na$_2$ solution,[37] the obtained polymers were first characterized by SEC (Figure 4.9). As summarized in Table 4.1, polymers in the range of 43,800 to 392,000 with low Đ (1.1-1.4) were obtained, which is in line with reference experiments in the bulk outside of the applied MOFs. As a prominent feature of ATRP, the ability to control molecular weight was probed first by using **1a** with different amounts of initiator (low MW attempt, abbreviated as *L*, and high MW attempt, abbreviated as *H*, with applied initiator concentration *L*:*H* = 2:1), and then by **2a** and **2b** with 0.25% and 0.66% grafted initiator, Brbdc. As shown in the SEC results, although Đ is low, the control over molecular weight is insufficient when using **1a**, forming polymers with similar degree of polymerization (*DP*, n) regardless of the applied initiator concentration, for example, PBzMA with *DP* of 398 *vs.* 414 and Đ = 1.1. Additionally, compared to polymerizations in the bulk much higher *DP* was observed for MOF-derived PMMA (537 *vs.* 200 in bulk), PBzMA (414 *vs.* 82 in bulk) and PEMA (534 *vs.* 189 in bulk). In the case of bulky IBMA little polymer formation inside of the MOF was observed (Figure S4, only limited amount of polymer can be identified from both ^{1}H and ^{13}C NMR), attributed to the monomer size that is too bulky to be incorporated in **1a** and consequently the **2a** and **2b** channels, while bulk polymerization outside of the MOF led to PIBMA as expected.

The over-shooting MW derived from 1a can be attributed to the compartmentalization effect in confined environment where polymerization kinetics is accelerated due to the suppressed deactivation and termination.[18-19, 96, 272] Study has proved that the polymerization in constrained MOF templates is predominately dependent on the initiation stage instead of reaction time, and therefore, long polymer chains are formed when the monomer is encapsulated in the confined MOF nanochannels.[37] Although the lower control of molecular weight due to inevitable compartmentalized effect, controlled polymerization can still be realized, yielding polymers with MW of 43,800-72,900 and low Đ (1.1-1.3).

Table 4.1 Characterization of MOF-derived polymers formed via (SI-)ARGET ATRP [a] and the corresponding block copolymer after chain extension with IBMA. [b]

Polymer	MOF	$M_{n,SEC}$ [c] ($\times 10^3$)	Đ [d]	DP [e]	Tacticity [f] mm:mr:rr	Co-polymer	$M_{n,Theo}$ [g] ($\times 10^3$)	$M_{n,SEC}$ [c] ($\times 10^3$)	Đ [d]
PMMA	Bulk Solution [h]	20.0	1.2	200	2:31:67	PMMA-b-PIBMA	-	-	-
	L-**1a** [i]	43.8	1.3	438	7:53:40		192	221	1.3
	H-**1a** [j]	53.8	1.2	537	8:39:53		104	97.5	1.1
	2a	392	1.4	3915	7:33:60		535	556	1.3
	2b	198	1.3	1978	11:36:53		313	295	1.4
PBzMA	Bulk Solution [h]	14.4	1.3	82	2:32:66	PBzMA-b-PIBMA	-	-	-
	L-**1a** [i]	70.2	1.1	398	7:35:58		362	355	1.4
	H-**1a** [j]	72.9	1.1	414	8:38:54		117	131	1.3
	2a	143	1.2	812	4:38:58		259	261	1.3
	2b	71.5	1.1	406	4:36:60		164	155	1.3
PEMA	Bulk Solution [h]	21.6	1.3	189	1:35:64	PEMA-b-PIBMA	-	-	-
	H-**1a** [j]	61.0	1.3	534	8:36:56		343	350	1.3
	2a	169	1.4	1481	10:36:54		355	368	1.4

[a] Polymerization condition: $[MMA]_0/[EBIB]_0/[CuBr_2]_0/[PMDETA]_0/[dabco]_0 = 100:1:0.15:0.36:0.6$; $[EMA]_0/[EBIB]_0/[CuBr_2]_0/[PMDETA]_0/[dabco]_0 = 88:1:0.15:0.36:0.6$; $[BzMA]_0/[EBIB]_0/[CuBr_2]_0/[PMDETA]_0/[dabco]_0 = 57:1:0.08:0.16:0.036$ (half amount of initiator was applied for the high molecular weight attempt) mixed with MOF (0.8 g) at RT for 24 hr, and polymerization at 50 ºC for 12 hr; [b] Chain extension condition: using the accommodated homopolymers as macroinitiators, $[IBMA]_0/[macroinitiator]_0/[CuBr_2]_0/[PMDETA]_0/[dabco]_0 = 2700:1: 2.5:5:10$, 50 ºC for 24 hr. [c] Determined by SEC in THF based on PMMA calibration. The calculation of theoretical molecular weight is according to the Equation S1. [d] Determined by SEC using PS standard. [e] DP = degree of polymerization, M_n/M_0. [f] Calculated by ^{13}C NMR. [g] Conversion determined by GC-MS. The theoretical number averaged molecular mass $M_{n,theo}$ was calculated as $MM_{initiator} + MM_{monomer} \times ([monomer]_0/[initiator]_0) \times$ conversion. [h] Polymer obtained from the bulk solution of Znbdc High. [i] The low molecular weight attempt. [j] The high molecular weight attempt.

Initiator functionalized MOFs were introduced to improve the polymerization control. Essentially, the polymerizations were carried out by the same process but with initiator-embedded **2a** (0.25% Brbdc incorporated) and **2b** (0.66% Brbdc incorporated) without initiator addition, and consequently no polymer product was found in the bulk because of the grafted initiator in the MOF nanochannel. Eventually, SEC showed significant improvement in polymer properties with low *Đ* and designable molecular weight (Table 4.1, Figure 4.9). In sharp contrast to polymerization in **1a**, a strong correlation between the amount of grafted initiator and MW is observed. As the amount of embedded Brbdc decreases by half, the MW of polymers increases by two as expected for a RDRP process. For instance, high MW PMMA can be prepared from **2a** (392,000) and **2b** (198,000), and the similar controlled results were obtained from BzMA and EMA.

Table 4.2 Calculated initiation efficiency of monomers in Znbdc and ZnBrbdc MOFs.

Polymer	MOF	Monomer Loading [a] (%)	Yield [b] (%)	$M_{n,Theo}$ [c] ($\times 10^3$)	Initiation Efficiency [d] (*f*, %)
PMMA	*L*-**1a** [e]	62.2	11.9	5.0	11.5
	H-**1a** [f]	64.3	11.5	10.0	18.8
	2a	58.8	14.1	263.0	67.1
	2b	59.2	15.5	95.0	48.2
PBzMA	*L*-**1a** [e]	23.5	11.6	5.0	7.2
	H-**1a** [f]	24.1	11.6	10.0	13.8
	2a	14.3	14.8	63.7	44.6
	2b	12.7	19.1	20.5	28.6
PEMA	*H*-**1a** [f]	46.5	12.5	10.0	16.5
	2a	34.1	15.7	152.0	90.1

[a] Determined by gravimetry via comparison of the empty MOF hosts (0.8 g) and the forming polymer@MOF complex after polymerization and intensive wash:

$$\text{Monomer Loading (\%)} = \frac{W_{m,inco}}{W_{m,ini}} \times 100\% = \frac{(W_{polyMOF} - W_{MOF})}{W_{m,ini}}$$

where $W_{m,ini}$ is the weight of applied monomer, $W_{m,inco}$ is the weight of incorporated monomer in the MOF host, W_{MOF} is the weight of empty MOF host and $W_{polyMOF}$ is the weight of polymer@MOF composite after washing.

[b] Obtained via gravimetric comparison of MOF-derived polymers and absorbed monomer amount:

$$\text{Yield (\%)} = \frac{W_{polymer}}{W_{m,inco}} \times 100\% = \frac{W_{polymer}}{(W_{polyMOF} - W_{MOF})}$$

where $W_{polymer}$ is the weight of accommodated polymer obtained after removing MOF frameworks by Na$_2$EDTA solution. The low yield is suggested to the loss of polymers during the EDTA treatment to decompose MOF hosts and the intensive wash of polymers to get rid of the EDTA salt.

[c] According to ICP results, the initiator ratio incorporated in **2a** and **2b** is 0.24% and 0.67% separately. The theoretical molecular weight was calculated with the assumption of 100% conversion. [d] The initiation efficiency was determined by $M_{n,Theo}/M_{n,SEC}$. [e] The low molecular weight attempt. [f] The high molecular weight attempt.

The absorbed amount of monomers in **1a** and functionalized **2a-b** and polymer yield can be utilized to calculate the initiation efficiency (*f*) under the assumption of homogeneous distribution and quantitative conversion (Table 4.2). The ratio between incorporated monomer and monomer outside of the MOF decreases with the increment of monomer size. Namely, **1a** can absorb more MMA (64%) than EMA (47%) and BzMA (24%). Furthermore, **1a** with larger pore size can accommodate more BzMA (24%) than **2b** with smaller pores (13%), revealing the trend of molecular size selection. In accordance with the SEC results, a significant improvement in calculated initiation efficiency of initiator-functionalized MOFs, **2a** and **2b**, compared to **1a** confirms the refined ability to modulate molecular weight especially in an attempt to higher target molecular weights. Owing to the grafted initiators which are well-distributed and installed directly inside the confined channel, less gradient effect resulting from different molecules in the feeding mixture is the case. The improved initiation efficiency and designable molecular chain lengths advocate the unique advantage of functionalized MOFs. Especially for SI-ARGET ATRP, where the initiators are already anchored to a planar surface, deactivation and termination processes are retarded, which allows the fabrication of well-defined polymers with much higher molecular weight than those prepared in native **1a**. Additionally, the molecular weight of MOF-derived polymers decreases with increased monomer size, because of the restricted mobility and fewer loading for larger monomers. However, MOF-derived polymers with high molecular weight can still be prepared in **2a** for MMA, EMA and BzMA. As a result, the MOFs can serve as nanoreactors for confined polymerization up to high molecular weight polymers (MW = 143,000-392,000) in a well-controlled fashion ($Đ$ = 1.2-1.4). The low yield is suggested to the loss of polymers during the EDTA treatment to decompose MOF hosts and the intensive wash of polymers to get rid of the EDTA salt.

The in-situ polymerization inside the MOF crystals is based on the adducted reagents containing monomers, initiators and catalyst/ligand complexes. A successful polymerization requires all of the above mentioned molecules be introduced into the given confined space. However, it is absolutely not guaranteed that the local concentrations inside MOF nanochannels for each species match the one of the bulk. Furthermore, in such confined space the capillary could be the main driving force for the introduction of reagents into the MOF nanochannels,[273-274] but the defects in the MOF crystals will hinder the distribution/adduction of reagents[275-276] and then halt the polymerization process as well. Therefore, although the crystal size of MOF hosts is around 5-20 μm, the polymer chain length can't reach such dimension owing to the less homogeneous distribution of polymerization ingredients and the innate crystal defects.

4.2.4 Microstructure of MOF-derived Polymers

The effect of space confinement on polymer stereostructure was studied via polymerization of three methacrylate monomers, MMA, EMA and BzMA in two confined environments (i.e. conventional ARGET ATRP in **1a** and SI-ARGET ATRP in **2a-b**). In such a way, the control over

tacticity can be correlated with the confinement effect induced by guest molecules (i.e. molecular size) and/or host frameworks (i.e. channel size). To avoid the misinterpretation resulting from remaining EDTA salt and impurity in polymers, the corresponding change in tacticity was calculated by ^{13}C NMR rather than the conventional ^{1}H NMR (Table 4.1, Figure 4.8; refer to Figure S5 for ^{1}H NMR spectra).[24, 277-280]
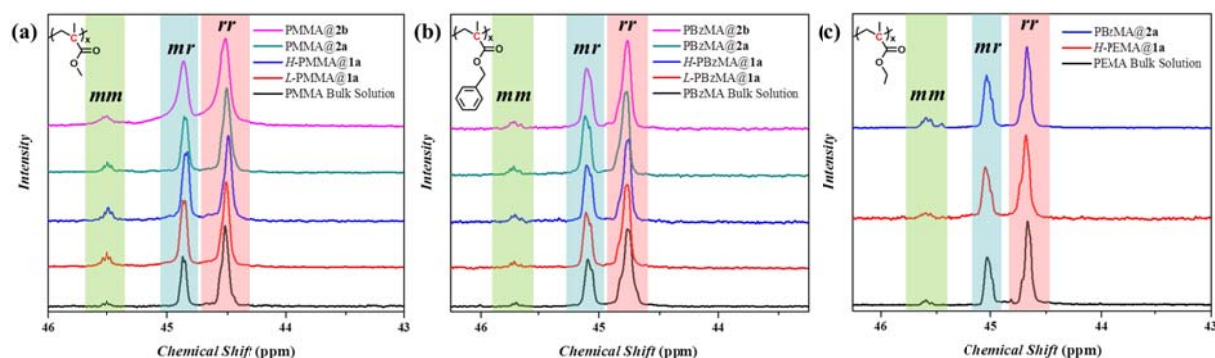
Figure 4.8 Comparison of ^{13}C NMR of (a) PMMA, (b) PBzMA and (c) PEMA obtained from ARGET ATRP in **1a** and SI-ARGET ATRP in **2a**/**2b** with a reference from bulk.

ARGET ATRP of MMA in **1a** led to an increase in the isotactic triad (mm) fraction of PMMA from 2% in bulk to 8% in confinement. When the polymerization was conducted in **2b**, the isotactic triad of PMMA was further increased to 11%. As revealed by previous studies, the stereoregularity of PMMA is highly dependent on the bulkiness of ligands in the MOF, i.e., large substituents narrow the pore dimension and induce formation of sterically less-demanding isotactic microstructure.[155] Therefore, the enriched isotactic triad in PMMA obtained from **2b** is mostly ascribed to the embedded bulky Brbdc directly insides the confined nanochannels.

A similar increase in mm fraction of PBzMA from 2% (in bulk solution) to 8% (in **1a**) was observed. However, unlike PMMA, only limited improvement in mm fraction (4%) was observed in PBzMA from **2a-b**, which can be ascribed to the expanded BzMA size with rigid benzyl group and the narrower channel size of **2a-b** than **1a**, hindering the steric reorganization of monomers. The phenomenon is in line with the decreased *DP* of PBzMA (812/406) compared to PMMA (3915/1978) (Table 4.1), meaning that BzMA is constrained and polymerized restrictedly in **2a-b**.

To further understand the effect of monomer molecular size on polymer microstructure in confined polymerization, EMA a monomer with molecular size between MMA and BzMA was studied. Because of proper molecular size, the regioregularity of the obtained PEMA is significantly enhanced compared to PMMA and PBzMA (Table 4.1 and Figure 4.8c). The regulation is already apparent even in the native **1a**, leading an increase in isotactic triad from 1% in bulk polymerization to 8%. Ultimately, with the combination of functionalized host, **2a**, 10% isotactic triad can be achieved, which is comparatively well-defined in terms of radical polymerization without specific catalysts/additives. In summary, by taking advantage of molecular size and confined nanochannels in

functionalized MOFs, enhanced control of polymer tacticity can be readily achieved.

4.2.5 Living Polymerization Properties

The chain-end functionality of MOF-derived polymers was assessed via chain extension with IBMA in a subsequent ARGET ATRP block copolymer formation (Figure 4.9a). The SEC eluograms of the formed block copolymers (Figure 4.9b-f) show a shift to lower retention times, which corresponds to increased chain length and hydrodynamic volume. The living property of **1a**-derived polymers can be demonstrated by the increase of molecular weight, e.g. from 43,800 (PMMA) to 221,000 (PMMA-*b*-PIBMA), 70,200 (PBzMA) to 355,000 (PBzMA-*b*-PIBMA), and 61,000 (PEMA) to 350,000 (PEMA-*b*-PIBMA). Regardless of the higher MW, polymers derived from **2a-b** also show high end group fidelity. After chain extension, the molecular weight of **2a-b**-derived polymers increased as well, e.g. from 392,000 (PMMA) to 556,000 (PMMA-*b*-PIBMA), 143,000 (PBzMA) to 261,000 (PBzMA-*b*-PIBMA), and 169,000 (PEMA) to 368,000 (PEMA-*b*-PIBMA), while maintaining low *Đ* (1.1-1.4) (as shown in Figure 4.9; Table 4.1).
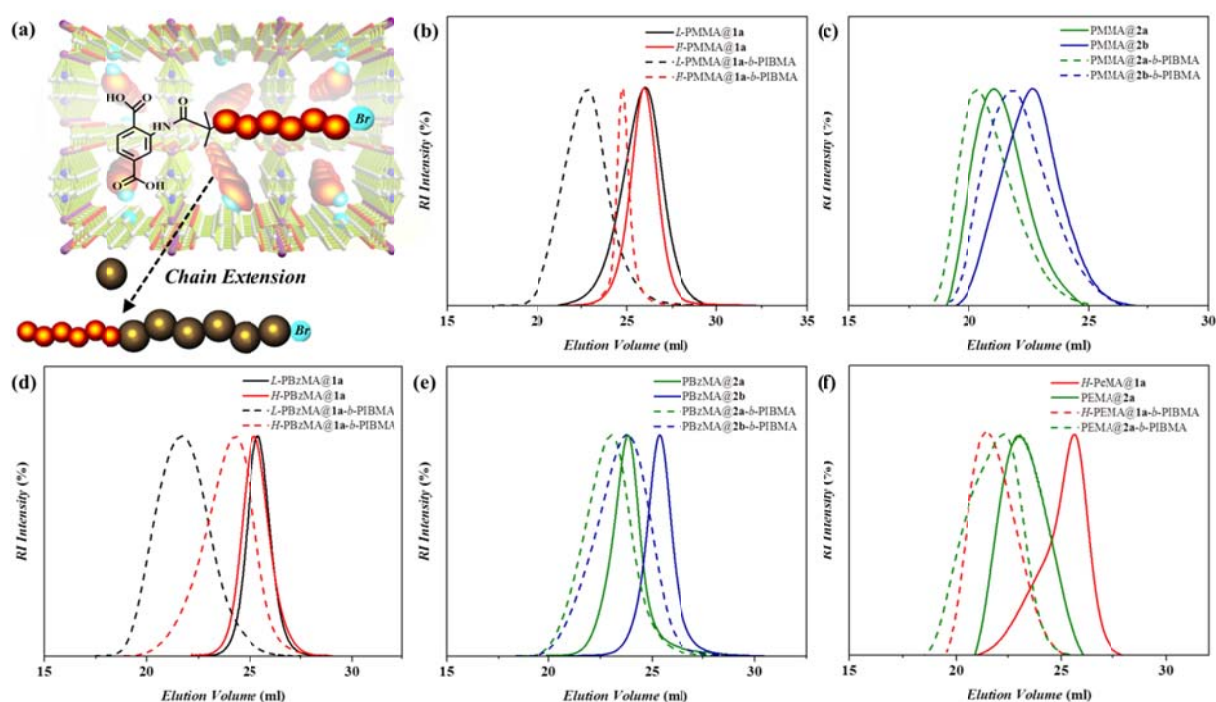
Figure 4.9 (a) Chain extension of MOF-derived polymers with IBMA. SEC chromatograms of polymer obtained from **1a** and **2a/b**: (b) PMMA obtained from **1a**, (c) PMMA obtained from **2a/2b**, (d) PBzMA obtained from **1a**, (e) PBzMA obtained from **2a/2b** and (f) PEMA obtained from **1a/2a** before and after chain extension with IBMA.

Clean chain extensions are used to be challenging for high molar mass polymers prepared by RDRP due to radical termination. However, adapting this strategy, although polymers with the relatively high molecular weight were formed in these MOF-derived systems, the living chain ends were preserved in both **1a** and functionalized **2a-b** systems. The successful block copolymerization

confirmed the preservation of halogen end groups, and the formed block copolymers using these macroinitiators were characterized by ^{1}H NMR, indicating the composition of two polymer blocks (Figure 4.10).
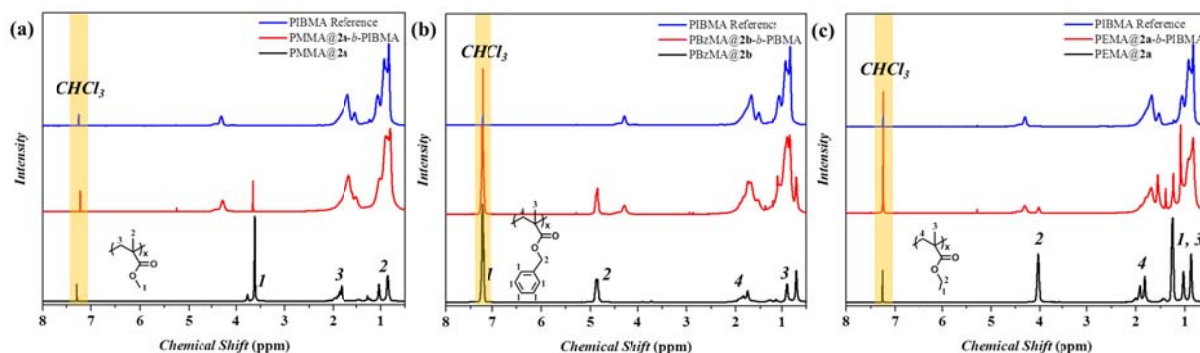
Figure 4.10 The corresponding ^{1}H NMR of accommodated polymers in chloroform-*d*: (a) PMMA, (b) PBzMA and (c) PEMA homopolymer and block copolymer after chain extension with IBMA

4.3 Conclusion

In summary, the controlled radical polymerization inside of MOFs was achieved through the combination of Znbdc/ZnBrbdc and ARGET/SI-ARGET, which relies on the confinement effect resulting from MOF pore structure and monomer size. In Znbdc well-defined polymers were obtained, although the control of molecular weight was limited (molecular weight ranged from 53,800 to 72,900 and *Đ* = 1.1-1.3). Compared to the polymer from bulk, the content of isotactic triad was improved from 2% to 8% in PMMA and PBzMA, and 1% to 8% in PEMA. Initiator functionalized MOFs advance control over polymerization, which enabled the synthesis of polymers with higher MW, low *Đ* and pre-determinable MW (PMMA with 392,000, PEMA with 169,000 and PBzMA with 143,000, *Đ* = 1.2-1.4). Additionally, enhanced microstructure could be achieved as well with an increase in isotactic triad to 11% in PMMA and 10% in PEMA. Moreover, chain extensions with IBMA were successfully performed, confirming preservation of end-group functionality. The results demonstrate that the combination of MOFs and controlled polymerization is a facile, robust and universal methodology to prepare high molecular weight polymers with low *Đ*, predetermined MW, high end-group fidelity and well-defined stereostructure.

5. Cu(II) MOF as recyclable catalyst for ARGET ATRP

5.1 Introduction

In addition to being used as templates for controlled polymerization of various monomers, MOFs comprised by metal ions and linking ligands are imparted with robust structures, and together with the intrinsic hybrid nature which is highly compatible to either organic or inorganic materials, tunable pore features, diversified components, ultrahigh specific surface area and easy separation, all point to application in heterogeneous catalysis.

As mentioned above, within various RDRP technologies, ATRP is one of the most significant synthetic techniques owing to its applicability and the capability to synthesize well-defined polymers with predetermined molecular weight, designed microstructure and tailored-made functionalities.[1-4] Based on the principle of ATRP, ARGET ATRP with the advantages of high oxygen tolerance and low metal catalyst requirement was developed to further advance the synthetic field.[5-8] However, the necessity for catalysts and associated ligands, inevitable interaction resulting from monomer, catalyst (i.e. 4-vinylpyridine (4VP) and CuBr)[9,10] and ligand (i.e. isoprene and PMDETA),[11-13] and the hardly removed, non-reusable catalyst limit the ubiquity of this methodology.[14-19] Although plenty of strategies have been launched and attempted to refine the current struggles, such as photocatalytic,[20] electrochemical-mediated polymerization[21] or functionalization with supporting materials,[22-24] heterogeneous catalysts feature more convenient handling for applications.
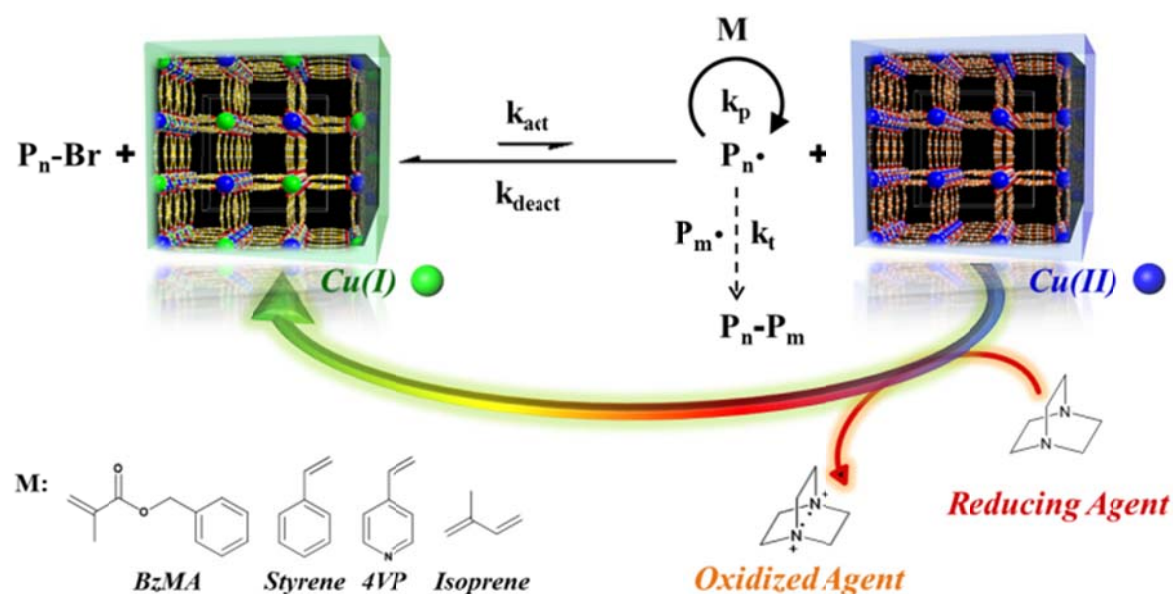
Scheme 5.1 Schematic illustration for the proposed mechanism of Cu(II) MOF-mediated ARGET ATRP for various monomers.
Parts of this chapter were reproduced from Lee, H.-C.; Antonietti, M.; Schmidt, B. V. K. J., *Polym. Chem.* **2016,** *7* (47), 7199-7203, with permission from Royal Society of Chemistry (2016)

In the present thesis, a novel approach towards ARGET polymerizations is presented. The utilization of Cu(II)-based MOF, namely Cu$_2$(bdc)$_2$(dabco) (bdc: terephthalic acid; dabco: 1,4-diazabicyclo[2.2.2]octane), as a heterogeneous polymerization catalyst is probed making use of the robust physical framework formed by ionic bonds. Scheme 5.1 illustrates the general concept of Cu(II) MOF-mediated ARGET ATRP universal to various monomers, such as benzyl methacrylate (BzMA), styrene, 4VP and isoprene. Compared to the conventional copper ion coordinated with halide anion, the copper MOF can act as a catalyst and a ligand complex at the same time. Thus, a sometimes tedious synthetic procedure is significantly simplified, and side reactions within the mixture of monomer, metallic catalyst and corresponding ligand are limited. Moreover, considering the particle size of a few hundred nanometers, the MOF catalyst can be easily collected by centrifugation and reused for other polymerizations. Since amine molecules possess the ability to reduce copper complexes from high-valent to low valent state as reducing agents in ARGET ATRP,[36,37] additional dabco was added to trigger the reduction of Cu(II) to active Cu(I).

5.2 Results and Discussion

5.2.1 Fabrication of Cu$_2$(bdc)$_2$(dabco)

The Cu(II) MOF were prepared under solvothermal condition.[38,39] After removing the included guest molecules, the as synthesized MOF was characterized with FE-SEM PXRD, and porosimetry. The crystal structure with uniform particle size around hundred nm was first observed in the FE-SEM image (Figure 5.1). The obtained PXRD pattern showed good accordance with literature, indicating accurate microstructure and pure phase (Figure 5.2a). The specific surface area *vs.* pore volume was determined by BET method with 2280 m^2/g *vs.* 0.91 cc/g, respectively (Figure 5.2b). The property of the ultrahigh specific surface area reveals the advantage of the given Cu(II) MOF as a catalyst for polymerization.
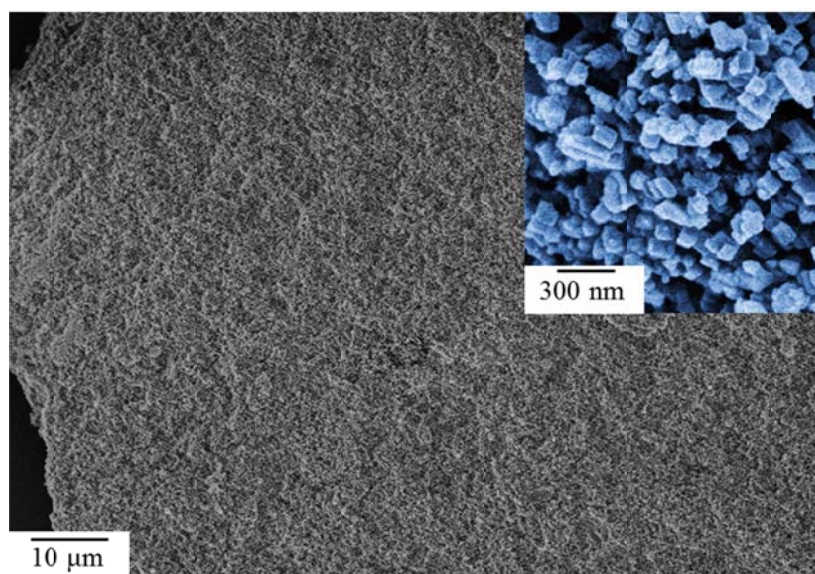
Figure 5.1 FE-SEM micrograph of the as fabricated Cu$_2$(bdc)$_2$(dabco).
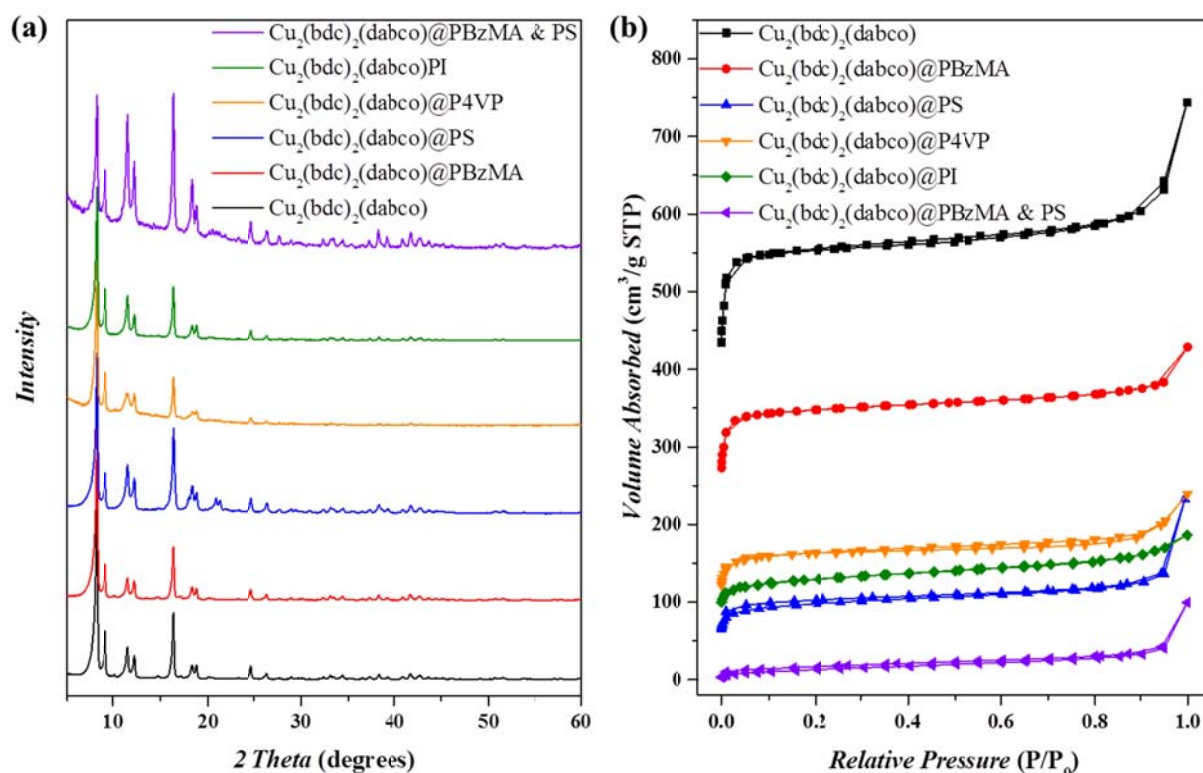
Figure 5.2 Corresponding (a) PXRD profiles and (b) N_2 adsorption-desorption isotherm of $Cu_2(bdc)_2(dabco)$ before and after polymerization of various monomers.

5.2.2. Kinetic Study of Polymerization Via $Cu_2(bdc)_2(dabco)$

After the MOF can be fabricated successfully, ARGET ATRP of various monomers was performed with Cu(II) MOF compared to conventional copper-halogen coordinated catalysts. At the beginning, polymerizations of common monomers, BzMA and styrene, were conducted. The time-dependent progressions of monomer conversions (Figure 5.3 a and b) reveal the constant concentration of the active propagating species in both PBzMA and PS systems, and 50% monomer conversion can be achieved within 10 hours under operational temperatures of 50 °C and 110 °C, respectively. As reference, PBzMA and PS were also synthesized through traditional ARGET ATRP with the utilization of CuBr/PMDETA. The kinetic behavior (Figure 5.3 a-d), time-dependent M_n evolution, and SEC distribution showed great resemblance between these two pathways in both polymer systems, (Figure S6) indicating the Cu(II) MOF as a comparable, yet heterogeneous catalyst for ARGET ATRP. Figure 5.4 a and b showed the dependency of molecular weight on conversion of BzMA and styrene mediated by Cu(II) MOF. The behaviour indicated the gradual growth of polymer chains and the feature of pre-determinable degree of polymerization which both are prerequisites to be regarded as a RDRP process. The well-controlled PBzMA and PS can be obtained by using Cu(II) MOF as an alternative, giving PBzMA with MW of 15500 ($Đ$ = 1.4) and PS with MW of 16800 ($Đ$ = 1.3) (Table 5.1).
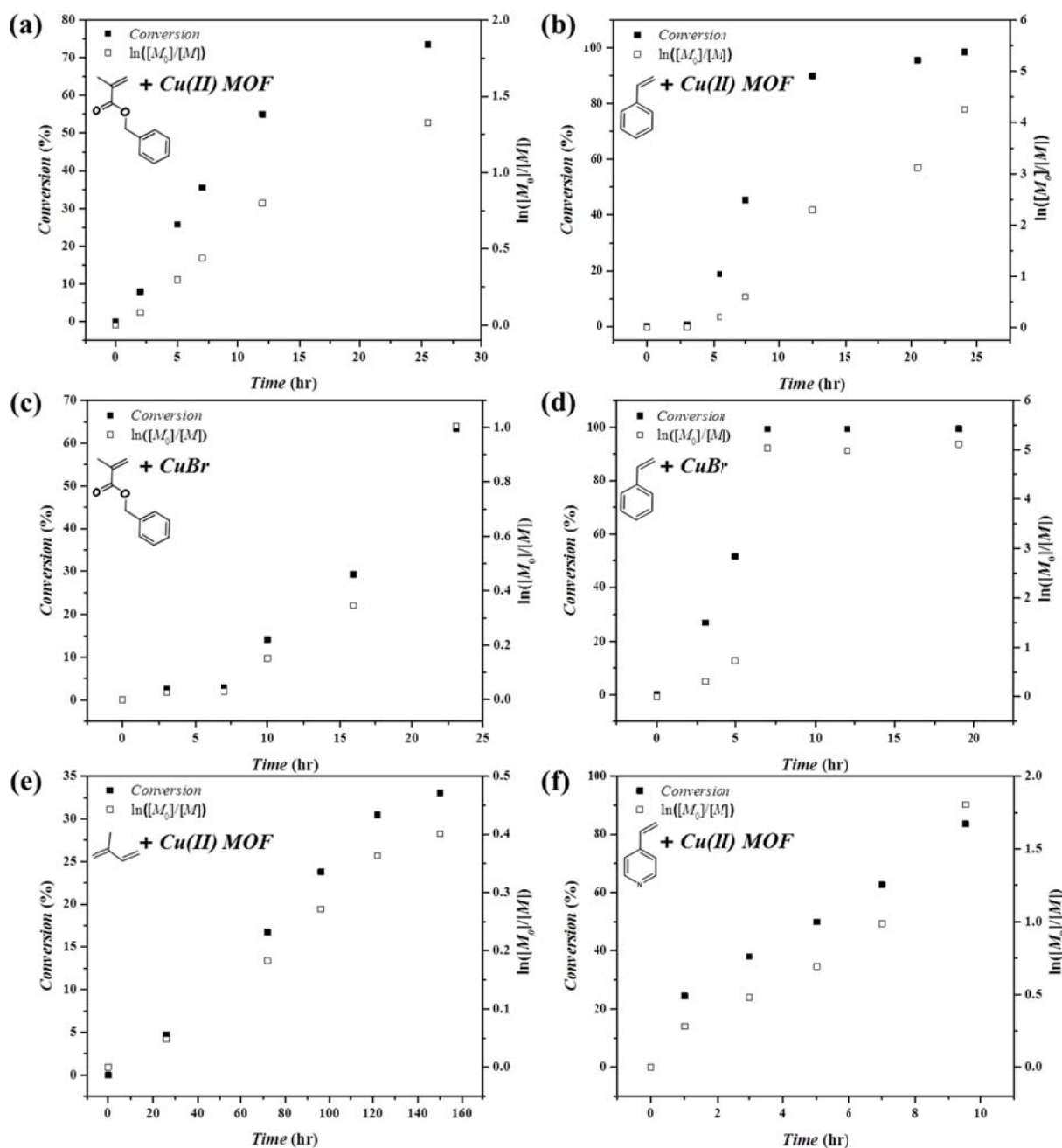
Figure 5.3 Kinetic evolution of monomer conversion with the utilization of Cu$_2$(bdc)$_2$(dabco): (a) PBzMA and (b) PS, compared to the polymerization conducted by conventional CuBr: (c) PBzMA and (d) PS. Polymerization of (e) isoprene and (f) 4VP with the utilization of Cu$_2$(bdc)$_2$(dabco).

In addition, ARGET polymerization of isoprene and 4VP catalysed via Cu(II) MOF was investigated. These monomers have proven to be rather challenging to polymerize via ATRP without the utilization of specified methods, such as enhanced ligands.[9,10] The polymerization kinetics for PI and P4VP exhibit distinct semilogarithmic plots (Figure 5.3 c and d), and a nearly linear increment of molecular weights in accordance with conversion (Figure 5.4 c and d) can be observed in both cases. The as-obtained PI and P4VP featured with MW of 23000 ($Đ$ = 1.4) and MW of 9200 ($Đ$ = 1.5),

respectively (Table 5.1; Figure 5.6 c and d). Note, owing to the low solubility, the PI and P4VP homopolymers were analyzed in NMP with PS as standard. It is speculated that the slightly lower molecular weight of the as synthesized polymers compared to the theoretical value is attributed to the leakage of the isoprene monomer at high temperature (120 °C), and the association of 4VP monomer on the surface of Cu(II) MOF. The superior polymerization results compared to non-MOF systems are probably due to the vexed coordination between monomers and free catalysts and/or ligand. Cu(II) MOF stabilized by the ionic bonding between Cu(II) ion and ligands in the framework is obviously able to effectively avoid side reactions, which at the end results in polymerizations with higher efficiency.
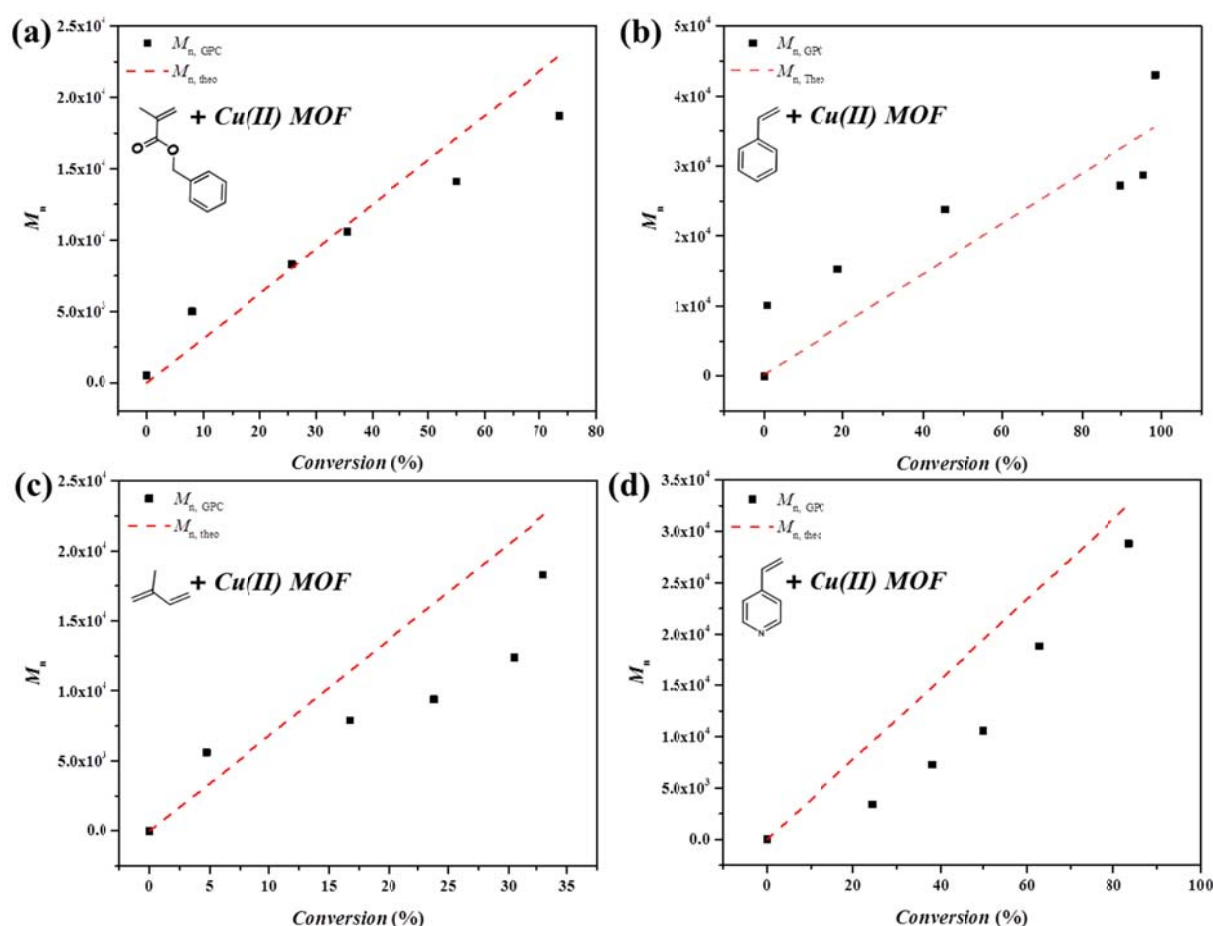
Figure 5.4 The evolution of M_n with conversion for (a) BzMA, (b) styrene (c) isoprene and (d) 4VP polymerization catalysed by the Cu(II) MOF.

PXRD (Figure 5.2a) was utilized to study the integrity of the MOF structure in each polymerization, revealing the preservation of the MOF structure, and the changes in relative peak intensities were attributed to the introduction of the guest molecules occupying the host nanochannels.[35] Therefore, it can be concluded that the MOF-based catalyst $Cu_2(bdc)_2(dabco)$ was stable under ARGET ATRP conditions. The decreased specific surface area of catalytic MOFs after

polymerization (Figure 5.2b) was attributed to the incorporation of the monomer in the porous texture, and the decrease in volume corresponded to the size of the applied monomers. The monomer incorporation effect was again confirmed via measurement of weight increase after recycling the catalyst (Figure 5.9b), which has to be considered when switching monomers between different runs of polymerization.

Table 5.1 Polymerization of monomers via $Cu_2(bdc)_2(dabco)$[a] and corresponding block copolymers resulting from chain extension with IBMA.[b]

Homo polym.	$M_{n,theo}$[c] ($\times 10^3$)	$M_{n,SEC}$[d] ($\times 10^3$)	$Đ$[e]	Copolym.	$M_{n,theo}$[c] ($\times 10^3$)	$M_{n,SEC}$[d] ($\times 10^3$)	$Đ$[e]
PBzMA	17.2	15.5	1.4	PBzMA-*b*-PIBMA	30.6	28.6	1.2
PS	11.2	16.8	1.3	PS-*b*-PIBMA	21.1	20.2	1.5
PI	21.8	23.0	1.4	PI-*b*-PIBMA	135.8	104.9	1.6
P4VP	11.6	9.2	1.5	P4VP-*b*-PIBMA	28.9	16.0	1.2

[a] Polymerization condition: $[BzMA]_0/[I]_0/[dabco]_0 = 180:1:2$, 50 °C for 12 hr; $[St]_0/[I]_0/[dabco]_0 = 110:1:5$, 110 °C for 6 hr; $[Isoprene]_0/[I]_0/[dabco]_0 = 805:1:5$, 120 °C for 36 hr; $[4VP]_0/[I]_0/[dabco]_0 = 370:1:5$, 60 °C for 5 hr. Polymerizations were performed with 5.7 wt.% Cu(II) MOF. [b] Chain extension condition: $[PBzMA\text{-}Br/PS\text{-}Br]_0/[IBMA]_0/[CuBr_2]_0/[Ligand]_0/[dabco]_0 = 1:400:0.4:1:2.4$, 50 °C for 24 hr; $[PI\text{-}Br]_0/[IBMA]_0/[CuBr_2]_0/[Ligand]_0/[dabco]_0 = 1:1100:1.1:2.75:6.6$, in 50 vol % dioxane at 50 °C for 24 hr; $[P4VP\text{-}Br]_0/[IBMA]_0/[CuBr_2]_0/[Ligand]_0/[dabco]_0 = 1:450:0.45:1.13:2.7$, in 50 vol.% dioxane at 50 °C for 24 hr. [c] Conversion determined by GC-MS. The theoretical number averaged molecular mass $M_{n,theo}$ was calculated as $MM_{initiator} + MM_{monomer} \times ([monomer]_0/[initiator]_0) \times$ conversion. [d] Determined by SEC according to equation S1, using PS standard in THF for the as-synthesized PS and PMMA as standard for the as-synthesized PBzMA (in THF), PI (in NMP) and P4VP (in NMP). [e] Determined by SEC using PS standard.

5.2.3 Microstructure of the Cu(II) MOF –Mediated PI and P4VP

PI synthesized by Cu(II) MOF appears to feature high regioselectivity, with an 1,4-addition above 80% (Figure 5.5a).[13] Additionally, referring to P4VP, the Cu(II) MOF catalyzed polymerization not only leaded to controlled molecular weights and end groups, but even an effect on the microstructure of polymer chains was observed, which has been rarely reported so far. As shown in the ^{13}C NMR profiles (Figure 5.5c), the assignment of mm and mr triad from C4 carbon were identified at 152 and 150 ppm,[40] and compared to free radical polymerization, the control over tacticity was improved in the Cu(II) MOF-mediated P4VP, as reflected by the increasing ratio of isotactic diads (mm) from 13 % to 25 %. It was speculated that the increased tacticity was due to the alignment of 4VP monomers along the MOF framework, because the Cu(II) MOF could act as Lewis acid forming strong coordination between comprised Cu ions and nitrogen atoms from 4VP monomer and/or polymer chains.[41] The

characteristic properties of these particular polymers was successfully passed on to the as-fabricated block copolymers as evidenced in the ^{1}H NMR (Figure 5.7c), indicating a promising avenue for the synthesis of more controlled functional materials.
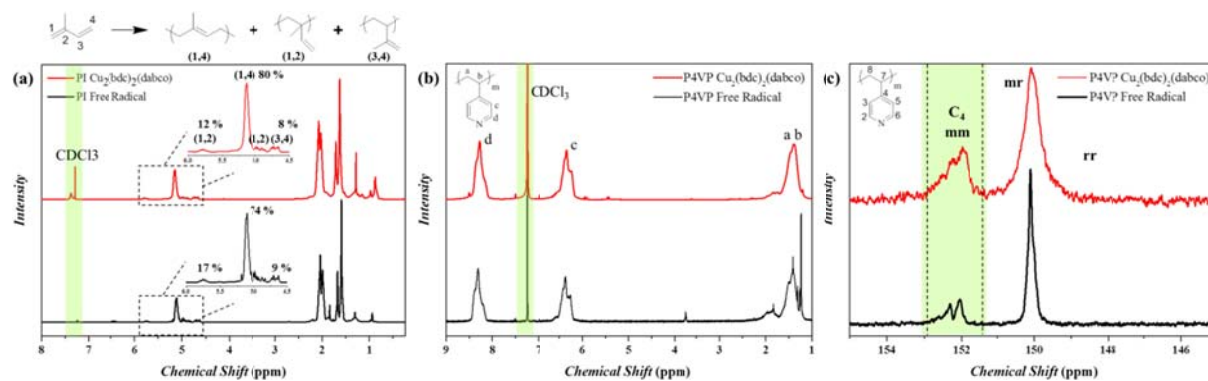
Figure 5.5 (a) The comparison of ^{1}H NMR spectra of PI synthesized by free radical polymerization and Cu(II) MOF-mediated ARGET ATRP which with the calculated ratio of (1,4) addition for 80%, (1,2) for 12% and 8% for (3,4) in chloroform-*d*, with respect to free radical polymerization with the ratio of 74%, 17% and 9%. The comparison of (b) ^{1}H and (c) ^{13}C NMR spectra of P4VP synthesized by free radical polymerization and Cu(II) MOF-mediated ARGET ATRP in chloroform-*d*.
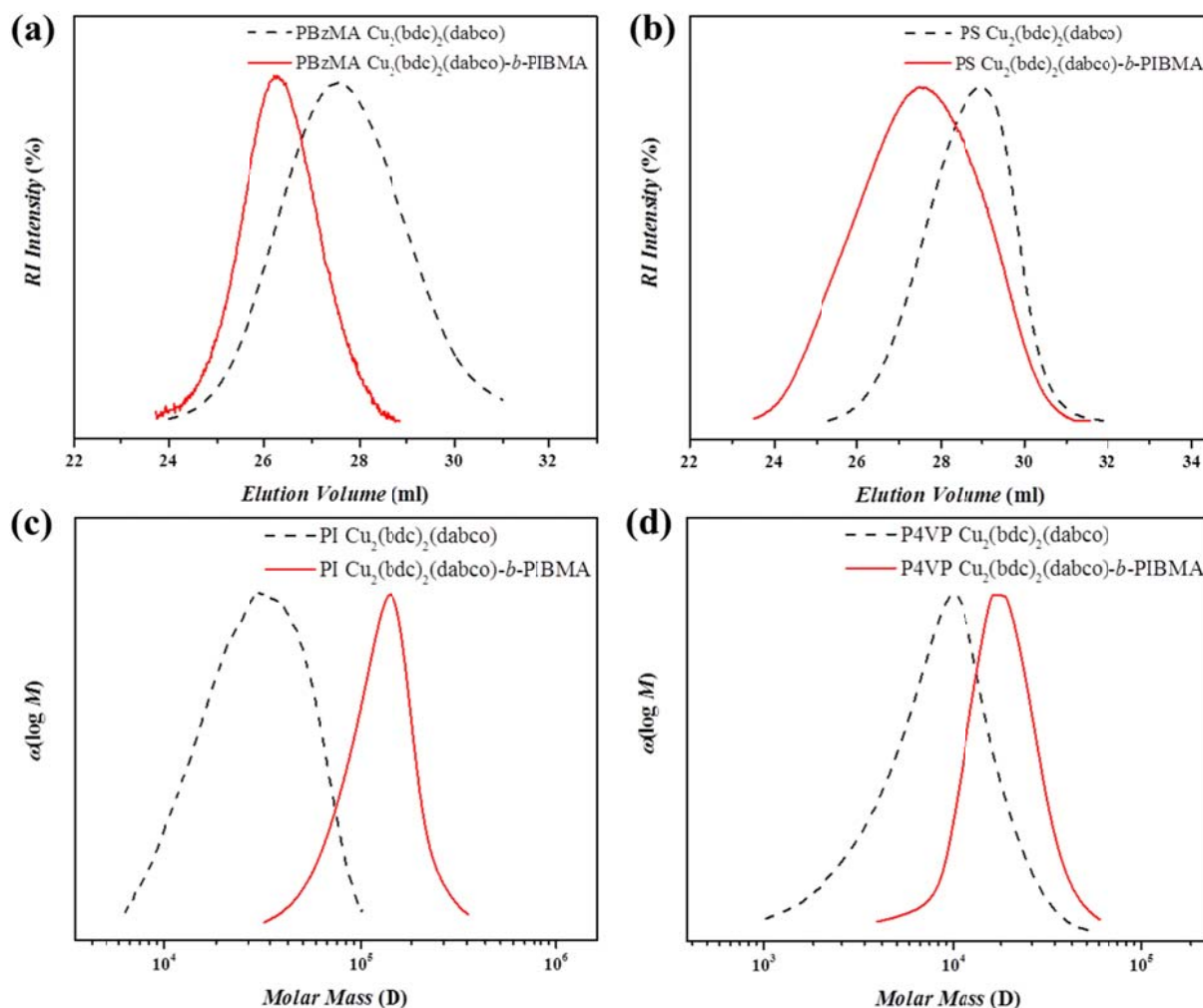
Figure 5.6 SEC chromatograms of the Cu(II) MOF-synthesized (a) PBzMA and (b) PS, and mass distribution of (c) PI and (b) P4VP before (dashed line) and after (solid line) chain extension with IBMA. The molecular weight is calculated according to equation S1, using PS standard in THF for the as-synthesized PS and PMMA as standard for the as-synthesized PBzMA (in THF), PI (in NMP) and P4VP (in NMP).

5.2.4 Living Polymerization Properties

Furthermore, functionality of the polymers synthesized with Cu(II) MOF in terms of initiator end-functionalization was investigated via chain extension with isobornyl methacrylate (IBMA) for the subsequent ARGET ATRP block copolymer formation. The SEC elugrams of the formed block copolymers (Figure 5.6) showed an obvious shift to lower retention times, which corresponds to increased MW from 15,500 (PBzMA) to 28,600 (PBzMA-*b*-PIBMA), from 16,800 (PS) to 20,200 g mol^{-1} (PS-*b*-PIBMA), from 23,000 (PI) to 104,900 (PI-*b*-PIBMA), and from 9,200 (P4VP) to 16,000 (P4VP-*b*-PIBMA). For PS-*b*-PIBMA a broadening of the molecular weight distribution is observed due to unfavourable chain extension with the methacrylate. Thus, chain extensions with styrene were probed that show no significant broadening (Figure S7). Therefore, the preservation of the halogen end

group via the ability to initiate the second polymerization can be stated. In summary, the Cu(II) MOF derived polymers can be regarded as dormant chains and the preparation process can be filed as a RDRP process. The formation of block copolymer with the utilization of these macro initiators can be again evidenced by the ^{1}H NMR spectra, indicating the composition of two polymer segments (Figure 5.7).
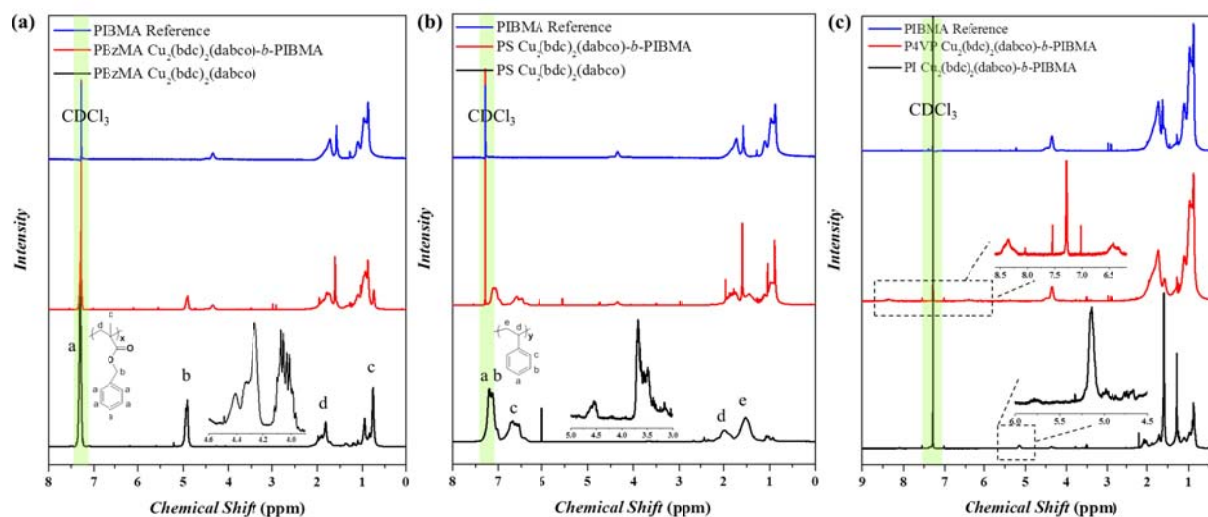
Figure 5.7 The corresponding ^{1}H NMR of Cu(II)-mediated ARGET in chloroform-*d*: (a) PBzMA (17,200 g/mol) and (b) PS (11,200 g/mol) homopolymer and block copolymer after chain extension with IBMA (PBzMA-*b*-PIBMA, 28,600 g/mol; PS-*b*-PIBMA, 20,200 g/mol). The inset indicates the ethyl end group given by the ARGET ATRP initiator (PBzMA: ester end group CH$_2$ 4.0-4.1 ppm) or the proton next to the bromide chain end (PS: CHBr 4.5 ppm, ester end group CH$_2$ 3.5 ppm). (c) PI and P4VP after chain extension with IBMA (PI-*b*-PIBMA, 104,900 g/mol; P4VP-*b*-PIBMA, 16,000 g/mol).

5.2.5 Catalytic Property of the Cu(II) MOF

The oxidation state of the MOF-derived Cu ions was traced by solid-state UV-Vis spectroscopy (Figure 5.8a). Resembling the CuBr$_2$ reference, the as-synthesized Cu(II) MOF exhibited a maximum absorption around 250-350 nm, indicating the higher oxidation state. In contrast, during the polymerization process, an obvious red shift towards 300-550 nm was identified, evidencing the reduction of the Cu(II) framework to Cu(I). After termination of the polymerization, the absorption peak of the Cu MOF retreated to lower wavelengths with a blue shift, matching perfectly with the initial Cu(II) MOF. Thus, a reversible generation of the catalytic Cu(I) species was stated. The transition in oxidation degree was again evidenced by the MOF with varied color. At first, the Cu(II) MOF exhibited the characteristic light blue color because of the comprised Cu(II) ions (Figure 5.8b), but once the ARGET ATRP proceeded, the suspension turns dark green owing to the reduction of Cu(II) into active Cu(I) with its intrinsic green color (Figure 5.8c).
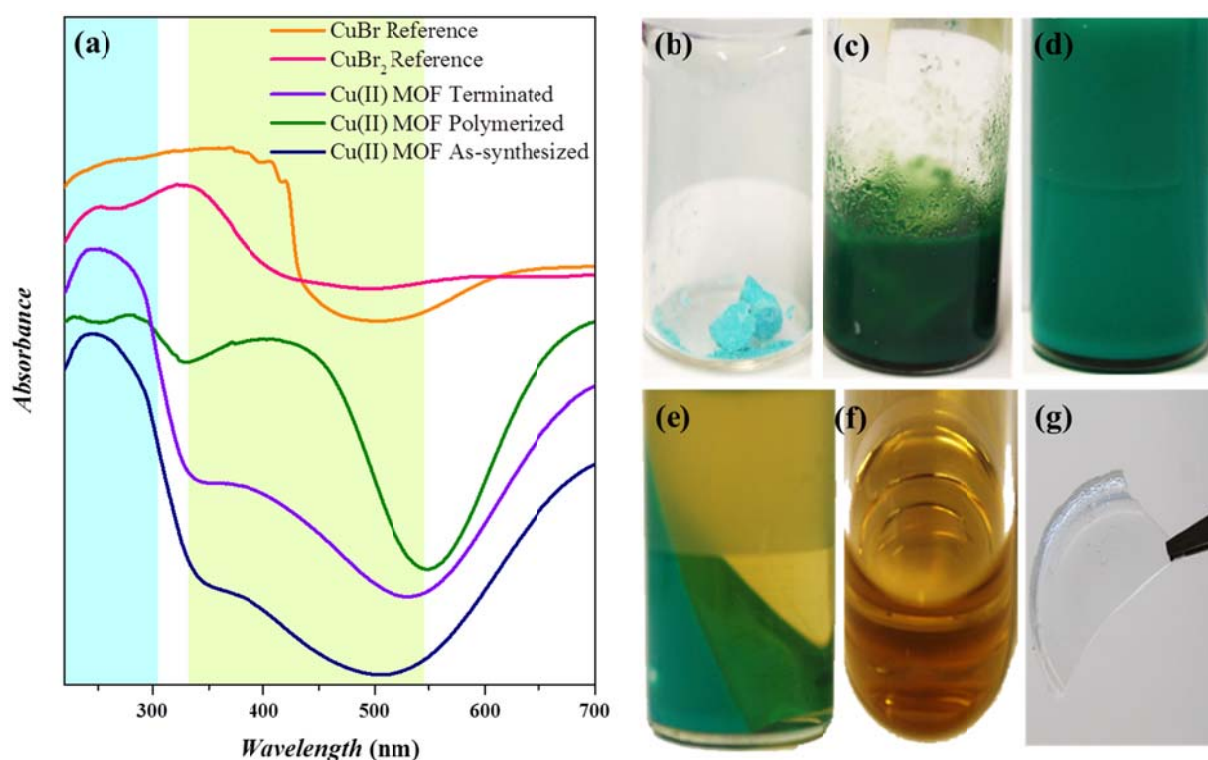
Figure 5.8 (a) Solid-state UV-Vis spectra of Cu catalysts, Cu(II) MOF and CuBr in different oxidation state. Photographs of $Cu_2(bdc)_2(dabco)$-mediated ARGET ATRP at different stages: (b) Cu(II) MOF before polymerization; (c) Cu(II) MOF during polymerization; (d) termination with solvent; (e) removal of catalytic complex via centrifugation; (f) polymer solution and (g) polymer bulk after precipitation.

5.2.6 Reusability of $Cu_2(bdc)_2(dabco)$ in Cascade ARGET

Due to the particle size around hundred nm (FE-SEM, Figure 5.1), Cu(II) MOF could be re-sorted by centrifugation and served as a heterogeneous catalyst for the next reactions (Figure 5.8 b-g). After removing the catalyst, the as-synthesized polymers was easily achieved from the suspension (Figure 5.8g). Furthermore, owing to the active-and-deactive property, the MOF-based catalyst was recycled at least six times conducting the polymerization of PBzMA and PS alternatively. As elaborated in Figure 5.9a, the monomer to polymer conversions and product yields remained stable during the whole six runs, which indicated promising applicability of utilizing this complex for various polymerizations. The discrepancy between conversion of styrene and yield of PS in the second cycle was ascribed to the styrene monomer incorporation in the porous structure of Cu(II) MOF. The smaller molecular size of styrene with respect to BzMA leaded to the mismatch of yield and conversion in the second cycle. However, yield and conversions are steady after the second cycle. The weight increment of the operated catalyst showed a similar trend with the most obvious weight increment at the first two cycles due to polymer incorporation, and the weight maintained constant with no significant loss afterward

(Figure 8.9b). Accordingly, the specific surface area declined from 2280 to 40 m^2/g (Figure 5.2b) after 6 cycles, which supported the proposed explanation. The consistent microstructure of Cu(II) MOF after 6-time polymerizations was analysed by PXRD (Figure 2a), advocating the eminent stability of MOF frameworks through the recycling procedure.
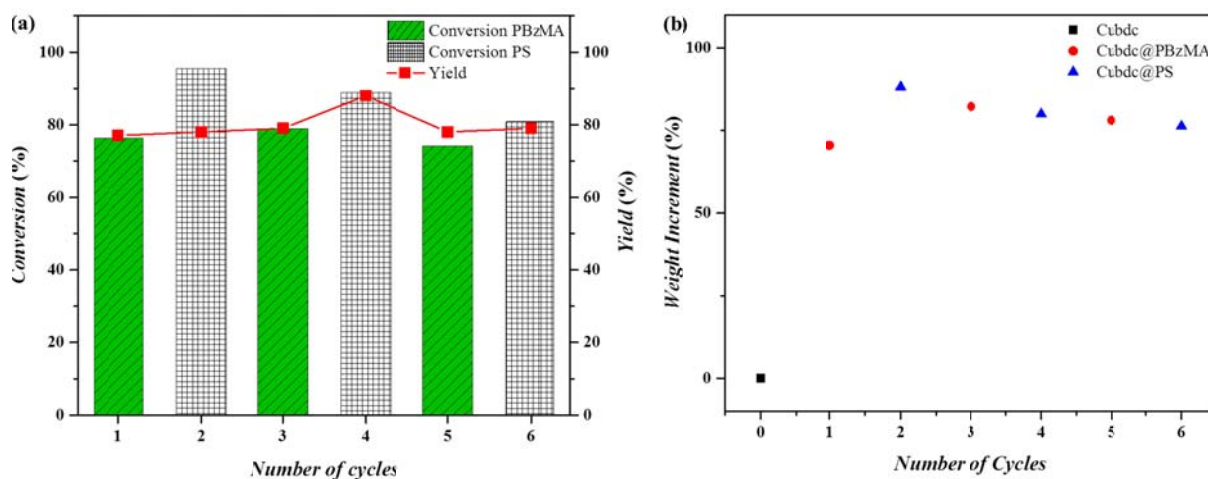
Figure 5.9 (a) Monomer conversion and polymer yield of $Cu_2(bdc)_2(dabco)$-mediated ARGET ATRP in catalyst recycling tests, executing the cascade polymerization of BzMA and styrene. (b) Evolutionary weight increment of the $Cu_2(bdc)_2(dabco)$ after different cycles of the PBzMA and PS cascade polymerization.

Possible leakage of Cu ions from the MOF template was investigated via inductively coupled plasma optical emission spectrometry (ICP-OES). After 6-time recycling, the contamination of polymer product by Cu ions was insignificant in both PBzMA and PS synthesis (0.07-0.01 mg/g after precipitation, Table 2). Compared to the traditional $CuBr_2$ catalyzed reaction, the products from crude bulk solutions of Cu(II) MOF mediated polymerization showed almost 10 times lower Cu ion concentration compared to the conventional strategy. As a result, the contamination with catalyst in polymer products was efficiently avoided by the utilization of Cu(II) MOF. Corresponding to the reversible UV-Vis profiles and PXRD, the ICP results supported the stability of the Cu(II) MOF during the ARGET-ATRP polymerization reactions.

One remarkable property of ARGET ATRP is the requirement of low catalyst concentrations in polymerization. Therefore, the polymerization of PBzMA was exerted with the utilization of merely 500 ppm Cu(II) MOF (approximately 112 ppm Cu(II) ions). Within this condition, still conversions up to 60% was reached after 65 hours in 50 ºC, and decent polymer with MW of 30,000-40,000 g/mol and *Đ* = 1.5-1.8 were obtained (Figure S8 and Table S2).

Table 5.2 The remaining Cu concentration (mg/g) in the polymer products formed via CuBr$_2$ and Cu$_2$(bdc)$_2$(dabco) catalysis. [a]

	CuBr$_2$		Cu$_2$(bdc)$_2$(dabco)	
	Bulk Solution[b]	Precipitation[c]	Bulk Solution[b]	Precipitation[c]
PBzMA	0.6 mg/g	0.1 mg/g	0.09 mg/g	0.07 mg/g
PS	2.1 mg/g	0.6 mg/g	0.19 mg/g	0.01 mg/g

[a] Determined via ICP-OES. [b] The as-synthesized polymer was extracted by THF, the solvent removed and the dry residue was analyzed by ICP. [c] The as-synthesized polymer was precipitated in methanol from THF with the volume ratio 1:4, the precipitate was isolated via centrifugation, vacuum dried and the residue was analyzed by ICP-OES.

5.3 Conclusion

In conclusion, Cu(II) MOFs were utilized in ARGET ATRP of various monomers. Styrene and BzMA were polymerized in controlled fashion according to RDRP standards as proven via a gradually increase of molecular weight with conversion and chain extension experiments. Furthermore, the challenging monomers 4VP and isoprene could be polymerized in a controlled way, as confinement of Cu(II) ions and ligands effectively supresses the side reactions between reagents and monomers to successfully perform RDRP. Furthermore, as a heterogeneous catalyst with particle size around one hundred nm, the copper catalyst can be separated simply from the polymer product by centrifugation, and be reused for further reactions. In summary, with the capability to simplify the polymerization procedure, to prevent side-effects in reactions and to solve the cumbersome catalyst removal, Cu(II) MOF is demonstrated as a powerful catalyst complex for comprehensive polymerization offering well-controlled and living properties of the polymers to expand the feasibility and applicability of ATRP in synthetic chemistry.

6. Synergic effect between nucleophilic monomers and Cu(II) MOF for visible light-triggered PRDRP

6.1 Introduction

Current advanced protocols, e.g. ATRP or ARGET ATRP,[5] have made significant contributions in the manipulation of the activation-deactivation equilibrium between the active $(P_n \cdot)$/dormant $(P_n\text{-X})$ species and Cu(II)/Cu(I) catalytic couple to obtain control in radical polymerization. However, except the traditional thermal treatment, several different external stimuli have been applied to trigger and control a polymerization process, such as pressure,[75] electrical current,[76, 281] mechanical forces,[282] and light.[35, 77, 80, 84, 260, 283-285] Special interest is imparted to photomediated polymerization because of several advantages over traditional polymerization, including adjustable photoactive catalysts, fast reaction rates, and spatio-temporal control (Scheme 6.1). Even though photoinduced catalytic reactions[256, 286-290] or polymerizations[35, 84, 86, 283, 291-294] have recently been widely developed, their use is often limited by the requirement of specialized photoinitiators and photosensitizers,[86, 295] and most importantly by the tedious removal of the non-recyclable catalysts.[296-298] In the case of Cu catalysts, the polymerization of strongly coordinating monomers (i.e. 4-vinylpyridine and 2-vinylpyridine) is limited by both inevitable association[299-300] and S_N2 type nucleophilic substitution which repulses the halide end groups of polymers and results in the formation of branched structures.[301] Therefore, such difficult monomers would benefit from the development of significantly more stable and heterogeneous catalyst.
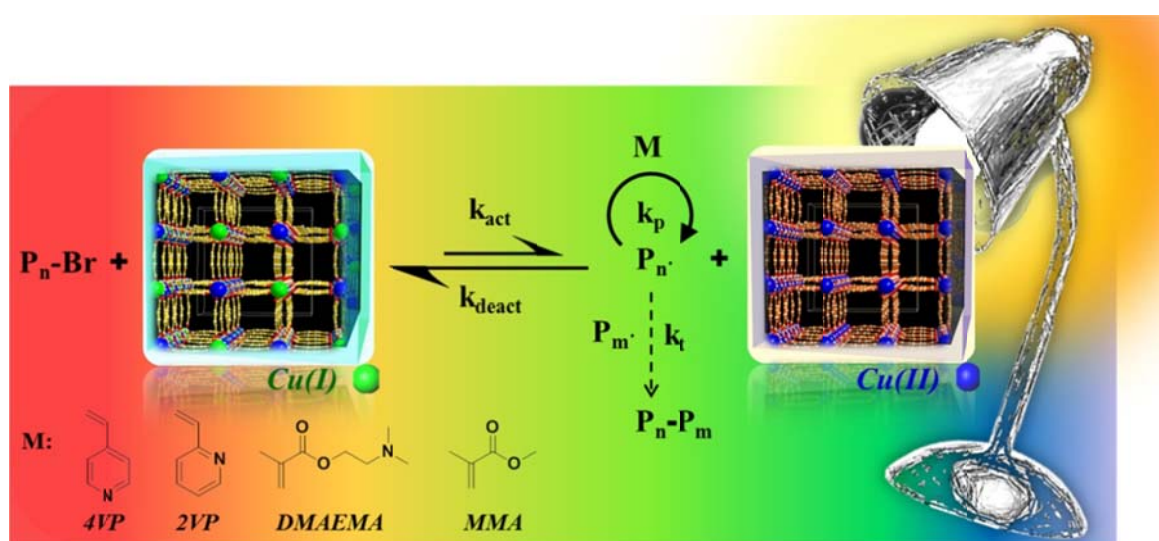
Scheme 6.1 Schematic illustration of the Cu(II) MOF-mediated ATRP.
Parts of this chapter were reproduced from Lee, H.-C.; Fantin, M.; Antonietti, M.; Matyjaszewski, K.; Schmidt, B. V. K. J., *Chem. Mater.* **2017,** *29* (21), 9445-9455, with permission from American Chemical Society (2017).

Due to the highly-tailorable composites or specific host-guest binding effects, optical properties of MOFs can be designed. Namely, the chosen linkers or associated molecules will affect the optical properties and the energy gap between the highest/lowest occupied/unoccupied molecular orbital (HOMO/LUMO),[195, 236, 302] resulting in diverse MOFs acting as photosensitizers with adjustable chemical and optical properties.[112, 195, 303-304] Once irradiated with light, the metal ions can act as photocatalytic centers for oxidation or reduction processes.[305-307] Furthermore, investigations have revealed that MOFs containing unsaturated metal sites acted as Lewis-acid centers with enhanced catalytic activity towards electron-rich molecules.[308-309] Moreover, nitrogen-containing ligands were introduced as potential reducing agents to activate the metal catalytic centers under light irradiation.[62, 256-257, 283]

Since, the catalytic property of $Cu_2(bdc)_2(dabco)$ as a heterogeneous catalyst to catalyze controlled polymerization of various monomers including in the term of ARGET ATRP has been demonstrated in Chapter 5, the Cu(II)-based MOF is in this Chapter demonstrated as an excellent catalyst for visible-light photoinduced Reversible-deactivation radical polymerization (PRDRP) of various nucleophilic monomers, namely 4VP, 2-vinylpyridine (2VP), 2-(dimethylamino)ethyl methacrylate (DMAEMA), and methyl methacrylate (MMA) (Scheme 6.1). The applied MOF is determined as 4/mmm primitive symmetry cell with channel size 7.5 x 7.5 Å,[310] which is composed of dication Cu_2 segments, with terephthalic acid (H_2bdc) as two-dimensional linker and with 1,4-diazabicyclo[2.2.2]octane (dabco) as both pillar and potential reducing motif under light irradiation. A series of photochemical and electrochemical properties of the Cu(II) MOF were investigated first. Then, PRDRP was carried out, under visible-light irradiation to reduce Cu(II) to the active Cu(I), i.e., without photo-specialized initiators, sensitizers or complexed ligands. Surpassing the conventional homogeneous catalyst, the Cu(II) MOF was found to tolerate strongly coordinating monomers. The presence of monomer affected the MOF's properties, influencing both photoabsorption and polymerization behaviors. Being a heterogeneous catalyst, the MOF could be easily separated from the polymerization mixture by centrifugation, and then reused for the PRDRP of 2VP and DMAEMA. Moreover, the on/off character of photoinduced reactions was exploited to obtain temporal control in the polymerization of 4VP.

6.2 Results and Discussion

6.2.1 Optical Properties of Monomer-$Cu_2(bdc)_2(dabco)$ Complexes

It was reported that N-containing monomers can reduce Cu(II) complexes in solution to the active Cu(I) oxidation state under light irradiation.[83] In the following sections, it is shown that nucleophilic N-containing monomers can both reduce the MOF to its Cu(I) state and enhance the light absorption of the MOF.

The optical properties of the Cu(II) MOF were modified by the inclusion of different monomers in the crystal structure, which altered the coordination microenvironment of the Cu(II) ions. As shown in Figure 6.1a, the as-synthesized Cu(II) MOF in methanol (MeOH) exhibited the characteristic cyan blue color of the Cu(II) ions, but pronounced color variations were observed once monomers were added. The suspensions with 4VP and 2VP both turned dark green due to high affinity of these two monomers to the metal centers. In contrast, addition of DMAEMA caused only small color transition to cyan-green, because of its lower coordination strength. Similarly, a limited color transition was observed for the least coordinating monomer, MMA. After exposure to visible light for 30 minutes (Figure 6.1b), the phenomenon of color transition was enhanced for 4VP and 2VP, yet to insignificant extent for the less coordinating DMAEMA and MMA.
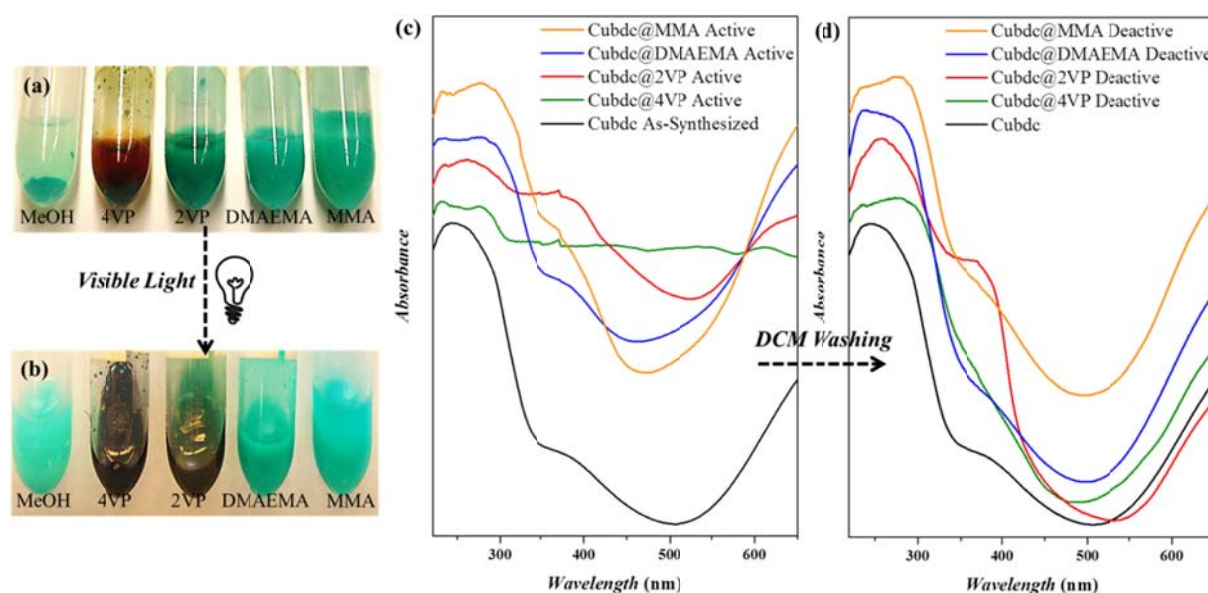
Figure 6.1 Images of Cu(II) MOF-monomer complexes with variation in emission color: (a) before and (b) after the exposure to visible light for 30 minutes (the as-synthesized Cu(II) MOF was dispersed in dry MeOH as a reference). Ultraviolet-visible diffuse reflectance spectra of the Cu MOF in association with different monomers: (c) during polymerization process (after 30 min light exposure, mostly reduced state); (d) after termination of the polymerization and washing with DCM (mostly oxidized state).

The shift in light absorption was also traced by solid-state UV-Vis spectroscopy. The corresponding optical band gap, E_G, was estimated from the UV-Vis profiles by the empirical Tauc plot formula:

$$(\alpha h\upsilon)^2 = A(h\upsilon - E_G) \tag{1}$$

where α is the absorption coefficient, h is the Planck constant, υ is the light frequency, and A is a constant that is a function of the refractive index of the material.[311-312] The as-synthesized Cu(II) MOF

has a maximum absorption around 250-350 nm and E_G of ~3.5 eV (black line in Figure 6.1c). Absorption properties changed upon forming coordination complex with monomers and 30-minute light irradiation (colored lines in Figure 6.1c). For 4VP and 2VP, the spectrum red-shifted towards visible-light region (300-600 nm), the band gap decreased to 2.6 eV, and the overall absorbance increased, especially in the case of 4VP. These changes were less prominent with DMAEMA and MMA, and the band gap decreased only to 3.1 eV. The red-shifted absorption indicated a smaller energy requirement, while the diminished band gap indicated stronger light-harvesting. These effects on the absorption spectra are not caused by the isolated monomers, which do not absorb visible light (Figure 6.2). As a result, it appears that 4VP and 2VP strongly associated to Cu(II) ions, tuning the band gap and enhancing the light harvested by extending absorption into the visible area. In contrast, molecules like MMA, which show less affinity to metallic ions, lead to insignificant variation in MOF light absorption.
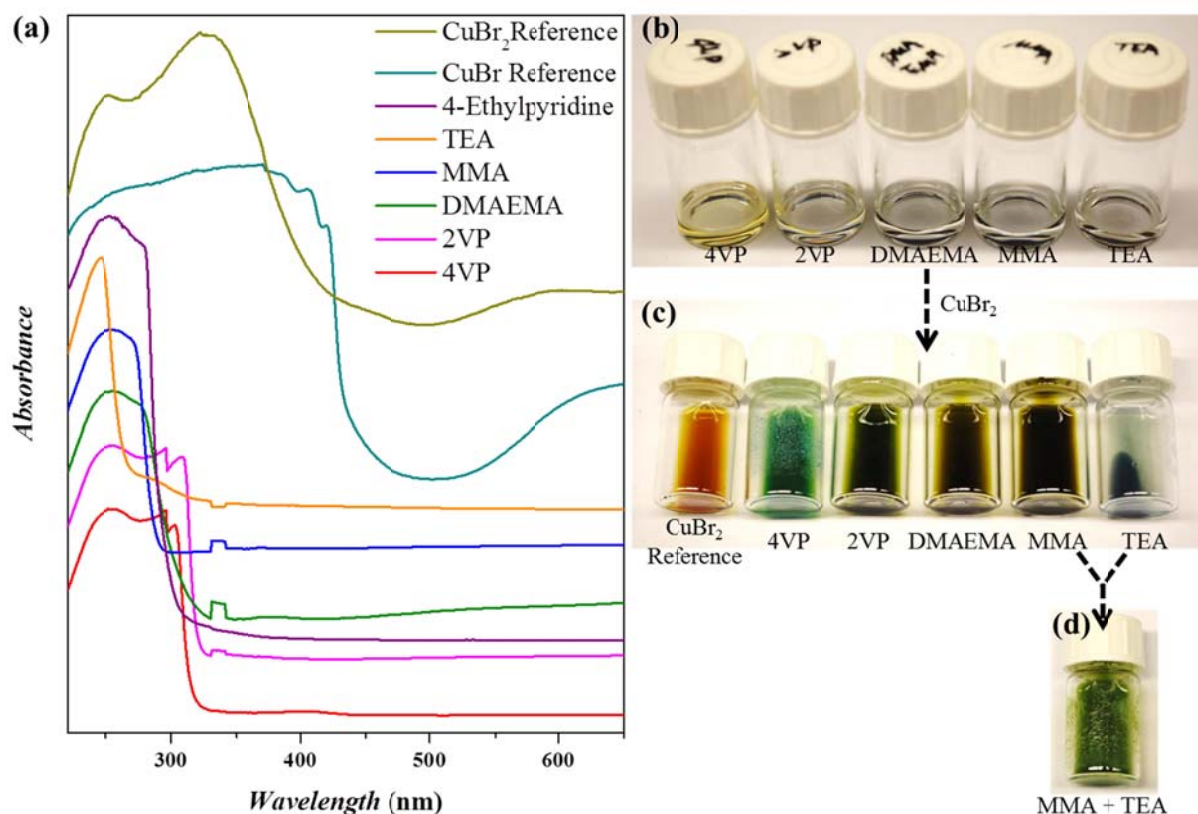
Figure 6.2 (a) Ultraviolet-visible spectra of the employed monomers, TEA and 4-ethylpyridine with conventional catalysts CuBr and CuBr$_2$ as references. Photographs of: (b) Original monomers with transparent color; (c) Monomers complex with CuBr$_2$ with obvious color transitions, and abundant precipitation can be observed in 4VP and TEA. (d) The varied behavior of MMA and CuBr$_2$ mixture, after the addition of TEA.

The absorption spectra also gave indication about the redox state of the MOF. For reference as shown in Figure 6.2a, the spectrum of Cu^IBr in solution was much red-shifted compared to that of $Cu^{II}Br_2$, indicating that the red shift in the UV-Vis spectra can be ascribed to the reduction of MOF-comprised Cu(II) to the Cu(I) state. Reduction efficiency was enhanced in agreement with the coordination ability of the monomers, with 4VP and 2VP promoting the strongest reduction. Interestingly, monomer coordination was reversible. Via facile solvent washing, the absorption shift resulting from monomer association was reversed (Figure 6.1d), with all monomer-MOF absorption profiles shifting back into the blue wavelengths, matching well with the initial Cu(II) MOF.

6.2.2 Electrochemical and Photo-Electrochemical Properties of Cu₂(bdc)₂(dabco)

The redox properties of the Cu(II) MOF were investigated by cyclic voltammetry (CV), after depositing the insoluble MOF on a glassy carbon electrode as described in the experimental section. The CV curve of the Cu(II) MOF presented two reduction waves, associated to two consecutive monoelectronic reductions of the transition metal to Cu(I) and Cu(0) (Figure 6.3a). Upon reaching more negative potentials (~ -0.45 V vs. SCE), a film of metallic copper deposited on the electrode, resulting in the decomposition of the MOF structure. The Cu(0) film was stripped from the electrode during the oxidation scan at ~0.2 V vs. SCE. A similar behavior was reported in other Cu(II) MOFs containing bdc as ligand.[313] To avoid the formation of Cu(0), the CV scan was repeated in a smaller electrochemical window (inset in Figure 6.3a).
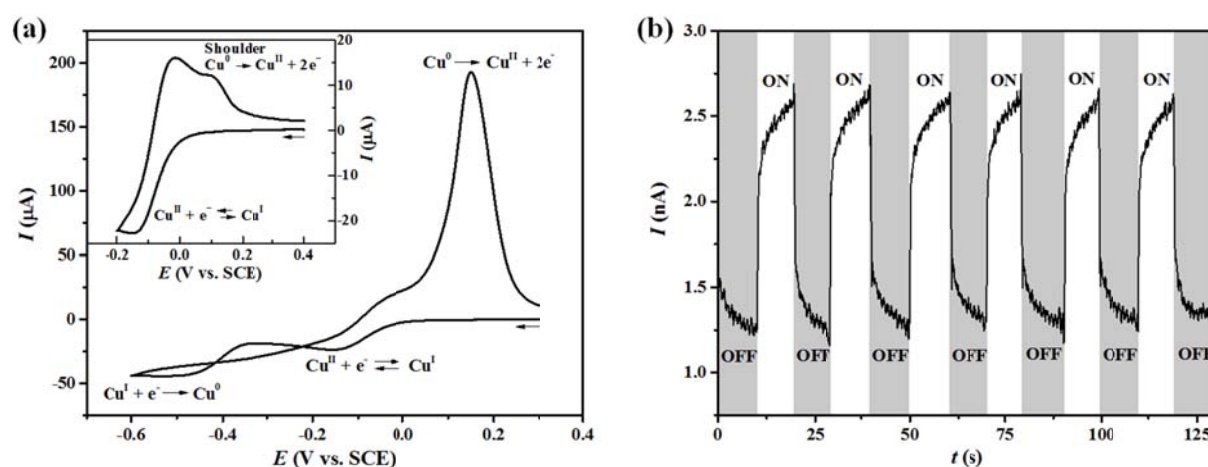
Figure 6.3 Electrochemical characterization of glassy carbon coated with Cu(II) MOF in 0.1 M NaNO₃ deionized water, at RT. (a) CV at scan rate = 0.2 V/s. Inset: CV with smaller electrochemical window to highlight the reversible monoelectronic reduction of Cu(II). (b) Chronoamperometry at +0.4 V vs. SCE under intermittent UV/Vis irradiation (peak intensity at 365 nm, 9 W power).

Interestingly, the CV curve in Figure 6.3a clearly showed the reversibility of the Cu(II)/Cu(I) redox couple, whose reduction potential was calculated as $E^\ominus \approx E_{1/2} = (E_{pc} + E_{pa}) = -0.084$ V vs. SCE

(where E_{pc} and E_{pa} are the cathodic and anodic peak potentials, respectively). The redox potential of the Cu(II)/Cu(I) couple in the MOF is more negative than that of active ATRP catalysts in aprotic solvent, e.g. $E^{\circ} = -0.02$ V vs. SCE for Cu(II)/tris(2-pyridylmethyl)amine^{2+} (TPMA) in CH$_3$CN,[314] but more positive then redox potential for Cu(II)/TPMA in water, $E_o = -0.34$ V vs. SCE.[315]

Overall, the Cu(II) MOF thereby can be expected to be a good ATRP catalyst due to the following properties: i) an accessible Cu(I) oxidation state, separated by ~0.4 V from the reduction to Cu(0); ii) a reversible Cu(II)/Cu(I) redox behavior, required for the ATRP equilibrium; iii) a reducing power (i.e. ATRP activity) comparable to that of the most active ATRP catalysts.[316]

The effect of light on the redox state of the Cu(II) MOF was studied subsequently (Figure 6.3b). In the dark, application of a steady potential of +0.4 V vs. SCE generated a small background current of ca. 1 nA, indicating no reactions at the electrode. Upon irradiating the electrode surface with UV/Vis light, a sudden increase in oxidation current was observed, which indicates the formation of Cu(I) species. In fact, it has been already shown that photoexcited amine ligands, such as dabco, can reduce Cu(II) to Cu(I).[83] When switching off the light, the current decayed to the background value quickly. The on/off cycles could be repeated for an arbitrary amount of times, which is an indication of the good reversibility of the redox reaction and stability of the MOF structure under irradiation.

6.2.3 Visible Light-Triggered Photopolymerization via Cu$_2$(bdc)$_2$(dabco)

The Cu(II) MOF was used to photo-polymerize the four monomers mentioned above, in the order of coordinating ability: 4VP, 2VP, DMAEMA, and MMA. A nearly linear semilogarithmic plot of monomer conversions against time for both P4VP and P2VP indicated a constant concentration of propagating radicals (Figure 6.4 a and b). In both cases, molecular weights increased linearly with conversion and agreed well with theoretical values (Figure 6.4 d and e). Polymerization rate of 4VP was the fastest, with near-quantitative conversion (> 85%) in 90 minutes. The slower rate with 2VP, 40% conversion in 90 minutes, was attributed to the different microstructure. The different position of the heteroatom in 2VP could affect the binding affinity towards the MOF due to steric hindrance,[317] diminishing the polymerization rate.[301, 318] Table 6.1 shows that well-defined polymers were synthesized, giving controlled P4VP with MW of 3,300 and Đ = 1.2, and a P2VP with MW of 5,300 and Đ = 1.4. The control over 2VP polymerization indicated limited side reactions such as intramolecular displacement of Br by penultimate 2VP unit.[301, 318] For both monomers, the free radical polymerization gave uncontrolled polymers with dispersity up to 9.7. The polymerization behavior of the two vinylpyridine monomers supported the proposed concept of synergistic effect resulting from highly nucleophilic monomer and metal ions. The MOF, which intrinsically harvests only near UV light, was sensitized to accept visible light, and thus improved polymerization efficiency.
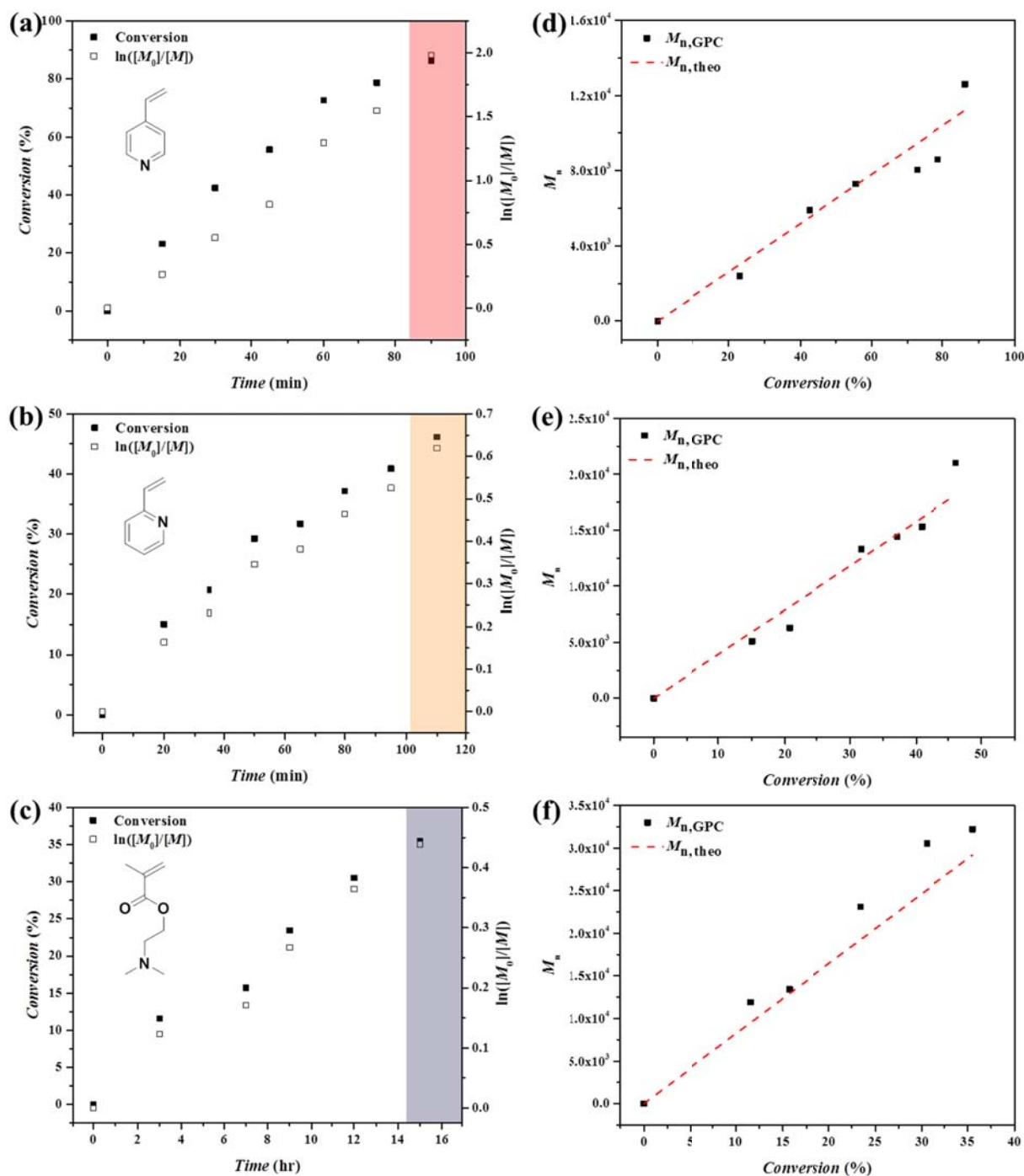
Figure 6.4 Kinetic evolution of monomer conversion in polymerization of (a) P4VP, (b) P2VP, and (c) PDMAEMA with the utilization of Cu$_2$(bd**c**)$_2$(dabco), and the corresponding evolution of M_n with conversion. [4VP]$_0$/[EBIB]$_0$ = 125:1; [2VP]$_0$/[EBIB]$_0$ = 370:1; [DMAEMA]$_0$/[EBIB]$_0$ = 500:1, with Cu(II) MOF 0.08 g and 2 g monomer.

Subsequently, DMAEMA, an alkyl amine-containing monomer with lower coordination strength toward the MOF, was polymerized. Although slower, i.e. 36% conversion in 15 h (Figure 6.4c), the polymerization of DMAEMA was controlled (Figure 6.4f), yielding PDMAEMA with MW of

18,900 and $Đ = 1.4$ (Table 6.1). The slower rate might be due to the weaker coordination between DMAEMA and embedded Cu ions, resulting in less significant photo-harvesting ability, as evaluated by UV/Vis spectra in Figure 6.1.

Table 6.1 Properties of (co)polymers obtained via conventional strategies and $Cu_2(bdc)_2(dabco)$ catalysis, at ambient temperature under visible light.

Homo polym.	Catalyst	k_p^{app} (h^{-1})	$M_{n,theo}$ (Conv./hr) [c]	$M_{n,SEC}$ [d]	$Đ$ [e]	Co polym. [f]	$M_{n,Theo}$ [c]	$M_{n,SEC}$ [d]	$Đ$ [e]
P4VP	Free Radical	-	-	11.3	6.4	-	-	-	-
	Cu(II) MOF[a]	1.32	2.8 (22%/0.25)	3.3	1.2	P4VP-*b*-POEGMA	15.5	13.9	1.2
P2VP	Free Radical	-	-	87.3	9.7	-	-	-	-
	Cu(II) MOF [a]	0.32	4.9 (13%/0.33)	5.3	1.4	P2VP-*b*-PIBA	15.9	13.8	1.3
PDMAEMA	CuBr$_2$/ PMDETA[a]	-	18.5 (79%/24)	15.2	1.2	-	-	-	-
	Cu(II) MOF[a]	0.029	2.3 (3%/0.5)	3.2	1.2	PDMAEMA-*b*-POEGMA	10.8	9.7	1.2
PMMA	CuBr$_2$/ PMDETA[a]	-	21.9 (93%/24)	20.0	1.2	-	-	-	-
	Cu(II) MOF/ TEA[a]	-	4.2 (13%/2)	19.4	1.3	-	-	-	-
	Cu(II) MOF/ 4-EP [a*]	-	4.5 (14%/6)	13.8	1.3	PMMA-*b*-PIBA	39.2	33.6	1.2
	Cu(II) MOF/ 4-EP [b*]	0.068	3.4 (11%/1.5)	3.7	1.2	-	-	-	-

[*] 4-EP = 4-ethylpyridine. [a] Using EBIB as initiator. [b] Using bromoacetonitrile as initiator. [c] Conversion determined by GC-MS. The theoretical number averaged molecular mass $M_{n,theo}$ was calculated as $MM_{initiator} + MM_{monomer} \times ([monomer]_0/[initiator]_0) \times$ conversion. The $M_{n,theo}$ was presented in $\times 10^3$. [d] Determined by SEC according to the equation S1 based on PMMA calibration ($\times 10^3$) in THF (for PDMAEMA and PMMA) or NMP (for P4VP and P2VP). [e] Determined by SEC using PMMA standard. [f] $[macroinitiator]_0/[OEGMA/ IBA]_0/[CuBr_2]_0/[PMDETA]_0/[dabco]_0 = 1:340:4:8.8:20$, at 50 °C for 24 h in 50 vol % methanol (P4VP and PDMAEMA) or DMF (P2VP and PMMA).

Last, the polymerization of non-nucleophilic MMA was attempted. Under conditions that were successful for 4VP, 2VP, and DMAEMA, MMA did not polymerize even after 20 hours of photoirradiation, as shown in Figure 6.5a. The retarded polymerization indicated that MOF-comprised dabco alone is an insufficient photo-reducing agent to trigger polymerization; instead, nucleophilic N-containing monomers are required. Indeed, when the MOF was deposited from a TEA/acetone 1:4 mixture instead of pure acetone, the photocurrent increased five-fold (Figure 6.5b). The enhanced absorption confirmed that N-containing compounds enhanced the photoreduction properties of the MOF. Unfortunately, the effect of monomers could not be directly probed by electrochemistry, because they prevent as such the deposition of compact MOF layers on the electrode.
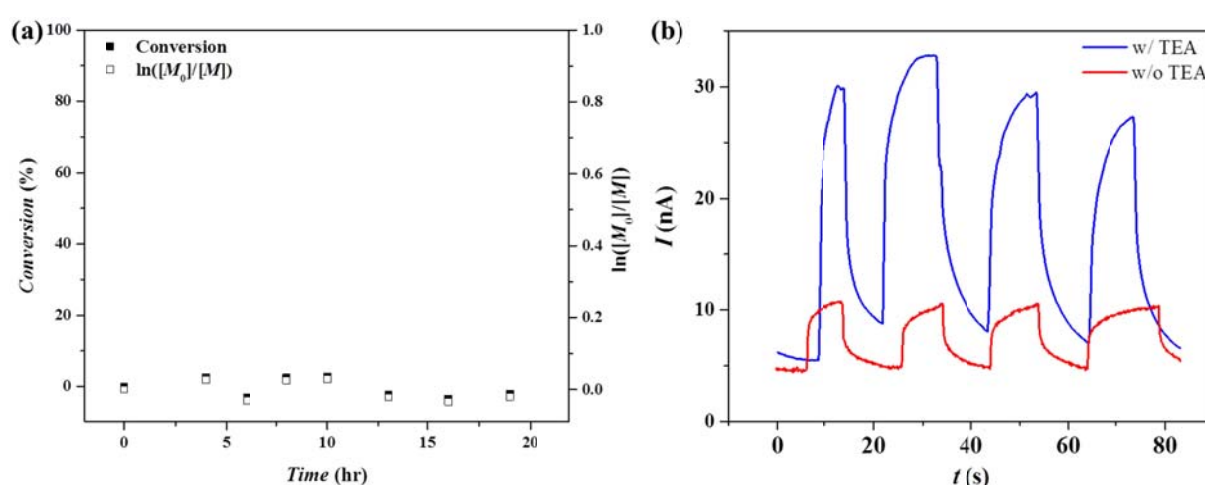
Figure 6.5 (a) Kinetic evolution of MMA conversion with the utilization of $Cu_2(bdc)_2(dabco)$ but without the addition of TEA. (b) Chronoamperometry of glassy carbon modified with Cu(II) MOF at +0.4 V vs. SCE under intermittent visible light irradiation, in 0.1 M $NaNO_3$ deionized water solution, at RT. The MOF was deposited from dry acetone or dry acetone/TEA 4:1 mixture. The light source was a white LED (13 W).

To enhance the light-harvesting properties during MMA polymerization, TEA and 4-ethylpyridine were added to trigger the polymerization. TEA and 4-ethylpyridine are nucleophiles and reducing agents that mimic DMEMA and vinylpyridines, respectively.[83] Indeed, addition of TEA promoted successful polymerization of MMA, giving 20% conversion (Figure 6.6a), but polymer with MW ($M_{n,SEC}$ = 194,000, $Đ$ = 1.3) higher than predicted ($M_{n,theo}$ = 4,200) was detected (Figure 6.6d). 4-ethylpyridine was more effective, and promoted polymerization up to 30% conversion (Figure 6.6b), resulting in PMMA with $Đ$ = 1.3 and $M_{n,SEC}$ = 13,800 ($M_{n,theo}$ = 4,500) (Figure 6.6e). These high values of $M_{n,SEC}$ are attributed to a low initiation efficiency by EBIB, which is a poor initiator for MMA due to a penultimate effect.[83, 319-320] When using bromoacetonitrile, a more active initiator, polymerization

rate increased, with 20% conversion after 3 hours instead of 10 hours (Figure 6.6c). Moreover, MWs were better controlled with $M_{n,SEC} = 3,700$, $M_{n,theo} = 3,400$, and $Đ = 1.2$ (Figure 6.6f).
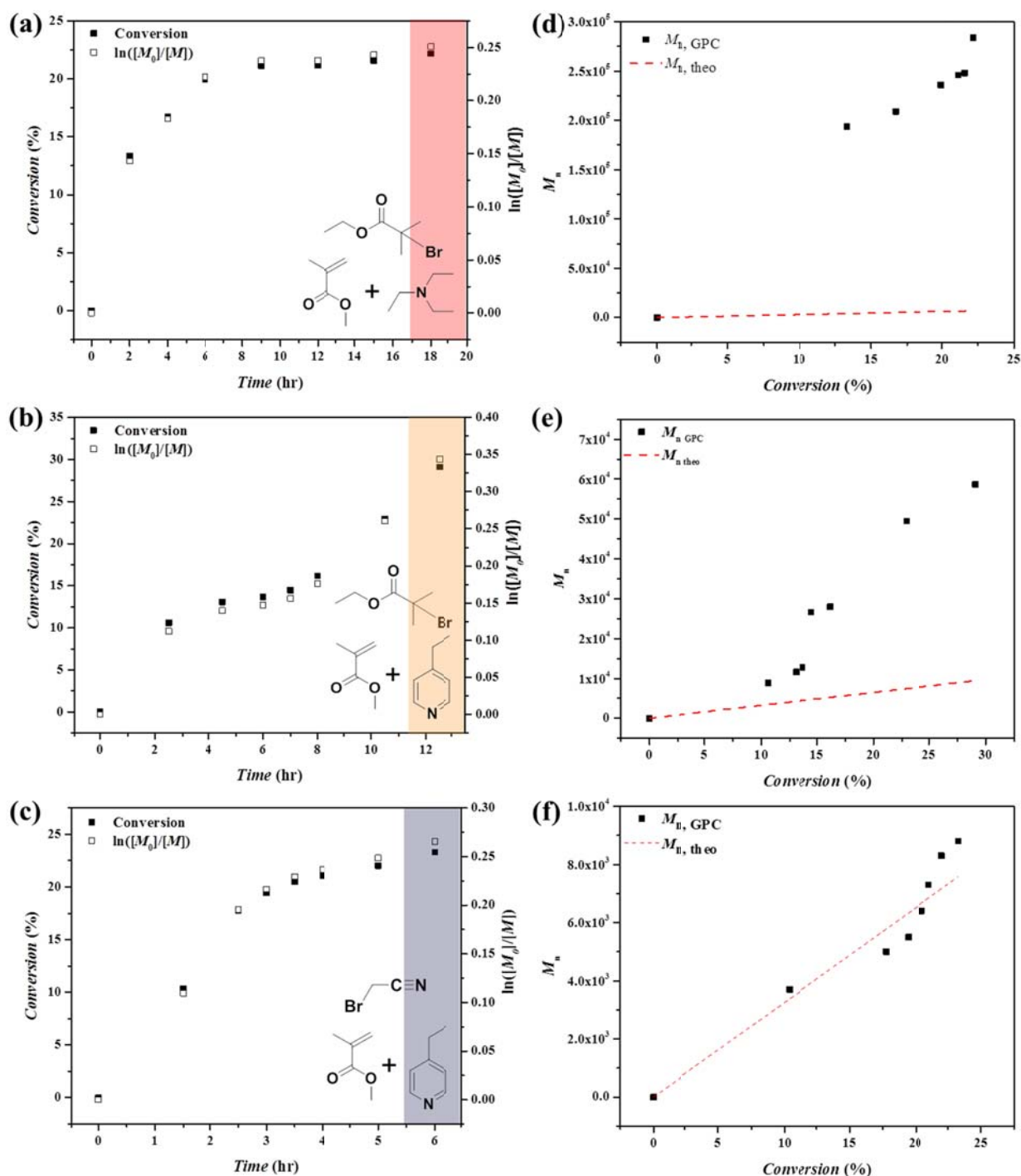
Figure 6.6 Kinetic evolution of MMA conversion with the utilization of $Cu_2(bdc)_2(dabco)$: (a) with the addition of TEA and EBIB as initiator, (b) with the addition of 4-ethylpyridine and EBIB as initiator, and (c) with the addition of 4-ethylpyridine and bromoacetonitrile as initiator, and the corresponding evolution of M_n on MMA conversion. $[MMA]_0/[EBIB/bromoacetonitrile]_0/[TEA/4-ethylpyridine]_0 = 325:1:8$, with Cu(II) MOF 0.08 g and 2 g monomer.

The improved efficiency with 4-ethylpyridine and bromoacetonitrile is in line with enhanced polymerization behavior of vinylpyridines compared to DMAEMA or the TEA/MMA system, advocating the versatility of PRDRP catalyzed by the Cu(II) MOF. Time-dependent SEC chromatograms and polymer properties of the homopolymers obtained during the kinetic analysis using $Cu_2(bdc)_2(dabco)$ as photocatalyst (Figure 6.5 d-f, 6.6f) are shown in Figure S10 and Table S3. Although the slightly higher Đ resulted from the crude extraction without precipitation, the increasing MW according to reaction time and conversion can be clearly observed with monodistributed molecular weight distribution, indicating the living chain end and limited nucleophilic substitution which replaces the bromide chain end with pyridine groups.

6.2.4 Stability of $Cu_2(bdc)_2(dabco)$

The electrochemical measurements suggested the stability of the MOF under photoirradiation (Figure 6.3b). Moreover, the conservation of the MOF structure during each polymerization was confirmed by PXRD (Figure 6.7a). Variations in relative peak intensities were attributed to the incorporation of the guest molecules in the host nanochannel.[37] Actually, due to the monomer incorporation in the porous framework, BET profiles showed decreased specific surface area (m^2/g)/pore volume (cc/g) from 2280/0.91 to 230/0.15, 560/0.25, 450/0.29 and 1050/0.36 after polymerization with P4VP, P2VP, PDMAEMA and PMMA, separately (Figure 6.7b). Interestingly, the decrease corresponds to the coordination ability of the used monomer (i.e. 4VP > 2VP > DMAEMA > MMA).
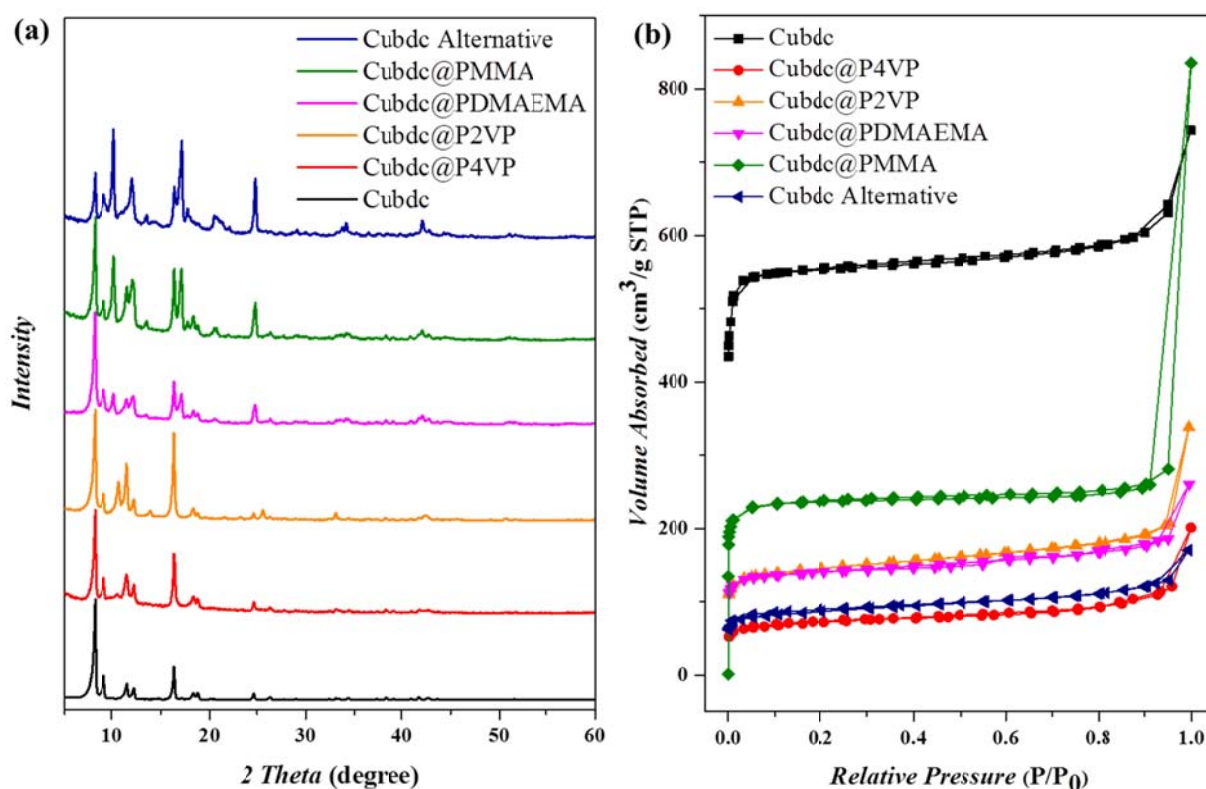
Figure 6.7 (a) PXRD profiles and (b) N_2 adsorption-desorption isotherm of $Cu_2(bdc)_2(dabco)$ before and after photopolymerization of various monomers.

Possible leakage of Cu ions from the MOF template was investigated by ICP-OES. Comparing to homogeneous ARGET, catalyzed by $CuBr_2$/PMDETA, Cu contamination in polymer product was reduced significantly in both Cu(II) MOF-synthesized PDMAEMA and PMMA, with Cu concentration decreasing from 8.7 to 0.26 mg/g, and from 0.53 to 0.062 mg/g, respectively (as shown in Table 6.2). The products from crude bulk solutions of Cu(II) MOF-mediated polymerization showed almost 30 times lower copper ion concentration comparing to ARGET ATRP under homogenous conditions. A slightly higher Cu concentration was detected for poly(vinylpyridines), which strongly coordinate to the Cu(II) ions of the MOF. However, it has to be noted that this strong association is also the basis of the successful polymerization of vinylpyridines, which is difficult with conventional catalysts. In fact, $CuBr_2$/PMDETA was unstable, and formed insoluble products in the presence of vinylpyridines, as can be seen in Figure 6.2c. The crystalline MOF is significantly more stable avoiding the chelating effect of nucleophilic monomers. In conclusion, the ICP and polymerization results supported the stability of the Cu(II) MOF during the photopolymerization, particularly in comparison with traditional copper catalysts.

Table 6.2 Residual Cu concentration (mg/g) in the polymer products synthesized via $CuBr_2$ and $Cu_2(bdc)_2(dabco)$ catalysis. [a]

	CuBr$_2$/PMDETA (mg/g) [b]	Cu$_2$(bdc)$_2$(dabco) (mg/g) [c]
Initial Bulk [d]	0.85	9.2
P4VP	-	2.5
P2VP	-	1.3
PDMAEMA	8.7	0.26
PMMA	0.53	0.062

[a] Determined via ICP-OES. [b] The as-synthesized polymer was extracted by DCM, and, after removing the solvent by vacuum, the dry residue was analyzed by ICP. [c] The as-synthesized polymer was dissolved in DCM, and the suspension was isolated via centrifugation to remove the Cu(II) MOF. After drying by vacuum, the residue was analyzed by ICP-OES. [d] The theoretical Cu amount in the initial bulk solution.

6.2.5 Proposed Mechanism of Cu-MOF Catalyzed Photopolymerization

The photocatalytic nature of Cu(II) MOF was strongly supported by both UV/Vis absorption (Figure 6.1) and photo-electrochemical analysis (Figure 6.3). Irradiating the MOF by light caused reduction of comprised Cu(II) to Cu(I), promoting controlled polymerization by ATRP in an ARGET-type process. Moreover, under irradiation, nucleophilic monomers (or additives, such as TEA and 4-ethylpyridine) further supported the (re)generation of activators (Scheme 6.2).[83] The faster polymerization and enhanced control in polymerization of vinylpyridines was related to their stronger coordination, which enhanced the light-absorption property of the monomer–Cu(II) complex. Polymerization rate in the presence of additives followed the same trend: 4-ethylpyridine, which mimics 4VP, gave faster reaction than TEA, which mimics DMAMEA. The reduction of Cu(II) in a mixture with P2VP has been described in the literature albeit at elevated temperature.[258] Nevertheless, irradiation might be able to provide the required energy for photoreduction of Cu(II). Overall, the photoreduction of Cu(II) is proceeding without pyridine or external amine addition as shown via CV (Figure 6.3), but pyridine or amine supported reduction might take place as well.
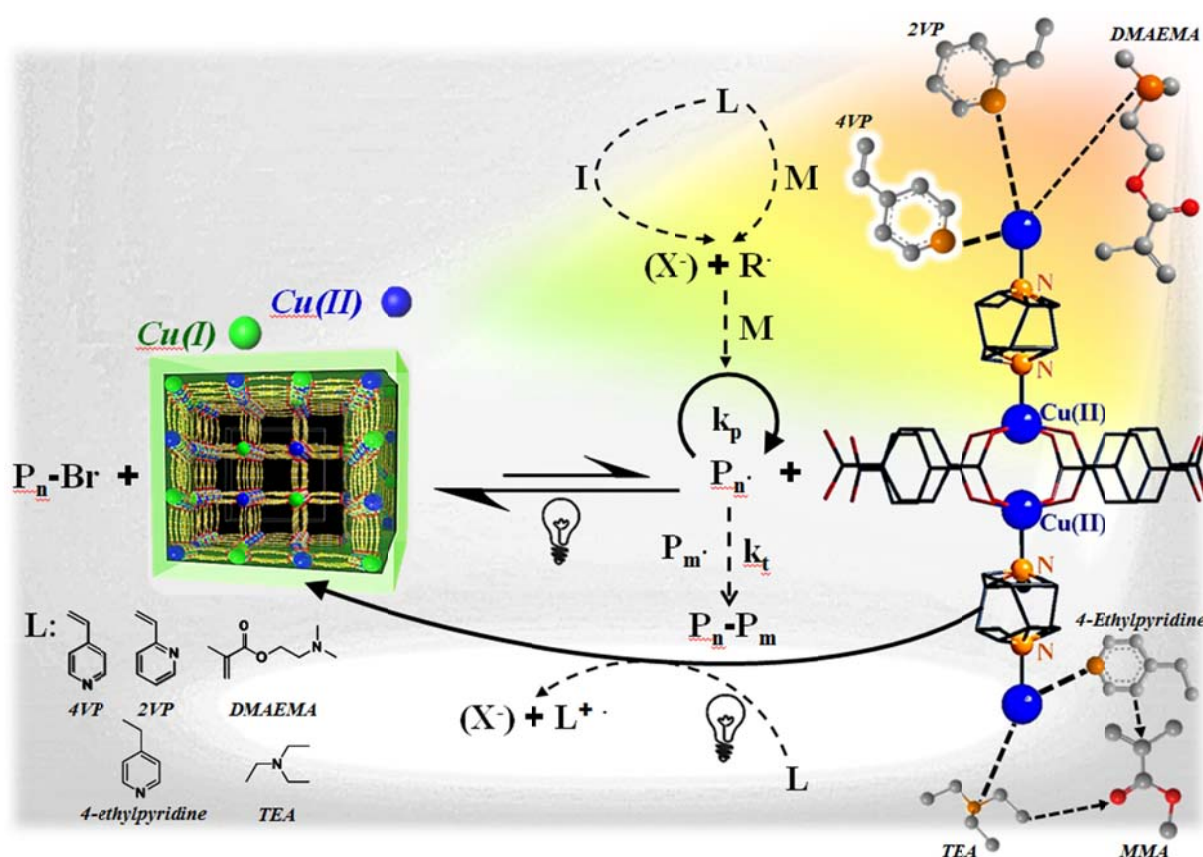
Scheme 6.2 Proposed mechanism of photopolymerization with the formation of the monomer–Cu(II) MOF complexes, giving adjustable photoabsorption and polymerization behavior.

ATRP activation requires Br atom transfer between chain-end and Cu. However, Br should be difficult to accommodate in the rigid structure of the MOF without distorting the coordination sphere. Conversely, vacant or defect sites on the MOF outer surface may be more accessible, acting as catalytic hot spots. Owing to the small size of the crystals (~100 nm), content of Cu on the surface should be a remarkable 5% of total Cu (considering 0.76 nm the average Cu–Cu distance from coordination structure,[310] see Appendix to Chapter 6 for detail estimation). Moreover, defects can increase accessibility of catalytic ions and then further enhance the reactivity.[321-322] Therefore, we suggest that the bulk polymerization is catalyzed by the MOF surface or the defect on MOF crystals, at which monomer, polymer and Br are able to interact with available coordination sites.

Besides Cu ions on the MOF surface, leaked Cu^{2+} could also deactivate radicals.[323] The Cu^{2+}/dabco complex, however, was an inactive ATRP catalyst, as shown in Figure 6.8a. Further proof of the inactivity of leaked Cu^{2+} was provided by blank polymerizations as negative control: no polymerization occurred when a typical reaction mixture (Cu(II) MOF, monomer, and initiator) was prepared, and then filtered to remove the MOF (Figure 6.8b). Additionally, no conversion was detected in the absence of initiator, indicating that the alkyl halide was the only source of radicals

(Figure 6.8c). To conclude this part, the surface of the MOF reacted with polymer chain ends to give controlled polymerization, while both MOF bulk and leaked Cu^{2+} were inactive.

Figure 6.8 (a) Cyclic voltammetry of 10^{-3} M $Cu^{II}(OTf)_2$ + 5×10^{-3} M dabco in DMF + 0.1 M Et_4NBF_4. T = 25 °C, v = 0.2 V s^{-1}. Multiple peaks and very large peak separation indicated the presence of a complicated speciation in solution, with no well-defined Cu(II)/Cu(I) redox couple. Addition of 3×10^{-3} M EBIB did not cause any significant modification of the cyclic voltammetry, indicating the negligible activity of Cu^{2+}/dabco as ARGET ATRP activator. The corresponding phenomenon can be observed in kinetic evolution of monomer conversion in the absence of (b) $Cu_2(bdc)_2(dabco)$ and (c) initiator.

6.2.6 Polymer Microstructure Resulting from Cu(II) MOF-Mediated Photopolymerization

Considering the strong association between nucleophilic monomers and the well-ordered Cu framework, the microstructure of the synthesized polymers was studied.[27, 34] The tacticity of each synthesized polymer was analyzed by ^{13}C NMR (Figure 6.9). Results were compared between MOF-mediated photopolymerization and traditional polymerization approaches (i.e. free radical polymerization or homogenous ARGET). Isotacticity increased for P4VP, with a content of isotactic triads of 27 % by photopolymerization, in comparison to 13 % by conventional free radical polymerization. The increased isotacticity can be attributed to the coordination and alignment of 4VP and P4VP along the MOF framework, because the comprised Cu ions act as Lewis acids, forming strong coordination with nitrogen atoms from 4VP monomer and/or polymer chains.[9, 38, 324] Except 4VP, the other monomers retained their original tacticity.[9] In the case of 2VP, this could result from the steric hindrance on the heteroaromatic ring, enabling only a free form to polymerize.[317] For methacrylates, this was attributed to their weak affinity toward Cu centers. Consequently, only the strongly coordinating 4VP showed significant increase in isotacticity.

Figure 6.9 Comparison of ^{13}C NMR spectra for (a) P4VP, (b) P2VP, (c) PDMAEMA, and (d) PMMA synthesized by free radical polymerization (or CuBr$_2$) and Cu(II) MOF-mediated photopolymerization in chloroform-*d*.

Another desirable feature in PRDRP is chain-end functionality, which was investigated by chain extension of all prepared polymers with either oligo(ethylene glycol) methyl ether methacrylate (OEGMA) or isobornyl acrylate (IBA) by ARGET ATRP under homogenous conditions (Figure 6.10 and Table 6.1). The SEC traces show monomodal increase of molecular weight, and thus preservation of the halogen end-group, which is typical of "living" polymerizations. The block copolymers were well-controlled with Đ = 1.2-1.3. The difference in composition between macroinitiators and block copolymers was also traced by ^{1}H NMR (Figure 6.11).
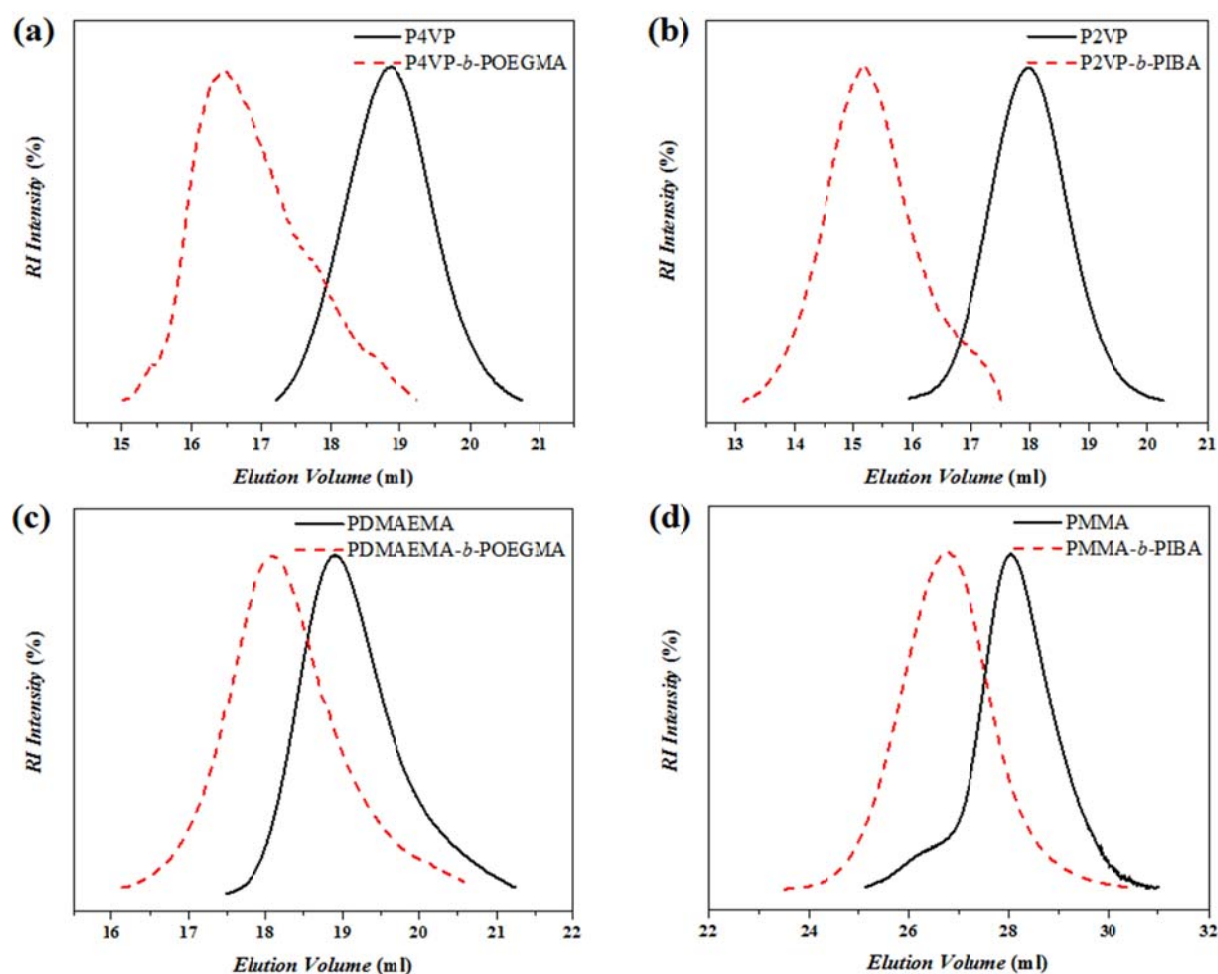
Figure 6.10 SEC chromatograms of (a) P4VP, (b) P2VP, (c) PDMAEMA, and (d) PMMA before (dark, solid line) and after (red, dashed line) chain extension with OEGMA or IBA in 50 vol % methanol (P4VP and PDMAEMA) or DMF (P2VP and PMMA) with [macroinitiator]$_0$/[OEGMA/IBA]$_0$/[CuBr$_2$]$_0$/[PMDETA]$_0$/[dabco]$_0$ = 1:340:4:8.8:20 at 50 °C for 24 hr. The molecular weight is calculated according to equation S1, using PMMA standard in NMP.
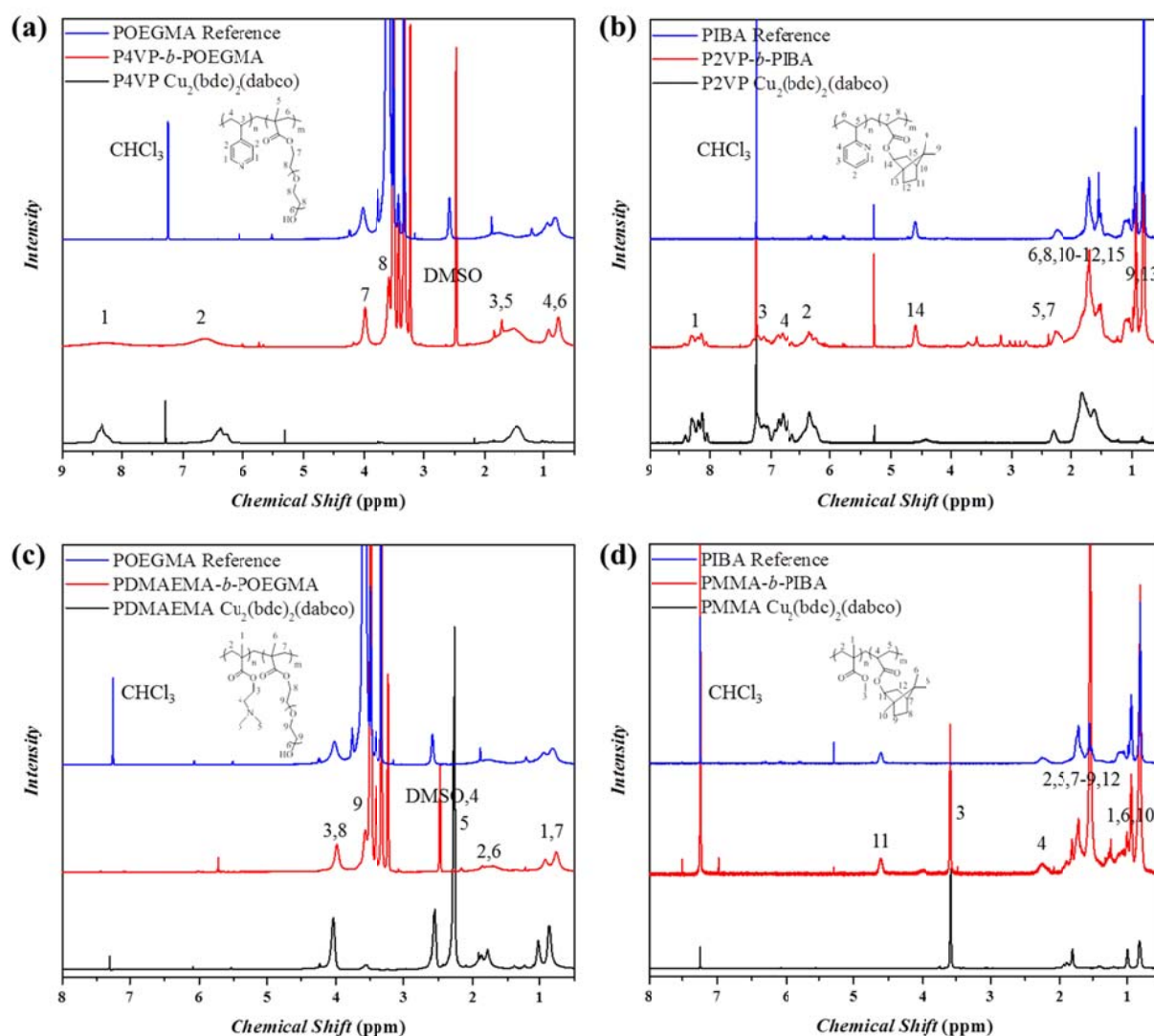
Figure 6.11 ^{1}H NMR of products of Cu(II) MOF-mediated photopolymerization in chloroform-d or dimethyl sulfoxide-d$_6$: (a) P4VP, (b) P2VP, (c) PDMAEMA, and (d) PMMA homopolymer and block copolymer after chain extension with OEGMA or IBA.

6.2.7 Reusability of Cu$_2$(bdc)$_2$(dabco)

As a heterogeneous catalytic complex with particle size ~100 nm, the Cu(II) MOF was easily separated via centrifugation, recovered by washing, and repeatedly utilized for subsequent photopolymerizations. As demonstrated in Figure 6.12a, the catalytic complex was recycled up to six times, conducting alternating polymerization of P2VP and PDMAEMA. Monomer conversion remained constant in each catalyst recycling step. The preservation of the MOF structure after the repeated tests was confirmed by PXRD in Figure 6.7a. The slight shift of position and intensity of the peaks resulted from the incorporation of 2VP, DMAEMA, and polymers during the subsequent polymerization tests. Incorporation of reagents was also confirmed by the gradual increment of catalyst weight (Figure 6.12b), by the decline of surface area from 2280 to 320 m^2/g, and by the

contraction of pore volume from 0.91 to 0.18 cc/g (Figure 6.7b). However, filling the channels of the MOF did not compromise its catalytic properties in the repeated polymerizations, confirming that the surface, not the bulk, is the active site for photopolymerization.
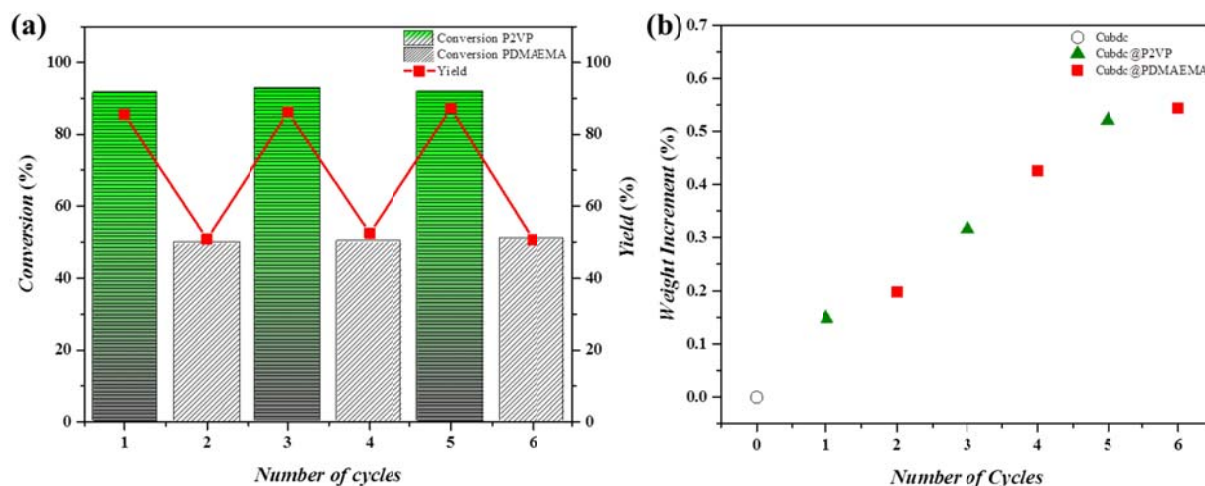
Figure 6.12 (a) Conversion of 2VP and DMAEMA in subsequent photopolymerizations with recycled Cu$_2$(bdc)$_2$(dabco). (b) Increase of weight of recycled Cu$_2$(bdc)$_2$(dabco) after each cycle of the P2VP and PDMAEMA repeated polymerization.

6.2.8 Temporal Control of Cu$_2$(bdc)$_2$(dabco) in P4VP Photopolymerization

On/off reactivity is an appealing characteristic of photopolymerization. Using intermittent light exposure and dark for specific times (i.e. 20, 10, and 60 min), the MOF-mediated polymerization of 4VP proceeded much faster when light irradiation was applied. Very limited activity was observed during the "dark" periods, which could be attributed to Cu(I) remaining in the system (Figure 6.13). As a result, the photo responsive-property of the Cu(II) MOF was confirmed by the temporal-control of polymerization.
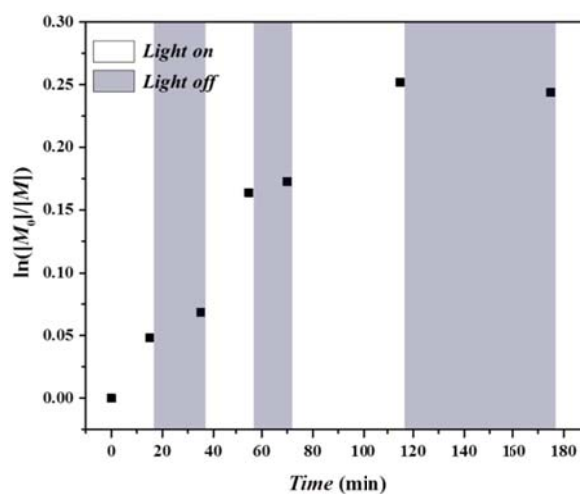
Figure 6.13 Semilogarithmic kinetic plot of 4VP consumption during intermittent light exposure, with consecutive light (white area) and dark treatments (shaded area).

6.3 Conclusion

The MOF $Cu_2(bdc)_2(dabco)$ was used for the controlled photopolymerization under visible light, without the need for external photoinitiators. N-containing monomers and additives (i.e. 4VP, 2VP, TEA, and 4-ethylpyridine) had a dual/synergistic effect on the MOF-mediated polymerization. On one hand, these compounds acted as reducing agents under irradiation. On the other hand, the formation of monomer-MOF complexes improved the photoabsorption properties of the MOF, which could harvest more visible light. The photoabsorption properties improved when stronger coordinating monomers were used, with 4VP > 2VP > DMAMEA > MMA. Interestingly, the rate of photopolymerization followed the same trend. The effect of the monomer coordination was reversible, as the original Cu(II) MOF could be recovered by simple washing with solvent. $Cu_2(bdc)_2(dabco)$ presented a well reversible Cu(II)/Cu(I) redox behavior, with $E^{\ominus} = -0.084$ V vs. SCE, suggesting excellent catalytic activity in ATRP. Photoreduction of Cu(II) to the active Cu(I) was also well reversible as traced by chronoamperometry under intermittent light irradiation. Controlled photopolymerization of highly nucleophilic monomers was achieved with the Cu(II) MOF, synthesizing polymers with predictable MW and low *Đ*, ranging from 1.2 to 1.4. After reaction, the catalyst was easily recycled for several polymerizations, avoiding significant contamination of catalytic ions. Moreover, photoreaction was temporally controlled, exploiting the stimuli-responsive redox nature of the Cu(II) MOF.

7. Dispersion of MOF Nanoparticles with Enhanced Photocatalytic Performance

7.1 Introduction

In the previous chapters, MOFs as highly-crystalline porous materials have been demonstrated as outstanding heterogeneous catalysts with promising catalytic performance, adjustable photo-absorption and highly compatible property for controlled polymerization, realizing the synthesis of various unique and challenging (co)polymers. However, the formation of polymer-MOF composite to contribute a bilateral improvement in both polymer and MOF area is the main consideration in this Chapter.

It is well known that the catalytic property can be profoundly improved through decreasing particle size or increasing dispersibility,[209, 325-326] but unfortunately the innate coordinated inorganic property makes MOF crystals usually brittle and easily aggregated or clogged which inevitably retards mass transfer, reduces interfacial area, and then hampers the catalytic capability.[327-328] Many solutions have been developed to conquer this long-term problem, such as synthesis of nanoscale MOFs with superstructures,[329-331] integration of MOF particle into membranes or films using extra binders or hot-pressing strategy,[327] and surface functionalization of MOF particles with dispersible polymer brushes.[149, 173, 259-260] However, these newly established strategies still suffer from a trade-off. Namely, the extremely small size with high surface energy frequently results in synthetic difficulty and less long-term stability,[332] and the incorporated binders/grafted polymers may cover and/or block the catalytically active sites.[173, 259-260] Thus, the performance of the designed composites is conversely restricted. Hence, a more facile and general strategy to circumvent these struggles and enable the potential catalytic property of MOFs is highly desirable.

Poly(2-(dimethylamino)ethyl methacrylate) (PDMAEMA) has attracted increasing interest owing to the pH and temperature responsive property.[270, 333] The chain conformation is strongly dependent on its lower critical solution temperature (LCST) and the corresponding solvent polarity. For instance, extended polymer chains can be observed in acidic/good solvent or when temperature below the LCST, and vice versa. Most interestingly, the amine group from each DMAEMA monomer enables coordination binding to metals or metallic ions,[334] serving as a potential stabilizer for universal MOFs. To avoid the adversely reduction of surface active sites on MOFs by using highly mobile, free-formed polymer chains, the surface-anchored polymer brushes are utilized in this study due to the constrained

Parts of this chapter were reproduced from Lee, H. C.; Heil, T.; Hwang, J.; Sun, J. K.; Schmidt, B.V. K. J., paper submission.

mobility from three dimensional (3D) to 2D and preserved space between each grafted brush. Therefore, the grafted PDMAEMA acts as high-aspect-ratio nano-tentacles[330] which extend and capture the MOF particles more efficiently with less inter-/intra-chain coupling.[171] Pollen grains with the advantages of ubiquitous resources, high mechanical and chemical resistance are frequently utilized as supporting pivoto which provides wide compatibility to diverse polymers owing to the easily functionalized surface, light weight, unique hierarchical porous structure.[335-336]

In this regard, for the first time, PDMAEMA grafted pollen (*P*-pollen) is demonstrated as a facile and universal support for MOFs, using pollen grain as a hollow spheroid decorated with PDMAEMA brushes as MOF-targeting tentacles (MOFs@*P*-pollen). Due to the intrinsic amine functionality, MOF particles can strongly coordinate with and be stabilized along well-defined PDMAEMA brushes. Besides, by taking advantage of the responsive property of PDMAEMA, adjustable chain conformations (i.e. stretching or recoiling) in response to environment (i.e. solvent or temperature) can be achieved reversibly (Scheme 7.1). Comparing to the highly crystalline MOF innate, the as-designed composites, MOFs@*P*-pollen, are characterized with adjustable dispersibliy and environment-responsive switching on/off property, by which significantly enhancing catalytic performance of MOFs in solution state with remarkable durability and reusability can be accomplished.
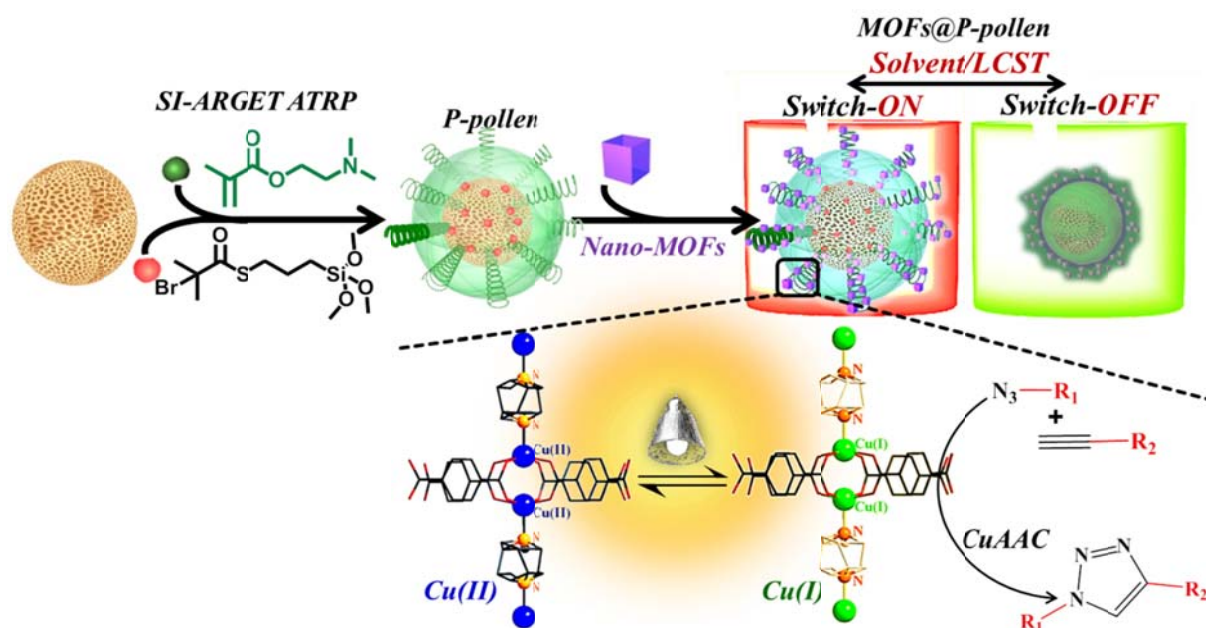
Scheme 7.1 Illustration of the environment-responsive MOF-pollen composite with adjustable dispersibility and innate catalytic property for visible light-triggered photoclick reaction.

The general process to fabricate the MOFs@*P*-pollen composites is illustrated in Scheme 7.1. The surface initiated activators regenerated by electron transfer atom transfer radical polymerization (SI-ARGET ATRP) was applied to graft well-defined PDMAEMA brushes from the surface of washed

pollens, giving "smart" *P*-pollen. Subsequently, MOFs were incorporated in DCM, one of the good solvent of PDMAEMA, in which the polymer chains were highly stretched, enabling efficient association between amine groups from comprised monomers with MOF's metallic ions. After forming association with MOF particles, the MOFs@*P*-pollen composites with environment-responsive dispersibility can be prepared successfully.

7.2 Results and Discussion

7.2.1 Fabrication PDMAEMA-Grafted Pollens (*P*-pollen)

The grafted initiator, MPTS-Br, was synthesized based on literature, and characterized by ^{1}H NMR (Figure 7.1a). Then, utilizing different concentration of grafted initiator, for example, 0.5, 1, 2, 3 and 5 wt%, the pollen grains with varied grafting density of initiator were prepared (Figure 7.1b). After the initiator-functionalized pollen was fabricated, SI-ARGET ATRP was carried out to graft PDMAEMA from the pollen surface.
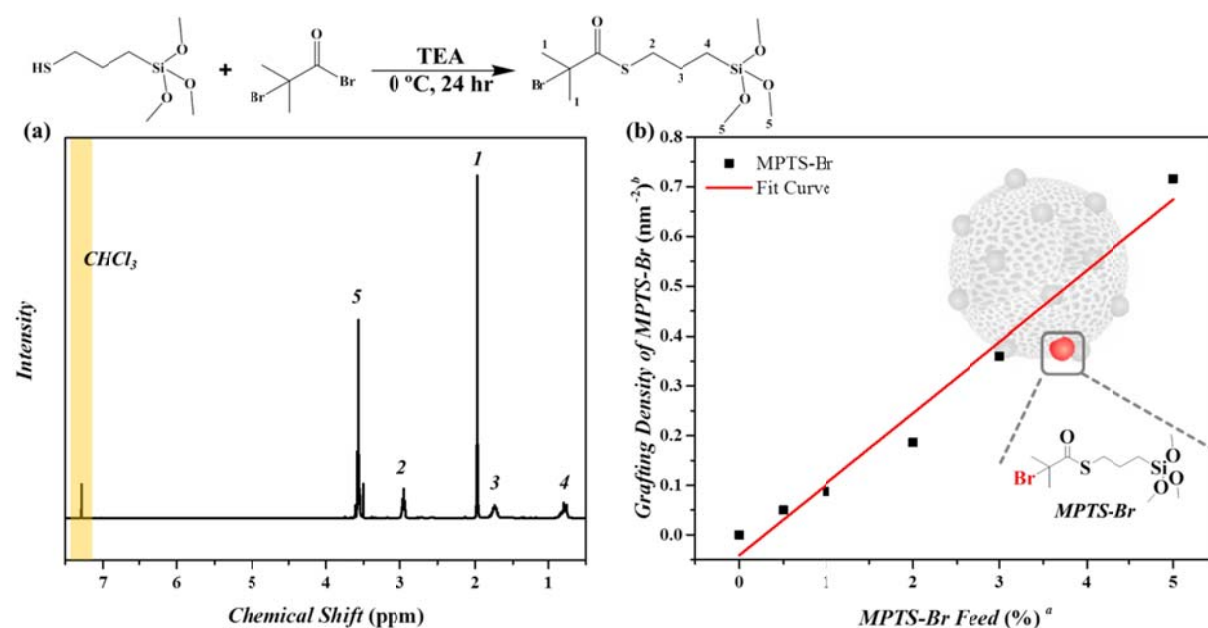
Figure 7.1 (a) ^{1}H NMR of the synthesized grafted initiator, MPTS-Br, in chloroform-*d*. (b) Calculated grafting density of MPTS-Br on pollen grains (σ_{Br}).[a] The feed concentration of MPTS-Br within the initial solution. [b] Determined via ICP-OES with Br element, and BET giving pollen surface area with 6.8 m[2]/g.

Due to the controlled property of SI-ARGET ATRP, the grafting density of polymer brushes (σ_p) was assessed by the grafting density of initiator (MPTS-Br, σ_{Br}) and the initiation efficiency (f_{ini}) depicted in Equation 1,[337] giving $\sigma_p = 0.32$ chain/nm[2]

$$\sigma_p = \sigma_{Br} f = \frac{(grafted\ amount\ of\ initiator) \times f_{ini}}{(surface\ area\ of\ pollen)} \qquad (1)$$

Considering particularly for thermal responsive polymers, a higher grafting density ($\sigma_p \geq 0.3$ nm^{-2}) is a core factor to further extends the grated polymers (exponential scaling behavior, depict in Equation 2) which contribute larger steric hindrance and act as steric stabilizers to prevent the agglomeration of nanoparticles, the highest feed concentration of initiator (5 wt%) was applied to give $\sigma_{Br} = 0.72$ and $\sigma_p = 0.32$ chain/nm^2,

$$h \propto N\sigma_p^n \qquad\qquad\qquad\qquad\qquad\qquad\qquad\qquad\qquad (2)$$

where h is the average length of extended brushes (layer thickness), N is the degree of polymerization, and n is an exponent correlated to solvent, grafting density and molecular properties.[338-339] The grafted PDMAEMA brush was cut from the pollen by 1% NaOH, and characterized by SEC with MW of 67,800 and Đ = 1.2 (Figure S11). The functionalization of pollen grains with PDMAEMA brushes was further confirmed by ATR-FTIR (Figure 7.2 b and c). Comparing to the original pollen grains (Figure 7.2b), the vanished signal between 3100-3400 cm^{-1} and the appearance of C=O signal around 1730 cm^{-1} indicated the immobilization of silane initiator with the consumption of hydroxyl group and the successful polymerization of DMAEMA.
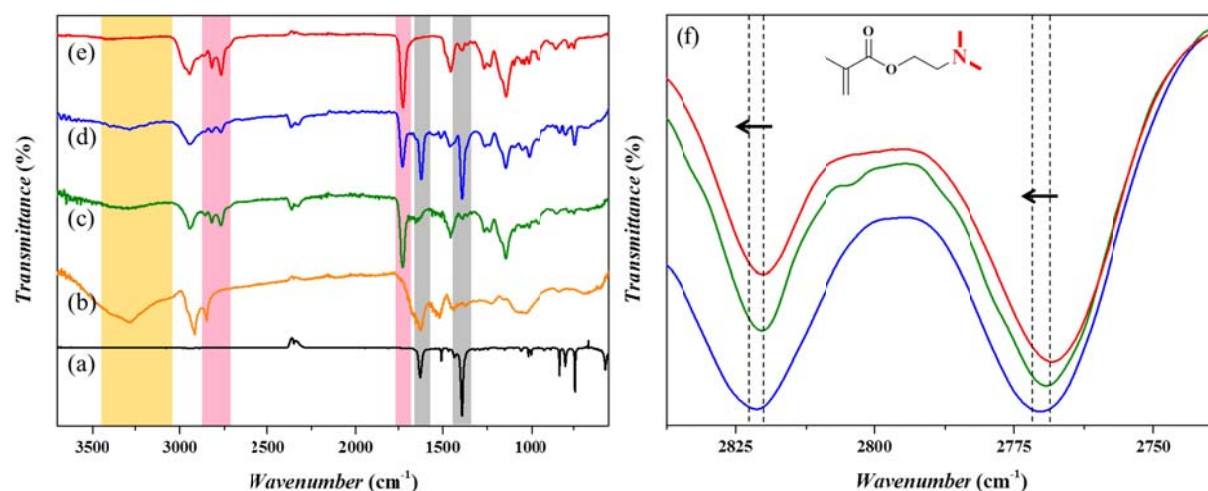
Figure 7.2 ATR-FTIR spectra: (a) as-synthesized Cu$_2$(bdc)$_2$(dabco), (b) pollen, (c) *P*-pollen, (d) Cu$_2$(bdc)$_2$(dabco)@ *P*-pollen, (e) PDMAEMA Reference and (f) the zoom-in amine signal of (c), (d) and (e).

7.2.2 Incorporation of MOFs on *P*-pollen

The representative MOF, Cu$_2$(bdc)$_2$(dabco), was chosen as an example to demonstrate the effectivity of our strategy. The obtained Cu$_2$(bdc)$_2$(dabco)@*P*-pollen composite was comprehensively characterized. As shown in Figure 7.3, energy dispersive X-ray spectroscopy (EDX) mapping revealed the well-distributed Cu$_2$(bdc)$_2$(dabco) nanocrystals on the *P*-pollen pivot. The morphology of the composite was then characterized by FE-SEM, showing the cubic Cu$_2$(bdc)$_2$(dabco) crystals with sizes

around 100 nm well-anchored on the hierarchically porous *P*-pollen. The microstructure was analyzed by powder x-ray diffraction (PXRD), giving the characteristic peak that matched well with as-synthesized $Cu_2(bdc)_2(dabco)$ crystals.
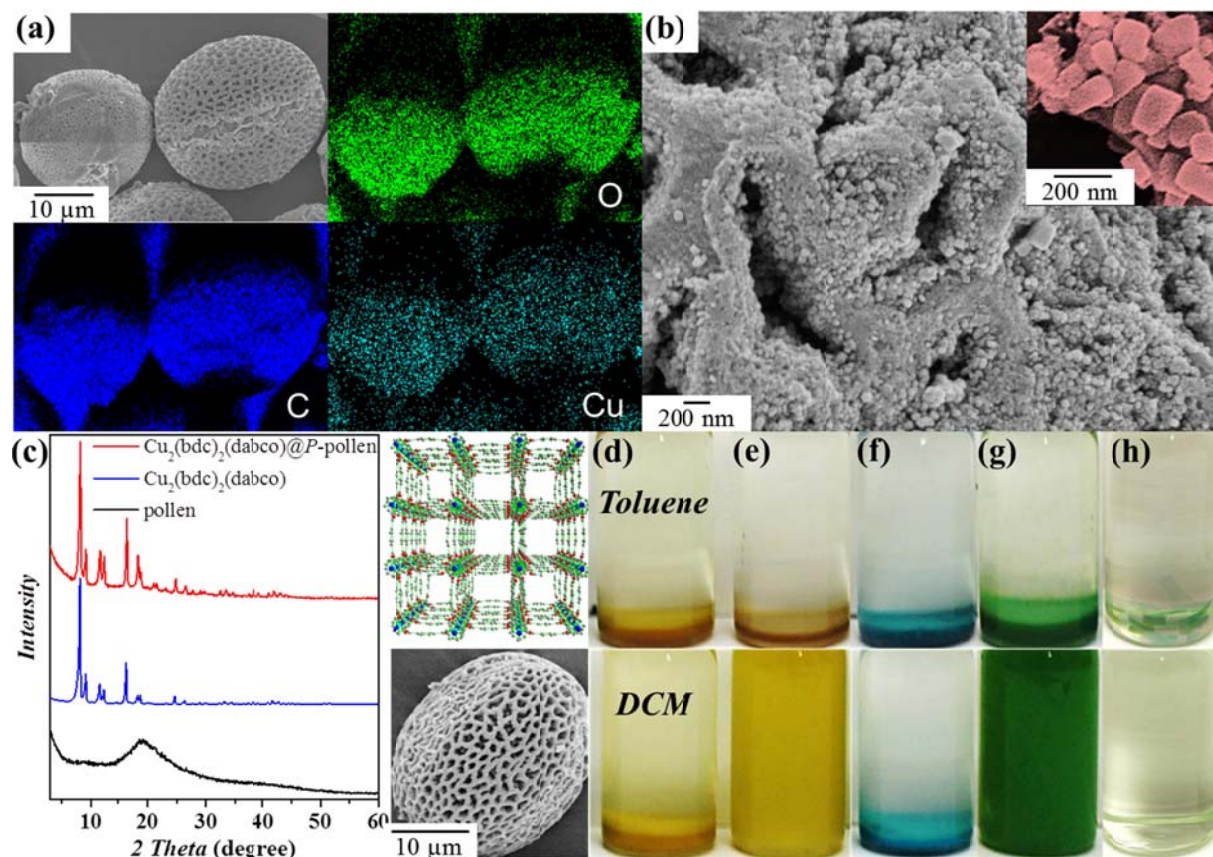
Figure 7.3 (a) FE-SEM EDX mapping of $Cu_2(bdc)_2(dabco)@P$-pollen. (b) The enlarged image of (a), revealing the well-distributed MOF nanoparticles throughout the pollen surface. (c) PXRD of the as-synthesized $Cu_2(bdc)_2(dabco)@P$-pollen with innate $Cu_2(bdc)_2(dabco)$ and pollen as references. Images of varied dispersibility in toluene (above, non-dispersable) *vs*. DCM (below, well-dispersed): (d) washed pollen; (e) *P*-pollen; (f) $Cu_2(bdc)_2(dabco)$; (g) $Cu_2(bdc)_2(dabco)@P$-pollen; (h) $PDMAEMA@Cu_2(bdc)_2(dabco)$.

The overall functionalized process from pollen, *P*-pollen to $Cu_2(bdc)_2(dabco)@P$-pollen was traced by ATR-FTIR spectra with the combined signals from pollen, PDMAEMA and $Cu_2(bdc)_2(dabco)$ (Figure 7.2 a-e). The shift of amine vibration (2768 and 2819 cm^{-1}) towards higher wavenumber (2819 and 2823 cm^{-1}) after incorporation of $Cu_2(bdc)_2(dabco)$ indicated the direct association between DMAEMA and MOF nanocrystals with increment in electron density.[340-341] The interaction between the MOF and *P*-pollen was further traced by solid-state UV-Vis spectroscopy (Figure 7.4a) to evaluate individual optical band gap, E_G, by the Tauc Equation:

$$(\alpha h\upsilon)^2 = A(h\upsilon - E_G) \tag{3}$$

where α is the absorption coefficient, h is the Planck constant, υ is the light frequency, and A is a constant that is a function of the refractive index of the material. The $Cu_2(bdc)_2(dabco)$ has a major absorption between 250-350 nm and E_G = ~3.5 eV. However, upon coordinating with *P*-pollen (E_G = ~1.7 eV), the spectrum showed a dramatic red-shift towards visible-light region (450-650 nm), with corresponding band gap decreased to 1.4 eV. The shifting absorption and significant improvement in light harvesting ability of MOF@*P*-pollen composite is attributed to the strong coordination between grafted PDMAEMA polymer and $Cu_2(bdc)_2(dabco)$ together with pollen serving as a photo-protector with eminent light absorption ranging from 200-900 nm.[342]
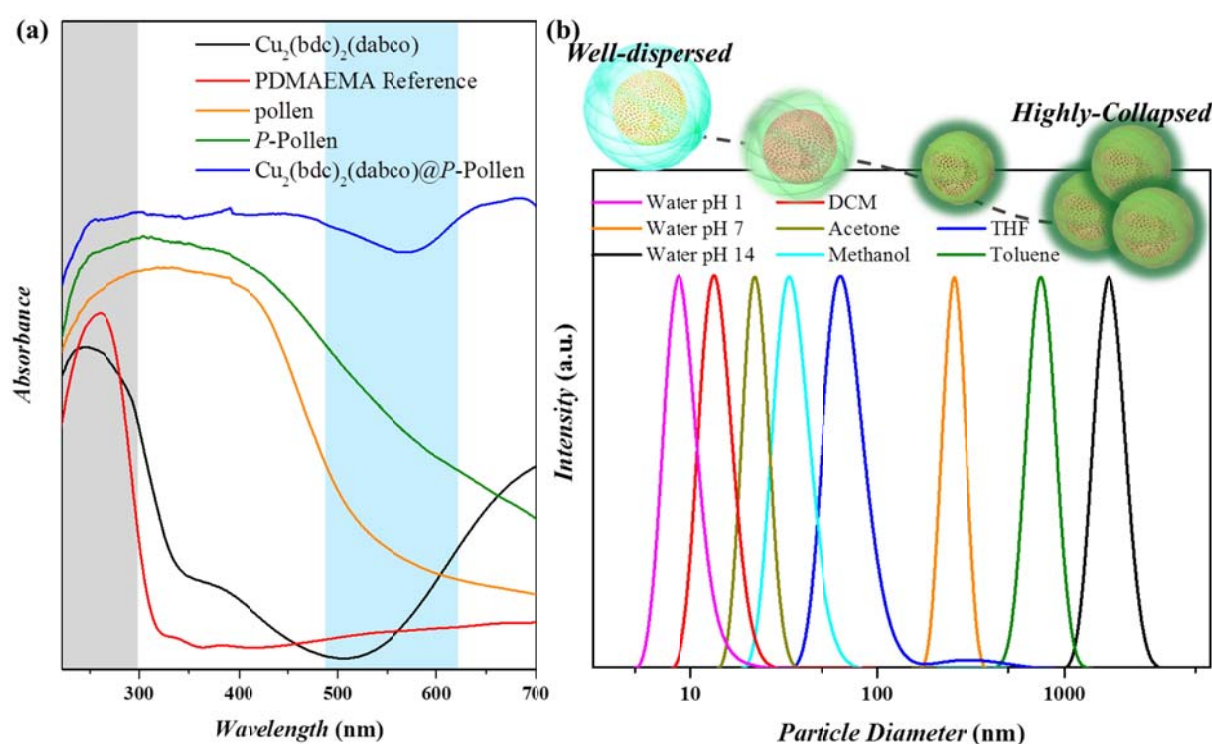
Figure 7.4 (a) Ultraviolet-visible diffuse reflectance spectra of the Cu(II) MOF before and after incorporation on the *P*-pollen. (b) Solvent-induced particle size change of free-formed PDMAEMA determined by DLS in different solvents and pH values with speculated morphology of *P*-pollen. Note: PDMAEMA chains cut from the *P*-pollen were determined.

7.2.3 Applicability of the *P*-pollen Strategy

To demonstrate the versatility of current method, other kinds of MOFs with varied microstructures, metallic ions and comprised linking agents were applied to form hybrid composites with as-designed *P*-pollen. Surprisingly, the route described here is general toward preparing a large variety of MOF@*P*-pollen with high dispersibilty in DCM solution. In the present thesis, the MOFs with different components, e.g. MOF-5, MOF-74-Zn, $Zn_2(bdc)_2(dabco)$, Cu(bdc), HKUST-1 and ZIF-

67-Co with loading mass between 18-36 wt% attached on P-pollen were investigated to demonstrate the universality of current strategy (Table 7.1). The high compatibility between the functional polymer tentacle immobilized on *P*-pollen and the different metal cations on MOFs strongly advocate the feasibility of current strategy. The association and preservation of the specific MOF structure was confirmed by FE-SEM and PXRD (Figure 7.5).

Table 7.1 Incorporated Amount of MOF [a] in the MOF@*P*-pollen composites [b]

	Type of Metallic Ion	Amount of Metallic Ion (mg/g)	Incorporated MOF (%)
MOF-74-Zn		99.2	24.6
MOF-5	Zn	155	23.0
$Zn_2(bdc)_2(dabco)$		113	24.9
$Cu_2(bdc)_2(dabco)$		62.9	28.3
Cu(bdc)	Cu	58.5	36.4
HKUST-1		55.3	17.5
ZIF-67	Co	65.4	24.5
PDMAEMA@ $Cu_2(bdc)_2(dabco)$ [c]	Cu	3.37	1.5

[a] Determined via ICP-OES. [b] Grafted PDMAEMA was characterized by SEC with MW of 67,800 and $Đ = 1.2$ (M_{theo} = 30,400, conversion = 98.4%, initiation efficiency (f_{ini}) = 44.8%). [c] The PDMAEMA brushes cut from *P*-pollen were utilized directly as the free-formed polymer chains to incorporate $Cu_2(bdc)_2(dabco)$ nanoparticles.
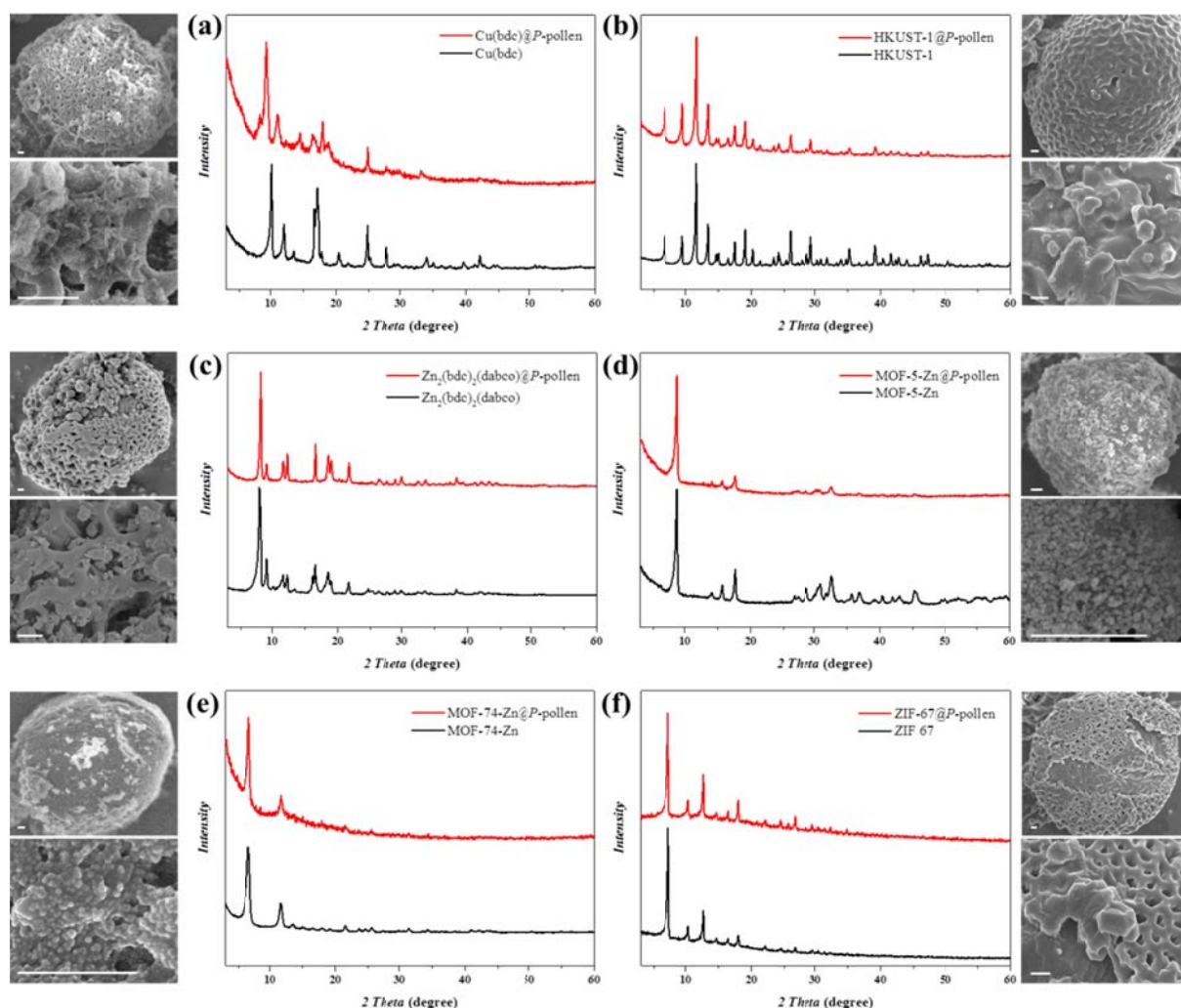
Figure 7.5 PXRD profiles of (a) Cu(bdc), (b) HKUST-1, (c) Zn$_2$(bdc)$_2$(dabco), (d) MOF-5 , (e) MOF-74 and (f) ZIF-67 before and after incorporation on the *P*-pollen. Corresponding SEM images of each MOF@*P*-pollen composite with the 1 μm scale bar.

7.2.4 Adjustable Dispersibility of MOF@*P*-pollen Composites

The incorporation of the stimuli-responsive polymer into MOF@*P*-pollen composite triggered our interest to test environment-responsive dispersibility. Considering to the large particle size of pollen (~40 μm), the solvent-dependent dispersibility was probed by dynamic light scattering (DLS) in various solvents and pH (i.e. DCM, THF, acetone, methanol, toluene and water with pH = 1, 7 and 14) using PDMAEMA chains cut from *P*-pollen (Figure 7.4b). The decreasing hydrodynamic size (*d*, nm) was correlated to the increasing solubility of PDMAEMA brushes in the applied solvent, i.e., the smallest hydration layer was detected in acid and DCM (8.7 and 13.5 nm) due to the highly dissolved PDMAEMA chains, and the value became larger in water and toluene (255 and 712 nm) owing to the recoiled morphology; the severe aggregation was eventually observed when using basic solution (*d* = 1.7 μm). As shown in Figure 7.3 d-h, dispersibility of native Cu$_2$(bdc)$_2$(dabco) crystals and pollen

grains was observed neither in DCM nor toluene. However, after incorporation into *P*-pollen, the Cu$_2$(bdc)$_2$(dabco)@*P*-pollen became well-dispersed in DCM for more than 3 weeks because of highly extended polymer chains in the good solvent. By contrast, in the poor solvent, toluene, the precipitation was observed within 3 min. Similar solvent-responsive dispersibility was observed in other MOF@*P*-pollen composites regardless of different metal ions and microstructures (Figure 7.6). Considering the stability of MOFs, the solutions of DCM and toluene were utilized to test the responsive dispersibility of as-fabricated MOF@*P*-pollen composites.
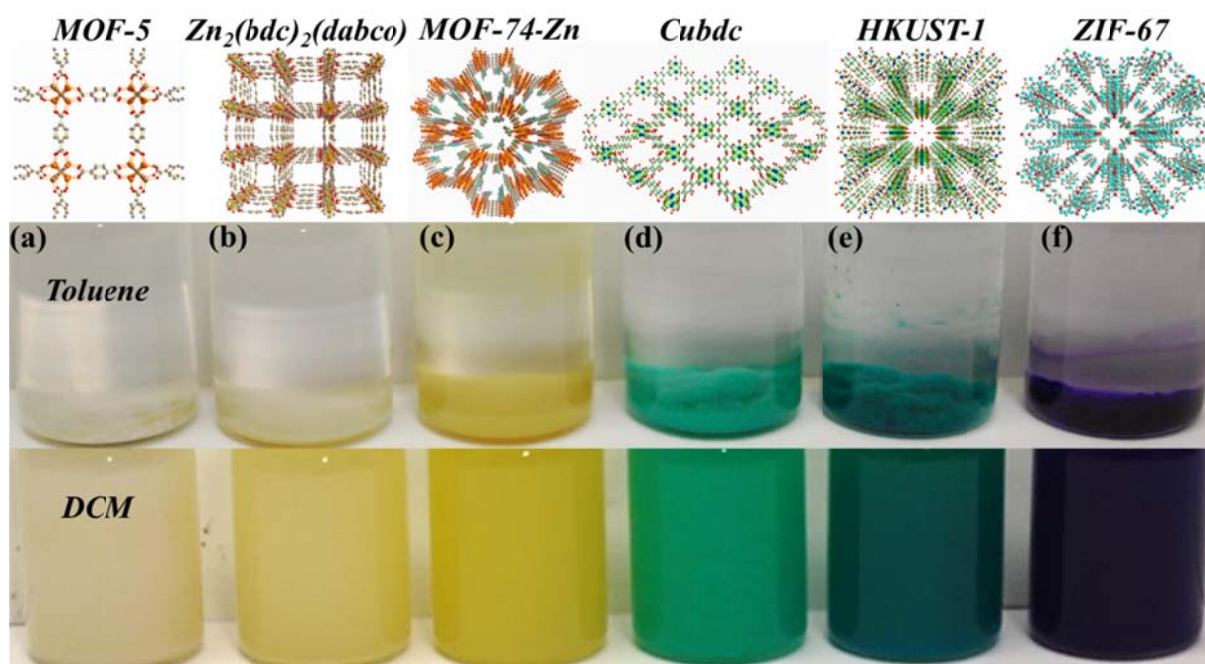
Figure 7.6 Adjustable dispersibility of various MOF@*P*-pollen composites: (a) MOF-5; (b) Zn$_2$(bdc)$_2$(dabco); (c) MOF-74-Zn; (d) Cu(bdc); (e) HKUST-1; (f) ZIF-67 in toluene (above, non-dispersable) *vs*. DCM (below, well-dispersed).

7.2.5 Environment-Responsive Visible Light-Triggered Cu(I)-Catalyzed Alkyne-Azide Cycloaddition (CuAAC) via Cu$_2$(bdc)$_2$(dabco)@*P*-pollen

The MOF@*P*-pollen with high dispersibility in DCM was investigated for liquid-phase heterogeneous catalysis. In the present thesis, the copper(I) catalyzed azide–alkyne cycloaddition (CuAAC) photoclick reaction was chosen as the model reaction. As shown in the previous chapter the Cu$_2$(bdc)$_2$(dabco) is sensitive to external light, which leads to in-situ reduction to Cu (I) by visible light (referring to Chapter 6, Figure 6.3).[343] The initial catalytic test indicated that Cu$_2$(bdc)$_2$(dabco)@*P*-pollen was active under the external light irradiation (Figure 7.7b) and the time-dependent gas chromatography–mass (GC-MS) profiles revealed the gradual consumption of starting alkyne, 4-pentyn-1-ol, and the accumulation of triazole product (Figure 7.7c). The chemical structure

of triazole product was also confirmed by ^{1}H NMR comparing to the originally synthesized 3-azido-1-propanol (Figure 7.8).
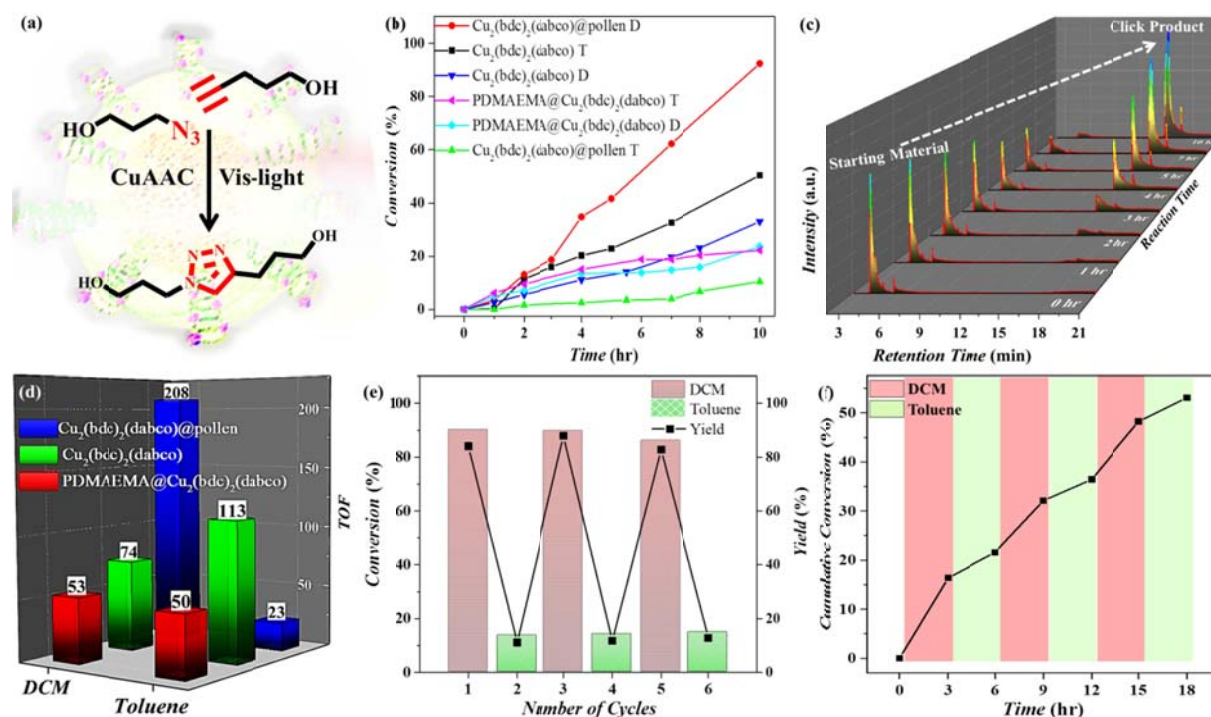
Figure 7.7 (a) Representative CuAAC coupling reaction in this study; (b) evolution of conversion with time for various Cu(II) MOF-mediated photoclick reaction in DCM (D) and toluene (T); (c) time-dependent GC-MS spectra of photoclick reaction catalyzed via $Cu_2(bdc)_2(dabco)@P$-pollen; (d) the calculated TON based on (b) in 10 hr.
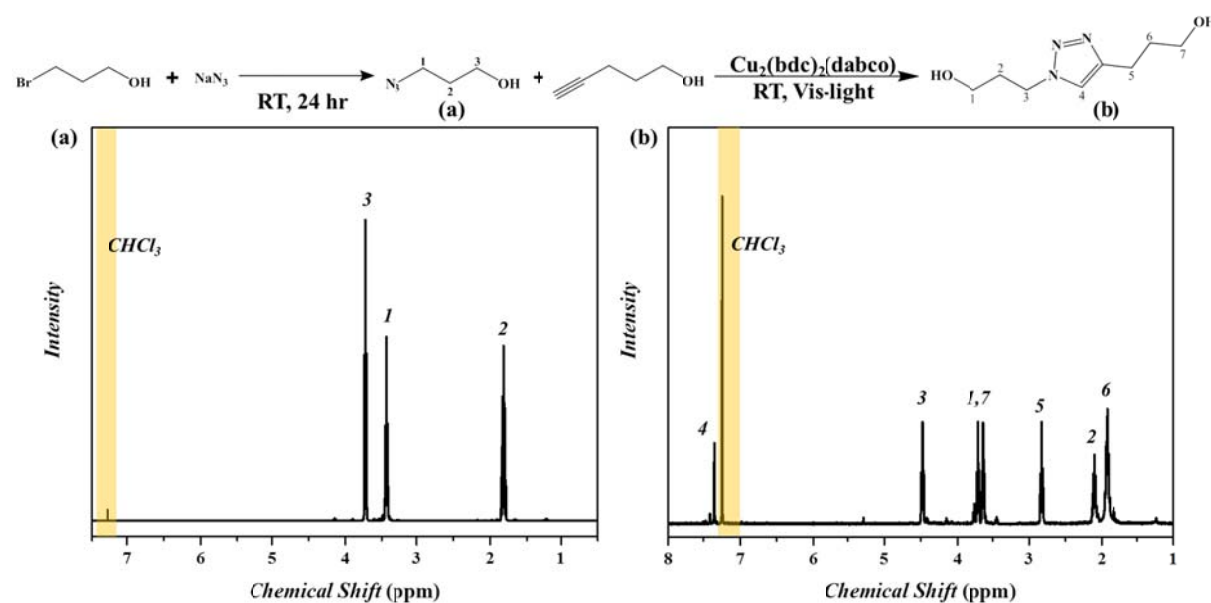
Figure7. 8 ^{1}H NMR of the as-synthesized (a) 3-azido-1-propanol and (b) triazole in chloroform-*d*.

The catalytic activity of the composite was evaluated via the calculation of turnover number (TON) and turnover frequency (TOF). Within these conditions, the best activity was achieved by $Cu_2(bdc)_2(dabco)@P$-pollen in DCM irradiated by visible light at RT, with ~93% conversion in 10 h, giving TON and TOF of 2078 and 208 h^{-1} respectively, which are, to the best of our knowledge, the highest values among the ever reported heterogeneous catalysts for CuAAC at RT without the addition of reducing agents.[173, 286-288] Such surprisingly high activity suggests that the present MOF composite is effective for the liquid-phase photocatalytic reaction.

It is reasonable that such unexpected high catalytic activity is ascribed to the well-dispersed MOF nanocrystals in DCM solvent, the non-blocked, highly-accessible catalytic sites distributed by PDMAEMA brushes in solution. To further demonstrate our hypothesis, control experiments by using $Cu_2(bdc)_2(dabco)$ catalyst was conducted under the same condition, with only ~ 33 % conversion in DCM after 10 hr, giving an activity (TOF: 74.3 hr^{-1}) lower than that of $Cu_2(bdc)_2(dabco)@P$-pollen (Figure 7.7d). The aggregated MOF crystals with less accessible Cu sites are responsible to the retarded catalytic capacity. Because the condensed-graft PDMAEMA brushes have a stronger ability to disperse the MOF crystals, catalytic reaction were also conducted by using $Cu_2(bdc)_2(dabco)@PDMAEMA$ as catalyst (without pollen pivot), regardless of the excellent dispersion in DCM (Figure 7.3h), the slowest reaction rate was detected with merely ~23% conversion after 10 hr (TOF: 53 hr^{-1}). Presumably, the highly-dissolved polymer chains which enhanced dispersion with the sacrifice of accessible catalytic sites due to the freely-jointed/folding conformation, lead to even lower activity than that of $Cu_2(bdc)_2(dabco)$. Since the pollen grain is inert to the catalytic reaction, the extremely high activity observed in $Cu_2(bdc)_2(dabco)@P$-pollen should be a result of the synergy effect from hierarchical hollow pollen structure with improved light-harvesting ability, favorable mass transfer, and most importantly, the enhanced accessibility of catalytic site by providing a pivot to grafted polymer tentacles.[329, 331]

Blank experiments were conducted as negative control to confirm the inert ability of applied pollen grain and PDMAEMA to reaction under the photoirradiation. Therefore, the $Cu_2(bdc)_2(dabco)$ is believed to be the only catalyst (Figure 7.9a). Since the PDMAEMA brush features LCST effect, the $Cu_2(bdc)_2(dabco)@P$-pollen-mediated CuAAC was also conducted at 65 ºC, a temperature higher than the critical point (Figure 7.9b).[333] Instead of thermal active phenomenon presented by blank condition and $Cu_2(bdc)_2(dabco)$ nanocrystals (TOF: 802 hr^{-1}), the $Cu_2(bdc)_2(dabco)@P$-pollen MOF served as a thermal switch which deactivated the reaction (TOF: 243 hr^{-1}) at temperature higher than the LCST due to seriously collapsed PDMAEMA blocking the catalytic sites temporarily from reagents. It is worth mentioning that the activity can be restored at RT. The thermal-responsive catalytic activity strongly points out that the synergy between 2D grafted PDMAEMA tentacles on pollen pivots and

associated MOFs provides a powerful platform to tune the activity MOF catalyst. The detailed catalytic performance is summarized in Table 7.2.
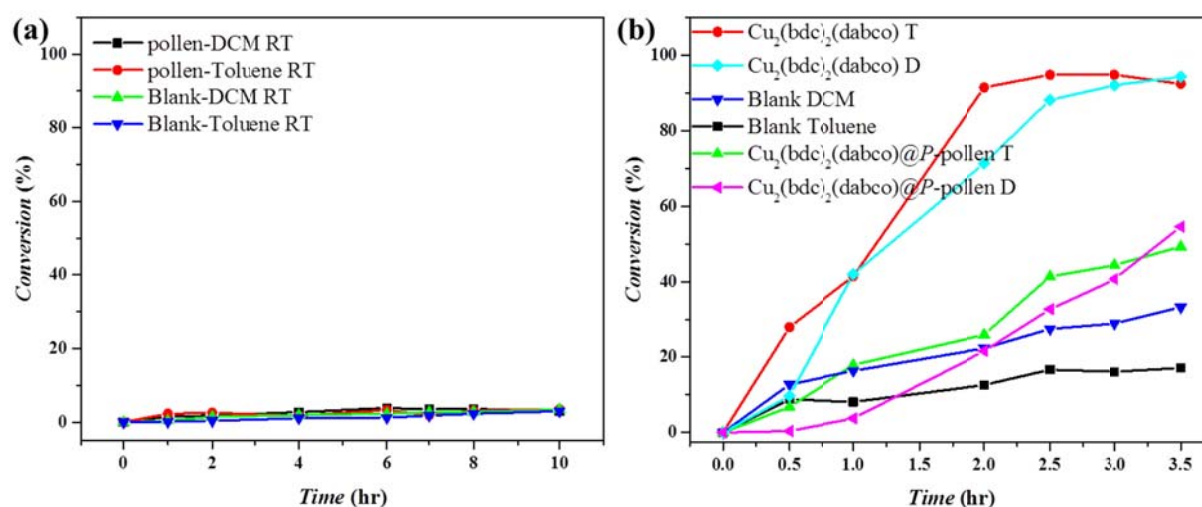
Figure 7.9 Evolution of conversion on time for photo-click reaction in DCM (D) or toluene (T) carried out by (a) pollen and without any catalyst as negative controls; (b) various Cu$_2$(bdc)$_2$(dabco) composites at 65 ºC

Table 7.2 Summary of catalytic performance at RT/65 ºC under visible light [a]

Temp.	Catalyst	Solvent	Conversion (%) [b]	TON [c]	TOF (hr^{-1}) [d]
RT	Cu$_2$(bdc)$_2$(dabco)	Toluene	50.4	1133.3	113.3
		DCM	33.1	742.7	74.3
	Cu$_2$(bdc)$_2$(dabco) @*P*-pollen	Toluene	10.4	235.6	23.6
		DCM	92.5	2077.8	207.8
	PDMAEMA @Cu$_2$(bdc)$_2$(dabco)	Toluene	22.3	499.6	50.0
		DCM	23.7	532.9	53.3
65 ºC	Cu$_2$(bdc)$_2$(dabco)	Toluene	91.4	2055.7	1027.9
		DCM	71.4	1604.3	802.1
	Cu$_2$(bdc)$_2$(dabco) @*P*-pollen	Toluene	25.9	583.9	291.9
		DCM	21.6	486.1	243.1

[a] The reaction was carried out at ambient temperature under visible light using Cu amount of 0.446 mg in each type of catalyst. [b] The conversion after 10 hours. [c] TON = turn over number , which was calculated based on the product amount after 10 hour (wt %) and Cu amount in the mixture (wt %). [d] TOF = turn over frequency, which was calculated based on the TON after 10 hours.
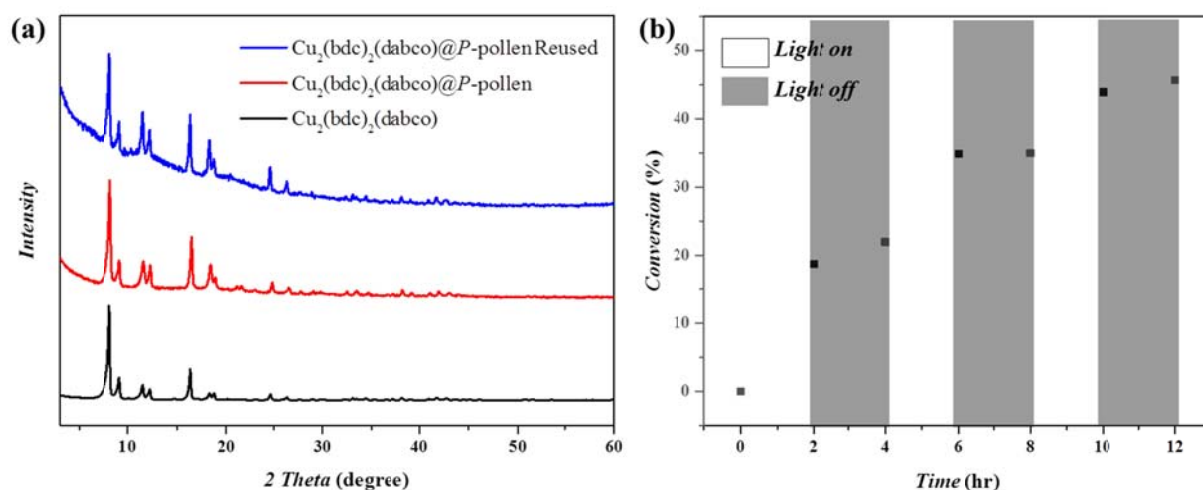
Figure 7.10 (a) PXRD profile of $Cu_2(bdc)_2(dabco)$@pollen after catalyzing click reaction in on/off control for 3 times. (b) Demonstration of temporal control through interlude light exposure: with consecutive light (white area) and dark treatment (shaded area).

7.2.6 Reusability of MOF@*P*-pollen Composites

Considering the heterogeneous and environment-responsive dispersiblity of $Cu_2(bdc)_2(dabco)$@*P*-pollen, the switchable catalysis system was conducted in which the catalysis is switched "off" once occurred in toluene with only ~10% conversion (TOF: 23 hr^{-1}), and is switched "on" when the system was isolated from toluene and then immerged in DCM (~ 88% conversion, TOF: 208) (Figure 7.7e). Such process can be repeated at least three times without noticeable change in activity. The ability to switch catalysis "on" and "off" should stem from the alternative exposure and burying of MOF catalytic sites by reversible extension-recoil of immobilized polymer brushes. The catalytic activity can even be online temporally controlled within the reactions. When the catalyst started in DCM solution, 19% product formation was observed in the first 3 h, while adding toluene (2 equivalent, equiv) generated the deactivated catalyst, resulting in retarded reaction in the next 3 h. The activity of catalyst was regained by adding another 2 equiv of DCM, and it was suppressed again with toluene (Figure 7.7f). The preserved MOF structure within the catalytic reaction was probed by PXRD, showing the characteristic peak in the $Cu_2(bdc)_2(dabco)$@*P*-pollen after 3-time use (Figure 7.10a). Possible leakage of Cu ions from the MOF template was investigated by ICP-OES. Comparing to initial bulk solution (0.45 mg/g), the Cu contamination in click product was significantly reduced while catalysing by $Cu_2(bdc)_2(dabco)$@*P*-pollen, resulting in Cu concentration 0.012 mg/g even lower than Cu(II) MOF particles (0.017 mg/g) and PDMAEMA@Cu(II) MOF (0.016 mg/g) (Table 7.3). The ICP together with the PXRD results both pointed out the robustness of as-prepared composites during the photoreactions.

Table 7.3 Residual Cu concentration (mg/g) in the click products synthesized via different catalytic composites. [a]

	Initial Bulk (mg/g) [b]	Outcome Product (mg/g) [c]
$Cu_2(bdc)_2(dabco)$	0.45	0.017 (16.9 ppm)
$Cu_2(bdc)_2(dabco)@P$-pollen	0.45	0.012 (10.5 ppm)
$PDMAEMA@Cu_2(bdc)_2(dabco)$	0.45	0.016 (15.8 ppm)

[a] Determined via ICP-OES. [b] The theoretical Cu amount in the initial bulk solution. The initial bulk contains the same amount of Cu ions contributed by different catalytic composites. [c] The as-synthesized click product was dissolved in methanol, and the suspension was isolated via centrifugation to remove the catalytic composites. After drying by vacuum, the product was analyzed by ICP-OES.

The spatial-control reactivity is a characteristic feature of photoreaction; that is, the reaction is on/off controlled using intermittent light irradiation and dark treatment. The $Cu_2(bdc)_2(dabco)@P$-pollen-mediated photoclick reaction proceeded much faster under light irradiation, and in contrast, very limited activity was detected during the "dark" periods, which could be explained by Cu(I) remaining in the system (Figure 7.10b). As a result, the photo responsive-property of the $Cu_2(bdc)_2(dabco)@P$-pollen was confirmed by the temporal-controlled CuAAC.

7.2.7 Visible Light-Triggered Dye Degradation via $Cu_2(bdc)_2(dabco)@P$-pollen

The present catalyst can be extended to other photocatalysis reactions with switchable catalytic activity. The photodegradation of Rhodamine B (RhB) was employed as another model reaction. The reaction process can be readily monitored by UV-vis spectra, recording the change of characteristic absorbance at 554 nm (assigned to RhB). As shown in Figure 7.11a, the catalyst in DCM achieved quantitative degradation in 165 min, while the catalysis was switched "off" in toluene, giving only ~20% degradation in the same period (Figure 7.11b). The pseudo-first-order rate constant (k) estimated from time-dependent UV-vis spectra revealed that the catalytic activity was modulated by more than two orders of magnitude on dynamic controlled aggregation/dispersion of MOF nanocrystals ($k_{DCM} = 1.26$ hr^{-1}; $k_{toluene} = 0.09$ hr^{-1}).
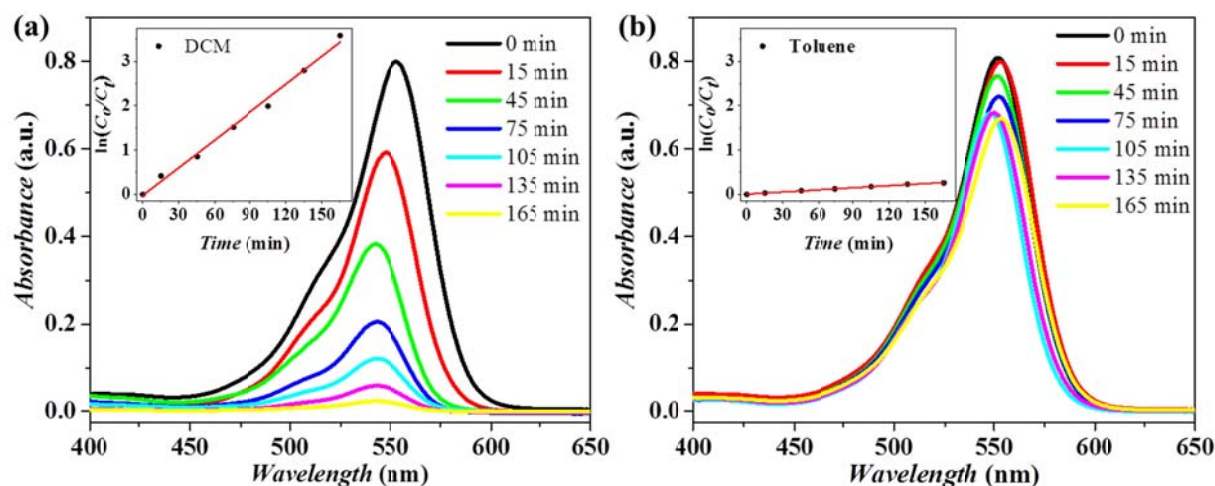
Figure 7.11 UV-vis spectra showing fast decomposition of Rhodamine-B by $Cu_2(bdc)_2(dabco)@P$-pollen in (a) DCM; in contrast, the slow degradation with retarded reactivity in (b) toluene, at RT illuminated under visible light. The inset indicates the linear time-dependent semilogarithmic plots during the whole reaction.

7.3 Conclusion

In summary, an alternative facile and win-win strategy to improve the dispersibility of MOF crystals without debilitating their catalytic potential is presented. The success of current strategy relies on the introduction of hollow pollen pivots with surface immobilized environment-responsive, highly-grafted PDMAEMA brushes. The as-designed modified *P*-pollen equipped with "smart" tentacle can effectively trap and stabilize a variety of nanoMOFs via the innate amine functionality, leading to well-dispersed MOF@*P*-pollen in solution with enhanced dispersibility and liquid-phase photocatalytic performance. Owing to the environment-responsive behavior of tentacle, the associated MOF nanocrystals can be exposed (catalytic active) or buried (catalytic inactive) reversibly to give a switchable on-off catalytic performance. Considering the highly compatible preparation procedure, the current work may open up new perspective in developing "smart" MOF heterogeneous catalysts in future.

8. Conclusion and Outlook

   To summarize, the synergic effect of a combination of controlled/living polymerization technique and crystalline MOFs has been comprehensibly presented in different direction. As a host for monomers, the nanochannel from inert MOFs or even better from initiator-functionalized MOFs can serve as an universal platform to synthesize high MW polymers with improved property. More than an accommodation, surpassing the conventional homogeneous catalyst, the heterogeneous MOF catalyst is found to tolerate strongly coordinating monomers and thus be able to catalyze polymerization of monomers with further expanded range. Not only using MOFs to advance polymer synthesis, MOF research can benefit from the concept of polyMOF as well. The highly crystalline and hardly dispersible drawbacks which have seriously restricted the applicability and catalytic property can be thus diminished via association with grafted polymer brushes.

As illustrated in Chapter 4, controlled radical polymerization was achieved inside MOFs through the combination of Znbdc/ZnBrbdc and ARGET/SI-ARGET (Scheme 8.1). The attempt of high MW polymers was realized eventually under MOF's microporous compartmentalized space, revealing the host – guest effect from MOF pore structure and monomer size. Generally, well-defined polymers with MW = 53,800 - 72,900 and Đ = 1.1 - 1.3 were obtained in Znbdc, although the control of molecular weight was limited. Compared to the bulk polymers with scarcely isotactic triad (1-2%), the accommodated polymers were characterized with higher isotactic ratio (8%). The controllability over polymers was further advanced by using initiator functionalized MOFs which enabled the synthesis of polymers with higher MW (up to 392,000), low Đ (1.2 - 1.4) and designable MW (i.e. via varying the blending ratio between original ligand, bdc, and initiator-functionalized one, Brbdc). Additionally, enhanced microstructure could be achieved with isotactic triad increasing up to 11%. Moreover, high end group fidelity was confirmed by chain extension to form block copolymer with IBMA. The results demonstrate that the combination of MOFs and controlled polymerization is a facile, robust and universal methodology to prepare high molecular weight

Scheme 8.1 Functionalized MOFs as robust confined environment for controlled polymerization to synthesize well-defined high molecular weight polymers with facile.

polymers with low *Đ*, predetermined MW and high end-group fidelity with refined microstructure.

In Chapter 5, the Cu(II)-based MOF, $Cu_2(bdc)_2(dabco)$, has been demonstrated as a heterogeneous, universal catalyst for ARGET ATRP with expanded monomer range (Scheme 8.2). In the case of standard monomers, a linear increase of molecular weight with conversion and successful chain extension meet the criterion of RDRP, give PS with *Đ* = 1.3 (MW = 16,800) and PBzMA with *Đ* = 1.4 (MW = 15,500). The challenging monomers, 4VP and isoprene, could be polymerized in a controlled way as well, e.g. synthesis of P4VP with *Đ* = 1.5 (MW = 9,200) and PI with *Đ* = 1.4 (MW = 23,000). Due to the highly crystalline structure with catalytic Cu ions intrinsically stabilized with linkers, the MOF can be regarded as a catalytic complex triggering the polymerization independently and thus avoiding side reactions resulting from reagents and monomers. Furthermore, due to the easy separation, the Cu(II) MOF was demonstrated as a heterogeneous catalytic complex able to catalyse polymerization for arbitrary times, simplify the reaction, and solve the cumbersome catalyst contamination/removal issue.
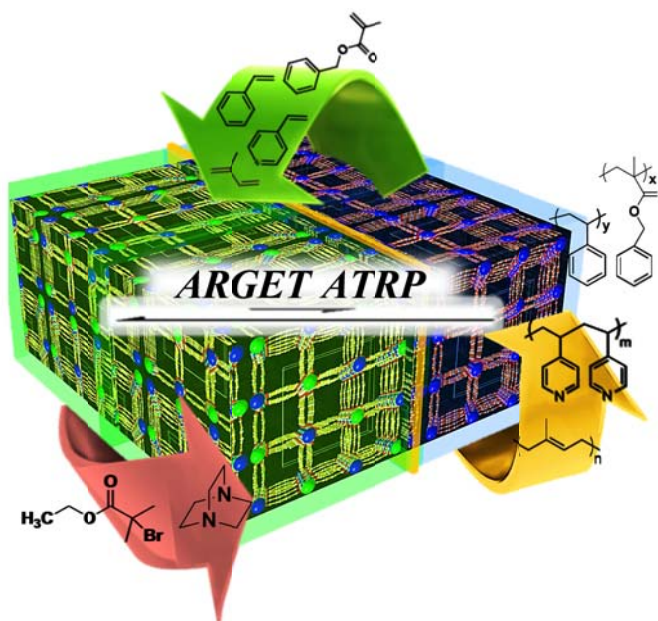
Scheme 8.2 Cu(II) MOF as a robust and recyclable heterogeneous catalyst for ARGET ATRP.

As presented in Chapter 6, the controlled photopolymerization under visible light was achieved by the same $Cu_2(bdc)_2(dabco)$ MOF catalytic complex requiring no external photoinitiators and reducing agents (Scheme 8.3). Through adapting different N-containing monomers or additives, for example 4VP, 2VP, TEA, and 4-ethylpyridine, a synergistic effect on photoabsorption property and the MOF-mediated polymerization was observed. The phenomenon was ascribed to the photo-reducing property of incorporated

Scheme 8.3 Synergic effect between associated molecules and Cu(II) MOF to adjust the photo-harvesting property and to conducted PRDRP under visible light.

compounds and the improved photoabsorption properties of the MOF due to the formation of guest-host complexes. The hypothesis was strongly supported by the improved photoabsorption properties once stronger coordinating monomers were used following the trend of 4VP > 2VP > DMAMEA > MMA. Furthermore, the same tendency was followed by photopolymerization rate as well. A well reversible Cu(II)/Cu(I) redox behavior, with $E^{\ominus}$ = -0.084 V vs. SCE determined by chronoamperometry, indicated excellent photocatalytic activity of Cu$_2$(bdc)$_2$(dabco) in ATRP. Controlled photopolymerization of highly nucleophilic monomers was achieved with the Cu(II) MOF, synthesizing polymers with predictable molecular weight and low Đ (1.2 - 1.4). The reusability and temporal controlled property were both exhibited by the Cu(II) MOF-mediated visible light photopolymerization.
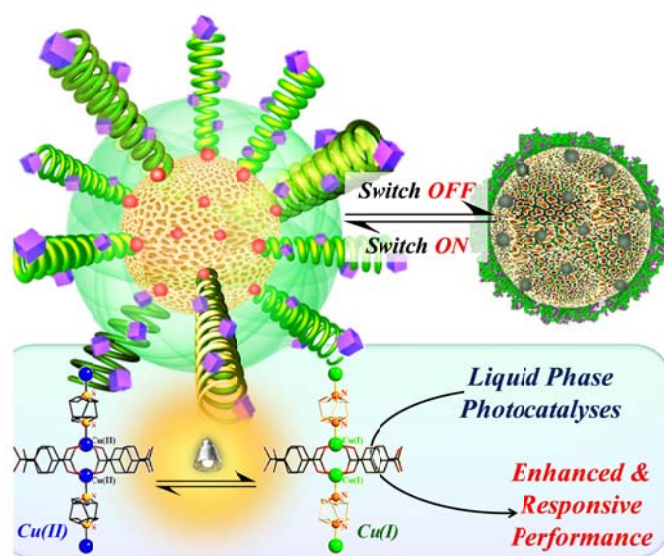
Scheme 8.4. Adjustable dispersibility of MOF nanoparticles with enhanced photocatalytic performance and environment-responsive property.

After utilization of MOF as polymerization catalysts, polymers were applied to refine the catalytic performance reversely. Illustrated in Chapter 7, to conquer the highly agglomerated and less dispersible nature of MOF solids, an universal strategy of forming MOF/polymer composites by surface functionalization on MOF particles with dispersible polymers was presented. However, avoiding to incorporate freely-joined polymers directly from MOF surface that conversely retard the reactivity, a two-step incorporation was proposed. That is, instead of directly binding on MOF surface, the polymer brushes were first grafted from a hollow and light pivot with proper grafting density to serve as a tentacle targeting on nanoMOFs. Then, MOF nanoparticles were incorporated and stabilized via the association between polymer functionalities and MOF components. In the present thesis, PDMAEMA-grafted pollen (*P*-pollen) was introduced and employed to capture various MOFs. Due to the high grafting density and environment-responsive property of PDMAEMA brushes, the associated MOF nanocrystals can be exposed (catalytic active) or buried (catalytic inactive) reversibly to give a switchable on-off catalytic performance (Scheme 8.4). Furthermore, the strengthened catalytic performance was identified in photo-click reaction (CuAAC), giving state-of-the-art catalytic property with the 10 hour-average turnover number (TON) as high as 2078. Based on our knowledge,

it is the highest value among reported heterogeneous catalytic composites for CuAAC at RT without extra reducing agents. This surprisingly high reactivity results from the well-distributed heterogeneous MOF particles and the non-blocked, widely-accessible catalytic sites distributed by PDMAEMA brushes in solution. Besides, the synergy effect resulting from hierarchical hollow structure of pollen grains which improved the light-harvesting ability, enforced the mass transfer, and enhanced the approachability of reagents towards catalytic centers realizes the currently best catalytic performance with highest TOF. The enhanced reactivity and environment-responsive dispersibility can be duplicated in dye degradation test as well. Considering the highly versatile preparation procedure, the current approach may open up new perspectives in developing "smart" MOF heterogeneous catalysts in the future.

As a result, MOFs are new-emerging porous materials going to revolutionize fundamental polymer science. With the utilization of MOFs, the controlled polymerization can be carried out directly inside in confined nanochannels, synthesizing accommodated polymers with high MW but remaining low Đ and high living end functionality as well as refined microstructure. As shown in the present thesis, the advantageous properties of MOF crystals highlight the resemblance to biomacromolecules equipping with the capacity to precisely control polymers over architectures, compositions and functionalities. The observed (photo)catalytic property of Cu(II)-based MOF can further expand the applicability of conventional RDRP with wider monomer feasibility, improved reusability and adjustable polymerization speed. On the other hand, the MOF solids can be released from the historical limitation of easy agglomeration and poor dispersibilityle via association with polymer brushes. Instead of freely-jointed polymer chains, polymer brushes grafted from hollow pollen pivots are applied to avoid the adverse retardation on catalytic performance. Following this concept, the adjustable dispersibility of various MOFs including MOF-5, MOF-74, Cu(bdc), HKUST-1, ZIF 67 and $M_2(bdc)_2(dabco)$ (M = Cu or Zn) can be now achieved in liquid phase. Owing to the improved dispersibility and reorganized combination, the enhanced photocatalytic property in response to applied environment can be confirmed by visible light-triggered photoclick coupling reaction and photodegradation of organic dye.

The abovementioned progresses advocate the perfect complementary properties between low dimensional polymer products and highly crystalline MOF solids, highlighting the great potential of this combing concept for improvement in technological, academic and industrial applications. However, there are still unclear observations requiring more investigation to disclose detailed mechanisms and to be able to further expand the scale in the future. For example, $Cu_2(bdc)_2(dabco)$, as an advantageous heterogeneous catalyst for ARGET ATRP, to get more insight on molecule transformation will be very helpful to deduce the catalytic pathway and reveal the host-guest interaction on the molecular level. For instance, how the microstructure switches between the active Cu(I) and deactive Cu(II) state, and how association happens between bdc linkers, abducted

monomers and initiating/propagating molecules. With more knowledge of structural transformation, the tailored catalysts can be specifically designed and employed to give materials with promising performance and unanticipated properties. Therefore, the initiator-functionalized $Cu_2(bdc)_2(dabco)$ can be fabricated and utilized as a host for compartmentalized polymerization such as in the case of $Zn_2(bdc)_2(dabco)$. Furthermore, due to the distinct reversible photocatalytic property of $Cu_2(bdc)_2(dabco)$ in ARGET ATRP polymerization, a all-in-one polymerization system can be devised to conduct controlled polymerization without additional catalysts ligands and reducing agents, resulting in an ultimately controlled polymerization.

Overall, through introducing MOFs into ARGET ATRP the thesis may pave the way towards ultimately controlled polymerization with refined properties in MW control, end group fidelity, stereoregularity and expanded monomer components. Moreover, the long-term dispersibility issue of MOF crystals can be efficiently eased via the reorganized association towards polymer brushes to give environment-responsive controllability with promising catalytic performance.

Appendices

Appendix I. List of Abbreviations

^{13}C-NMR	carbon nuclear magnetic resonance
^{1}H-NMR	proton nuclear magnetic resonance
2VP	2-vinylpyridine
4VP	4-vinylpyridine
AIBN	2,2'-azobis(2-methylpropionitrile)
ATRP	atom transfer radical polymerization
ATR-FTIR	attenuated total reflection fourier transform infrared
BIBB	α-bromoisobutyryl bromide
bdc	terephthalic acid
BzMA	benzyl methacrylate
CuAAC	copper (I) catalyzed azide-alkyne cycloaddition
CUS	coordinatively unsaturated sites
dabco	diazabicyclo[2.2.2]octane
DP	degree of polymerization
DCM	dichloromethane
DLS	dynamic light scattering
DMAEMA	*N,N*-dimethylaminoethyl methacrylate
DMF	*N,N*-dimethylformamide
DNA	desoxyribonucleic acid
EBIB	ethyl α-bromoisobutyrate
EDTA	ethylenediaminetetraacetic acid disodium salt
equiv	equivalents
f	initiator efficiency
GC-MS	gas chromatography-mass spectrometry
ICP-OES	inductively coupled plasma-optical emission apectrometry
IBA	isobornyl acrylate
IBMA	isobornyl methacrylate
K_{ATRP}	rate coefficient of ATRP polymerization
k_{act}	rate coefficient of activation
k_{deact}	rate coefficient of deactivation
k_{p}	rate coefficient of propagation
k_{t}	rate coefficient of termination
λ	wavelength
LCST	lower critical solution temperature
LED	light-emitting diode
MeOH	methanol
MMA	methyl methacrylate
M	mol/L
*M*n	number-average molecular weight
*M*w	weight-average molar mass
MPTS	3-mercaptopropyl)trimethoxysilane
MOF	metal organic framework
N$_3$	azide termination
PDI (Đ)	polydispersity index
pH	-log c(H^{+})
PMDETA	*N,N,N',N'',N''*-pentamethyldiethyltriamine
PS	polystyrene
PSD	pore size distribution

PSM	post-synthetic modification
PXRD	powder X-ray diffraction
RDRP	reversible deactivation radical polymerization
RT	room temperature
SCE	saturated calomel electrode
SBU	specific secondary building unit
SEC	size exclusion chromatography
SEM	scanning electron microscopy
SSA	specific surface area
TEA	triethylamine
TEM	transmission electron microscopy
TGA	thermo gravimetric analysis
THF	tetrahydrofuran
TPV	total pore volume
UV	ultra-violet
UV/Vis	ultra-violet/visible
vol %	volume %
wt %	weight %

Appendices

Appendix II. Applied Materials

Materials. All reagents, catalyst and solvents were used as received unless otherwise noted. Methyl methacrylate (MMA, Alfa Aesar, 99%), ethyl methacrylate (EMA, Alfa Aesar, 98%) benzyl methacrylate (BzMA, Alfa Aesar, 98%) isobornyl methacrylate (IBMA, Acros, 85-90%), styrene (St, Acros, 99%), 4-vinylpyridine (4VP, Sigma Aldrich, ≥95 %), 2-vinylpyridine (2VP, Alfa Aesar, 97%), 2-(dimethylamino)ethyl methacrylate (DMAEMA, Sigma Aldrich, 98%), poly(ethylene glycol) methyl ether methacrylate (OEGMA, Sigma Aldrich, average M_n 300), isobornyl acrylate (IBA, Alfa Aesar, 85%) and isoprene (Sigma Aldrich, >99 %) were filtered through a basic aluminum oxide (Brockman type I, Acros, 50-200 μm, 60 A) column to remove inhibitor. 2,2'-Azobis (isobutyronitrile) (AIBN, Sigma-Aldrich, 98 %) was recrystallized from methanol. Ethyl α-bromoisobutyrate (EBIB, Sigma Aldrich, 98%), 1,1,4,7,7-pentamethyldiethylentriamine (PMDETA, Acros, >98%), $CuBr_2$ (Alfa Aesar, 99%), bromoacetonitrile (Sigma Aldrich, 97%), 4-ethylpyridine (Sigma Aldrich, 98%), α-bromoisobutyryl bromide (Sigma Aldrich, 98%), triethylamine (TEA, Roth, ≥99.5%), 2-Aminoterephthalic acid (NH_2bdc, Sigma Aldrich, 99%), 4-diazabicyclo[2.2.2]octane (dabco, Alfa Aesar, 97%), (3-Mercaptopropyl)trimethoxysilane (MPTS, Sigma-Aldrich, 95%), $Cu(NO_3)_2 \cdot 3H_2O$ (Sigma-Aldrich, ≥ 99.9%), $Zn(NO_3)_2 \cdot 6H_2O$ (Sigma Aldrich, ≥98%), $Zn(OAc)_2 \cdot 2H_2O$ (Sigma-Aldrich, 99.9%), $Co(NO_3)_2 \cdot 6H_2O$ (Sigma-Aldrich, ≥ 99.9%), 2,5-dihydroxyterephtalic acid (H_4dobdc, Sigma-Aldrich, 98%), 1,2,4-benzenetricarboxylic acid (H_3btc, Sigma-Aldrich, ≥ 99%), 2-methylimidazole (Hmim, Sigma-Aldrich, 99%), sodium azide (Roth, ≥ 98%), 3-Bromo-1-propanol (Sigma Aldrich, 97%), 4-pentyn-1-ol (Alfa Aesar, 97%), 1,4-terephthalic acid (H_2bdc, Alfa Aesar, >98%), copper(II) acetate monohydrate (Roth, ≥ 98%), $NaNO_3$ (Acros, ACS grade), ethylenediaminetetraacetic acid disodium salt (EDTA-Na_2, Sigma Aldrich, > 99%), dimethylformamide (DMF, VWR, ACS grade), methanol (MeOH, Fisher Scientific, for analysis), tetrahydrofuran (THF, VWR, HPLC grade), toluene (Fisher, HPLC grade), 1,4-dioxane (Acros, 99.5%, extra dry over molecular sieve), dichloromethane (DCM, Sigma-Aldrich, HPLC grade), ethanol (J.T.Baker, HPLC grade), diethyl ether (Sigma-Aldrich, ACS grade), acetone (J.T.Baker, HPLC grade) and acetic acid (Merck, 100% anhydrous for analysis) were used as received. Rape pollen grains were purchased from Yier Biofarm (Shandong, China), washed intensively with KOH, acetic acid and methanol to remove the intine layer; the washed pollen was dried under RT, and stored at 4 ºC. As light source, a 50 W LED chip (Bridgelux BXRA-50C5300; λ > 410nm) connected to a home-made circuit and cooling system is utilized. The emission spectrum is shown in Figure S9.

Appendix III. Applied Methods

Nuclear Magnetic Resonance (NMR) Spectroscopy. NMR spectroscopy is a prevalent technique to determine the chemical structure of a molecule, revealing the number and the chemical environment of hydrogen (^{1}H-NMR) or carbon (^{13}C-NMR) atoms within a molecule. The technique is fundamentally based on the Zeeman Effect. Namely, via the application of an external magnetic field, the spins of atom nuclei split into distinct energy levels, for example, two energy levels exist in ^{1}H and ^{13}C atoms. In the solution state NMR, once the well-dissolved molecules are exposed to a strong magnetic field (around 2-10 Tesla, T), spins of the nuclei realign and process along the magnetic field direction. Subsequently, a short radio pulse with frequency characteristic to the nucleus is applied to irradiate the molecules to unbalance the equilibrium between two energy levels. After absorption of energy, some nuclei are promoted to a higher energetic level, and retreat back to the equilibrium state while the radiation cycle is terminated. The energy released during the cycle can be detected and recorded by the radiofrequency detector. The electronic microenvironment of the nucleus, including electron number, density and distribution, differentiates the strength of magnetic field and the resonating frequency of corresponding nucleus. The variation in the resonance energy serves as a molecular fingerprint can be observed by series chemical shift in comparison to a reference compound.

In the present thesis, the ^{1}H-NMR and ^{13}C-NMR spectra were recorded at ambient temperature at 400 MHz for ^{1}H and 100 MHz for ^{13}C with a Bruker Ascend400 at a concentration of 1 wt % for proton, and 10 wt % for carbon analysis.

Nitrogen Physisorption. Nitrogen physisorption is a widely employed and powerful tool to analyze the pore feature of a porous material. The measurement reveals information coming from three basic parts: the specific surface area (SSA), the total pore volume (TPV), and the pore size distribution (PSD) of a material. Generally, the adsorbed volume of the adsorbate (N_2) on the adsorbent (in the present thesis MOFs complexes) is measured according to the relative pressure (p/p_0) of the adsorptive. Measurements are usually conducted at 77 K under atmosphere pressure to ensure the equilibrium of N_2 gas, and only weak interactions like Van der Waals interaction occur between the adsorbate and the adsorbent, rendering the physisorption behavior and forming multilayer adsorption. During the analysis, nitrogen is gradually and slowly dosed into a measured tube containing the sample, and the adsorbed volume is recorded against to the relative pressure and stop while (p/p_0) reaching 1.0. Subsequently, the desorption isotherm is recorded by lowering the pressure again, presenting the corresponding hysteresis. The recorded points represent the characteristic isotherm of adsorption, and the shape of adsorption-desorption isotherm shows the specific interactions between adsorbates and adsorbent as well as the pore morphology (size and shape). The porous structures are categorized by the IUPAC into three groups based on the internal diameter (*d*): micropores (d < 2 nm), mesopores (2

nm ≤ d < 50 nm), and macropores (d ≥ 50 nm)[344]with up to eight kinds of isotherms been identified (Figure S1).[345]
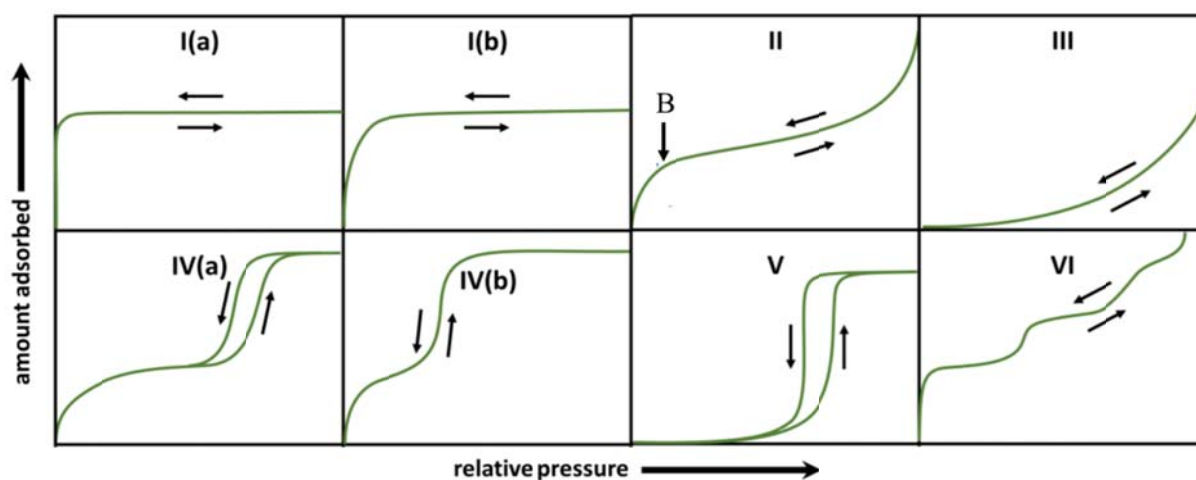
Figure S1. Currently eight kinds of absorption-desorption isotherms referring to IUPAC. Figure reprinted with permission from De Gruyter (2015).[345]

A reversible type I isotherm is identified in microporous materials with very limited external surface, and the featuring sharp absorption at low pressure is ascribed to the enhanced absorption in confined micropores but with low capacity. Type I(a) indicates the majority of pore size with diameter (*d*) less than 1 nm, but larger micropores or small mesopores with d ≤ 2.5 nm can be detected in type I(b). A reversible type II isotherm with unrestricted monolayer-multilayer adsorption is referred to a non-porous or only microporous bulk. An obvious junction (point B) means the saturated absorption on the monolayer. A reversible type III isotherm represents the non-porous or macroporous property of materials with limited interactions between adsorbate and adsorbent, resulting clustered adsorbate without B point. A reversible type IV isotherm is representative for mesoporous materials, with adsorbent interacting with condensed adsorbate. The pore condensation happens at higher pressure, by which gas molecules condense inside a pore at pressures lower than the bulk liquid's saturation pressure (p_0). Once the pore diameter is larger than 4 nm, a hysteresis can be identified as well due to the occurrence of capillary condensation, resulting in a type IV(a) isotherm or a type IV(b) with comparatively small pore size. Type V and type VI isotherms are relatively rare, indicating a porous material with weak adsorbent-adsorbate interactions or a layer-by-layer adsorption on a non-porous material.

Furthermore, based on the shape and the pressure range of the hysteresis, the structure and inter-connectivity of mesopores can be interpreted, and six types of hysteresis loops have been defined by IUPAC (Figure S2).[345]
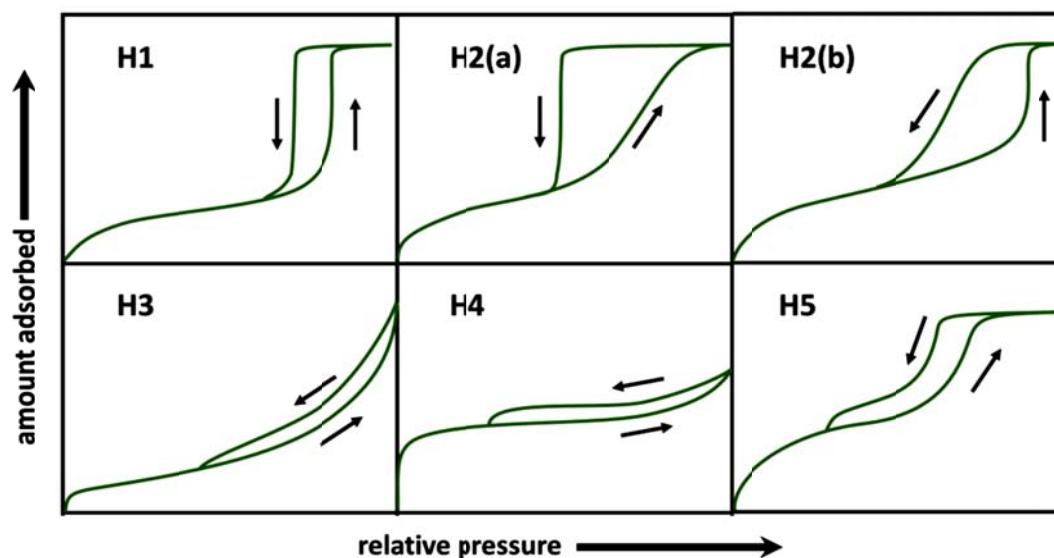
Figure S2 Classification of physisorption hysteresis loops according to IUPAC. Figure reprinted with permission from De Gruyter (2015).[345]

A H1 hysteresis loop is referred to an uniform and well-defined mesoporous structure, characterized with a highly parallel adsorption-desorption isotherm. By contrast, H2 loops are suggested to complicated or interconnected pore networks combining multiple pore sizes and/or pore necks. Typically, a H2(a) loop implies the presence of varied sized mesopores with uniform pore necks, and a H2(b) type vice versa. Compared to H2 loops, a lower-limited desorption can be seen in the H3 hysteresis, pointing out an existence of cavitation in the bulk materials. In a H4 loop, the adsorption behavior is between type I and type II isotherm, meaning the co-existence multiple dimension pores. The H5 type is less common, but exhibits with the co-existence of open- and blocked mesopores. Frankly speaking, the distinct isotherm and hysteresis types mentioned above are classified based on an ideal assumption. However, for a "real" material, an intermediate or combined phenomenon is frequently observed.

More than pore shapes, the SSA and TPV can be calculated by the recorded points within a process via model mappings. Via estimation of adsorbed layers, the covered area and namely the surface area of the material can be deduced. The BET-theory founded by Brunauer, Emmett and Teller is one of the most prevalent models to analyze and interpret the physisorption results.

In the present thesis, the nitrogen adsorption and desorption experiments were performed using Quantachrome Quadrasorb at the boiling temperature of liquid nitrogen, and the results were analyzed on the basis of the Brunauer, Emmett and Teller (BET) method. All samples were degassed at 110 °C for 20 hours before measurements and analyzed with QuadraWin software (version 5.05).

Size Exclusion Chromatography (SEC). SEC is applied to evaluate the molecular weight and the polydispersity (*Đ*) of a polydispersed polymer in a relative concept. Basically, a polymer solution is fractionated via passing through a column with stationary phase comprised of highly interpenetrated polystyrene resin and pore sizes ranging from 10 to 1000 Å. Depending on the hydrodynamic volume and specific molecular interaction within the pores, the retention time of polymer chains inside the column varies. Usually, the elution of polymers with larger hydrodynamic volumes is earlier than the smaller ones due to the less preference towards small pores. The elution of the polymer can be detected with a refractive index (RI) or an UV detector against to elution volume. According to the obtained eluograms, the molecular weight of investigated polymers can be determined in comparison to a calibration curve of a standard polymer with low *Đ* and narrow molecular weight distribution by using the following equation:

$$V_t = V_g + V_i + V_0 \qquad\qquad \text{Equation S1}$$

where V_t is the total elution volume, V_g is the volume of stationary phase, V_i is the volume held in the colum pores and V_0 is the free volume outside of the pores.

In the present thesis, SEC was conducted in either THF or NMP as mobile solvent. While THF was applied, SEC was measured in THF with toluene as internal standard at 25 °C using a column system by PSS SDV 1000/10000/1000000 column (8 x 300 mm, 5 μm particle size) with a PSS SDV pre-column (8 x 50 mm), a SECcurity RI detector and a SECcurity UV/VIS detector and a calibration with PMMA or PS standards from PSS. On the other hand, SEC was conducted in NMP (Fluka, GC grade) with 0.05 mol L^{-1} LiBr and BSME as internal standard at 70 °C using a column system by PSS GRAM 100/1000 column (8 x 300 mm, 7 μm particle size) with a PSS GRAM precolumn (8 x 50 mm) and a Shodex RI-71 detector and a PMMA or PS calibration with standards from PSS. The polydispersity is defined as $Đ = M_w/M_n$. The theoretical number averaged molecular mass $M_{n,\text{theo}}$ was calculated as $MM_{initiator} + MM_{monomer} \times ([\text{monomer}]_0/[\text{initiator}]_0) \times \text{conversion}$.

Dynamic light scattering (DLS). Dynamic light scattering (DLS) is a facile technique to detect hydrodynamic diameters of molecules in a given solution. Through DLS, the particle size distribution is estimated by tracing the random changes in light scattering intensity from a suspension or solution. DLS is most commonly used to analyze nanoparticles with size between submicrons to nanometers. In a suspension, small particles are continuously moving in a random and thermal-state way, the so-called Brownian motion. Through simulation, the random particle motion can be related to particle size, resulting in the Stokes-Einstein equation which connects the diffusion coefficient measured by dynamic light scattering to particle size:

$$D_h = \frac{k_B T}{3\pi\eta D_t}$$

where D_h is the hydrodynamic diameter (two times of radius), D_t is the translational diffusion coefficient (obtained from DLS), k_B is Boltzmann's constant (1.38×10^{-23} J/K), T is temperature and η is dynamic viscosity. To evaluate the hydrodynamic diameter in a reliable way, the temperature is one of the most critical parameter, since it appears directly in the equation and influences the viscosity as well. Referring to the equation, the outcome particle size is determined in the form of sphere with the calculated hydrodynamic diameter. Worth to mention, the hydrodynamic radius is not exactly the same as the radius of gyration. To converse hydrodynamic sizes to radii of gyration, the specific chain conformations shall be considered as well, such as chain stiffness, degree of branching and the comprised ration between random coil, hard sphere, globular and dendrimer.

In the present thesis, DLS measurements of the highly diluted aqueous dispersions were performed at 25°C using the Zetasizer Nano-ZS (Malvern Instruments, United Kingdom).

Scanning Electron Microscopy (SEM) and Energy-dispersive X-ray spectroscopy (EDX). SEM characterization is based on the analysis of different radiations resulted from the interaction between incident electron and material surface, in most of the cases, from secondary and backscattered electrons. Therefore, via probing the number and energy of the interacting electrons together with a proper detector, the morphology of a given sample can be visualized. Furthermore, combining the information resulting from secondary and backscattered electrons, a more detailed topology and intrinsic structure can be disclosed. That is, once interacting with the incident electrons, valence electrons of a detecting material undergo emission and produce secondary electrons. Due to the low energy and limited transmitting ability, only the secondary electrons generated approximately to the surface can be detected, exhibiting the surface morphology. By contrast, backscattered electrons with higher energy can transmit through the material and represent electrons scattered from the atoms, illuminating information from the solid insight. The number of backscattered electrons correlates directly to the atomic number (i.e. mass) of material-comprised atoms, resulting in a brighter image with heavier elements.

Component and qualitative information of the sample can be detected by EDX. When, the incident electrons excite electrons from an inner shell of atoms, the emission electrons generate specific radiation referring to individual elements, by which qualitative measurement and elemental mapping can be achieved to investigate the local distribution of elements in a material.

In the present thesis, the SEM images were performed on a FE-SEM (Field Emission SEM) LEO 1550 Gemini instrument using field emission source to liberate electrons. Samples for EDX were placed on

carbon coated aluminum holder and measured without any additional coating. For FE-SEM measurements, non-conductive samples were sputtered with Au/Pt in advance.

Fourier Transform Infrared Spectroscopy (FTIR). Fourier transform (FT) infrared (IR) spectroscopy is a facile and non-destructive technique to identify laser-excited molecular structures using the unique vibration and/or rotation as fingerprints. One basic requirement to receive rotations/oscillations FTIR signal is a variable dipole moment of a molecule while exposing to laser. Therefore, existence of specialized functionalities and comprised components in a material or in the associated microenvironment can be distinguished through FTIR. The IR spectrum is based on scanning of the illuminated laser energy with the percentage of beam transmitted through or absorbed by the material against the frequency-proportional wavenumber (cm^{-1}). In comparison to reference substance, the position and relative intensity of the signals provides insight into the molecular structure of materials in a complexed way.

FT-IR spectra were directly recorded on a FTS 6000 spectrometer equipped with an attenuated total reflection (ATR) cell (BioRad).

Gas Chromatography-Mass Spectrometry (GC-MS). Combining two powerful techniques, GC-MS is able to identify and quantify compounds in a comprehensive fashion. The only requirement for the technique is the material must be volatilizable, since once the sample is injected, volatilization is the first step conducted in the GC chamber. The sample is carried and passed through a stationary column in its gas form, and via different association affinity, the comprised compounds can be preliminarily separated. Upon compounds leaving the GC column, the conjugated MS is applied to fragment the molecule in a recognizable way by electron impact. The charged fragments are then detected, and by browsing through a database the obtained spectrum can be referred to an individual molecule. Due to the reproducibility of MS fragmentation patterns, the quantitative measurements are also feasible via GC-MS.

In the present thesis, all GC-MS analyses were performed under an Agilent Technologies 5975 gas chromatograph equipped with a MS detector and a capillary column (HP-5MS, 30 m, 0.25 mm, 0.25 micron). Besides, the installed database launched by National Institute of Standards and Technology (NIST) was used as references.

Inductive Coupled Plasma-Optical Emission Spectroscopy (ICP-OES). ICP-OES is a methodology based on the element-characteristic atom spectra, serving as a complementary alternative of conventional elementary analysis. Typically, a material is first separated by passing through a column, and then the ions emission induced by argon plasma is applied to quantitatively identify a material composition. When exposing the analysis to an external plasma energy, the comprised atoms are

excited and then emitted with radiation (i.e. spectrum rays). The radiation spectra are corresponded to specific photon absorption and referred to individual atoms. The comprised elements type and amount are deduced by the position and the intensity of the outcome photon irradiations. The plasma source is usually provided by ionizing argon under high frequency current to produce plasma with high electron density and temperature (10000K) for the excitation-emission of comprised compounds. Through the determination of plasma-induced optical emission, the ICP-OES is predominant over conventional atomic absorption spectrophotometers due to the high sensitivity, expanded usability to other atoms which are used to be challenging (i.e. P, B, Zr, Ta, etc.), and improved stability.

In the present thesis, the ICP-OES measurements were conducted on Perkin Elmer Optima 8000, calibrated with standard solutions containing the targeting element.

Ultraviolet-Visible Spectroscopy (UV-Vis). UV-Vis spectroscopy is prevalently used to determine the photo- and electrical properties or conjugating state of a material either in solution or solid state. The uptake light source is exactly in the ultraviolet-visible range, and namely, measurements are highly related to the color of samples. Due to the electronic transition, the comprised molecules in a material are able to interact with light radiation within the matched energy region. Basically for the solution state measurement, the UV-Vis spectra are based on scanning of the illuminated light against the percentage of beam transmitted through a transparent cuvette with defined thickness and a dilute solution in it. The absorbance is depicted by the Beer-Lambert law:

$$A = -log\left(\frac{I_1}{I_0}\right) = \varepsilon_\lambda \cdot c \cdot l$$

where A is the measured absorbance, I_1 is the transmitted light intensity, I_0 is the initial light intensity, ε_λ is a wavelength-dependent molar absorptivity coefficient ($M^{-1}cm^{-1}$), c is the analyte concentration and l is the path length. To evaluate the absorption behavior in a reliable way, UV-Vis spectroscopy has to be conducted within the linear Beer-Lambert law. The nonlinearity usually happens in the following conditions:

(1) high concentrations (> 0.01M)
(2) particle aggregation
(3) other coincident emissions in the system (i.e. fluorescence or phosphorescence)

In the present thesis, the solution state UV-vis measurements were conducted with a T70+ UV/Vis Spectrometer (PG Instruments Ltd), and the solid state UV-vis spectra were recorded on UV-2501PC/2550 (Shimadzu Corporation, Japan) at RT.

Powder X-Ray Diffraction (PXRD). PXRD is a widely employed technique to characterize the microstructure of crystalline substances. XRD is performed based on the interaction between an applied X-ray beam and the electrons of atoms in the material. The X-ray beam is generated by high-energy electrons, directed to collide on material, and thus deaccelerated, resulting in a continuous X-ray irradiation from the whole material. The monochromatic X-rays produced by the line-spectrum are utilized for the X-ray diffraction identification. Both elastic and inelastic interactions happen under X-ray exposure, and the inelastic collisions give rise to coherent scattering signals. However, diffraction appears only if the X-ray wavelength matches with the lattice distance (d) of measured materials. Once the matched wavelength is introduced, considering to the well-defined crystal, a 3D diffraction lattice pattern can be detected in a XRD pattern. Referring to the Bragg's Law, where the constructive interference appears when the optical path difference (Δ) is an integral multiple of the wavelength (λ). Therefore, positive interference occurs only at specific diffraction angles (Θ), leading to a distinct diffractogram of the investigated material. The characteristic repeating diffraction pattern can be mathematically illustrated by Bragg's Law:

$$\Delta = n\lambda = 2d\sin(\theta) \ (n \in N)$$

The association between radiation wavelength, diffraction angle and the lattice spacing in a crystal can be demonstrated via this law.

In the present thesis the PXRD measurements were conducted on a Bruker D8 Advance device with a scintillator detector (KeveX Detector) and *2θ* between 3.0° and 70.0°. The analysis was conducted under a step of 0.05° with a measurement time of 2 second/step and Cu-Kα radiation ($\lambda = 0.154$ nm) was used.

Single Crystal X-ray Analyses. Single-crystal X-ray diffraction is a non-destructive analytical technique which enables precise determination of crystalline substances, revealing detailed information within a unit cell, including cell dimensions, bond-lengths, bond-angles and the 3D atom position. X-ray diffraction pattern is based on constructive interference between monochromatic X-rays and the crystalline material. The monochromatic spectra are generated by a cathode ray tube, filtered to eliminate discrete frequencies, collimated to focus, and then directed toward the sample. Constructive interference occurs during the process, once irradiation conditions obey Bragg's Law. These diffracted X-rays are then detected, processed and counted. By tuning the geometry of the incident rays, the orientation of the analyzed crystal and the detector, all possible diffraction signals of the lattice can be collected and interpreted to determin the material structure.

In the present thesis, the single crystal X-ray analyses were carried out under the cooperation with Professor Dr. Uwe Schilde using a StadiVari diffractometer (Stoe). For X-ray structure determinations

the crystals were embedded in perfluoropolyalkylether oil and mounted within a MicroGripper. The data collection were performed at 210 K on a STOE StadiVari diffractometer equipped with a four-circle goniometer (open Eulerian cradle), a Genix Microfocus X-ray source (Mo) with a graded multilayer mirror and a Dectris 200 K Pilatus.

Appendix **IV. Supporting Information to Chapter 4**

Synthesis of Initiator-Functionalized Terephthalic Acid (Brbdc). The initiator-functionalized ligand, Brbdc, was first synthesized according to the literature.[270] α-bromoisobutyryl bromide (5.92 g, 25.7 mmol) was added dropwise to the ice-bath-cooled solution of 2-aminoterephthalic acid (4.67 g, 25.6 mmol) and triethylamine (2.59 g, 25.6 mmol) in dry THF (50 mL) under a nitrogen atmosphere. The mixture was then stirred overnight at RT. The salt was removed by centrifugation, and the remaining solution was precipitated in toluene. The solid was collected, washed by deionized water and acetone. After drying at RT under vacuum, the pure Brbdc was obtained (7.27 g, 22.02 mmol, 86%).The chemical structure was analyzed by NMR (Figure 4.1), giving ^{1}H NMR (400 MHz, ethanol-d_6): δ = 2.07 (s, 6H, CH$_3$), 7.78 (1H, CH), 8.19 (1H, CH), 8.21 (1H, CH) 9.35 (1H, NH), and ^{13}C NMR (100 MHz, ethanol-d_6): δ = 30.92 (CH3), 59.06 (C-Br), 120.98 and 119.85 (C2 and C6, aromatic),123.52 (C4, aromatic), 131.16 (1C, C3, aromatic), 135.71 (C5, aromatic), 140.92 (C1, aromatic), 166.98 and 169.26 (COOH), 170.62 (C=O).

Fabrication of Native Zn MOFs. The Zn$_2$(bdc)$_2$(dabco) (Znbdc, denoted as **1a**) was synthesized under solvothermal condition at 85 ºC in DMF,[40] and after removing the incorporated guest molecules by vacuum at 110 ºC for 20 hours, the porous MOF was obtained. The synthesized MOFs were characterized with FE-SEM (Figure S3), nitrogen adsorption/desorption measurements (Chapter 4, Figure 4. 3), powder X-ray diffraction (PXRD) (Chapter 4, Figure 4.5). Before polymerization, the incorporated guest solvent molecules, DMF, were removed by solvent exchanged with DCM for three time and one day a time, and then the incorporated DCM molecules were removed by vacuum at 110 ºC for 20 hours, giving the solvent-free MOF frameworks as polymerization hosts.

Fabrication of Initiator-Functionalized Zn MOFs. Brbdc was mixed with H$_2$bdc in specific molar ratio, and incorporated uniformly in the MOF framework through co-crystallization in DMF under solvothermal condition at 85 °C. Incorporated guest molecules were removed under vacuum at 110 °C for 20 hr. The ATRP-oriented MOFs were synthesized with varied amount of Brbdc, i.e., 10% (**2a**), 20% (**2b**) and 50% (**2c**) compared to bdc. However, the actually incorporated amount of Brbdc was determined by inductively coupled plasma optical emission spectrophotometry (ICP-OES). The microstructure of **2b** and **2c** was determined by single-crystal X-ray analysis. All the synthesized MOFs were characterized with nitrogen adsorption/desorption measurements (Chapter 4, Figure 4.3), powder X-ray diffraction (PXRD) (Chapter 4, Figure 4.5) and Field-emission scanning electron microscopy (FE-SEM) (Figure S3). Before polymerization, the incorporated guest solvent molecules, DMF, were removed by solvent exchanged with DCM for three time and one day a time, and then the incorporated DCM molecules were removed by vacuum at 110 ºC for 20 hours, giving the solvent-free MOF frameworks as polymerization hosts.

ARGET ATRP in Nanochannel of MOFs. The polymerization of MMA, EMA, BzMA and IBMA in native **1a** was as follows. In a glass vial **1a** (0.8 g) was added to the bulk solution of MMA (3 g, 30 mmol, 666.7 equiv), ethyl α-bromoisobutyrate (EBIB) (0.116/0.058 g, 0.6/0.3 mmol, 13.3/6.7 equiv), $CuBr_2$ (0.01 g, 0.045 mmol, 1 equiv), PMDETA (0.019 g, 0.11 mmol, 2.4 equiv) and dabco (0.02 g, 0.18 mmol, 4 equiv) under argon. The mixture was kept stirring at RT for 24 hours, ensuring the infiltration of monomer in MOF channels. The polymerization was performed at 50 ºC for 12 h under argon atmosphere. After termination by exposure to air, the solid product was intensively washed with THF for three times, and dried under vacuum. The unincorporated and washed out bulk solution was collected to evaluate the incorporation amount of monomer/polymer in MOF hosts. The as-synthesized PMMA can be obtained after removing the MOF host by 0.5% $EDTA-Na_2$ water solution.[37] PEMA, PBzMA and PIBMA were synthesized by the same procedures with the condition: $[MMA]_0/[EBIB]_0/[CuBr_2]_0/[PMDETA]_0/[dabco]_0 = 100:1:0.15:0.36:0.6$; $[EMA]_0/[EBIB]_0/[CuBr_2]_0/[PMDETA]_0/[dabco]_0 = 88:1:0.15:0.36:0.6$; $[BzMA]_0/[EBIB]_0/[CuBr_2]_0/[PMDETA]_0/[dabco]_0 = 57:1:0.08:0.16:0.036$ (half amount of initiator was applied for the high molecular weight attempt); $[IBMA]_0/[EBIB]_0/[CuBr_2]_0/[PMDETA]_0/[dabco]_0 = 45:1:0.15:0.36:0.6$. The same condition was utilized for **2a** and **2b** hosts, but without addition of EBIB.

Chain Extension with Isobornyl Methacrylate (IBMA). The accommodated homopolymers obtained from **1a/2a-b** were utilized as macroinitiators to form block copolymers comprised with IBMA. $[IBMA]_0/[macroinitiator]_0/[CuBr_2]_0/[PMDETA]_0/[dabco]_0 = 2700:1: 2.5:5:10$. In a glass vial $CuBr_2$ (1.27 mg, 0.0057 mmol, 2.5 equiv), PMDETA (2.0 mg, 0.0114 mmol, 5 equiv) and dabco (2.6 mg, 0.0228 mmol, 10 equiv) was added to the IBMA solution (1.4 g, 6.2 mol, 2700 equiv) under stirring. Subsequently, the mixture was added to the macroinitiators, for example, the PMMA obtained from *L*-**1a** with M_n = 43,800 (100 mg, 0.0023 mmol, 1 equiv). The polymerization was performed at 50 ºC for 24 hours under Argon. The reaction was quenched by THF, the solution was passed through a neutral aluminum oxide column, precipitated in methanol, and then dried under vacuum.

Single Crystal X-ray Structure determinations of 2a and 2b. For X-ray structure determinations the crystals were embedded in perfluoropolyalkylether oil and mounted within a MicroGripper. The data collection were performed at 210 K on a STOE StadiVari diffractometer equipped with a four-circle goniometer (open Eulerian cradle), a Genix Microfocus X-ray source (Mo) with a graded multilayer mirror and a Dectris 200 K Pilatus detector (**2b**: 3102 frames, Δω=0.5°, 10 s exposure time per frame; **2c**: 2373 frames, Δω=0.5°, 15 s exposure time per frame). The data were corrected for absorption and for Lorentz and polarization effects using the program X-Area. The structures were solved by direct methods using SHELXS-2013/1 and refined by full-matrix least squares on F using the program SHELXL-2014/7.[346]* For the visualization the program DIAMOND was used.* All non-hydrogen atoms were refined anisotropically with the exception of the carbon atoms of the dabco moiety in **2b**.

The dabco ligand was found to be rotationally disordered about the nitrogen axis (see CIF files for details). The hydrogen atoms were placed in their expected positions with C−H distances of 0.94 Å and 1.08 Å (AFIX 43 and AFIX 23). The hydrogen atom on the phenyl ring was refined as riding with

U_{iso}(H) = 1.2 U_{eq}(C). The hydrogen atoms of the ethylene moiety of dabco were taken into account but their coordinates, s.o.f and U were fixed. The unit cell contains channels filled with disordered solvent molecules. In spite of several attempts, no chemically reasonable solution could be received for the solvent species in the channels of the crystal material. Very high displacement parameters, high estimates and partial occupancy due to the disorder make it impossible to determine accurate atomic positions for the molecules. PLATON/SQUEEZE* calculated the solvent-accessible void volume and the corresponding number of electrons in the unit cell [**2b**: 2483 Å^3, 56.7 % of the total cell volume, 548 electrons, agreeing with about a half of a DMF molecule (0.428x40x32=548); **2c**: 2530 Å^3, 64.8 % of the total cell volume, 530 electrons, also agreeing with about a half of a DMF molecule (0.552x40x24=530)]. The contribution of the disordered solvent species was subtracted from the structure factor calculations by the SQUEEZE instruction of PLATON. CCDC 1579809 (**2b**) and CCDC 1579776 (**2c**) contain the supplementary crystallographic data for this paper and can be obtained free of charge from The Cambridge Crystallographic Data Centre via www.ccdc.cam.ac.uk/data_request /cif. Crystal structure determination of complex **2b**: crystal data: Zn$_2$(bdc)$_2$(dabco)· 3.44 DMF; M = 863.52 g/mol; crystal dimensions: 0.08 x 0.11 x 0.30 mm; tetragonal: a = b = 15.0812(5) Å, c = 19.2621(8) Å; V = 4381.0(3) Å^3; T = 210 K; space group: $I4/mcm$ (no. 140); Z = 4; 43453 reflections measured; 1048 unique (R_{int} = 0.0821); R = 0.0389; wR = 0.0907 [$I > 2\sigma(I)$]. Crystal structure determination of complex **2c**: crystal data: Zn$_2$(bdc)$_2$(dabco) · 4.40 DMF; M = 863.52 g/mol; crystal dimensions: 0.14 x 0.21 x 0.26 mm; hexagonal: a = b = 21.5725(5) Å, c = 9.6834(3) Å; V = 3902.6(2) Å^3; T = 210 K; space group: $P6/mmm$ (no. 191); Z = 3; 64193 reflections measured; 1383 unique (R_{int} = 0.0510); R = 0.0273; wR = 0.0744 [$I > 2\sigma(I)$].

* The method is applied according to (1) Stoe & Cie (2015). *X-Area.* Darmstadt, Germany; (2) G. M. Sheldrick, *SHELXS-2013/1*, Program for the Crystal Structure Solution, University Göttingen, Germany, 2013; (3) M. Sheldrick, *SHELXL-2014/7*, Program for the Crystal Structure Refinement, University Göttingen, Germany, 2014; (4) K. Brandenburg, *DIAMOND 4.4.1.*, Crystal Impact, Bonn, Germany, 2017; (5) Spek, A. L., *Acta Cryst.* 2009, **D65**, 148-155.
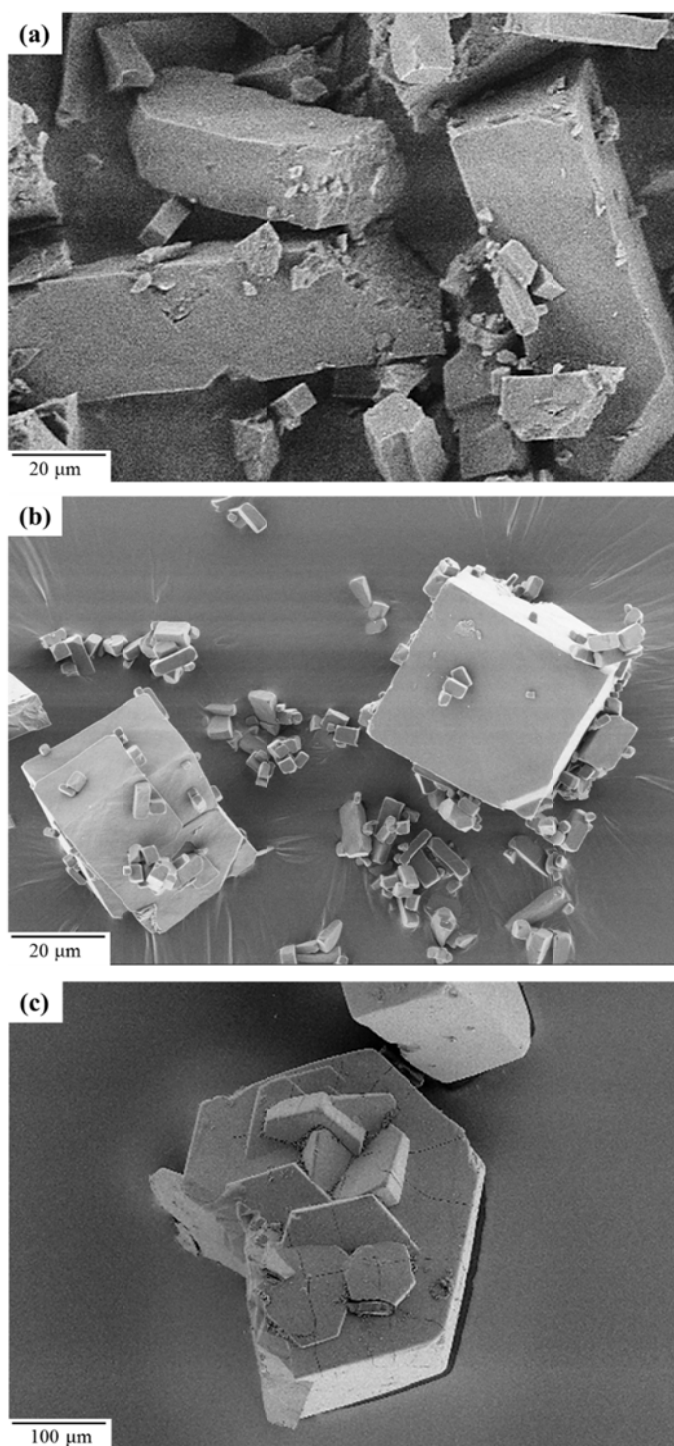
Figure S3. FE-SEM micrographs of the as fabricated (a) **1a**, (b) **2b** and (c) **2c**.

Table S1. Physical Adsorption Properties of MOFs before and after Polymerization of various monomers.

MOF	Monomer	BET surface area (m²/g)		pore volume (ml/g)	
		Before	After	Before	After
1a	MMA	2200	550	0.73	0.23
	EMA		840		0.41
	BzMA		1040		0.45
	IBMA		1970		0.71
2a	MMA	2000	930	0.76	0.37
	EMA		1090		0.50
	BzMA		1380		0.55
2b	MMA	2100	1200	0.78	0.48
	BzMA		1630		0.62
2c	-	1970	-	0.74	-
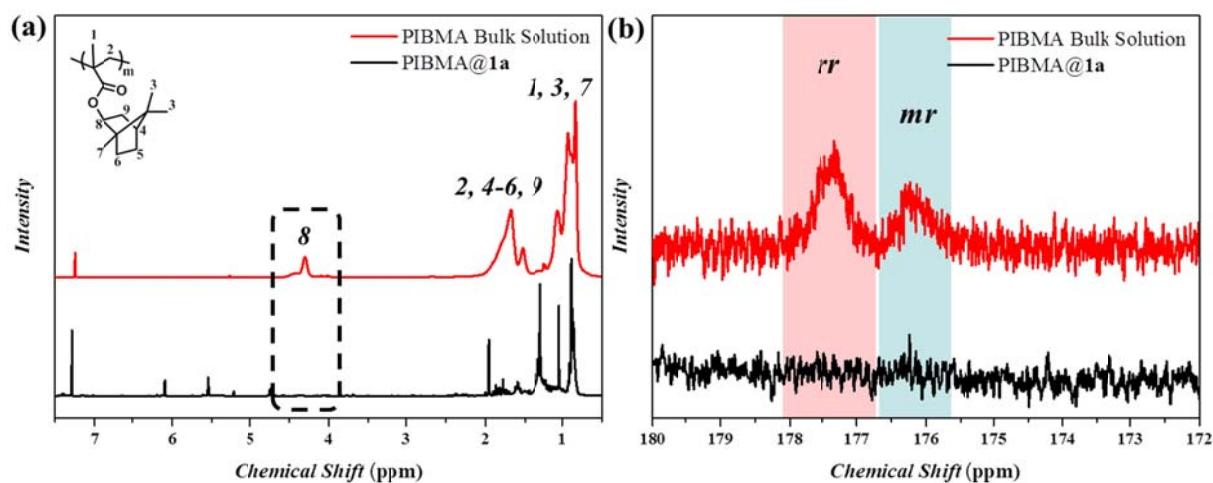
Figure S4. Comparison of NMR spectrum of PIBMA obtained from ARGET ATRP in **1a** with a reference from bulk polymerization, indicating little polymer comes out from the MOF host: (a) ^{1}H NMR and (b) ^{13}C NMR.
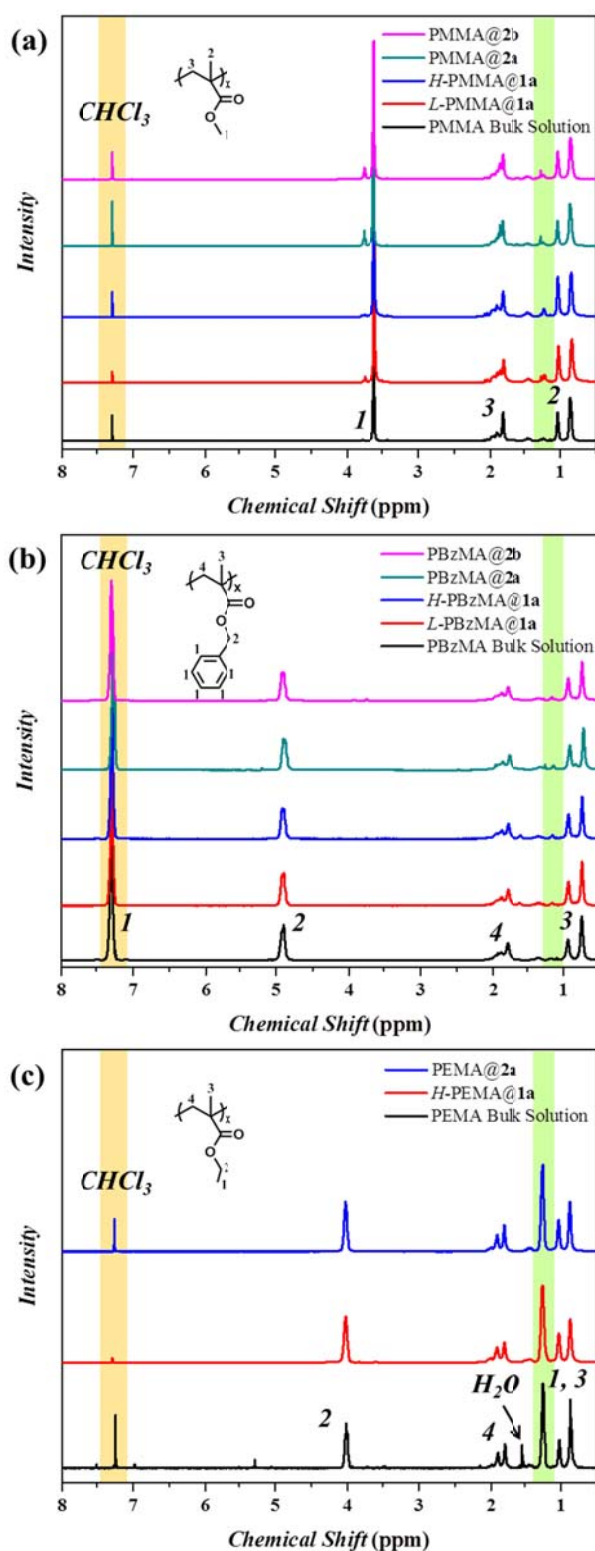
Figure S5. The corresponding ^{1}H NMR of accommodated homopolymers obtained from native (**1a**) and functionalized (**2a**, **2b**) MOFs in chloroform-*d*: (a) PMMA, (b) PBzMA and (c) PEMA, with the bulk polymer as stereo-control reference.

Appendix V. Supporting Information to Chapter 5

Fabrication of Cu$_2$(bdc)$_2$(dabco) (Cu(II) MOF). Cu$_2$(bdc)$_2$(dabco) was employed as the Cu(II) MOF to catalyze polymerization processes demonstrated in this chapter. The Cu(II) MOF was prepared under solvothermal condition,[34, 310] and after removing of the incorporated guest molecules, the as synthesized MOF was characterized with FE-SEM (Chapter 5, Figure 5.1), PXRD (Chapter 5, Figure 5.2a) and nitrogen adsorption-desorption measurements (Chapter 5, Figure 5.2b). The obtained PXRD pattern shows good accordance with the literature, indicating the accurate with pure phase. The specific surface area and the pore volume was calculated as 2280 m^2/g and 0.91 cc/g, respectively via the BET method. The property of the ultrahigh specific surface area reveals the advantage of the given Cu(II) MOF as a catalyst for polymerization. Besides, the crystal structure with uniform particle size around hundred nm can be observed in the FE-SEM image.

Cu(II) MOF-Mediated ARGET ATRP. A typical polymerization of BzMA was as follows:[347] [BzMA]$_0$/[I]$_0$/[RA]$_0$ = 180:1:2, 50 °C for 6 hr; [styrene]$_0$/[I]$_0$/[RA]$_0$ = 110:1:5, 110 °C for 12 hr;[270] [isoprene]$_0$/[I]$_0$/[RA]$_0$ = 805:1:5, 120 °C for 72 hr;[348] [4VP]$_0$/[I]$_0$/[RA]$_0$ = 370:1:5, 60 °C for 9 hr.[301] In a glass vial Cu(II) MOF (0.8 g) was added to the bulk solution of BzMA (13 g). Ethyl α-bromoisobutyrate (EBIB) (0.078 g) and dabco (0.09 g) were added under stirring. The polymerization was performed at 50 ℃ for 12 hr under Argon. The reaction was terminated by THF, and after removing the Cu(II) MOF by centrifugation, the solution was precipitated in methanol and the polymer product was dried under vacuum. For the kinetic analysis, after the reaction was terminated by THF at specific time, the solution was centrifuged and the clear suspension was filtered for GC-MS to evaluate the monomer conversion.

Chain Extension with Isobornyl Methacrylate (IBMA). The homopolymers obtained from Cu(II) MOF-mediated ARGET ATRP were utilized as macroinitiators for the block copolymer comprised with IBMA. [PBzMA-Br/ PS-Br]$_0$/[IBMA]$_0$/[CuBr$_2$]$_0$/[PMDETA]$_0$/[dabco]$_0$ = 1:400:0.4:1:2.4, 50 °C for 24 hr; [PI-Br]$_0$/[IBMA]$_0$/[CuBr$_2$]$_0$/[PMDETA]$_0$/[dabco]$_0$ = 1:1100:1.1:2.75:6.6, in 50 vol% dioxane at 50 °C for 24 hr; [P4VP-Br]$_0$/[IBMA]$_0$/[CuBr$_2$]$_0$/[PMDETA]$_0$/[dabco]$_0$ = 1:450:0.45:1.13:2.7, in 50 vol% dioxane at 50 °C for 24 hr.

Reference ARGET ATRP Polymerization. The conventional homogeneous polymerization of BzMA and styrene (St) was as follows. In a glass vial CuBr$_2$ (1.83 mg) and PMDETA (2.9 mg) were added to the bulk solution of BzMA (3.0 g) under stirring. Subsequently, ethyl α-bromoisobutyrate (EBIB) (0.04 g) and dabco (0.43 mg) was introduced in the solution. The polymerization was performed at 50 ℃ for 12 hr under Argon. The reaction was terminated by THF, passed through a neutral aluminum oxide column, precipitated in methanol and the product was dried under vacuum.

The PS was synthesized by the same procedure with the condition: 110 °C for 12 hr; $[St]_0/[EBIB]_0/[CuBr_2]_0/[PMDETA]_0/[dabco]_0 = 245:1:1:2:0.45$.

Recycling of Cu(II) MOF in Cascade ARGET ATRP of Benzyl Methacrylate and Styrene. The given amount of Cu(II) MOF (0.1 g) was utilized to polymerize BzMA and styrene alternatively referring to the reaction condition in Cu(II) mediated-ARGET ATRP, and the polymerization was three times repeated for each monomer. The conversion of the given cycle was determined by GC-MS, and the yield was measured by the weight of polymer product. After every polymerization, the Cu(II) MOF was washed via THF once a day for 3 days, dried under vacuum, and then the weight increment was recorded before the next reaction.
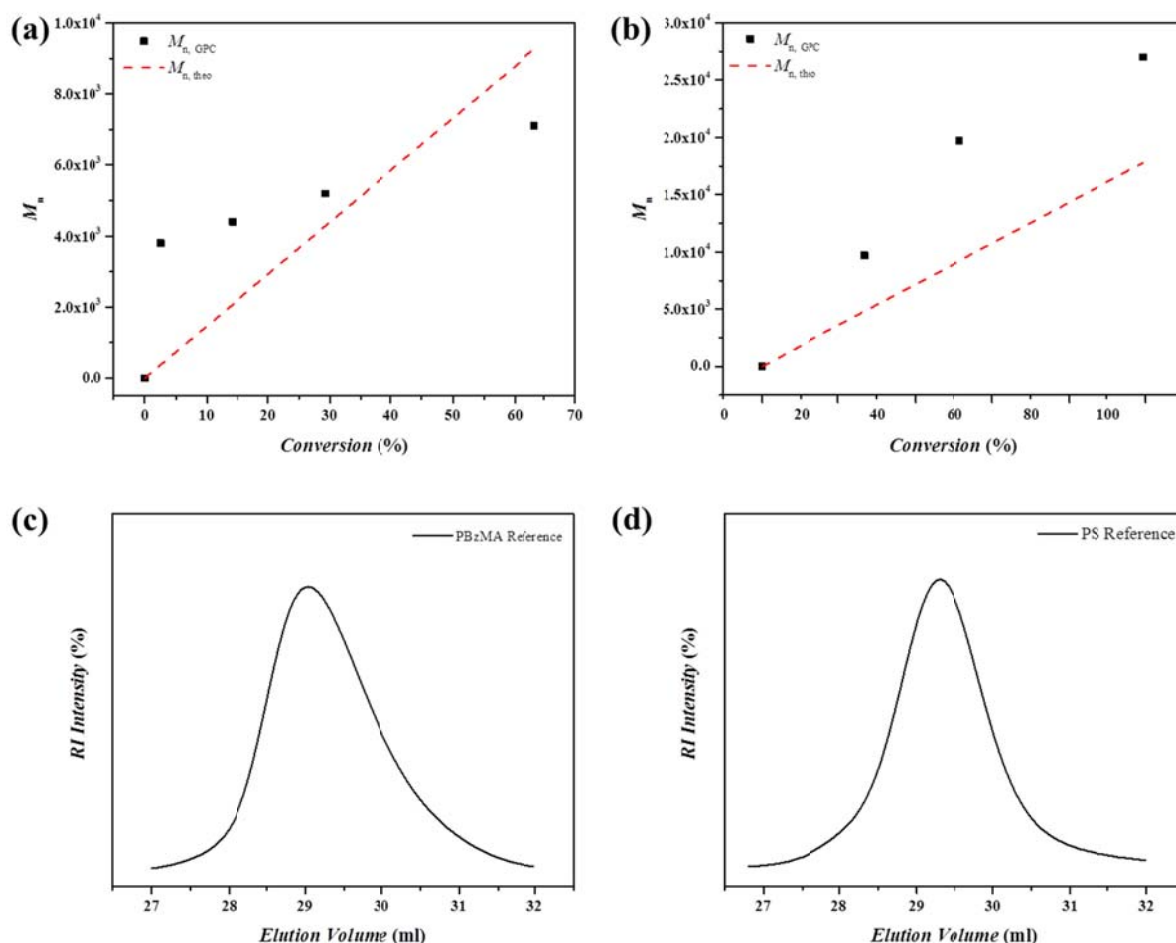
Figure S6. The evolution of M_n with conversion for CuBr$_2$-catalyzed (a) PBzMA and (b) PS polymerization. SEC chromatograms of the as synthesized (c) PBzMA ($M_n = 5,800$ g/mol and $Đ = 1.2$) and (d) PS ($M_n = 10,500$ g/mol and $Đ = 1.2$) measured in THF using PMMA and PS as standard, respectively.
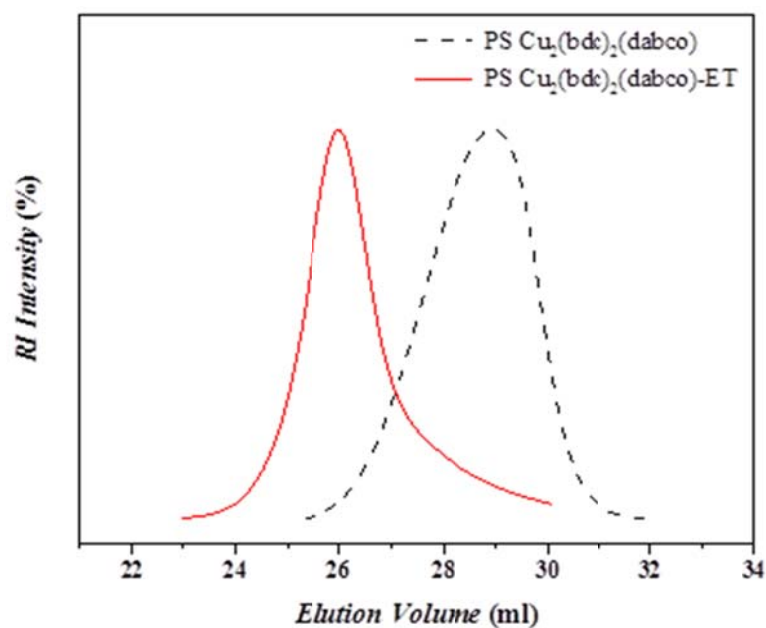
Figure S7. The SEC chromatogram of the Cu(II) MOF-mediated PS after chain extension with PS (M_n = 32,200 g/mol and $Đ$ = 1.4), using PS as standard in THF.
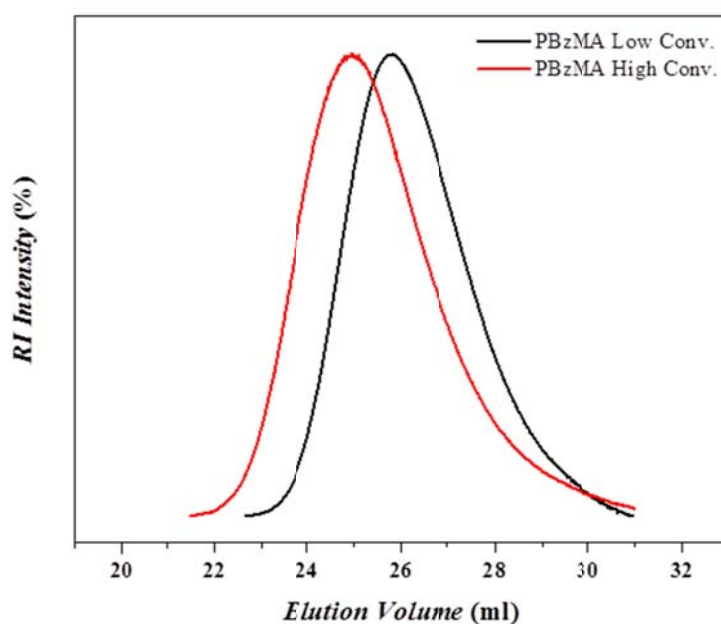
Figure S8. SEC chromatograms of the PBzMA synthesized by $Cu_2(bdc)_2(dabco)$ with the concentration of 500 ppm (approximately 112 ppm Cu(II) ion) with different conversions, using PMMA as standard in THF.

Table S2. Polymerization of PBzMA via $Cu_2(bdc)_2(dabco)$ [a] with the concentration of 500 ppm Cu(II) MOF (approximately 112 ppm Cu(II) ions).

Homopolymer	Time (hr)	Conv. (%)	$M_{n,theo}$ [b] (x 10^3)	$M_{n,SEC}$ (x 10^3)	Đ
PBzMA	40	33	12800	31400	1.52
	65	60	23500	40500	1.81

[a] Polymerization condition: $[BzMA]_0/[I]_0/[dabco]_0$ = 220:1:2, 50 ºC. [b] Conversion determined by GC-MS. The theoretical number averaged molecular mass $M_{n,theo}$ was calculated as $MM_{initiator} + MM_{monomer} \times ([monomer]_0/[initiator]_0) \times conversion$.

Appendix VI. Supporting Information to Chapter 6

Fabrication of Cu₂(bdc)₂(dabco) (Cu(II) MOF). $Cu_2(bdc)_2(dabco)$ was employed as the Cu(II) MOF to catalyze the photopolymerization demonstrated in this study. The Cu(II) MOF was prepared under solvothermal condition,[34, 310] and after removing of the incorporated guest molecules, the as synthesized MOF was characterized with FE-SEM (Chapter 5, Figure 5.1), PXRD (Chapter 6, Figure 6.7a), and nitrogen adsorption and desorption measurements (Chapter 5, Figure 6.7b). At beginning, the crystal structure with uniform particle size around hundred nm can be identified through the FE-SEM image. The obtained PXRD pattern reveals high accordance with the literature, indicating the accurate microstructure formed by the applied metallic ion and organic ligands with in specific ratio. The BET surface area and the pore volume were identified as 2280 m^2/g and 0.91 cc/g via the BET method.

Electrochemical Characterization of Cu(II) MOF. Electrochemical analyses were performed on a PARC 263A potentiostat/galvanostat using a three-electrode cell with deionized water/0.1 M $NaNO_3$ as solvent. The reference electrode was standard calomel (SCE), the counter electrode was a Pt wire, and the working electrode was a glassy carbon disc (Metrohm, 3 mm diameter) coated with a film of Cu(II) MOF. The MOF was dropcasted from dry acetone or TEA:dry acetone 1:4 mixtures (5 drops of a dispersion of 10 mg MOF in 5 mL solvent, sonicated for 30 min before casting). The film was protected by dropcasting two drops of a solution of 1 wt% Paraloid B-72 in acetone, which forms a porous layer incorporated with 0.02±0.01 mg of MOF.[313] Prior to each surface deposition, the electrode was polished with a 0.1 µm alumina paste, and rinsed in ultrasonic bath. Photoelectrochemistry experiments were performed by illuminating the electrode surface with either a UV/Vis lamp or a white LED in a distance of 1 cm.

Cu(II) MOF-Mediated Photopolymerization of 4VP, 2VP, and DMAEMA. The typical polymerization equivalents were as follows: $[4VP]_0/[I]_0 = 125:1$ for 1 hr; $[2VP]_0/[I]_0 = 370:1$ for 2 hr; $[DMAEMA]_0/[I]_0 = 500:1$ for 12 hr. In a glass vial Cu(II) MOF (0.08 g) was added to the bulk solution of monomer (2 g) under Argon, and then ethyl α-bromoisobutyrate (EBIB) (0.03 g) was added while stirring. The polymerization was carried out via exposing the reaction mixture to a 50 W visible-light LED in a distance of 15 cm. The reaction was terminated at given time by DCM. After centrifugation, the polymer product was precipitated in water and the solid product was dried under vacuum. For kinetic analysis, the reaction was terminated by DCM at specific time, the solution was centrifuged, and the clear suspension was filtered for GC-MS to evaluate monomer conversion.

Cu(II) MOF-Mediated Photopolymerization of MMA. The typical polymerization equivalents were as follows: $[MMA]_0/[I]_0 = 325:1$ for 24 hr. In a glass vial Cu(II) MOF (0.08 g) was added to the bulk solution of MMA (2 g) under Argon, and then ethyl α-bromoisobutyrate (EBIB) or bromoacetonitrile

(0.03 g) was added while stirring. Furthermore, TEA (0.124 g) or 4-ethylpyridine (0.131 g) or none of them was added. The polymerization was carried out via exposing the reaction mixture to a 50 W visible-light LED in a distance of 15 cm. The reaction was terminated at given time by THF. After centrifugation, the polymer product was precipitated in methanol, and the solid product was dried under vacuum. For kinetic analysis, the reaction was terminated by DCM at specific time, the solution was centrifuged, and the clear suspension was filtered for GC-MS to evaluate monomer conversion.

Chain Extension with Poly(ethylene glycol) Methyl Ether Methacrylate (OEGMA) or Isobornyl Acrylate (IBA). The homopolymers obtained from Cu(II) MOF-mediated photopolymerization were utilized as macroinitiators for the block copolymer comprised with OEGMA or IBA. [macroinitiator]$_0$/[OEGMA/ IBA]$_0$/[CuBr$_2$]$_0$/[PMDETA]$_0$/[dabco]$_0$ = 1:340:4:8.8:20, at 50 °C for 24 hr in 50 vol% methanol (i.e. P4VP and PDMAEMA) or DMF (i.e. P2VP and PMMA).

Synthesis of Reference Polymers. The reference P4VP and P2VP was synthesized through free radical polymerization using AIBN as initiator at 60 ºC. The typical polymerization of DMAEMA and MMA was carried out by ARGET ATRP as follows. In a glass vial CuBr$_2$ (9.3 mg) and PMDETA (17.3 mg) were added to the bulk solution of DMAEMA (3.0 g) under stirring. Subsequently, ethyl α-bromoisobutyrate (EBIB) (0.025 g) and dabco (18 mg) was introduced in the solution. The polymerization was performed at 90 ºC for 24 hours under Argon. The reaction was terminated by DCM, the solution was passed through a neutral aluminum oxide column, precipitated in methanol, and the product dried under vacuum. The PMMA was synthesized by the same procedure at 50 ºC for 24 hr.

Repeated Photopolymerization of 2VP and DMAEMA. The given amount of Cu(II) MOF (0.1 g) was utilized to polymerize 2VP and DMAEMA alternatively referring to the reaction condition in Cu(II) mediated-photopolymerization, and the polymerization was three times repeated for each monomer. The conversion of the given cycle was determined by GC-MS, and the yield was measured by the weight of obtained polymer product. After every polymerization, the Cu(II) MOF was washed via DCM once a day for 3 days, dried under vacuum, and then the weight increment was recorded before the next reaction.

Calculation of Cu Atom on MOF Surface. Number of total Cu atoms considering a perfect cube geometry with approximate side length of 100 nm and Cu atom distance of 0.76 nm: N(Cu cube) $\approx$ $(100/0.76)^3 \approx 2278029$ atoms

Number of Cu atoms on the surface considering a perfect square geometry with approximate side length of 100 nm and Cu atom distance of 0.76 nm: N(Cu surface) $\approx 6*(100/0.76)^2 \approx 103878$ atoms

Ratio between surface and total Cu atoms: N(Cu surface)/N(Cu cube) ≈ 5%
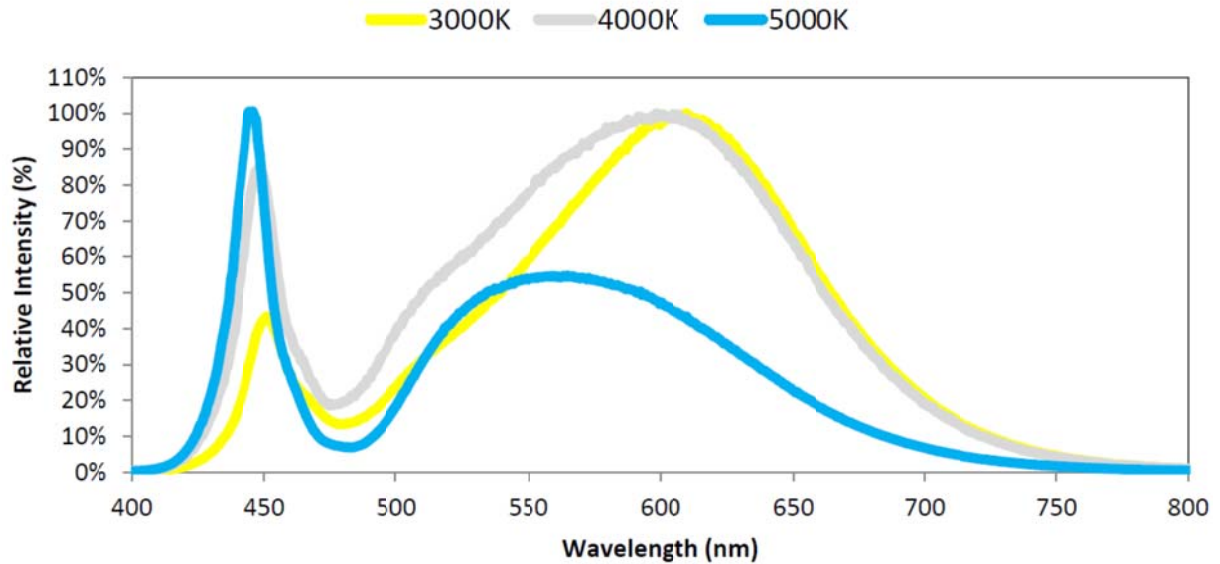
Figure S9. Typical emission spectrum of the visible-light source used in the present thesis. Note: the spectra were measured at rated current with the junction temperature at 25 °C: spectrum for warm white is 3000 K and 80 color rendering index (CRI), spectrum for neutral white is 4000 K and 80 CRI, and spectrum for cool white is 5000 K and 70 CRI. (information source: www.bridgelux.com)
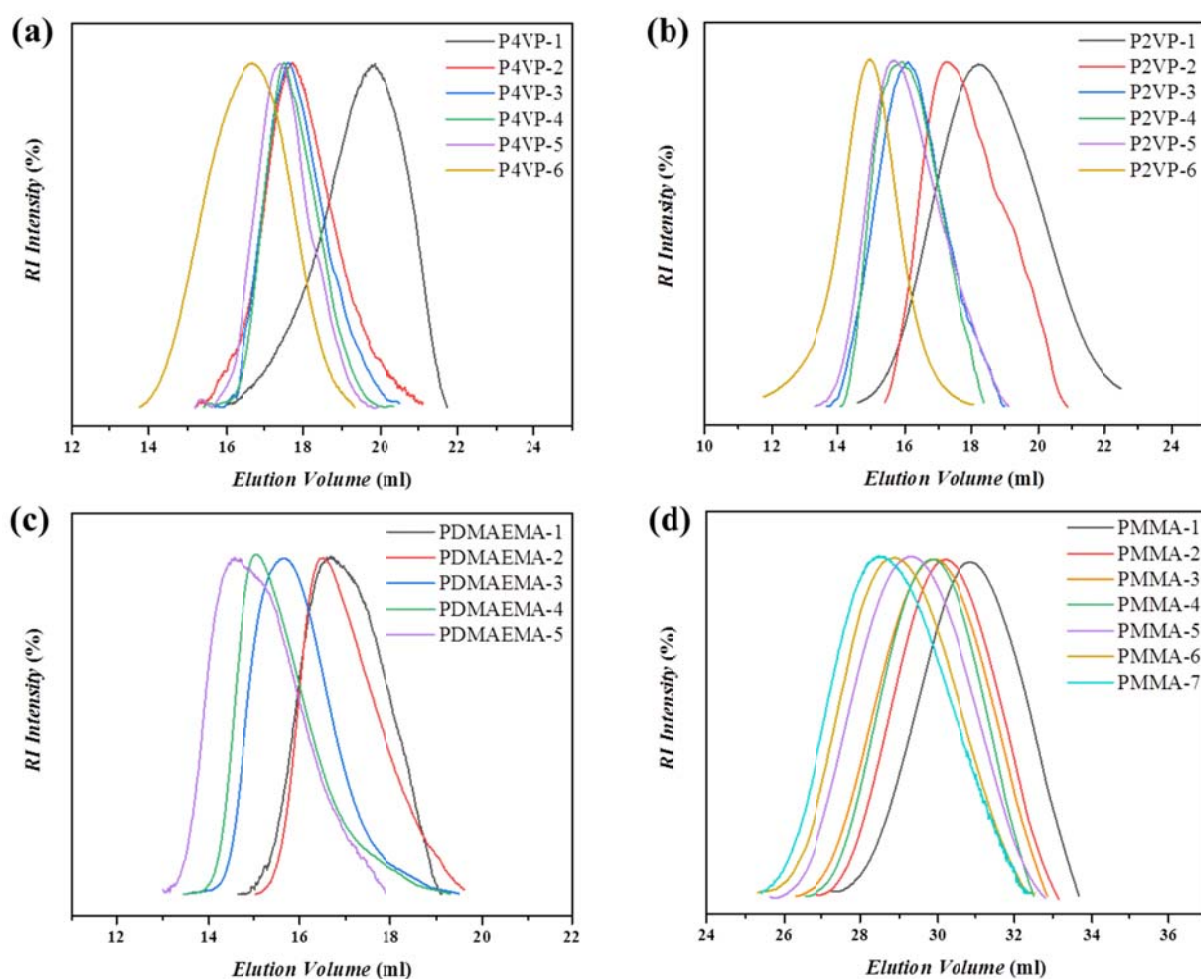
Figure S10. Time-dependent SEC chromatograms of (a) P4VP, (b) P2VP, (c) PDMAEMA and (e) PMMA obtained from the crude extraction during the kinetic evolution of monomer conversion analysis, using PMMA as standard in NMP.

Table S3. Properties of homopolymers obtained during the kinetic evolution of monomer conversion analysis using Cu$_2$(bdc)$_2$(dabco). [a]

Homo polym.	Point	Time	Conversion (%)	$M_{n,theo}$ [b] (×10^3)	$M_{n,SEC}$ (×10^3)	Đ
P4VP	1	15 min	23.2	3000	2400	1.6
	2	30 min	42.4	5500	5900	1.6
	3	45 min	55.6	7200	7300	1.4
	4	60 min	72.7	9500	8050	1.3
	5	75 min	78.7	10200	8600	1.3
	6	90 min	86.2	11200	12600	1.4
P2VP	1	20 min	15.1	5900	5100	1.6
	2	35 min	20.7	8200	6300	1.7
	3	65 min	31.7	12500	13300	1.5
	4	80 min	37.1	14600	14400	1.4
	5	95 min	40.9	16100	15300	1.6
	6	110 min	46.2	18200	21000	1.4
PDMAEMA	1	3 hr	11.6	9500	11900	1.5
	2	7 hr	15.7	12900	13400	1.4
	3	9 hr	23.4	19200	23100	1.4
	4	12 hr	30.5	25100	30500	1.5
	5	15 hr	35.5	29200	32200	1.4
PMMA	1	1.5 hr	10.4	3400	3700	1.4
	2	2.5 hr	17.8	5800	5000	1.4
	3	3 hr	19.5	6300	5500	1.4
	4	3.5 hr	20.5	6700	6400	1.5
	5	4 hr	21.1	6900	7300	1.4
	6	5 hr	22.1	7200	8300	1.4
	7	6 hr	23.3	7600	8800	1.3

[a] The polymers obtained from the kinetic studies shown in Figure 6.4 Because the SEC was measured after the analysis of GC-MS using the same crude extraction without precipitation, the outcome Đ is slightly higher. However, the unimodal distribution in each monomer system indicates the living polymerization property with limited nucleophilic substitution in the chain end. [b] Conversion determined by GC-MS. The theoretical number averaged molecular mass $M_{n,theo}$ was calculated as $MM_{initiator} + MM_{monomer} \times ([monomer]_0/[initiator]_0) \times conversion$.

Appendix VII. Supporting Information to Chapter 7

Synthesis of Initiator-Functionalized Silane (MPTS-Br). According to literature,[270] α-bromoisobutyryl bromide (5.92g, 25.7 mmol) was added dropwise to the ice-cold-bath of 3-(mercaptopropyl)trimethoxysilane (5.03 g, 25.6 mmol) and triethylamine (2.59 g, 25.6 mmol) in dry toluene (42.5 mL) with stirring. The mixture was then stirred overnight at RT. The salt was removed by filtration, and the remaining solution was removed under reduced pressure to give the initiator-functionalized silane 2-bromothioisobutyrate (MPTS-Br) (85% yield). ^{1}H NMR (400 MHz, CHCl$_3$): δ = 3.57 (9H, SiOCH$_3$), 2.95 (2H, SCH$_2$), 1.97 (6H, C(CH$_3$)$_2$Br), 1.74 (2H, CCH$_2$C), 0.78 (2H, CH$_2$Si) (Chapter 7, Figure 7.1a).

Synthesis of 3-Azido-Propanol. Sodium azide (4.6 g, 70.8 mmol, 1.5 equiv) was placed in a 250 mL flask and dissolved in a mixture of acetone (72 mL) and deionized water (12.0 mL). 3-Bromo-1-propanol (3.92 mL, 44.8 mmol, 1.0 equiv) was added, and the mixture was refluxed overnight. Acetone was evaporated under reduced pressure at RT, and then deionized water (60 mL) was added. The aqueous phase was extracted with diethyl ether (3 x 60 mL). The extracted organic mixture was dried over anhydrous magnesium sulfate. The solvent was removed under reduced pressure to give 3-azido-1-propanol as yellow oil (3.81 g, 37.7 mmol, 84% yield). ^{1}H NMR (400 MHz, CHCl$_3$): δ = 3.72 (t, 1H, OH), 3.43 (t, 2H, CH$_2$OH), 1.82 (p, 4H, N$_3$-CH$_2$CH$_2$)[349] (Chapter 7, Figure 7.8a)

Preparation of PDMAEMA-Functionalized Pollens (*P*-pollen). Via using different concentration of grafted initiator, for example, 0.5, 1, 2, 3 and 5 wt %, the pollen grains with varied grafting density were prepared (as shown in the ICP-OES result in Chapter 7, Figure 7.1b). Typically, the washed pollen (0.1 g) was immersed into a solution of the MPTS-Br (5 wt %) in toluene (10 mL), and the mixture was gently refluxed for 24 h. The MPTS-Br functionalized pollen was washed by toluene (3 x 10 ml) and dried under vacuum at RT. After the initiator-functionalized pollen was fabricated, SI-ARGET ATRP was carried out to graft PDMAEMA from the pollen surface. DMAEMA (0.5 g, 31.75 mmol), CuBr$_2$ (0.0013 g, 0.0056 mmol), PMDETA (0.0023 g, 0.13 mmol), dabco (0.012 g, 0.0001 mmol) and anhydrous methanol (0.5 ml) were introduced into a 5 mL vial and mixed. Then the 5% initiator-functionalized pollen (0.5 g) was added into the mixture, and the polymerization was conducted at 65 ºC for 24 h with conversion 98%. The PDMAEMA-grafted pollen was washed and re-suspended by DCM. The grafted PDMAEMA brushes were cut from *P*-pollens by 1% NaOH, and characterized by ^{1}H NMR (400 MHz, CHCl$_3$): δ = 4.04 (2H, OCH2), 2.55 (2H, CH2N), 2.26 (6H, N(CH3)2), 2.05-1.63 (2H, CH$_2$C main chain), 1.42-0.73 (3H, CCH$_3$), and SEC: MW of 67,800 (Đ = 1.2) (Figure S11).

Fabrication of Cu$_2$(bdc)$_2$(dabco). Cu$_2$(bdc)$_2$(dabco) was employed as a Cu(II)-based MOF to catalyze the photocatalytic reactions demonstrated in this chapter. The Cu$_2$(bdc)$_2$(dabco) was prepared

under solvothermal condition,[34, 310] and after removing of the non-coordinated molecules by washing with DMF and DCM, the as-synthesized $Cu_2(bdc)_2(dabco)$ was characterized with FE-SEM (Chapter 7, Figure 7.3b), PXRD (Chapter 7, Figure 7.3c), and then remained in DCM.

Fabrication of Cu(bdc). The $Cu(bdc)_2$ was synthesized by solvothermal condition according to literature.[242, 350] H_2bdc (166 mg, 1.0 mmol) and $Cu(NO_3)_2 \cdot 3H_2O$ (242 mg, 1.0 mmol) was dissolved separately in 10 mL DMF. The metal ion solution was poured into the ligand solution stirring at RT for 2 hr, and then the mixture was refluxed at 100 °C for 2 days. The forming precipitate was collected by centrifugation, and after removing the non-coordinated molecules by washing with DMF and DCM, the Cu(bdc) was obtained. The synthesized MOF was characterized with FE-SEM and PXRD (Chapter 7, Figure 7.5a), and remained in DCM before utilization.

Fabrication of HKUST-1. The HKUST-1 was synthesized according to literature at RT.[192] H_3btc (500 mg, 2.4 mmol) and $Cu(OAc)_2 \cdot H_2O$ (860 mg, 4.31 mmol) was dissolved separately in 12 mL DMF-ethanol-water mixture (volume ratio = 1:2:3). The metal ion solution was poured into the ligand solution stirring at RT overnight. The forming precipitate was collected by centrifugation, and after removing the non-coordinated molecules by washing with DMF and DCM, the HKUST-1 was obtained. The synthesized MOF was characterized with FE-SEM and PXRD (Chapter 7, Figure 7.5b), and remained in DCM before utilization.

Fabrication of $Zn_2(bdc)_2(dabco)$. The $Zn_2(bdc)_2(dabco)$ was synthesized under solvothermal condition at 85 °C for 24 hr in DMF,[40] and after removing the non-coordinated molecules by washing with DMF and DCM, the $Zn_2(bdc)_2(dabco)$ MOF was obtained. The synthesized MOF was characterized with FE-SEM and PXRD (Chapter 7, Figure 7.5c) and then remained in DCM before utilization.

Fabrication of MOF-5. The MOF-5 was synthesized according to literature at RT.[351] H_2bdc (0.5 g, 3 mmol) and TEA (0.85 mL) were dissolved in 40 mL of DMF. $Zn(OAc)_2 \cdot 2H_2O$ (1.7 g, 7.7 mmol) was dissolved in 50 mL of DMF, and then added to the organic mixture stirred overnight. The forming precipitate was collected by centrifugation, and after removing the non-coordinated molecules by washing with DMF and DCM, the MOF-5 was obtained. The as-synthesized MOF-5 was characterized with FE-SEM and PXRD (Chapter 7, Figure 7.5d), and remained in DCM before utilization.

Fabrication of MOF-74-Zn. The MOF-74-Zn was synthesized according to literature at RT.[351] H_4dobdc (239 mg, 1.2 mmol) and $Zn(OAc)_2 \cdot 2H_2O$ (686 mg, 3.1 mmol) was dissolved separately in 20 mL DMF. Then the ligand solution was added into the zinc salt solution stirred overnight. The forming precipitate was collected by centrifugation, and after removing the non-coordinated molecules by

washing with DMF and DCM, MOF-74-Zn was obtained. The as-synthesized MOF-74 was characterized with FE-SEM and PXRD (Chapter 7, Figure 7.5e), and remained in DCM before utilization.

Fabrication of ZIF-67. The ZIF-67 was synthesized according to literature at RT.[352] Hmim (5.5 g, 0.067 mol) was dissolved in 20 mL water, and $Co(NO_3)_2 \cdot 6H_2O$ (0.45 g, 1.54 mmol) was dissolved in 3 mL water, separately. The metal ion solution was poured into the ligand solution stirred overnight. The forming precipitate was collected by centrifugation, and after removing the non-coordinated molecules by washing with water and methanol, the ZIF-67 was obtained. The synthesized MOF was characterized with FE-SEM and PXRD (Chapter 7, Figure 7.5f), and remained in DCM before utilization.

Incorporation of MOFs on *P*-pollen (MOFs@*P*-pollen). The as-synthesized *P*-pollen (0.1 g) was suspended in DCM (10 ml), and various MOFs (0.1 g) were added individually. The mixture was gently shacked overnight. The non-incorporated MOF particles were removed by low-speed centrifugation, and the suspension was dried under reduced pressure at RT, giving MOFs@*P*-pollen. The incorporated amount of each MOF in the MOFs@*P*-pollen composite was determined by ICP-OES using the comprised metallic ions in individual MOF framework (Chapter 7, Table 7.1). The as-prepared MOF@*P*-pollen composites were characterized by PXRD and FE-SEM comparing to the native MOFs (Chapter 7, Figure 7.5).

$Cu_2(bdc)_2(dabco)$-mediated Photoclick reaction. The given amount of $Cu_2(bdc)_2(dabco)$ was utilized to catalyze click reaction under visible light in DCM or toluene. Typically, $Cu_2(bdc)_2(dabco)$ (0.002 g) was add to the mixture of 4-pentyn-1-ol (0.231 g, 2.75 mmol), 3-azido-1-propanol (0.275 g, 2.75 mmol) and solvent (0.5 ml). After 30-min stirring, the click reaction was carried out by exposing the reaction mixture to a 50 W visible-light LED in a distance of 15 cm. The conversion rate at the given time was determined by GC-MS. Alternatively referring to the reaction condition catalyzed by native $Cu_2(bdc)_2(dabco)$, $Cu_2(bdc)_2(dabco)$@*P*-pollen (0.0071 g) and PDMAEMA@$Cu_2(bdc)_2(dabco)$ (0.133 g) were utilized separately as different type of $Cu_2(bdc)_2(dabco)$ composite to catalyze the photoclick reaction.

Repeated photoclick reaction in DCM and Toluene. The given amount of $Cu_2(bdc)_2(dabco)$@*P*-pollen (0.0071 g) was utilized to catalyze photoclick reaction in DCM and toluene alternatively referring to the reaction condition in $Cu_2(bdc)_2(dabco)$-mediated photoclick reaction, and the reaction was three times repeated for each solvent. The conversion of the given cycle was determined by GC-MS, and yield was measured by the weight of obtained triazole product. After each reaction, $Cu_2(bdc)_2(dabco)$@*P*-pollen was washed with methanol (3 x 5 ml), dried under vacuum at RT, and then utilized for the next reaction.

Cu$_2$(bdc)$_2$(dabco)-mediated Photodegradation of Rhodamine B (RhB). The given amount of Cu$_2$(bdc)$_2$(dabco) was utilized to degrade RhB under visible light in DCM or toluene. Typically, Rhodamine B (1.1 mg) and K$_2$(SO$_3$)$_2$ (0.027 g) were dissolved in water/methanol (1.2 ml, 1:1 volume ratio), and then Cu$_2$(bdc)$_2$(dabco) (2.5 mg) as well as the test solvent (3ml) were add to the mixture. The dye degradation reaction was carried out by exposing the reaction mixture to a 50 W visible-light LED in a distance of 15 cm. The conversion rate at the given time was determined by UV-Vis based on the absorbance at 554 nm which was assigned to RhB.
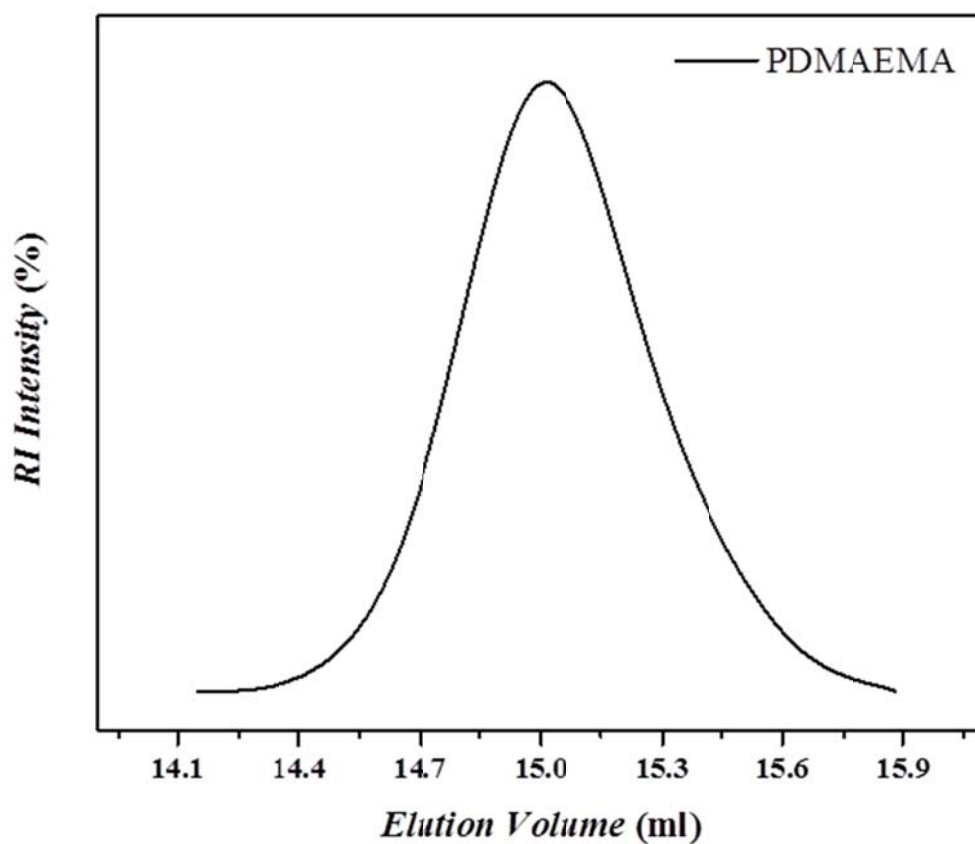

Figure S11. SEC chromatogram of the grafted PDMAEMA cut from *P*-pollen, giving MW of 67,800 and *Đ* = 1.2, using PMMA as standard in NMP.

Appendix VIII. References and Notes

1.   Ouchi, M.; Badi, N.; Lutz, J.-F.; Sawamoto, M., *Nat. Chem.* **2011,** *3* (12), 917-924.
2.   Szwarc, M., *Nature Material* **1956,** *178*, 1168.
3.   Goto, A.; Fukuda, T., *Prog. Polym. Sci.* **2004,** *29* (4), 329-385.
4.   Kamigaito, M.; Ando, T.; Sawamoto, M., *Chem. Rev.* **2001,** *101* (12), 3689-3746.
5.   Matyjaszewski, K., *Macromolecules* **2012,** *45* (10), 4015-4039.
6.   Matyjaszewski, K.; Xia, J., *Chem. Rev.* **2001,** *101* (9), 2921-2990.
7.   Nicolas, J.; Guillaneuf, Y.; Lefay, C.; Bertin, D.; Gigmes, D.; Charleux, B., *Prog. Polym. Sci.* **2013,** *38* (1), 63-235.
8.   Gregory, A.; Stenzel, M. H., *Prog. Polym. Sci.* **2012,** *37* (1), 38-105.
9.   Lutz, J.-F.; Neugebauer, D.; Matyjaszewski, K., *J. Am. Chem. Soc.* **2003,** *125* (23), 6986-6993.
10.   Matsumoto, A., Control of Stereochemistry of Polymers in Radical Polymerization. In *Handbook of Radical Polymerization*, John Wiley & Sons, Inc.: U.S.A., 2003; pp 691-773.
11.   Badi, N.; Lutz, J.-F., *Chem. Soc. Rev.* **2009,** *38* (12), 3383-3390.
12.   Pasparakis, G.; Krasnogor, N.; Cronin, L.; Davis, B. G.; Alexander, C., *Chem. Soc. Rev.* **2010,** *39* (1), 286-300.
13.   ten Brummelhuis, N., *Polym. Chem.* **2015,** *6* (5), 654-667.
14.   Kobayashi, S.; Uyama, H.; Kimura, S., *Chem. Rev.* **2001,** *101* (12), 3793-3818.
15.   Bukau, B.; Horwich, A. L., *Cell* **1998,** *92* (3), 351-366.
16.   Kim, Y. E.; Hipp, M. S.; Bracher, A.; Hayer-Hartl, M.; Hartl, F. U., *Annu. Rev. Biochem.* **2013,** *82* (1), 323-355.
17.   Saiki, R.; Gelfand, D.; Stoffel, S.; Scharf, S.; Higuchi, R.; Horn, G.; Mullis, K.; Erlich, H., *Science* **1988,** *239* (4839), 487-491.
18.   Benetti, E. M.; Kang, C.; Mandal, J.; Divandari, M.; Spencer, N. D., *Macromolecules* **2017,** *50* (15), 5711-5718.
19.   Zetterlund, P. B.; Kagawa, Y.; Okubo, M., *Macromolecules* **2009,** *42* (7), 2488-2496.
20.   Akagi, K.; Piao, G.; Kaneko, S.; Sakamaki, K.; Shirakawa, H.; Kyotani, M., *Science* **1998,** *282* (5394), 1683-1686.
21.   Serizawa, T.; Hamada, K.-i.; Akashi, M., *Nature* **2004,** *429* (6987), 52-55.
22.   Tseng, W.-H.; Chen, C.-K.; Chiang, Y.-W.; Ho, R.-M.; Akasaka, S.; Hasegawa, H., *J. Am. Chem. Soc.* **2009,** *131* (4), 1356-1357.
23.   Kageyama, K.; Tamazawa, J.-i.; Aida, T., *Science* **1999,** *285* (5436), 2113-2115.
24.   Moller, K.; Bein, T.; Fischer, R. X., *Chem. Mater.* **1998,** *10* (7), 1841-1852.
25.   Wu, C.-G.; Bein, T., *Science* **1994,** *266* (5187), 1013-1015.
26.   Ng, S. M.; Ogino, S.-i.; Aida, T.; Koyano, K. A.; Tatsumi, T., *Macromol. Rapid Commun.* **1997,** *18* (12), 991-996.
27.   Uemura, T.; Yanai, N.; Kitagawa, S., *Chem. Soc. Rev.* **2009,** *38* (5), 1228-1236.
28.   Park, I.-H.; Medishetty, R.; Lee, H.-H.; Mulijanto, C. E.; Quah, H. S.; Lee, S. S.; Vittal, J. J., *Angew. Chem., Int. Ed.* **2015,** *54* (25), 7313-7317.
29.   Furukawa, H.; Cordova, K. E.; O'Keeffe, M.; Yaghi, O. M., *Science* **2013,** *341* (6149).
30.   Li, J.-R.; Kuppler, R. J.; Zhou, H.-C., *Chem. Soc. Rev.* **2009,** *38* (5), 1477-1504.
31.   Kreno, L. E.; Leong, K.; Farha, O. K.; Allendorf, M.; Van Duyne, R. P.; Hupp, J. T., *Chem. Rev.* **2012,** *112* (2), 1105-1125.
32.   Zacher, D.; Shekhah, O.; Woll, C.; Fischer, R. A., *Chem. Soc. Rev.* **2009,** *38* (5), 1418-1429.
33.   Bai, Y.; Feng, X.; Xing, H.; Xu, Y.; Kim, B. K.; Baig, N.; Zhou, T.; Gewirth, A. A.; Lu, Y.; Oldfield, E.; Zimmerman, S. C., *J. Am. Chem. Soc.* **2016,** *138* (35), 11077-11080.

34.   Lee, H.-C.; Antonietti, M.; Schmidt, B. V. K. J., *Polym. Chem.* **2016,** *7* (47), 7199-7203.

35.   Nguyen, H. L.; Vu, T. T.; Le, D.; Doan, T. L. H.; Nguyen, V. Q.; Phan, N. T. S., *ACS Catal.* **2017,** *7* (1), 338-342.

36.   Wu, C.-D.; Hu, A.; Zhang, L.; Lin, W., *J. Am. Chem. Soc.* **2005,** *127* (25), 8940-8941.

37.   Uemura, T.; Ono, Y.; Kitagawa, K.; Kitagawa, S., *Macromolecules* **2008,** *41* (1), 87-94.

38.   Kitao, T.; Zhang, Y.; Kitagawa, S.; Wang, B.; Uemura, T., *Chem. Soc. Rev.* **2017**.

39.   Gao, L.; Li, C.-Y. V.; Chan, K.-Y., *Chem. Mater.* **2015,** *27* (10), 3601-3608.

40.   Dhakshinamoorthy, A.; Alvaro, M.; Garcia, H., *Chem. Commun.* **2012,** *48* (92), 11275-11288.

41.   Braunecker, W. A.; Matyjaszewski, K., *Prog. Polym. Sci.* **2007,** *32* (1), 93-146.

42.   Matyjaszewski, K.; Tsarevsky, N. V., *Nat Chem* **2009,** *1* (4), 276-288.

43.   Matyjaszewski, K., *Science* **2011,** *333* (6046), 1104-1105.

44.   Matyjaszewski, K.; Xia, J., Fundamentals of Atom Transfer Radical Polymerization. In *Handbook of Radical Polymerization*, John Wiley & Sons, Inc.: 2003; pp 523-628.

45.   Hawker, C. J.; Bosman, A. W.; Harth, E., *Chem. Rev.* **2001,** *101* (12), 3661-3688.

46.   Moad, G.; Chong, Y. K.; Postma, A.; Rizzardo, E.; Thang, S. H., *Polymer* **2005,** *46* (19), 8458-8468.

47.   Barner-Kowollik, C., Introduction. In *Handbook of RAFT Polymerization*, Wiley-VCH Verlag GmbH & Co. KGaA: 2008; pp 1-4.

48.   Matyjaszewski, K., Controlled/Living Radical Polymerization: State of the Art in 2002. In *Advances in Controlled/Living Radical Polymerization*, American Chemical Society: 2003; Vol. 854, pp 2-9.

49.   di Lena, F.; Matyjaszewski, K., *Prog. Polym. Sci.* **2010,** *35* (8), 959-1021.

50.   Matyjaszewski, K., *Macromol. Symp.* **1996,** *111* (1), 47-61.

51.   Litvinenko, G.; Müller, A. H. E., *Macromolecules* **1997,** *30* (5), 1253-1266.

52.   Tang, W.; Matyjaszewski, K., *Macromolecules* **2006,** *39* (15), 4953-4959.

53.   Tang, W.; Kwak, Y.; Braunecker, W.; Tsarevsky, N. V.; Coote, M. L.; Matyjaszewski, K., *J. Am. Chem. Soc.* **2008,** *130* (32), 10702-10713.

54.   Matyjaszewski, K.; Paik, H.-j.; Zhou, P.; Diamanti, S. J., *Macromolecules* **2001,** *34* (15), 5125-5131.

55.   Tang, W.; Tsarevsky, N. V.; Matyjaszewski, K., *J. Am. Chem. Soc.* **2006,** *128* (5), 1598-1604.

56.   Qiu, J.; Matyjaszewski, K.; Thouin, L.; Amatore, C., *Macromol. Chem. Phys.* **2000,** *201* (14), 1625-1631.

57.   Tsarevsky, N. V.; Matyjaszewski, K., *Chem. Rev.* **2007,** *107* (6), 2270-2299.

58.   Matyjaszewski, K.; Göbelt, B.; Paik, H.-j.; Horwitz, C. P., *Macromolecules* **2001,** *34* (3), 430-440.

59.   Xia, J.; Zhang, X.; Matyjaszewski, K., The Effect of Ligands on Copper-Mediated Atom Transfer Radical Polymerization. In *Transition Metal Catalysis in Macromolecular Design*, American Chemical Society: 2000; Vol. 760, pp 207-223.

60.   Jakubowski, W.; Matyjaszewski, K., *Macromolecules* **2005,** *38* (10), 4139-4146.

61.   Jakubowski, W.; Min, K.; Matyjaszewski, K., *Macromolecules* **2006,** *39* (1), 39-45.

62.   Dong, H.; Matyjaszewski, K., *Macromolecules* **2008,** *41* (19), 6868-6870.

63.   Anastasaki, A.; Nikolaou, V.; Zhang, Q.; Burns, J.; Samanta, S. R.; Waldron, C.; Haddleton, A. J.; McHale, R.; Fox, D.; Percec, V.; Wilson, P.; Haddleton, D. M., *J. Am. Chem. Soc.* **2014,** *136* (3), 1141-1149.

64.   Kwak, Y.; Matyjaszewski, K., *Polym. Int.* **2009,** *58* (3), 242-247.

65.   Matyjaszewski, K.; Jakubowski, W.; Min, K.; Tang, W.; Huang, J.; Braunecker, W. A.; Tsarevsky, N. V., *Proc. Nat. Acad. Sci.* **2006,** *103* (42), 15309-15314.

66.   Simakova, A.; Averick, S. E.; Konkolewicz, D.; Matyjaszewski, K., *Macromolecules* **2012,** *45* (16), 6371-6379.

67.   Averick, S. E.; Bazewicz, C. G.; Woodman, B. F.; Simakova, A.; Mehl, R. A.; Matyjaszewski, K., *Eur. Polym. J.* **2013,** *49* (10), 2919-2924.

68.   Matyjaszewski, K.; Dong, H.; Jakubowski, W.; Pietrasik, J.; Kusumo, A., *Langmuir* **2007,** *23* (8), 4528-4531.

69.   Shivapooja, P.; Ista, L. K.; Canavan, H. E.; Lopez, G. P., *Biointerphases* **2012,** *7* (1), 32.

70.   Leibfarth, F. A.; Mattson, K. M.; Fors, B. P.; Collins, H. A.; Hawker, C. J., *Angew. Chem., Int. Ed.* **2013,** *52* (1), 199-210.

71.   Tanabe, M.; Vandermeulen, G. W. M.; Chan, W. Y.; Cyr, P. W.; Vanderark, L.; Rider, D. A.; Manners, I., *Nat Mater* **2006,** *5* (6), 467-470.

72.   Yamago, S.; Nakamura, Y., *Polymer* **2013,** *54* (3), 981-994.

73.   Chen, M.; Zhong, M.; Johnson, J. A., *Chem. Rev.* **2016,** *116* (17), 10167-10211.

74.   Rzayev, J.; Penelle, J., *Macromolecules* **2002,** *35* (5), 1489-1490.

75.   Rzayev, J.; Penelle, J., *Angew. Chem., Int. Ed.* **2004,** *43* (13), 1691-1694.

76.   Magenau, A. J. D.; Strandwitz, N. C.; Gennaro, A.; Matyjaszewski, K., *Science* **2011,** *332* (6025), 81-84.

77.   Fors, B. P.; Hawker, C. J., *Angew. Chem., Int. Ed.* **2012,** *51* (35), 8850-8853.

78.   Poelma, J. E.; Fors, B. P.; Meyers, G. F.; Kramer, J. W.; Hawker, C. J., *Angew. Chem., Int. Ed.* **2013,** *52* (27), 6844-6848.

79.   Tasdelen, M. A.; Uygun, M.; Yagci, Y., *Macromol. Rapid Commun.* **2011,** *32* (1), 58-62.

80.   Tasdelen, M. A.; Uygun, M.; Yagci, Y., *Macromol. Chem. Phys.* **2010,** *211* (21), 2271-2275.

81.   Taskin, O. S.; Yilmaz, G.; Tasdelen, M. A.; Yagci, Y., *Polym. Int.* **2014,** *63* (5), 902-907.

82.   Tasdelen, M. A.; Ciftci, M.; Yagci, Y., *Macromol. Chem. Phys.* **2012,** *213* (13), 1391-1396.

83.   Ribelli, T. G.; Konkolewicz, D.; Bernhard, S.; Matyjaszewski, K., *J. Am. Chem. Soc.* **2014,** *136* (38), 13303-13312.

84.   Konkolewicz, D.; Schröder, K.; Buback, J.; Bernhard, S.; Matyjaszewski, K., *ACS Macro Lett.* **2012,** *1* (10), 1219-1223.

85.   Kwak, Y.; Matyjaszewski, K., *Macromolecules* **2010,** *43* (12), 5180-5183.

86.   Tasdelen, M. A.; Uygun, M.; Yagci, Y., *Macromol. Chem. Phys.* **2011,** *212* (18), 2036-2042.

87.   Mosnáček, J.; Ilčíková, M., *Macromolecules* **2012,** *45* (15), 5859-5865.

88.   Lewis, F.; Crompton, E., SET Addition of Amines to Alkenes. In *CRC Handbook of Organic Photochemistry and Photobiology, Volumes 1 & 2, Second Edition*, CRC Press: 2003.

89.   Warson, H., *Polym. Int.* **1996,** *41* (3), 352-352.

90.   Ma, J. W.; Cunningham, M. F.; McAuley, K. B.; Keoshkerian, B.; Georges, M. K., *Macromol. Theory Simul.* **2002,** *11* (9), 953-960.

91.   Zetterlund, P. B.; Okubo, M., *Macromol. Theory Simul.* **2005,** *14* (7), 415-420.

92.   Qiu, J.; Pintauer, T.; Gaynor, S. G.; Matyjaszewski, K.; Charleux, B.; Vairon, J.-P., *Macromolecules* **2000,** *33* (20), 7310-7320.

93.   Zetterlund, P. B.; Kagawa, Y.; Okubo, M., *Chem. Rev.* **2008,** *108* (9), 3747-3794.

94.   Cunningham, M. F., *Prog. Polym. Sci.* **2008,** *33* (4), 365-398.

95.   Min, K.; Matyjaszewski, K., *Cent. Eur. J. Chem.* **2009,** *7* (4), 657.

96.   Kagawa, Y.; Zetterlund, P. B.; Minami, H.; Okubo, M., *Macromol. Theory Simul.* **2006,** *15* (8), 608-613.

97.   Nakamura, T.; Okubo, M., *Macromolecules* **2007,** *40* (24), 8663-8672.

98.   Zetterlund, P. B.; Alam, M. N.; Minami, H.; Okubo, M., *Macromol. Rapid Commun.* **2005,** *26* (12), 955-960.

99.   Okubo, M.; Minami, H.; Zhou, J., *Colloid Polym. Sci.* **2004,** *282* (7), 747-752.

100.   Prescott, S. W.; Ballard, M. J.; Gilbert, R. G., *J. Polym. Sci., Part A: Polym. Chem.* **2005,** *43* (5), 1076-1089.

101.   Simms, R. W.; Cunningham, M. F., *Macromolecules* **2008,** *41* (14), 5148-5155.

102.   Simms, R. W.; Cunningham, M. F., *Macromolecules* **2007,** *40* (4), 860-866.

103.   Janiak, C., *Dalton Trans.* **2003,** (14), 2781-2804.

104.   Cheetham, A. K.; Rao, C. N. R.; Feller, R. K., *Chem. Commun.* **2006,** (46), 4780-4795.

105.   O'Keeffe, M., *Chem. Soc. Rev.* **2009,** *38* (5), 1215-1217.

106.   Long, J. R.; Yaghi, O. M., *Chem. Soc. Rev.* **2009,** *38* (5), 1213-1214.

107.   Slater, A. G.; Cooper, A. I., *Science* **2015,** *348* (6238).

108.   Horcajada, P.; Gref, R.; Baati, T.; Allan, P. K.; Maurin, G.; Couvreur, P.; Férey, G.; Morris, R. E.; Serre, C., *Chem. Rev.* **2012,** *112* (2), 1232-1268.

109.   Sumida, K.; Rogow, D. L.; Mason, J. A.; McDonald, T. M.; Bloch, E. D.; Herm, Z. R.; Bae, T.-H.; Long, J. R., *Chem. Rev.* **2012,** *112* (2), 724-781.

110.   Lee, J.; Farha, O. K.; Roberts, J.; Scheidt, K. A.; Nguyen, S. T.; Hupp, J. T., *Chem. Soc. Rev.* **2009,** *38* (5), 1450-1459.

111.   Yu, J.; Cui, Y.; Wu, C.; Yang, Y.; Wang, Z.; O'Keeffe, M.; Chen, B.; Qian, G., *Angew. Chem., Int. Ed.* **2012,** *51* (42), 10542-10545.

112.   Talin, A. A.; Centrone, A.; Ford, A. C.; Foster, M. E.; Stavila, V.; Haney, P.; Kinney, R. A.; Szalai, V.; El Gabaly, F.; Yoon, H. P.; Léonard, F.; Allendorf, M. D., *Science* **2014,** *343* (6166), 66-69.

113.   Kitaura, R.; Kitagawa, S.; Kubota, Y.; Kobayashi, T. C.; Kindo, K.; Mita, Y.; Matsuo, A.; Kobayashi, M.; Chang, H.-C.; Ozawa, T. C.; Suzuki, M.; Sakata, M.; Takata, M., *Science* **2002,** *298* (5602), 2358-2361.

114.   Janiak, C.; Vieth, J. K., *New J. Chem.* **2010,** *34* (11), 2366-2388.

115.   Kaes, C.; Katz, A.; Hosseini, M. W., *Chem. Rev.* **2000,** *100* (10), 3553-3590.

116.   LaDuca, R. L., *Coord. Chem. Rev.* **2009,** *253* (13), 1759-1792.

117.   Biradha, K.; Sarkar, M.; Rajput, L., *Chem. Commun.* **2006,** (40), 4169-4179.

118.   Fujita, M.; Tominaga, M.; Hori, A.; Therrien, B., *Acc. Chem. Res.* **2005,** *38* (4), 369-378.

119.   Abu-Shandi, K.; Janiak, C.; Kersting, B., *Acta Cryst. C* **2001,** *57* (11), 1261-1264.

120.   Pichon, A.; Lazuen-Garay, A.; James, S. L., *CrystEngComm* **2006,** *8* (3), 211-214.

121.   Kuroda, R.; Sato, T.; Imai, Y., *CrystEngComm* **2008,** *10* (12), 1881-1890.

122.   Son, W.-J.; Kim, J.; Kim, J.; Ahn, W.-S., *Chem. Commun.* **2008,** (47), 6336-6338.

123.   Mueller, U.; Schubert, M.; Teich, F.; Puetter, H.; Schierle-Arndt, K.; Pastre, J., *J. Mater. Chem.* **2006,** *16* (7), 626-636.

124.   Ferey, G., *Chem. Soc. Rev.* **2008,** *37* (1), 191-214.

125.   Jhung, S. H.; Yoon, J. W.; Hwang, J.-S.; Cheetham, A. K.; Chang, J.-S., *Chem. Mater.* **2005,** *17* (17), 4455-4460.

126.   Tompsett, G. A.; Conner, W. C.; Yngvesson, K. S., *ChemPhysChem* **2006,** *7* (2), 296-319.

127. Stock, N.; Biswas, S., *Chem. Rev.* **2012,** *112* (2), 933-969.

128. O'Keeffe, M.; Eddaoudi, M.; Li, H.; Reineke, T.; Yaghi, O. M., *J. Solid State Chem.* **2000,** *152* (1), 3-20.

129. Kuppler, R. J.; Timmons, D. J.; Fang, Q.-R.; Li, J.-R.; Makal, T. A.; Young, M. D.; Yuan, D.; Zhao, D.; Zhuang, W.; Zhou, H.-C., *Coord. Chem. Rev.* **2009,** *253* (23), 3042-3066.

130. Deng, H.; Grunder, S.; Cordova, K. E.; Valente, C.; Furukawa, H.; Hmadeh, M.; Gándara, F.; Whalley, A. C.; Liu, Z.; Asahina, S.; Kazumori, H.; O'Keeffe, M.; Terasaki, O.; Stoddart, J. F.; Yaghi, O. M., *Science* **2012,** *336* (6084), 1018-1023.

131. Tranchemontagne, D. J.; Mendoza-Cortes, J. L.; O'Keeffe, M.; Yaghi, O. M., *Chem. Soc. Rev.* **2009,** *38* (5), 1257-1283.

132. Kitagawa, S.; Kitaura, R.; Noro, S.-i., *Angew. Chem., Int. Ed.* **2004,** *43* (18), 2334-2375.

133. Deng, H.; Doonan, C. J.; Furukawa, H.; Ferreira, R. B.; Towne, J.; Knobler, C. B.; Wang, B.; Yaghi, O. M., *Science* **2010,** *327* (5967), 846-850.

134. Tanabe, K. K.; Cohen, S. M., *Chem. Soc. Rev.* **2011,** *40* (2), 498-519.

135. Eddaoudi, M.; Kim, J.; Rosi, N.; Vodak, D.; Wachter, J.; O'Keeffe, M.; Yaghi, O. M., *Science* **2002,** *295* (5554), 469-472.

136. Banerjee, R.; Furukawa, H.; Britt, D.; Knobler, C.; O'Keeffe, M.; Yaghi, O. M., *J. Am. Chem. Soc.* **2009,** *131* (11), 3875-3877.

137. Devic, T.; Horcajada, P.; Serre, C.; Salles, F.; Maurin, G.; Moulin, B.; Heurtaux, D.; Clet, G.; Vimont, A.; Grenèche, J.-M.; Ouay, B. L.; Moreau, F.; Magnier, E.; Filinchuk, Y.; Marrot, J.; Lavalley, J.-C.; Daturi, M.; Férey, G., *J. Am. Chem. Soc.* **2010,** *132* (3), 1127-1136.

138. Wang, Z.; Cohen, S. M., *Chem. Soc. Rev.* **2009,** *38* (5), 1315-1329.

139. Hoskins, B. F.; Robson, R., *J. Am. Chem. Soc.* **1990,** *112* (4), 1546-1554.

140. Wang, Z.; Cohen, S. M., *J. Am. Chem. Soc.* **2007,** *129* (41), 12368-12369.

141. Garibay, S. J.; Wang, Z.; Tanabe, K. K.; Cohen, S. M., *Inorg. Chem.* **2009,** *48* (15), 7341-7349.

142. Wang, Z.; Tanabe, K. K.; Cohen, S. M., *Inorg. Chem.* **2009,** *48* (1), 296-306.

143. Tanabe, K. K.; Wang, Z.; Cohen, S. M., *J. Am. Chem. Soc.* **2008,** *130* (26), 8508-8517.

144. Kawamichi, T.; Kodama, T.; Kawano, M.; Fujita, M., *Angew. Chem., Int. Ed.* **2008,** *47* (42), 8030-8032.

145. Wang, Z.; Cohen, S. M., *J. Am. Chem. Soc.* **2009,** *131* (46), 16675-16677.

146. Qiu, S.; Xue, M.; Zhu, G., *Chem. Soc. Rev.* **2014,** *43* (16), 6116-6140.

147. Denny Jr, M. S.; Moreton, J. C.; Benz, L.; Cohen, S. M., **2016,** *1*, 16078.

148. Zhu, Q.-L.; Xu, Q., *Chem. Soc. Rev.* **2014,** *43* (16), 5468-5512.

149. Kitao, T.; Zhang, Y.; Kitagawa, S.; Wang, B.; Uemura, T., *Chem. Soc. Rev.* **2017,** *46* (11), 3108-3133.

150. Bein, T., Conjugated and conducting nanostructures in zeolites. In *Studies in Surface Science and Catalysis*, Chon, H.; Woo, S. I.; Park, S. E., Eds. Elsevier: 1996; Vol. 102, pp 295-322.

151. Chikada, M.; Sada, K.; Miyata, M., *Polym. J.* **1999,** *31* (11_2), 1061-1064.

152. Cardin, D. J., *Adv. Mater.* **2002,** *14* (8), 553-563.

153. Enzel, P.; Bein, T., *J. Chem. Soc., Chem. Commun.* **1989,** (18), 1326-1327.

154. Sozzani, P.; di Silvestro, G.; Gervasini, A., *J. Polym. Sci., Part A: Polym. Chem.* **1986,** *24* (5), 815-825.

155. Uemura, T.; Ono, Y.; Hijikata, Y.; Kitagawa, S., *J. Am. Chem. Soc.* **2010,** *132* (13), 4917-4924.

156.   Uemura, T.; Uchida, N.; Higuchi, M.; Kitagawa, S., *Macromolecules* **2011,** *44* (8), 2693-2697.

157.   Uemura, T.; Kitagawa, K.; Horike, S.; Kawamura, T.; Kitagawa, S.; Mizuno, M.; Endo, K., *Chem. Commun.* **2005,** (48), 5968-5970.

158.   Uemura, T.; Kaseda, T.; Kitagawa, S., *Chem. Mater.* **2013,** *25* (18), 3772-3776.

159.   Uemura, T.; Kaseda, T.; Sasaki, Y.; Inukai, M.; Toriyama, T.; Takahara, A.; Jinnai, H.; Kitagawa, S., **2015,** *6*, 7473.

160.   Distefano, G.; Suzuki, H.; Tsujimoto, M.; Isoda, S.; Bracco, S.; Comotti, A.; Sozzani, P.; Uemura, T.; Kitagawa, S., *Nat Chem* **2013,** *5* (4), 335-341.

161.   Hunt, M. A.; Jung, D. W.; Shamsheer, M.; Uyar, T.; Tonelli, A. E., *Polymer* **2004,** *45* (4), 1345-1347.

162.   Kobayashi, Y.; Horie, Y.; Honjo, K.; Uemura, T.; Kitagawa, S., *Chem. Commun.* **2016,** *52* (29), 5156-5159.

163.   Uemura, T.; Kitaura, R.; Ohta, Y.; Nagaoka, M.; Kitagawa, S., *Angewandte Chemie* **2006,** *118* (25), 4218-4222.

164.   Gospodinova, N.; Terlemezyan, L., *Prog. Polym. Sci.* **1998,** *23* (8), 1443-1484.

165.   Dhara, B.; Ballav, N., *RSC Adv.* **2013,** *3* (15), 4909-4913.

166.   Uemura, T.; Kadowaki, Y.; Yanai, N.; Kitagawa, S., *Chem. Mater.* **2009,** *21* (18), 4096-4098.

167.   Park, I.-H.; Chanthapally, A.; Zhang, Z.; Lee, S. S.; Zaworotko, M. J.; Vittal, J. J., *Angew. Chem., Int. Ed.* **2014,** *53* (2), 414-419.

168.   Furukawa, Y.; Ishiwata, T.; Sugikawa, K.; Kokado, K.; Sada, K., *Angew. Chem., Int. Ed.* **2012,** *51* (42), 10566-10569.

169.   Zhang, Z.; Nguyen, H. T. H.; Miller, S. A.; Cohen, S. M., *Angew. Chem., Int. Ed.* **2015,** *54* (21), 6152-6157.

170.   Nagata, S.; Kokado, K.; Sada, K., *Chem. Commun.* **2015,** *51* (41), 8614-8617.

171.   Edmondson, S.; Osborne, V. L.; Huck, W. T. S., *Chem. Soc. Rev.* **2004,** *33* (1), 14-22.

172.   Zhang, Y.; Feng, X.; Li, H.; Chen, Y.; Zhao, J.; Wang, S.; Wang, L.; Wang, B., *Angew. Chem., Int. Ed.* **2015,** *54* (14), 4259-4263.

173.   Xie, K.; Fu, Q.; He, Y.; Kim, J.; Goh, S. J.; Nam, E.; Qiao, G. G.; Webley, P. A., *Chem. Commun.* **2015,** *51* (85), 15566-15569.

174.   Liu, H.; Zhu, H.; Zhu, S., *Macromol. Mater. Eng.* **2015,** *300* (2), 191-197.

175.   Corma, A.; García, H.; Llabrés i Xamena, F. X., *Chem. Rev.* **2010,** *110* (8), 4606-4655.

176.   Farrusseng, D.; Aguado, S.; Pinel, C., *Angew. Chem., Int. Ed.* **2009,** *48* (41), 7502-7513.

177.   Rodenas, T.; van Dalen, M.; García-Pérez, E.; Serra-Crespo, P.; Zornoza, B.; Kapteijn, F.; Gascon, J., *Adv. Funct. Mater.* **2014,** *24* (2), 249-256.

178.   Gascon, J.; Corma, A.; Kapteijn, F.; Llabrés i Xamena, F. X., *ACS Catal.* **2014,** *4* (2), 361-378.

179.   Chughtai, A. H.; Ahmad, N.; Younus, H. A.; Laypkov, A.; Verpoort, F., *Chem. Soc. Rev.* **2015,** *44* (19), 6804-6849.

180.   Goesten, M. G.; Kapteijn, F.; Gascon, J., *CrystEngComm* **2013,** *15* (45), 9249-9257.

181.   Hasegawa, S.; Horike, S.; Matsuda, R.; Furukawa, S.; Mochizuki, K.; Kinoshita, Y.; Kitagawa, S., *J. Am. Chem. Soc.* **2007,** *129* (9), 2607-2614.

182.   Valvekens, P.; Vermoortele, F.; De Vos, D., *Catal. Sci. Technol.* **2013,** *3* (6), 1435-1445.

183.   Venkataraman, D.; Gardner, G. B.; Lee, S.; Moore, J. S., *J. Am. Chem. Soc.* **1995,** *117* (46), 11600-11601.

184.   Seo, J. S.; Whang, D.; Lee, H.; Jun, S. I.; Oh, J.; Jeon, Y. J.; Kim, K., **2000,** *404*, 982.

185.   Meilikhov, M.; Yusenko, K.; Esken, D.; Turner, S.; Van Tendeloo, G.; Fischer, R. A., *Eur. J. Inorg. Chem.* **2010,** *2010* (24), 3701-3714.

186.   Juan-Alcaniz, J.; Gascon, J.; Kapteijn, F., *J. Mater. Chem.* **2012,** *22* (20), 10102-10118.

187.   Férey, G.; Mellot-Draznieks, C.; Serre, C.; Millange, F.; Dutour, J.; Surblé, S.; Margiolaki, I., *Science* **2005,** *309* (5743), 2040-2042.

188.   Cavka, J. H.; Jakobsen, S.; Olsbye, U.; Guillou, N.; Lamberti, C.; Bordiga, S.; Lillerud, K. P., *J. Am. Chem. Soc.* **2008,** *130* (42), 13850-13851.

189.   Colombo, V.; Galli, S.; Choi, H. J.; Han, G. D.; Maspero, A.; Palmisano, G.; Masciocchi, N.; Long, J. R., *Chem. Sci.* **2011,** *2* (7), 1311-1319.

190.   Huang, L.; Wang, H.; Chen, J.; Wang, Z.; Sun, J.; Zhao, D.; Yan, Y., *Microporous Mesoporous Mater.* **2003,** *58* (2), 105-114.

191.   Hausdorf, S.; Wagler, J.; Moβig, R.; Mertens, F. O. R. L., *J. Phys. Chem. A* **2008,** *112* (33), 7567-7576.

192.   Chui, S. S.-Y.; Lo, S. M.-F.; Charmant, J. P. H.; Orpen, A. G.; Williams, I. D., *Science* **1999,** *283* (5405), 1148-1150.

193.   Alvaro, M.; Carbonell, E.; Ferrer, B.; Llabrés i Xamena, F. X.; Garcia, H., *Chemistry – A European Journal* **2007,** *13* (18), 5106-5112.

194.   Tachikawa, T.; Choi, J. R.; Fujitsuka, M.; Majima, T., *J. Phys. Chem. C* **2008,** *112* (36), 14090-14101.

195.   Gascon, J.; Hernández-Alonso, M. D.; Almeida, A. R.; van Klink, G. P. M.; Kapteijn, F.; Mul, G., *ChemSusChem* **2008,** *1* (12), 981-983.

196.   Gomes Silva, C.; Luz, I.; Llabrés i Xamena, F. X.; Corma, A.; García, H., *Chemistry – A European Journal* **2010,** *16* (36), 11133-11138.

197.   Gascon, J.; Aktay, U.; Hernandez-Alonso, M. D.; van Klink, G. P. M.; Kapteijn, F., *J. Catal.* **2009,** *261* (1), 75-87.

198.   Vermoortele, F.; Vandichel, M.; Van de Voorde, B.; Ameloot, R.; Waroquier, M.; Van Speybroeck, V.; De Vos, D. E., *Angew. Chem., Int. Ed.* **2012,** *51* (20), 4887-4890.

199.   Kitagawa, S.; Noro, S.-i.; Nakamura, T., *Chem. Commun.* **2006,** (7), 701-707.

200.   Ingleson, M. J.; Bacsa, J.; Rosseinsky, M. J., *Chem. Commun.* **2007,** (29), 3036-3038.

201.   Lun, D. J.; Waterhouse, G. I. N.; Telfer, S. G., *J. Am. Chem. Soc.* **2011,** *133* (15), 5806-5809.

202.   Guillerm, V.; Gross, S.; Serre, C.; Devic, T.; Bauer, M.; Ferey, G., *Chem. Commun.* **2010,** *46* (5), 767-769.

203.   Kim, M.; Cahill, J. F.; Fei, H.; Prather, K. A.; Cohen, S. M., *J. Am. Chem. Soc.* **2012,** *134* (43), 18082-18088.

204.   Serre, C.; Millange, F.; Surblé, S.; Férey, G., *Angew. Chem., Int. Ed.* **2004,** *43* (46), 6285-6289.

205.   Kleist, W.; Jutz, F.; Maciejewski, M.; Baiker, A., *Eur. J. Inorg. Chem.* **2009,** *2009* (24), 3552-3561.

206.   Kleist, W.; Maciejewski, M.; Baiker, A., *Thermochim Acta* **2010,** *499* (1), 71-78.

207.   Huang, Y.; Gao, S.; Liu, T.; Lü, J.; Lin, X.; Li, H.; Cao, R., *ChemPlusChem* **2012,** *77* (2), 106-112.

208.   Noro, S.-i.; Kitagawa, S.; Yamashita, M.; Wada, T., *Chem. Commun.* **2002,** (3), 222-223.

209.   Sun, J.-K.; Zhan, W.-W.; Akita, T.; Xu, Q., *J. Am. Chem. Soc.* **2015,** *137* (22), 7063-7066.

210.   Li, Y.; Pink, M.; Karty, J. A.; Flood, A. H., *J. Am. Chem. Soc.* **2008,** *130* (51), 17293-17295.
211.   Wang, J.-L.; Wang, C.; Lin, W., *ACS Catal.* **2012,** *2* (12), 2630-2640.
212.   Singh, A.; Palakollu, V.; Pandey, A.; Kanvah, S.; Sharma, S., *RSC Adv.* **2016,** *6* (105), 103455-103462.
213.   Climent, M. J.; Corma, A.; Iborra, S., *Chem. Rev.* **2011,** *111* (2), 1072-1133.
214.   Lin, W., *J. Solid State Chem.* **2005,** *178* (8), 2486-2490.
215.   Liu, Y.; Xuan, W.; Cui, Y., *Adv. Mater.* **2010,** *22* (37), 4112-4135.
216.   Ma, L.; Abney, C.; Lin, W., *Chem. Soc. Rev.* **2009,** *38* (5), 1248-1256.
217.   Spanggaard, H.; Krebs, F. C., *Sol. Energy Mater Sol. Cells* **2004,** *83* (2), 125-146.
218.   Tumbleston, J. R.; Collins, B. A.; Yang, L.; Stuart, A. C.; Gann, E.; Ma, W.; You, W.; Ade, H., **2014,** *8*, 385.
219.   Li, Y.; Xu, H.; Ouyang, S.; Ye, J., *Phys. Chem. Chem. Phys.* **2016,** *18* (11), 7563-7572.
220.   Zhang, T.; Lin, W., *Chem. Soc. Rev.* **2014,** *43* (16), 5982-5993.
221.   Wang, S.; Wang, X., *Small* **2015,** *11* (26), 3097-3112.
222.   Suh, M. P.; Cheon, Y. E.; Lee, E. Y., *Coord. Chem. Rev.* **2008,** *252* (8), 1007-1026.
223.   Allendorf, M. D.; Bauer, C. A.; Bhakta, R. K.; Houk, R. J. T., *Chem. Soc. Rev.* **2009,** *38* (5), 1330-1352.
224.   Givaja, G.; Amo-Ochoa, P.; Gomez-Garcia, C. J.; Zamora, F., *Chem. Soc. Rev.* **2012,** *41* (1), 115-147.
225.   Marcus, R. A., *J. Chem. Phys.* **1956,** *24* (5), 966-978.
226.   Nasalevich, M. A.; Goesten, M. G.; Savenije, T. J.; Kapteijn, F.; Gascon, J., *Chem. Commun.* **2013,** *49* (90), 10575-10577.
227.   Savenije, T. J.; Ferguson, A. J.; Kopidakis, N.; Rumbles, G., *J. Phys. Chem. C* **2013,** *117* (46), 24085-24103.
228.   Bellitto, C.; Dessy, G.; Fares, V., *Inorg. Chem.* **1985,** *24* (18), 2815-2820.
229.   Serpone, N.; Emeline, A. V., *J. Phys. Chem. Lett.* **2012,** *3* (5), 673-677.
230.   Chen, X.; Shen, S.; Guo, L.; Mao, S. S., *Chem. Rev.* **2010,** *110* (11), 6503-6570.
231.   Pasveer, W. F.; Cottaar, J.; Tanase, C.; Coehoorn, R.; Bobbert, P. A.; Blom, P. W. M.; de Leeuw, D. M.; Michels, M. A. J., *Phys. Rev. Lett.* **2005,** *94* (20), 206601.
232.   Coropceanu, V.; Cornil, J.; da Silva Filho, D. A.; Olivier, Y.; Silbey, R.; Brédas, J.-L., *Chem. Rev.* **2007,** *107* (4), 926-952.
233.   Kaake, L. G.; Barbara, P. F.; Zhu, X. Y., *J. Phys. Chem. Lett.* **2010,** *1* (3), 628-635.
234.   Silva, C. G.; Corma, A.; Garcia, H., *J. Mater. Chem.* **2010,** *20* (16), 3141-3156.
235.   Hendon, C. H.; Tiana, D.; Walsh, A., *Phys. Chem. Chem. Phys.* **2012,** *14* (38), 13120-13132.
236.   Fuentes-Cabrera, M.; Nicholson, D. M.; Sumpter, B. G.; Widom, M., *J. Chem. Phys.* **2005,** *123* (12), 124713.
237.   Civalleri, B.; Napoli, F.; Noel, Y.; Roetti, C.; Dovesi, R., *CrystEngComm* **2006,** *8* (5), 364-371.
238.   Kuc, A.; Enyashin, A.; Seifert, G., *J. Phys. Chem. B* **2007,** *111* (28), 8179-8186.
239.   Bordiga, S.; Lamberti, C.; Ricchiardi, G.; Regli, L.; Bonino, F.; Damin, A.; Lillerud, K. P.; Bjorgen, M.; Zecchina, A., *Chem. Commun.* **2004,** (20), 2300-2301.
240.   Llabrés i Xamena, F. X.; Corma, A.; Garcia, H., *J. Phys. Chem. C* **2007,** *111* (1), 80-85.
241.   Wang, D.; Huang, R.; Liu, W.; Sun, D.; Li, Z., *ACS Catal.* **2014,** *4* (12), 4254-4260.
242.   Carson, C. G.; Hardcastle, K.; Schwartz, J.; Liu, X.; Hoffmann, C.; Gerhardt, R. A.; Tannenbaum, R., *Eur. J. Inorg. Chem.* **2009,** *2009* (16), 2338-2343.

243.   Li, H.; Eddaoudi, M.; O'Keeffe, M.; Yaghi, O. M., **1999,** *402*, 276.

244.   Laurier, K. G. M.; Vermoortele, F.; Ameloot, R.; De Vos, D. E.; Hofkens, J.; Roeffaers, M. B. J., *J. Am. Chem. Soc.* **2013,** *135* (39), 14488-14491.

245.   Shi, L.; Wang, T.; Zhang, H.; Chang, K.; Meng, X.; Liu, H.; Ye, J., *Advanced Science* **2015,** *2* (3).

246.   Liang, R.; Jing, F.; Shen, L.; Qin, N.; Wu, L., *J. Hazard. Mater.* **2015,** *287* (Supplement C), 364-372.

247.   Dan-Hardi, M.; Serre, C.; Frot, T.; Rozes, L.; Maurin, G.; Sanchez, C.; Férey, G., *J. Am. Chem. Soc.* **2009,** *131* (31), 10857-10859.

248.   Fu, Y.; Sun, D.; Chen, Y.; Huang, R.; Ding, Z.; Fu, X.; Li, Z., *Angewandte Chemie* **2012,** *124* (14), 3420-3423.

249.   Sun, D.; Ye, L.; Li, Z., *Appl. Catal., B* **2015,** *164* (Supplement C), 428-432.

250.   Horiuchi, Y.; Toyao, T.; Saito, M.; Mochizuki, K.; Iwata, M.; Higashimura, H.; Anpo, M.; Matsuoka, M., *J. Phys. Chem. C* **2012,** *116* (39), 20848-20853.

251.   Boutinaud, P.; Cavalli, E., *Chem. Phys. Lett.* **2011,** *503* (4), 239-243.

252.   Yaghi, O. M.; O'Keeffe, M.; Ockwig, N. W.; Chae, H. K.; Eddaoudi, M.; Kim, J., **2003,** *423*, 705.

253.   Yang, L.-M.; Fang, G.-Y.; Ma, J.; Ganz, E.; Han, S. S., *Cryst. Growth Des.* **2014,** *14* (5), 2532-2541.

254.   Hadjichristidis, N.; Iatrou, H.; Pitsikalis, M.; Mays, J., *Prog. Polym. Sci.* **2006,** *31* (12), 1068-1132.

255.   Ouchi, M.; Terashima, T.; Sawamoto, M., *Chem. Rev.* **2009,** *109* (11), 4963-5050.

256.   Li, P.-Z.; Wang, X.-J.; Liu, J.; Lim, J. S.; Zou, R.; Zhao, Y., *J. Am. Chem. Soc.* **2016,** *138* (7), 2142-2145.

257.   Discekici, E. H.; Pester, C. W.; Treat, N. J.; Lawrence, J.; Mattson, K. M.; Narupai, B.; Toumayan, E. P.; Luo, Y.; McGrath, A. J.; Clark, P. G.; Read de Alaniz, J.; Hawker, C. J., *ACS Macro Lett.* **2016,** *5* (2), 258-262.

258.   Lyons, A. M.; Vasile, M. J.; Pearce, E. M.; Waszczak, J. V., *Macromolecules* **1988,** *21* (11), 3125-3134.

259.   Finsy, V.; Ma, L.; Alaerts, L.; De Vos, D. E.; Baron, G. V.; Denayer, J. F. M., *Microporous and Mesoporous Materials* **2009,** *120* (3), 221-227.

260.   Zhang, Y.; Feng, X.; Li, H.; Chen, Y.; Zhao, J.; Wang, S.; Wang, L.; Wang, B., *Angew. Chem.* **2015,** *127* (14), 4333-4337.

261.   Arita, T.; Buback, M.; Janssen, O.; Vana, P., *Macromol. Rapid Commun.* **2004,** *25* (15), 1376-1381.

262.   Carmean, R. N.; Becker, T. E.; Sims, M. B.; Sumerlin, B. S., *Chem* **2017,** *2* (1), 93-101.

263.   Xue, L.; Agarwal, U. S.; Lemstra, P. J., *Macromolecules* **2002,** *35* (22), 8650-8652.

264.   Grimaud, T.; Matyjaszewski, K., *Macromolecules* **1997,** *30* (7), 2216-2218.

265.   Jakubowski, W.; Kirci-Denizli, B.; Gil, R. R.; Matyjaszewski, K., *Macromol. Chem. Phys.* **2008,** *209* (1), 32-39.

266.   Kong, X.; Deng, H.; Yan, F.; Kim, J.; Swisher, J. A.; Smit, B.; Yaghi, O. M.; Reimer, J. A., *Science* **2013,** *341* (6148), 882-885.

267.   Le Ouay, B.; Kitagawa, S.; Uemura, T., *J. Am. Chem. Soc.* **2017,** *139* (23), 7886-7892.

268.   Dybtsev, D. N.; Chun, H.; Kim, K., *Angew. Chem., Int. Ed.* **2004,** *43* (38), 5033-5036.

269.   Chun, H.; Dybtsev, D. N.; Kim, H.; Kim, K., *Chem. – Eur. J.* **2005,** *11* (12), 3521-3529.

270.   Lee, H.-C.; Hsueh, H.-Y.; Jeng, U. S.; Ho, R.-M., *Macromolecules* **2014,** *47* (9), 3041-3051.

271.   Schneemann, A.; Bon, V.; Schwedler, I.; Senkovska, I.; Kaskel, S.; Fischer, R. A., *Chem. Soc. Rev.* **2014,** *43* (16), 6062-6096.

272.   Min, K.; Matyjaszewski, K., *Open Chem.* **2009,** *7* (4), 657.

273.   Mondloch, J. E.; Katz, M. J.; Planas, N.; Semrouni, D.; Gagliardi, L.; Hupp, J. T.; Farha, O. K., *Chem. Commun.* **2014,** *50* (64), 8944-8946.

274.   Ajayan, P. M.; Iijima, S., *Nature* **1993,** *361*, 333.

275.   Fang, Z.; Bueken, B.; De Vos, D. E.; Fischer, R. A., *Angew. Chem., Int. Ed.* **2015,** *54* (25), 7234-7254.

276.   Sholl, D. S.; Lively, R. P., *The Journal of Physical Chemistry Letters* **2015,** *6* (17), 3437-3444.

277.   Spevacek, J.; Schneider, B.; Straka, J., *Macromolecules* **1990,** *23* (12), 3042-3051.

278.   Kitayama, T.; Fujimoto, N.; Terawaki, Y.; Hatada, K., *Polymer Bulletin* **1990,** *23* (3), 279-286.

279.   Spěváček, J.; Schneider, B., *Colloid Polym. Sci.* **1980,** *258* (5), 621-625.

280.   Goh, T. K.; Tan, J. F.; Guntari, S. N.; Satoh, K.; Blencowe, A.; Kamigaito, M.; Qiao, G. G., *Angew. Chem., Int. Ed.* **2009,** *48* (46), 8707-8711.

281.   Fantin, M.; Isse, A. A.; Matyjaszewski, K.; Gennaro, A., *Macromolecules* **2017,** *50* (7), 2696-2705.

282.   Wang, Z.; Pan, X.; Yan, J.; Dadashi-Silab, S.; Xie, G.; Zhang, J.; Wang, Z.; Xia, H.; Matyjaszewski, K., *ACS Macro Lett.* **2017,** *6* (5), 546-549.

283.   Anastasaki, A.; Nikolaou, V.; Zhang, Q.; Burns, J.; Samanta, S. R.; Waldron, C.; Haddleton, A. J.; McHale, R.; Fox, D.; Percec, V.; Wilson, P.; Haddleton, D. M., *J. Am. Chem. Soc.* **2014,** *136* (3), 1141-1149.

284.   Comito, R. J.; Fritzsching, K. J.; Sundell, B. J.; Schmidt-Rohr, K.; Dincă, M., *J. Am. Chem. Soc.* **2016,** *138* (32), 10232-10237.

285.   Pan, X.; Tasdelen, M. A.; Laun, J.; Junkers, T.; Yagci, Y.; Matyjaszewski, K., *Prog. Polym. Sci.* **2016,** *62*, 73-125.

286.   Wang, B.; Durantini, J.; Nie, J.; Lanterna, A. E.; Scaiano, J. C., *J. Am. Chem. Soc.* **2016,** *138* (40), 13127-13130.

287.   Fu, Q.; Xie, K.; Tan, S.; Ren, J. M.; Zhao, Q.; Webley, P. A.; Qiao, G. G., *Chem. Commun.* **2016,** *52* (82), 12226-12229.

288.   Karan, C. K.; Sau, M. C.; Bhattacharjee, M., *Chem. Commun.* **2017,** *53* (9), 1526-1529.

289.   Discekici, E. H.; Treat, N. J.; Poelma, S. O.; Mattson, K. M.; Hudson, Z. M.; Luo, Y.; Hawker, C. J.; de Alaniz, J. R., *Chem. Commun.* **2015,** *51* (58), 11705-11708.

290.   Mattson, K. M.; Pester, C. W.; Gutekunst, W. R.; Hsueh, A. T.; Discekici, E. H.; Luo, Y.; Schmidt, B. V. K. J.; McGrath, A. J.; Clark, P. G.; Hawker, C. J., *Macromolecules* **2016,** *49* (21), 8162-8166.

291.   Zhang, J.; Dumur, F.; Horcajada, P.; Livage, C.; Xiao, P.; Fouassier, J. P.; Gigmes, D.; Lalevée, J., *Macromol. Chem. Phys.* **2016,** *217* (22), 2534-2540.

292.   Corrigan, N.; Shanmugam, S.; Xu, J.; Boyer, C., *Chem. Soc. Rev.* **2016,** *45* (22), 6165-6212.

293.   Niu, J.; Lunn, D. J.; Pusuluri, A.; Yoo, J. I.; O'Malley, M. A.; Mitragotri, S.; Soh, H. T.; Hawker, C. J., *Nat. Chem.* **2017,** *9* (6), 537-545.

294.   Eibel, A.; Schmallegger, M.; Zalibera, M.; Huber, A.; Bürkl, Y.; Grützmacher, H.; Gescheidt, G., *Eur. J. Inorg. Chem.* **2017,** *2017* (18), 2469-2478.

295.   Fouassier, J. P.; Lalevée, J., Basic Principles and Applications of Photopolymerization Reactions. In *Photoinitiators for Polymer Synthesis*, Wiley-VCH Verlag GmbH & Co. KGaA: 2012; pp 1-1.

296.   Ding, M.; Jiang, X.; Zhang, L.; Cheng, Z.; Zhu, X., *Macromol. Rapid Commun.* **2015,** *36* (19), 1702-1721.

297.   Cheng, C.; Khoshdel, E.; Wooley, K. L., *Nano Lett.* **2006,** *6* (8), 1741-1746.

298.   Jasinski, N.; Lauer, A.; Stals, P. J. M.; Behrens, S.; Essig, S.; Walther, A.; Goldmann, A. S.; Barner-Kowollik, C., *ACS Macro Lett.* **2015,** *4* (3), 298-301.

299.   Kwak, Y.; Magenau, A. J. D.; Matyjaszewski, K., *Macromolecules* **2011,** *44* (4), 811-819.

300.   Soum, A.; Fontanille, M., *Die Makromolekulare Chemie* **1980,** *181* (4), 799-808.

301.   Xia, J.; Zhang, X.; Matyjaszewski, K., *Macromolecules* **1999,** *32* (10), 3531-3533.

302.   Yang, L.-M.; Vajeeston, P.; Ravindran, P.; Fjellvåg, H.; Tilset, M., *Inorg. Chem.* **2010,** *49* (22), 10283-10290.

303.   Butler, K. T.; Hendon, C. H.; Walsh, A., *J. Am. Chem. Soc.* **2014,** *136* (7), 2703-2706.

304.   Nasalevich, M. A.; van der Veen, M.; Kapteijn, F.; Gascon, J., *CrystEngComm* **2014,** *16* (23), 4919.

305.   Pham, H. Q.; Mai, T.; Pham-Tran, N.-N.; Kawazoe, Y.; Mizuseki, H.; Nguyen-Manh, D., *J. Phys. Chem. C* **2014,** *118* (9), 4567-4577.

306.   Lin, C. K.; Zhao, D.; Gao, W. Y.; Yang, Z.; Ye, J.; Xu, T.; Ge, Q.; Ma, S.; Liu, D. J., *Inorg Chem* **2012,** *51* (16), 9039-44.

307.   Deng, X.; Li, Z.; García, H., *Chem. – Eur. J.* **2017,** *23* (47), 11189-11209.

308.   Gao, W.-Y.; Chen, Y.; Niu, Y.; Williams, K.; Cash, L.; Perez, P. J.; Wojtas, L.; Cai, J.; Chen, Y.-S.; Ma, S., *Angew. Chem., Int. Ed.* **2014,** *53* (10), 2615-2619.

309.   Beyzavi, M. H.; Klet, R. C.; Tussupbayev, S.; Borycz, J.; Vermeulen, N. A.; Cramer, C. J.; Stoddart, J. F.; Hupp, J. T.; Farha, O. K., *J. Am. Chem. Soc.* **2014,** *136* (45), 15861-15864.

310.   Seki, K.; Mori, W., *J. Phys. Chem. B* **2002,** *106* (6), 1380-1385.

311.   Tauc, J.; Grigorovici, R.; Vancu, A., *Phys. Status Solidi B* **1966,** *15* (2), 627-637.

312.   Butler, M. A., *J. Appl. Phys.* **1977,** *48* (5), 1914-1920.

313.   Doménech, A.; García, H.; Doménech-Carbó, M. T.; Llabrés-i-Xamena, F., *J. Phys. Chem. C* **2007,** *111* (37), 13701-13711.

314.   Lorandi, F.; Fantin, M.; Isse, A. A.; Gennaro, A., *Polymer* **2015,** *72*, 238-245.

315.   Fantin, M.; Isse, A. A.; Gennaro, A.; Matyjaszewski, K., *Macromolecules* **2015,** *48* (19), 6862-6875.

316.   Fantin, M.; Isse, A. A.; Bortolamei, N.; Matyjaszewski, K.; Gennaro, A., *Electrochimica Acta* **2016,** *222*, 393-401.

317.   Shin, Y.-D.; Han, S.-H.; Samal, S.; Lee, J.-S., *J. Polym. Sci. A Polym. Chem.* **2005,** *43* (3), 607-615.

318.   Tsarevsky, N. V.; Braunecker, W. A.; Brooks, S. J.; Matyjaszewski, K., *Macromolecules* **2006,** *39* (20), 6817-6824.

319.   Lin, C. Y.; Coote, M. L.; Petit, A.; Richard, P.; Poli, R.; Matyjaszewski, K., *Macromolecules* **2007,** *40* (16), 5985-5994.

320.   Nanda, A. K.; Matyjaszewski, K., *Macromolecules* **2003,** *36* (22), 8222-8224.

321.   Chaemchuen, S.; Luo, Z.; Zhou, K.; Mousavi, B.; Phatanasri, S.; Jaroniec, M.; Verpoort, F., *Journal of Catalysis* **2017,** *354*, 84-91.

322.   Zou, R.-Q.; Sakurai, H.; Han, S.; Zhong, R.-Q.; Xu, Q., *J. Am. Chem. Soc.* **2007,** *129* (27), 8402-8403.

323.   Hong, S. C.; Neugebauer, D.; Inoue, Y.; Lutz, J.-F.; Matyjaszewski, K., *Macromolecules* **2003,** *36* (1), 27-35.

324.   Ray, B.; Isobe, Y.; Morioka, K.; Habaue, S.; Okamoto, Y.; Kamigaito, M.; Sawamoto, M., *Macromolecules* **2003,** *36* (3), 543-545.

325.   Zhu, C.; Fu, S.; Shi, Q.; Du, D.; Lin, Y., *Angewandte Chemie International Edition*, n/a-n/a.

326.   Mavila, S.; Eivgi, O.; Berkovich, I.; Lemcoff, N. G., *Chem. Rev.* **2016,** *116* (3), 878-961.

327.   Chen, Y.; Li, S.; Pei, X.; Zhou, J.; Feng, X.; Zhang, S.; Cheng, Y.; Li, H.; Han, R.; Wang, B., *Angew. Chem., Int. Ed.* **2016,** *55* (10), 3419-3423.

328.   Czaja, A. U.; Trukhan, N.; Muller, U., *Chem. Soc. Rev.* **2009,** *38* (5), 1284-1293.

329.   Carné-Sánchez, A.; Imaz, I.; Cano-Sarabia, M.; Maspoch, D., *Nat. Chem.* **2013,** *5* (3), 203-211.

330.   Rodenas, T.; Luz, I.; Prieto, G.; Seoane, B.; Miro, H.; Corma, A.; Kapteijn, F.; Llabrés i Xamena, F. X.; Gascon, J., *Nat Mater* **2015,** *14* (1), 48-55.

331.   Liu, W.; Huang, J.; Yang, Q.; Wang, S.; Sun, X.; Zhang, W.; Liu, J.; Huo, F., *Angewandte Chemie International Edition* **2017,** *56* (20), 5512-5516.

332.   Yang, X.-F.; Wang, A.; Qiao, B.; Li, J.; Liu, J.; Zhang, T., *Acc. Chem. Res.* **2013,** *46* (8), 1740-1748.

333.   Schacher, F.; Ulbricht, M.; Müller, A. H. E., *Adv. Funct. Mater.* **2009,** *19* (7), 1040-1045.

334.   Warren, S. C.; Messina, L. C.; Slaughter, L. S.; Kamperman, M.; Zhou, Q.; Gruner, S. M.; DiSalvo, F. J.; Wiesner, U., *Science* **2008,** *320* (5884), 1748-1752.

335.   Potroz, M. G.; Mundargi, R. C.; Gillissen, J. J.; Tan, E.-L.; Meker, S.; Park, J. H.; Jung, H.; Park, S.; Cho, D.; Bang, S.-I.; Cho, N.-J., *Adv. Funct. Mater.* **2017,** *27* (31), 1700270-n/a.

336.   Fadiran, O. O.; Meredith, J. C., *J. Mater. Chem. A* **2014,** *2* (40), 17031-17040.

337.   Vasicek, T. W.; Jenkins, S. V.; Vaz, L.; Chen, J.; Stenken, J. A., *J. Colloid Interface Sci.* **2017,** *506* (Supplement C), 338-345.

338.   Hahn, M. W.; Abadzic, D.; O'Melia, C. R., *Environ. Sci. Technol.* **2004,** *38* (22), 5915-5924.

339.   Moh, L. C. H.; Losego, M. D.; Braun, P. V., *Langmuir* **2011,** *27* (7), 3698-3702.

340.   Peris, E.; A. Mata, J.; Moliner, V., *Journal of the Chemical Society, Dalton Transactions* **1999,** (21), 3893-3898.

341.   Coates, J., Interpretation of Infrared Spectra, A Practical Approach. In *Encyclopedia of Analytical Chemistry*, John Wiley & Sons, Ltd: 2006.

342.   Atkin, S. L.; Barrier, S.; Cui, Z.; Fletcher, P. D. I.; Mackenzie, G.; Panel, V.; Sol, V.; Zhang, X., *Journal of Photochemistry and Photobiology B: Biology* **2011,** *102* (3), 209-217.

343.   Lee, H.-C.; Fantin, M.; Antonietti, M.; Matyjaszewski, K.; Schmidt, B. V. K. J., *Chem. Mater.* **2017,** *29* (21), 9445-9455.

344.   Sing, K. S. W.; Everett, D. H.; Haul, R. A. W.; Moscou, L.; Pierotti, R. A.; Rouquerol, J.; Siemieniewska, T., Reporting Physisorption Data for Gas/Solid Systems. In *Handbook of Heterogeneous Catalysis*, Wiley-VCH Verlag GmbH & Co. KGaA: 2008.

345.   Thommes, M.; Kaneko, K.; Neimark Alexander, V.; Olivier James, P.; Rodriguez-Reinoso, F.; Rouquerol, J.; Sing Kenneth, S. W., Physisorption of gases, with special reference to the evaluation of surface area and pore size distribution (IUPAC Technical Report). In *Pure and Applied Chemistry*, 2015; Vol. 87, p 1051.

346.   Sheldrick, G., *Acta Cryst. C* **2015,** *71* (1), 3-8.

347.   Williams, V. A.; Matyjaszewski, K., *Macromolecules* **2015,** *48* (18), 6457-6464.

348.   Gavranovic, G. T.; Csihony, S.; Bowden, N. B.; Hawker, C. J.; Waymouth, R. M.; Moerner, W. E.; Fuller, G. G., *Macromolecules* **2006,** *39* (23), 8121-8127.

349.   Gondi, S. R.; Vogt, A. P.; Sumerlin, B. S., *Macromolecules* **2007,** *40* (3), 474-481.

350.   Kim, H. K.; Yun, W. S.; Kim, M.-B.; Kim, J. Y.; Bae, Y.-S.; Lee, J.; Jeong, N. C., *J. Am. Chem. Soc.* **2015,** *137* (31), 10009-10015.
351.   Tranchemontagne, D. J.; Hunt, J. R.; Yaghi, O. M., *Tetrahedron* **2008,** *64* (36), 8553-8557.
352.   Qian, J.; Sun, F.; Qin, L., *Mater. Lett.* **2012,** *82* (Supplement C), 220-223.

Appendix IX. Publications and Conference Contributions

Publication

A Cu(II) metal–organic framework as a recyclable catalyst for ARGET ATRP
Lee, H. C.; Antonietti, M.; Schmidt, B. V. K. J., *Polym. Chem.* **2016**, *7* (47), 7199-7203.

Synergic Effect between Nucleophilic Monomers and Cu(II)-Metal-Organic Framework for Visible Light-Triggered Controlled Photopolymerization
Lee, H. C.; Fantin, M.; Antonietti, M.; Matyjaszewski, K.; Schmidt, B. V. K. J., *Chem. Mater.* **2017**, *29* (21), 9445-9455.

Free radical and RAFT polymerization of vinyl esters in metalorganic-frameworks
Hwang, J.; **Lee, H. C.**; Antonietti, M.; Schmidt, B.V. K. J., *Polym. Chem.* **2017,** 8 (40), 6204-6208.

Toward Ultimate Control of Radical Polymerization: Functionalized Metal–Organic Frameworks as a Robust Environment for Metal-Catalyzed Polymerizations
Lee, H. C.; Hwang, J.; Schilde, U.; Antonietti, M.; Matyjaszewski, K.; Schmidt, B.V. K. J., *Chem. Mater.* **2017**, *30* (9), 2983-2994.

Dispersion of Nano-MOFs via a Stimuli-Responsive Biohybrid System with Enhanced Photocatalytic Performance
Lee, H. C.; Hwang, J.; Heil, T.; Sun, J. -K.; Schmidt, B.V. K. J., paper submission.

Conference Contribution

Lee, H. C.; Hwang, J.; Antonietti, M.; Schmidt, B. V. K. J. Max Planck Institute of Colloids and Interfaces Alumni-Meeting, Potsdam, Germany, **2016**.

Lee, H. C.; Antonietti, M.; Schmidt, B. V. K. J. Polydays 2016: Integrating function into polymers, Potsdam, Germany, **2016**.

Lee, H. C.; Antonietti, M.; Schmidt, B. V. K. J. Axel Holmberg Annual Meeting, Berlin, Germany, **2016**.

Lee, H. C.; Matyjaszewski, K.; Antonietti, M.; Schmidt, B. V. K. J. Academic Meet Evonic, Potsdam, Germany, **2017**.

Lee, H. C.; Matyjaszewski, K.; Antonietti, M.; Schmidt, B. V. K. J. Advanced Polymers via Macromolecular Engineering, Ghent, Belgium, **2017**.

Lee, H. C.; Matyjaszewski, K.; Antonietti, M.; Schmidt, B. V. K. J. Bayreuth Polymer Symposium 15th International Symposium on Polymeric Materials, Bayreuth, Germany, **2017**.

Appendix X. Declaration

Die vorliegende Dissertation entstand im Zeitraum zwischen October 2015 und November 2017 am Max‑Planck‑Institut für Kolloid‑ und Grenzflächenforschung unter Betreuung von Prof. Dr. Dr. h.c. Markus Antonietti und Dr. Bernhard V. K. J. Schmidt.

Hiermit erkläre ich, dass die vorliegende Arbeit selbstständig angefertigt wurde und keine anderen als die angegebenen Hilfsmittel und Quellen verwendet wurden.

The present dissertation was conducted during the period from October, 2015 to November, 2017 at Max Planck Institute of Colloids and Interfaces under the supervision of Prof. Dr. Dr. h.c. Markus Antonietti and Dr. Bernhard V. K. J. Schmidt.

I declare that this work was written by myself with the mentioned assistances and references.

Hui-Chun Lee

Potsdam, 27.11.2017